This electronic thesis or dissertation has been downloaded from Explore Bristol Research, http://research-information.bristol.ac.uk

Author:
Jenkins, Alex

Title:
The effects of large tectonic earthquakes on transcrustal magmatic systems

General rights
Access to the thesis is subject to the Creative Commons Attribution - NonCommercial-No Derivatives 4.0 International Public License. A copy of this may be found at https://creativecommons.org/licenses/by-nc-nd/4.0/legalcode This license sets out your rights and the restrictions that apply to your access to the thesis so it is important you read this before proceeding.

Take down policy
Some pages of this thesis may have been removed for copyright restrictions prior to having it been deposited in Explore Bristol Research. However, if you have discovered material within the thesis that you consider to be unlawful e.g. breaches of copyright (either yours or that of a third party) or any other law, including but not limited to those relating to patent, trademark, confidentiality, data protection, obscenity, defamation, libel, then please contact collections-metadata@bristol.ac.uk and include the following information in your message:

- Your contact details
- Bibliographic details for the item, including a URL
- An outline nature of the complaint

Your claim will be investigated and, where appropriate, the item in question will be removed from public view as soon as possible.

The effects of large tectonic earthquakes on transcrustal magmatic systems

By

Alexander Paul Jenkins

Department of Earth Sciences
University of Bristol

A dissertation submitted to the University of Bristol
in accordance with the requirements of the degree of
Doctor of Philosophy in the Faculty of Science.

September 2022

Word count: 35,838

ABSTRACT

The crustal stress field is an important control on transcrustal magmatic systems. However, several processes alter the crustal stress field over a variety of distances and timescales, with potential implications for magmatism. Notably, stress changes from large earthquakes can trigger eruptions at nearby volcanoes, although the prevalence and mechanisms of eruption triggering remain unclear, and volcanoes also exhibit non-eruptive responses to large earthquakes. To further elucidate tectono-magmatic relationships, this thesis conducts statistical analyses of earthquake and eruption records and modelling of earthquake-driven stress changes on magmatic systems.

First, the transcrustal magmatic system concept is explored. This combines reviews of magnetotelluric studies at Andean volcanoes and laboratory-derived electrical conductivity relationships. In general, the electrical conductivity anomalies beneath Andean volcanoes are consistent with a three layer transcrustal model, comprising a deep (>10 km) vertically-extensive partial melt reservoir, overlain by intermediate depth (≈5 km) saline magmatic fluids, and capped by shallow (<3 km) clay alteration layers.

Next, modern earthquake and eruption records are used to generate global time-series of large earthquakes and volcanic eruptions. The global time-series exhibit decadal timescale variations, with global seismic moment release positively correlated with global eruption rate. However, regional time-series do not display a consistent correlation, which discounts eruption triggering by nearby large earthquakes as the cause of the global correlation. Instead, distant eruption triggering or external factors must be responsible.

At more local scales, systematic analyses of modern earthquake and eruption records provide evidence for eruption triggering, with eruption rates around 25% above average within 750 km and 1 year following $M_w \geq 7$ earthquakes. However, eruption rates are also around 10% below average within 750 km and 182 days before $M_w \geq 7$ earthquakes. Furthermore, deep earthquakes have the greatest effect on eruption rates, while earthquakes with different slip orientations affect eruption rates differently.

Finally, modelling of the spatial distribution of static stress changes produced by subduction zone megathrust earthquakes reveals complex effects. Based on the normal stress changes in three mutually-perpendicular directions, seven stress change regimes are defined. Three of these regimes encourage magma ascent by unclamping vertical magmatic pathways and clamping horizontal pathways. However, two of the regimes encourage deep magma storage by unclamping horizontal pathways at depth.

Overall, this thesis demonstrates the importance and complexity of tectono-magmatic relationships. Understanding these relationships, as well as how other processes that alter the crustal stress field, influence magmatic systems and the occurrence of earthquakes represents an excellent opportunity for future research.

ACKNOWLEDGEMENTS

First and foremost, I must sincerely thank my two excellent supervisors, Juliet Biggs and Alison Rust, for all of their support and guidance throughout this PhD. Without our weekly meetings and their ability to retrieve me from down rabbit holes, I fear that I may have fallen so deep that this thesis would now concern the dynamics of the core-mantle boundary. I am also grateful to Juliet and Alison for ensuring that the PhD process has gone smoothly and for helping me to grow in confidence in my research over the last four years.

My thanks also go to my co-authors of the various chapters/publications, Jon Blundy, Jonty Rougier, and Rosa Jara. Their expertise was of invaluable help to me and has greatly contributed to the quality of this thesis.

I am also grateful to my APM panel, Max Werner and Frances Cooper, for their input and support, and my viva examiners, James Verdon and Sebastian Watt, for their scrutiny of my work and subsequent feedback.

Within the broader school of earth sciences, there are too many people to name who have helped me during this process, be it scientifically, with admin, or just by making some days that little bit better. However, special thanks must go to all the members of the COMET and GCB research groups, as well as those with whom I have shared an office. In particular, thanks to Robbie for his knowledge of coding and earthquakes (and extra thanks for putting up with me talking about volcanoes), Luke for his knowledge of tectonics, Mark and Stanley for their knowledge of volcanoes, Fabien for his knowledge of everything, y también a Jessica por ayudarme a aprender algo de español, que por desgracia (¡o por suerte para los Peruanos!) nunca pude poner en practica (muchas gracias a la pandemia mundial...).

This PhD was funded by NERC, with support from BHP, so my thanks also go to my funding bodies and all the relevant people involved in facilitating this.

Last but far from least, this project would not have been possible without the support of my family and friends. Especially Becca, who has both put up with the highs and lows of my PhD during the last four years and essentially looked after me and kept me sane during these last two months of writing.

AUTHOR'S DECLARATION

I declare that the work in this dissertation was carried out in accordance with the requirements of the University's Regulations and Code of Practice for Research Degree Programmes and that it has not been submitted for any other academic award. Except where indicated by specific reference in the text, the work is the candidate's own work. Work done in collaboration with, or with the assistance of, others, is indicated as such. Any views expressed in the dissertation are those of the author.

SIGNED: .....ALEX JENKINS................... DATE: .....09/09/2022..............

TABLE OF CONTENTS

LIST OF TABLES

LIST OF FIGURES

FIGURE **Page**

A NOTE ON PREVIOUS PUBLICATION

The backbone of this PhD thesis consists of four independent, but broadly related, science chapters. At the time of thesis submission, two of these science chapters are published as articles in scientific journals (Chapter 3 as Jenkins, Biggs, Rust & Rougier (2021) and Chapter 5 as Jenkins, Biggs, Rust & Jara (2021)), while the remaining two science chapters are in preparation for publication. For all chapters, the scientific research and initial drafting of the manuscript were performed solely by myself. My supervisors and co-authors provided research guidance and direction, as well as suggestions to improve the manuscripts.

The science chapters included here are essentially unaltered from their publication form, only with their supplementary materials inserted into the main text where appropriate and some minor alterations and additions performed at the examiners request. Consequently, each science chapter may be read as a standalone contribution, complete with introduction, methods, results, discussion, and conclusion. To provide a coherent thesis, the science chapters are bookended by a broad introduction covering all the necessary background and a conclusion which links these works together and further builds upon their findings. With this approach, some duplication of material is unfortunately unavoidable. I would also like to highlight the non-linear trajectory of (at least my) scientific research; the science chapters are ordered here so as to make the most sense to the reader, which differs from the order in which the work was performed.

By this point, the reader likely finds themselves quaking with excitement and about to erupt with anticipation, so please do turn over and begin...

CHAPTER 1

INTRODUCTION

'We see, therefore, that in 1835, the earthquake of Chile, the activity of the train of neighbouring volcanos, the elevation of the land around Concepcion, and the submarine eruption at Juan Fernandez, took place simultaneously, and were parts of one and the same great phenomenon.'

—Charles Darwin (1840) on witnessing the 1835 Concepción earthquake.

1.1 Motivation

This thesis concerns the relationship and interactions between large earthquakes and magmatic systems. As potentially devastating natural events, there is some rationality in envisaging a connection between earthquakes and volcanic eruptions, which represent the surface expression of magmatism. This is especially true considering that for much of human history, such natural disasters were predominantly attributable to the whims of the local deity(ies). From a more scientific perspective, a spatial connection between large earthquakes and volcanoes is evidenced by their coincidence along regions that are now known to be tectonic plate boundaries, in particular at subduction zones. Similarly, the ubiquity of lower magnitude earthquakes at local scales during volcanic unrest and eruption demonstrates a temporal connection between seismicity and magmatism.

Beyond the fundamental spatial correlation between large earthquakes and magmatism, much recent work has considered the potential for interactions between large earthquakes and magmatic systems. The focus of this work has been on the triggering of volcanic eruptions following nearby large earthquakes (e.g. Linde & Sacks 1998, Watt et al. 2009, Sawi & Manga 2018). The eruption triggering hypothesis postulates that stress changes caused by earthquakes, either due to the passage of seismic waves or the relaxation of the crust, are able to destabilise magmatic systems and initiate volcanic eruptions (Hill et al. 2002, Seropian et al. 2021). However, some studies also consider the reverse; that large earthquakes can sometimes inhibit volcanic activity (e.g. Ebmeier et al. 2016, Namiki et al. 2019, Farías & Basualto 2020), or that stress changes generated by magmatism or volcanic eruptions can trigger or inhibit large earthquakes (e.g. Nostro et al. 1998, Walter & Amelung 2006, Feuillet et al. 2006). There also exists a third class of study, which examines the possibility that external factors, such as tides, climate, or even the rotation of the Earth, are able to affect the occurrence of earthquakes and/or volcanic eruptions (e.g. Kasahara 2002, Scholz et al. 2019, Huybers & Langmuir 2009, Olivieri & Spada 2015, Bendick & Bilham 2017, Levin et al. 2019).

Although the relationships between earthquakes and magmatism have been well-studied recently, this thesis identifies opportunities to improve our understanding of tectono-magmatic interactions. Namely, this thesis studies the spatiotemporal relationships between large earthquakes and volcanic eruptions more objectively, rather than only considering how one event triggers another. Furthermore, this thesis also considers the effects of large earthquakes across the entire magmatic system, in addition to how earthquakes affect volcanism specifically. These novel approaches help to reveal new relationships between large earthquakes and magmatism across a range of scales.

To begin, the remainder of this introductory Chapter forms a literature review summarising the relevant background necessary to provide context for this thesis. The topics covered include contemporary views on the structure and controls of magmatic systems, the seismic cycle and stress changes associated with earthquakes, and the interactions between large earthquakes and magmatism.

1.2 Transcrustal magmatic systems

Over recent decades, the classical concept of a shallow melt-dominated magma chamber located some kilometers beneath volcanoes has been superseded by a new model of lower melt fraction, vertically extensive magmatic systems that may span the entire thickness of the crust (Sparks et al. 2019). An important driver of this paradigm shift is the lack of evidence from geophysical studies for large volumes of sub-surface molten rock (Magee et al. 2018, Pritchard et al. 2018). Instead, geophysical observations are more consistent with large volumes of low melt fraction crystal mush, with high melt fraction reservoirs being heterogeneously distributed at smaller scales throughout the system (Cashman et al. 2017). This model is also consistent with geochemical studies on volcanic rocks, which show that magmatic systems can persist for thousands to millions of years in a mushy state, but that volcanic phenocrysts spend only years to centuries in their host magma prior to eruption (Sparks et al. 2019, Turner & Costa 2007, Cooper 2017). Consequently, classical large high melt fraction reservoirs are now mainly believed to be transient features (Sparks & Cashman 2017, Cashman et al. 2017) (Figure 1.1).

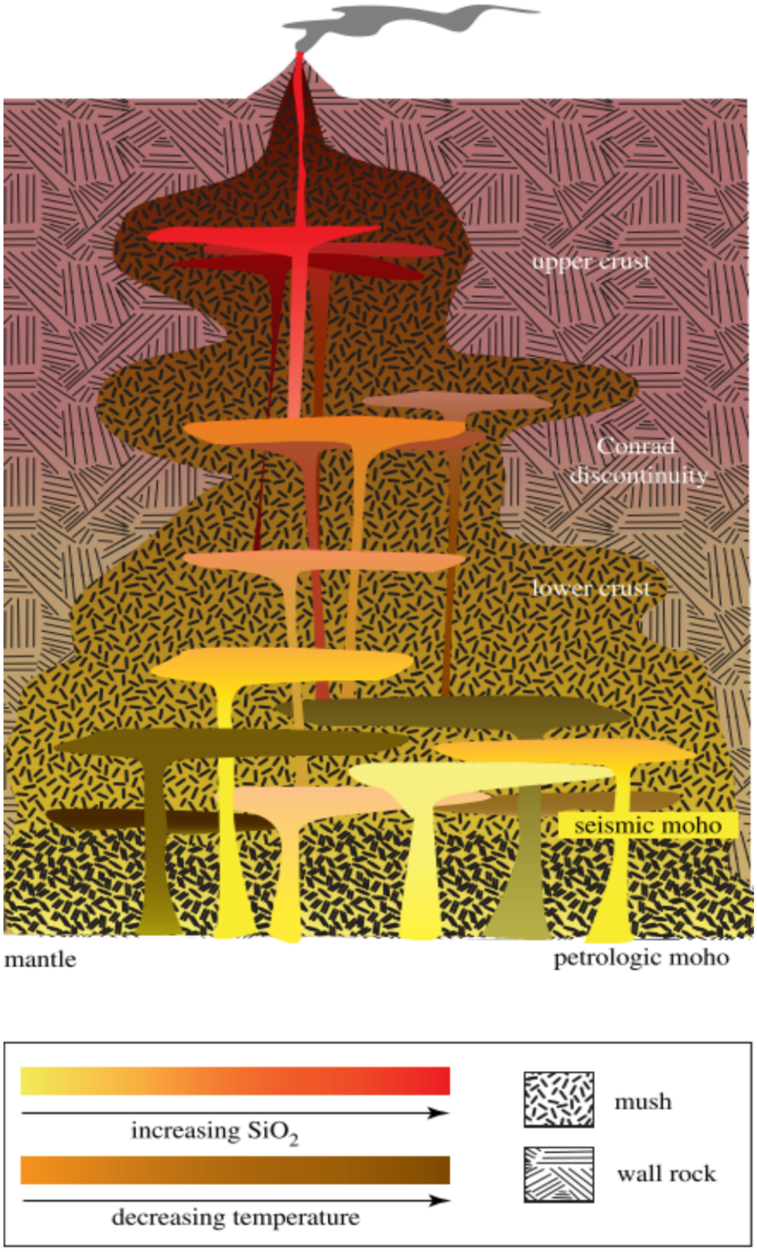

Figure 1.1: Schematic of a transcrustal magmatic system, consisting of high melt fraction lenses within a low melt fraction mush. Figure from Cashman et al. (2017).

The concept of the thermally mature transcrustal magmatic system, with ephemeral high melt fraction lenses existing within a volumetrically larger low melt fraction crystal mush, is perhaps best applied to subduction zones, where the majority of the Earth's sub-aerial volcanoes are located. At subduction zones, the release of fluids from the subducted oceanic slab into the overlying mantle wedge causes partial melting and the generation of basaltic melts (Tatsumi 1989). The primitive basaltic melts then ascend from the mantle wedge to the deep crust, where due to favourable thermal conditions, they are able to accumulate (Hildreth & Moorbath 1988, Comeau et al. 2016). Magmatic differentiation and melt segregation in these deep melt reservoirs then provides a source of more evolved melts to the overlying crust, where if the melt injection rate is sufficiently high, a thermally mature transcrustal magmatic system can develop (Solano et al. 2012). At shallower levels within the transcrustal magmatic system, the exsolution of volatile phases from the melt due to decreasing pressure is also an important process. Exsolved volatiles within melts can be important drivers of volcanic eruptions (Edmonds & Woods 2018), but volatiles can also separate from the melt to form a saline brine lens which overlies the magmatic system (Scott et al. 2017, Afanasyev et al. 2018). In subduction settings, these brine lenses may be preserved as large volumes of hydrothermally altered and potentially mineralised rocks, known as porphyry copper deposits (Sillitoe 2010).

1.3 Controls on magma ascent and storage

Magma transport and storage in the Earth's crust are complex topics (e.g. Gonnermann & Taisne 2015, Kavanagh 2018, Gudmundsson 2020). Nonetheless, melt transfer through the crust is believed to primarily occur by flow within fractures such as dykes (Rubin 1995). Dyke propagation is driven by magmatic overpressure (P_o), which depends on the magma density (ρ_m) relative to the host rock density (ρ_r), the normal stress acting on the dyke (σ_n), and, assuming the dyke is fed from a deeper source of magma, the excess magma pressure above lithostatic in the source reservoir (P_e),

$$P_o = P_e + (\rho_r - \rho_m)gh + \sigma_d, \tag{1.1}$$

where g is the acceleration due to gravity, h is the height above the source reservoir at which P_o is calculated, and

$$\sigma_d = \sigma_l - \sigma_n, \tag{1.2}$$

where σ_l is the lithostatic or overburden stress at the depth where P_o is calculated and σ_n is the normal stress acting on the dyke at the depth where P_o is calculated (Gudmundsson

2012). Dykes generally occupy mode I extensional fractures, which preferentially open parallel to the minimum principal stress direction (σ_3), such that $\sigma_n = \sigma_3$ (Anderson 1951). However, dykes may also follow existing weaknesses in the host rock, such as faults, joints, or layering (Ziv et al. 2000, Magee et al. 2013, Rivalta et al. 2015).

Only a small fraction of dykes reach the surface to feed an eruption; instead, the majority of dykes are arrested or deflected into sills (Crisp 1984, Gudmundsson et al. 1999, Gudmundsson 2005). Equation 1.1 shows that dyke propagation may halt due to a decrease in the buoyancy of the magma, an increase in the normal stress acting on the dyke, or a decrease in the excess pressure in the source reservoir. Dyke arrest may also occur due to cooling and solidification of the magma, especially for more felsic dykes which have higher viscosities (Lister 1995). However, the principal reason for dyke arrest or deflection is believed to be due to layering in the crust (Gudmundsson 2006, 2011). Layers of rocks with different elastic properties cause local rotations of the crustal stress field, such that continued propagation of a dyke becomes unfavourable due to an increase in σ_n (Kavanagh et al. 2006, Menand 2008) (Figure 1.2). Different rock layers may also have different toughness properties (the resistance of the rock to fracture), which can similarly present a barrier to dyke propagation through a layer (Gudmundsson 2011).

Where dykes are deflected into sills, often at interfaces between layers, it is possible for new magma reservoirs to develop. Magma reservoirs can grow from sills when the frequency of dykes being injected into the sill is sufficiently high to prevent cooling and solidification of the sill between dyke injections (Glazner et al. 2004, Annen 2009). Once a magma reservoir is formed, it may act as a magma source for new dyke injections into the overlying rock. The simplest condition for the rupture of a magma reservoir is that the total magma pressure in the reservoir (P_t) is greater than or equal to the minimum principal stress (σ_3) and the tensile strength of the host rock (T_0)

$$P_t \geq \sigma_3 + T_0, \tag{1.3}$$

where,

$$P_t = P_l + P_e, \tag{1.4}$$

where P_l is the lithostatic pressure at the depth of the magma reservoir and P_e is the excess magma pressure above lithostatic in the reservoir (Gudmundsson 2012). Assuming that prior to the generation of any excess magma pressure, the magma reservoir was in lithostatic equilibrium with the host rock (i.e. $P_l = \sigma_1 = \sigma_2 = \sigma_3$), it can be seen that the failure criteria becomes

$$P_l + P_e \geq P_l + T_0, \tag{1.5}$$

so most magma reservoirs fail when $P_e \geq T_0$ (Gudmundsson 2012). Equation 1.3 shows that magma reservoir rupture and formation of a new dyke may occur due to an increase in P_e, which may be caused by the injection of new magma into the reservoir or the exsolution of dissolved volatiles, or a change in the crustal stress field that reduces σ_3.

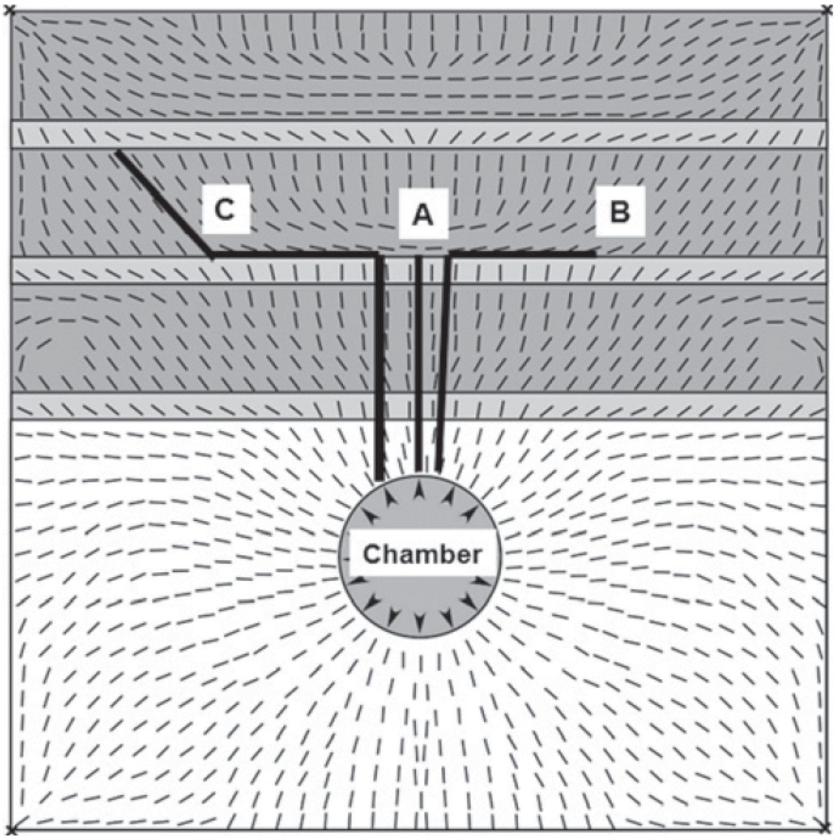

Figure 1.2: The trajectories of the maximum principal stress direction (σ_1, tick marks) in layered media subjected to loading due to excess pressure of 5 MPa in the spherical magma reservoir. The thin layers have a soft Young's modulus of 1 GPa, while the thick layers have a stiff Young's modulus of 100 GPa. Dykes injected from the magma reservoir (thick black lines) preferentially follow the trajectories of σ_1 and can become arrested (A,B) or deflected (B,C) at layer contacts. Figure from Gudmundsson (2020).

1.4 Timescales of volcanotectonic processes

As shown by Equation 1.1 and Equation 1.3, the crustal stress field is an important control on both the stability of melt reservoirs and the transport of melt in dykes. At the regional scale (100s of kilometers), the primary control on the crustal stress field is plate tectonics, with average stress orientations consistent with those expected due to plate motions (Zoback & Zoback 1980, Townend et al. 2012). However, even for a given tectonic setting, the crustal stress regime can be variable. For example, at subduction zones, which host the majority of Earth's sub-aerial volcanoes, there can be variable convergence angles and velocities between the two plates, variable dip angles of the down-going slab, and heterogeneity in the structures present both on the subducted slab and within the overriding plate, all of which may affect the long-term crustal stress regime (Jarrard 1986, Dominguez et al. 1998, Doglioni et al. 2007, Hayes et al. 2018).

Variable stress regimes at subduction zones can affect magmatic systems in the associated volcanic arcs. For example, shallow magma reservoirs (<5 km depth) and high volcanic output rates are more common in volcanic arcs with extensional or strike-slip stress regimes than in arcs under compressional regimes (Chaussard & Amelung 2014, Acocella & Funiciello 2010). The interplay between the crustal stress field and structures in the volcanic arc is also important. For example, in the Southern Volcanic Zone of the Andes, volcanoes located along structures that strike perpendicular to the minimum principal stress direction (σ_3) mainly erupt primitive basalts to basaltic andesites, whereas volcanoes located along structures that strike perpendicular to the maximum principal stress direction (σ_1) mainly erupt rhyolites (Cembrano & Lara 2009).

Although plate tectonics is the main control on the crustal stress field, many other process also affect the crustal stress field over a wide range of distance and timescales. Some of these processes are shown in Figure 1.3 and can be divided into those related to topography (collapse events, volcanic edifice building, and mountain building) and those related to tectonics (earthquake-driven stress changes, geologic structures, and mountain building). Although both topography and tectonics are primarily driven by global plate motions, and hence are not truly independent of one another and plate tectonics, it is notable that topographic and tectonic processes change the crustal stress field over shorter timescales than the geodynamic change that drives plate tectonics. Consequently, crustal field stress changes generated by topographic and tectonic processes may occur over timescales more relevant for influencing magma transport and storage.

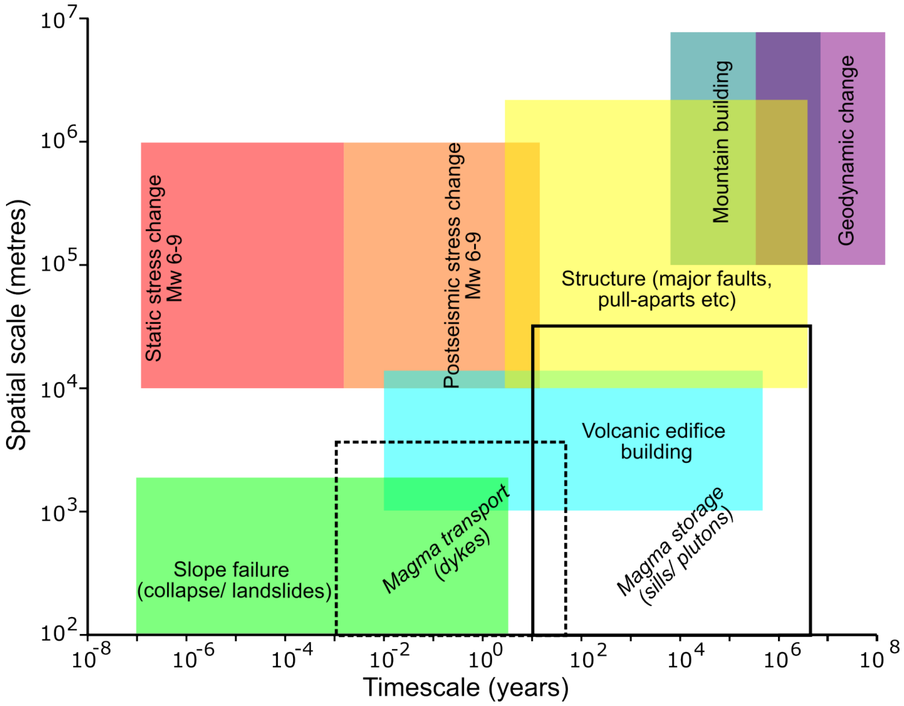

Figure 1.3: An approximate indication of the distance and time scales over which various processes affect the crustal stress field (coloured boxes), compared with the distance and time scales involved in magma ascent and storage (black outline boxes).

For example, collapse events are common at volcanoes due to their steepened topography, and the sudden unloading of the crust following collapses can affect the stability of underlying magma reservoirs (Siebert et al. 1987, Voight 2000, Voight et al. 2006). The collapse of the northern sector of Mount St. Helens in 1980, itself likely triggered by an earthquake, is a famous example of unloading that resulted in magmatic explosions and a devastating lateral blast (Voight et al. 1983). However, volcanic edifice destruction does not necessarily promote volcanic eruptions, and edifice destruction can sometimes actually increase the stability of the magma reservoir (Pinel & Jaupart 2005, Grosfils 2007, Albino et al. 2010).

The presence of a volcanic edifice also influences the development of magmatic systems. A volcanic edifice rotates the stress field so that ascending dykes may become focused beneath the edifice, leading to growth of a magma reservoir and favouring eruptions through the edifice (Maccaferri et al. 2011) (Figure 1.4). However, horizontal stresses are also induced beneath volcanic edifices, which can impede magma ascent and act as a density filter, preventing denser basaltic magmas reaching the surface and favouring magma evolution towards increasingly evolved and less dense compositions (Pinel & Jaupart 2000). At larger scales, the effects of the topographic load from the growth and evolution of an entire volcanic arc will also have an effect on the underlying transcrustal magmatic system.

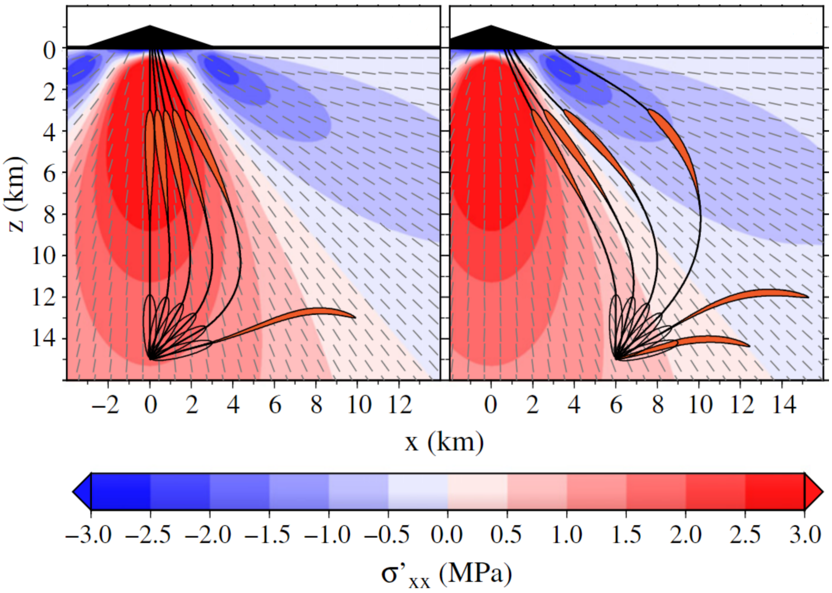

Figure 1.4: An example stress field induced by loading from a volcanic edifice. The tick marks show the orientation of the maximum principal stress, while the shading shows the horizontal deviatoric stress. Note that compressive horizontal stresses are induced beneath the edifice, while dyke trajectories (solid black lines) focus towards the edifice, favouring the growth of magma reservoirs and eruptions through the edifice. Figure adapted from Maccaferri et al. (2011).

1.5 Earthquakes-driven stress changes

Figure 1.3 shows that earthquakes can alter the crustal stress field over a range of distances and timescales. However, earthquakes themselves occur as the result of stresses built up in the Earth's crust, primarily due to tectonic plate motions (Scholz 2019). During an earthquake, slip across a fault surface releases some of the built up stress in the form of heat and seismic waves, while the movement of the fault blocks also acts to redistribute elastic stresses within the surrounding crust. Because earthquakes are both driven by stress and redistribute stress, earthquakes are not independent events, with aftershock sequences the most obvious evidence for interactions between earthquakes.

Many aftershocks occur on or near the main earthquake fault plane, particularly around the rupture tips, and so are associated with stress concentrations resulting from the slip distribution (Mendoza & Hartzell 1988). However, aftershocks also occur within off-fault lobes at distances of up to one or two rupture lengths from the mainshock (King et al. 1994), while seismicity following large earthquakes is also sometimes observed at great distances of >1000 km (Hill et al. 1993, Prejean et al. 2004). At great distances, stress changes due to the elastic relaxation of the crust have magnitudes lower than those caused by lunar tides, so remote triggered seismicity is instead attributed to the dynamic passage of seismic waves (Freed 2005). While dynamic triggering may also explain some of the aftershocks located closer to the mainshock, the distribution of off-fault aftershocks is often consistent with the pattern of static elastic stress redistribution (Stein et al. 1992, Toda et al. 1998) (Figure 1.5). Specifically, aftershocks are more common in regions where the Coulomb stress change ($\Delta\sigma_c$) imposed on faults is positive,

$$\Delta\sigma_c = \Delta\tau - \mu(\Delta\sigma_n - \Delta p), \tag{1.6}$$

where τ is the shear stress on the fault, μ is the coefficient of friction, σ_n is the normal stress on the fault, and p is the pore fluid pressure (Stein 1999). In other words, aftershocks are promoted in regions where the faults receive a shear stress increase and/or a normal stress decrease, whereas aftershocks are suppressed in regions where the faults receive a shear stress decrease and/or a normal stress increase.

Coulomb stress changes caused by large earthquakes can also affect the occurrence of future large earthquakes (Reasenberg & Simpson 1992, Freed 2005). For example, the combined effects of the four previous $M > 5$ earthquakes within 50 km of the 1992 M_w 7.3 California Landers earthquake (1975 M 5.2 Galway Lake, 1979 M 5.2 Homestead Valley, 1986 M 6.0 North Palm Springs, and 1992 M 6.1 Joshua Tree earthquakes) acted to raise the Coulomb stress at the site of the future Landers rupture by around 0.1 MPa (King et al. 1994). Furthermore, only 3 hours after the Landers earthquake, the M_w 6.5 Big Bear earthquake struck <50 km away in an area where the Landers earthquake had raised the Coulomb stress by around 0.3 MPa (King et al. 1994) (Figure 1.5). Examples of Coulomb stress change interactions between large earthquakes have also been observed in Japan (Pollitz & Sacks 1997), New Zealand (Doser & Robinson 2002), Chile (Lin & Stein 2004), and Turkey (Stein et al. 1997), amongst others. However, static stress transfer cannot explain why aftershocks and large earthquakes sometimes still occur in areas of Coulomb stress decrease, showing that other means of stress transfer must also be important (e.g. Freed & Lin 2001, Bosl & Nur 2002, Meier et al. 2014).

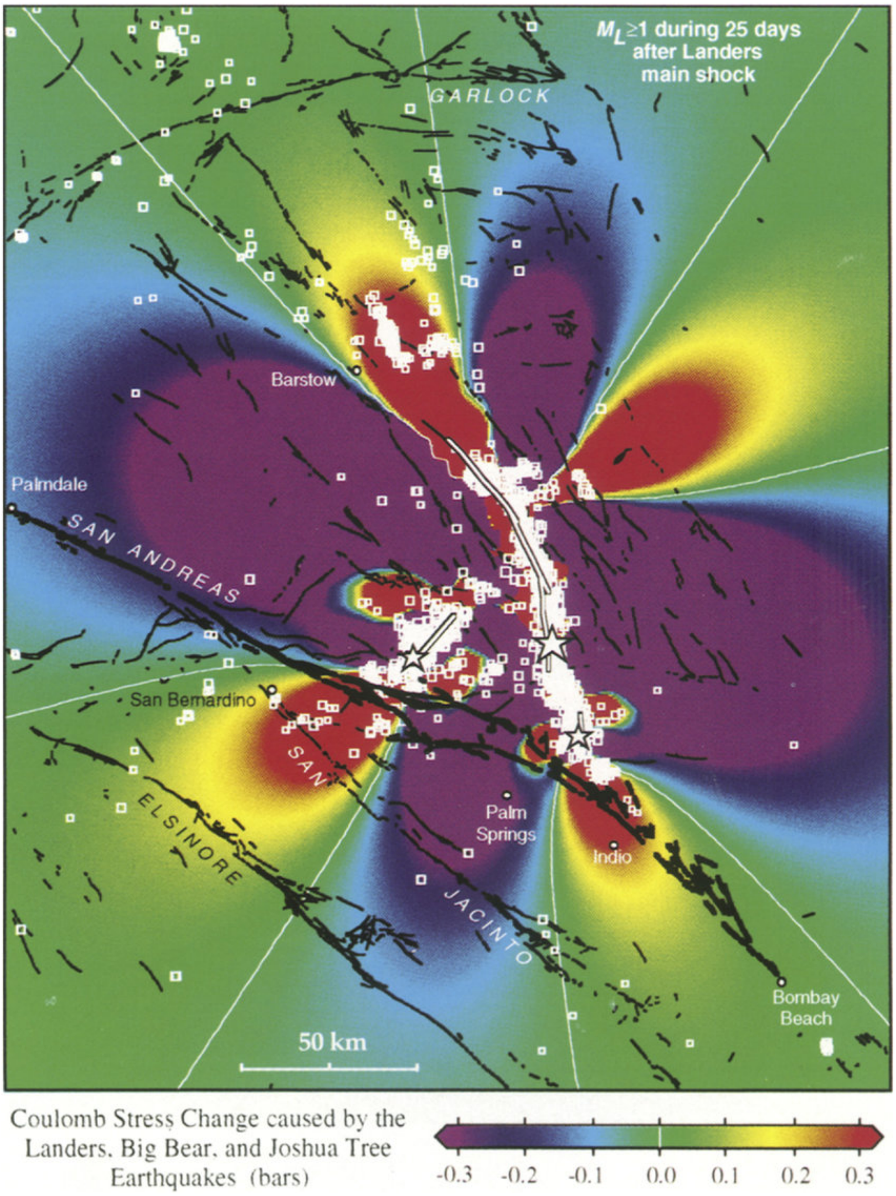

Figure 1.5: Location of $M_L \geq 1$ aftershocks (white squares) within 25 days after the 28 June 1992 M_w 7.3 Landers earthquake in California, USA (large star). Also shown are the M_w 6.5 Big Bear earthquake (left smaller star), which occurred 3 hours after the Landers event, and the M_w 6.1 Joshua Tree earthquake (right small star), which occurred on 23 April 1992. The shading shows the combined Coulomb stress change on optimally orientated faults at 6.25 km depth from the Landers, Big Bear, and Joshua Tree earthquakes. Figure from King et al. (1994).

The Coulomb stress changes capable of affecting seismicity rates have very low magnitudes (generally <1 MPa: Freed 2005). These stress changes represent only a small fraction of typical earthquake stress drops (3-10 MPa: Kanamori & Anderson 1975) and an even smaller fraction of the crustal differential stress under Byerlee's law (potentially 100s MPa at >5 km depth: Byerlee 1978, Lund & Zoback 1999). Therefore, static stress changes do not cause earthquakes but rather only trigger them (Rydelek & Sacks 1999, Freed 2005). Nonetheless, the importance of such small stress changes in triggering earthquakes implies that either many faults exist in a critically stressed state close to failure (McGarr 2014, Sibson 2017), or that faults are weak and can only support relatively small differential stresses (Holdsworth 2004, Collettini et al. 2009). The extent to which each of these statements is true remains unclear; direct stress measurements in boreholes support the argument for a strong crust with high differential stresses (Brudy et al. 1997, Lund & Zoback 1999), but stress field rotations observed following large earthquakes suggest that the crust is weak and earthquakes relieve a large proportion of the built up differential stresses (Asano et al. 2011, Hardebeck & Okada 2018).

1.6 Earthquake-magmatic interactions

The idea that large earthquakes can trigger volcanic eruptions is at least centuries old, based on numerous case examples of volcanoes that erupted shortly after nearby large earthquakes (e.g. Michell 1759, Darwin 1840, Bautista et al. 1996, Lara et al. 1994). However, the discovery that earthquakes can trigger other large earthquakes (King et al. 1994) renewed interest in the triggering of volcanic eruptions by earthquakes. Notably, several global statistical studies find that more volcanic eruptions than expected occur following nearby large earthquakes. For example, Linde & Sacks (1998) show that a peak in volcanic eruption rates occurs within 750 km and a few days following $M > 8$ earthquakes, or within 250 km following $M > 7$ earthquakes. By contrast, Sawi & Manga (2018) find no evidence for eruption triggering within 5 days and 800 km following $M > 6$ earthquakes, although they do show that eruption rates increase by around 10% within 2 months to 2 years following $M > 6$ earthquakes. Nishimura (2017) also finds evidence for longer-term triggering of eruptions, reporting a 50% increase in the number of eruptions within 200 km and 5 years following $M_w \geq 7.5$ earthquakes. Several studies at regional scales also report evidence for eruption triggering (Alam & Kimura 2004, Walter & Amelung 2007, Watt et al. 2009, Eggert & Walter 2009, Bonali et al. 2013).

Consequently, it is now generally accepted that large earthquakes can trigger volcanic eruptions (Seropian et al. 2021). However, the physical mechanisms responsible for eruption triggering are less well understood. Many different triggering mechanisms have been proposed, including those resulting from static stress changes due to the relaxation of the crust and those which invoke dynamic stress changes associated with seismic waves (Figure 1.6). Static stress changes can be either compressional or extensional, depending on the earthquake slip orientation and the relative locations of the earthquake and volcano, and both extensional and compressional static stresses have been implicated in eruption triggering (Hill et al. 2002). Extensional static stress changes decrease the normal stresses acting on magmatic pathways ('unclamping': Nostro et al. 1998, Walter & Amelung 2007, Bonali et al. 2013) and may also encourage volatile exsolution from the magma (Shimomura et al. 2006), both of which increase magma overpressure. By contrast, compressional static stress changes conceptually may act to squeeze magma upwards (Kimura 1994, Nostro et al. 1998), although this mechanism has been criticised (Rikitake & Sato 1989). Instead, compressional static stress changes may increase the normal stresses acting on magmatic pathways, therefore decreasing magma overpressure ('clamping': Ebmeier et al. 2016, Maccaferri et al. 2016). How static stress changes affect magmatic systems also depend heavily on the orientation of the magmatic structures, as this controls the stress changes resolved onto those structures (Seropian et al. 2021).

Eruption triggering which invokes dynamic stress changes requires a mechanism to generate permanent effects from transient stress changes. For example, dynamic stress changes may induce exsolution of volatiles and the nucleation and growth of bubbles in a magma reservoir through a variety of mechanisms, causing an increase in magma overpressure (Manga & Brodsky 2006, Cannata et al. 2010, Linde et al. 1994, Brodsky et al. 1998). Alternatively, dynamic stress changes may affect magma reservoirs themselves by causing physical movement of the reservoir, leading to a variety of processes that could destabilise the reservoir ('sloshing': Namiki et al. 2016, 2019). Finally, dynamic stress changes may affect magmatism indirectly, by affecting hydrothermal systems overlying magma reservoirs. Hydrothermal systems are extremely sensitive to dynamic stress changes from earthquakes (Hill et al. 1993, Prejean et al. 2004, Peng et al. 2010), due to either volatile effects or processes which generate permeability variations (Linde et al. 1994, Crews & Cooper 2014, Manga et al. 2012, Barbosa et al. 2019). Destabilisation of the hydrothermal system due to dynamic stress changes may then lead to top-down destabilisation of the entire magmatic system (Jolly 2019).

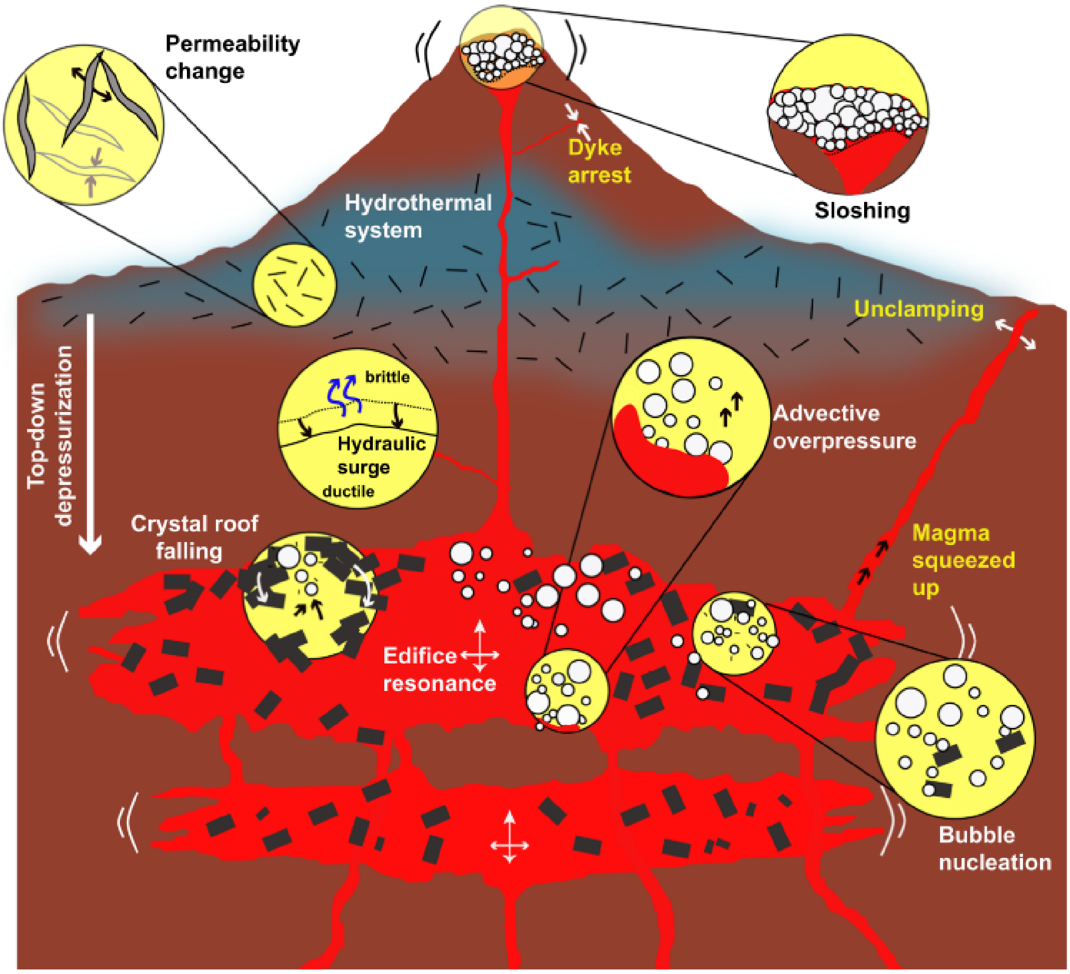

Figure 1.6: A schematic representation of some of the more common mechanisms invoked to explain eruption triggering by earthquakes. Mechanism names in yellow represent those caused by static stress changes, while those in black or white are for those due to dynamic stress changes. Figure from Seropian et al. (2021).

Whichever mechanisms are responsible for eruption triggering, it is generally believed that a volcano must already be in a critical state close to eruption in order for an eruption to be triggered by an earthquake (Manga & Brodsky 2006, Eggert & Walter 2009, Bebbington & Marzocchi 2011, Seropian et al. 2021, Nishimura 2017). As the monitoring and remote sensing of volcanoes improves, non-eruptive responses of volcanoes to nearby large earthquakes are also being discovered. These responses include increased seismicity (Cannata et al. 2010, Mora-Stock et al. 2012, Lin 2017), surface deformation (Takada & Fukushima 2013, Pritchard et al. 2013), and thermal and degassing anomalies (Harris & Ripepe 2007, Cigolini et al. 2007, Delle Donne et al. 2010, Hill-Butler et al. 2020). By contrast, earthquakes may also cause a decrease in activity and unrest at volcanoes, suggesting that earthquakes are also capable of stabilising magmatic systems under certain circumstances (Ebmeier et al. 2016, Farías & Basualto 2020). This range of responses shown by volcanoes to nearby large earthquakes highlights the complex interactions between earthquakes and magmatism and the need for continued study of this topic.

1.7 Thesis structure

This main body of this thesis consists of four independent, but broadly related, science chapters. Chapter 2 begins with an investigation into the transcrustal magmatic system concept, combining reviews of magnetotelluric surveys at Andean volcanoes and laboratory-derived electrical conductivity relationships to develop generalised models of typical magmatic systems. Chapter 3 then analyses modern global earthquake and eruption records to identify statistical relationships in the decadal timescale occurrences of large earthquakes and volcanic eruptions at global and regional scales. Chapter 4 also analyses modern global earthquake and eruption records, but instead focuses on the statistical relationships between large earthquakes and volcanic eruptions over shorter timescales and at more localised scales. Chapter 5 then considers how static stress changes caused by subduction zone megathrust earthquakes affect transcrustal magmatic systems located below volcanic arcs (as described in Chapter 2). Finally, the concluding Chapter summarises the findings of the thesis as a whole and identifies opportunities for further development of the work presented here.

CHAPTER 2

THE MAGNETOTELLURIC SIGNATURES OF PARTIAL MELT AND SALINE MAGMATIC FLUID RESERVOIRS BENEATH VOLCANOES

Knowledge of the architecture of active magmatic systems is important for both volcanic hazard assessment and evaluating potential geothermal energy and metals production from magmatic fluids. Increasingly, magmatic systems are imaged using magnetotellurics to detect electrically conductive partial melt and saline magmatic fluids. We review recent magnetotelluric studies at eight Andean volcanoes, revealing electrical conductivity anomalies with variable magnitudes and locations. Nonetheless, most volcanoes exhibit three electrical conductivity anomalies, located at shallow (< 3 km), intermediate (≈ 5 km), and deep (>10 km) depths. The shallow anomalies are often thin and laterally extensive, consistent with clay alteration layers, while the deep anomalies are generally interpreted as partial melt reservoirs. The intermediate depth anomalies, although generally attributed to partial melt, have less clear origins. By analysing laboratory-derived electrical conductivity relationships for clay and sulphide minerals, saline fluids, and silicate melts, we show that the intermediate depth anomalies are generally most consistent with saline magmatic fluids. However, other geophysical and petrological data suggest that intermediate depth anomalies probably also act as melt conduits, or contain localised partial melt. Therefore, the intermediate depth anomalies can be interpreted as active porphyry (copper) systems. Using a model consisting of a deep melt reservoir overlain by saline magmatic fluids, we relate the electrical conductivity structures observed at Andean volcanoes to the sub-surface pressure and temperature conditions.

2.1 Introduction

In recent decades, perspectives on magma storage in the Earth's crust have shifted towards the concept of low melt fraction systems that extend through the thickness of the crust (Cashman et al. 2017). Within this framework, shallow melt-dominated reservoirs are believed to be transient features, with melt instead being heterogeneously distributed throughout a transcrustal system (Sparks & Cashman 2017, Sparks et al. 2019, Edmonds et al. 2019). At active volcanoes, knowledge of the architecture of the magmatic system may therefore provide information about the eruption risk and associated volcanic hazards (Becerril et al. 2013, Chaussard & Amelung 2014, Edmonds & Woods 2018). Locating melt, and particularly exsolved saline magmatic fluid reservoirs, is also of emerging industry interest, due to their potential as sources of high-enthalpy geothermal energy and important metals (Reinsch et al. 2017, Watanabe et al. 2017, Blundy et al. 2021).

Direct identification of sub-surface melt or magmatic fluid is only possible by drilling boreholes. Although conventional geothermal energy projects exist near many volcanoes, drilling is mainly restricted to shallow hydrothermal systems that display little magmatic fluid input (Elders et al. 2014, Kruszewski & Wittig 2018, Stimac et al. 2015). Only a few boreholes have penetrated into deeper magma or saline magmatic fluid reservoirs, which are typically isolated from overlying hydrothermal systems by a permeability barrier at the brittle-ductile transition (Fournier 1999, Kasai et al. 1998, Elders et al. 2014, Blundy et al. 2021). The exact conditions and structure of active magmatic systems are therefore poorly known, and studies must rely primarily on indirect methods, including petrological analyses of erupted material (Kesler et al. 2013, Cooper 2019) and geophysical methods such as seismic tomography, gravity surveying, and electromagnetic imaging (Magee et al. 2018). Understanding and integrating the information provided by each of these methods is a key challenge for furthering our understanding of magmatic systems.

In this study, we explore what the magnetotelluric method can reveal about melt and saline magmatic fluid reservoirs beneath volcanoes. We begin by reviewing the findings of recent magnetotelluric surveys at eight Andean volcanoes, in order to identify any similarities or differences in the electrical conductivity anomalies imaged. To constrain the origins of these anomalies, we then review laboratory experiments that characterise the electrical conductivity of silicate melts and saline fluids as a function of pressure, temperature, and composition, and discuss the degree to which magnetotellurics is able to distinguish between partial melt and saline magmatic fluids. We also briefly consider the role of electrically conductive clay and sulphide minerals in generating electrical conductivity anomalies beneath volcanoes. Finally, to integrate the laboratory-derived relationships with the anomalies observed at Andean volcanoes, we develop simplified models of magmatic systems and calculate their electrical conductivity structures as a function of the sub-surface pressure and temperature conditions.

2.2 Volcano magnetotellurics

2.2.1 The magnetotelluric method

Natural variations in the Earth's magnetic field induce electric currents within the crust, with a magnitude that depends on the electrical resistivity. Magnetotelluric surveying involves measuring time variations in the electric and magnetic fields at the Earth's surface, then using these data to determine the underlying electrical resistivity structure. For modern 3D magnetotelluric surveys, this step is performed by computer inversion, which attempts to generate an electrical resistivity model that minimises both the misfit to the observed data and the model roughness. Importantly, magnetotellurics can probe depths ranging from hundreds of meters to hundreds of kilometers, due to the wide frequency range over which the magnetic field varies; high frequency variations generated by lightening strikes sample the shallow structure, whereas low frequency variations caused by the interaction of the solar wind with the Earth's magnetosphere sample the deeper structure. For a full description of magnetotelluric surveying and inversion, the reader is referred to Simpson & Bahr (2005) and Chave & Jones (2012).

Magnetotellurics is particularly suited to imaging magmatic systems because it is sensitive to the low electrical resistivity (i.e. high electrical conductivity) of both silicate melts and saline magmatic fluids relative to crustal rocks (Pommier & Le-Trong 2011). Furthermore, depending on the spatial connectivity of melt or magmatic fluids within the host rock, only a small fluid fraction may be needed to generate a detectable electrical conductivity anomaly (i.e. a region of low electrical resistivity) (Glover et al. 2000). Magnetotellurics may therefore be able to detect the low melt fractions thought to characterise most magmatic systems (Bachmann & Huber 2016, Cooper 2017). This possibility has been reflected by the recent increase in the number of volcano magnetotelluric studies conducted, both in the Andes and globally, making our review timely.

However, magnetotellurics also has some important limitations. For example, sensitivity analyses show that magmatic bodies typically require dimensions of several kilometers to be detectable, depending on their electrical conductivity and the magnetotelluric station spacing (Díaz et al. 2015, Piña-Varas et al. 2018, Cordell et al. 2018). Magnetotelluric inversion can also suffer from a lack of sensitivity beneath strong electrical conductivity anomalies, as well as smearing of anomalies due to smoothing. Finally, as with all geophysical methods, the inversion and interpretation of magnetotelluric data are non-unique, so different studies and methods can produce contrasting results.

2.2.2 Andean volcano magnetotelluric studies

Volcano magnetotelluric studies are typically conducted to focus on either shallow hydrothermal systems, or the deeper magmatic system. We restrict our review to the latter type, which includes studies using broadband and/or long-period magnetotelluric stations distributed across a large survey area, producing electrical resistivity models to a depth of ≥10 km. For consistency, we consider only studies which utilize 3D magnetotelluric methods. The Andean volcanic arc is the site of numerous recent volcano magnetotelluric studies meeting these criteria, which combined with the well-studied geodynamics (e.g. Cembrano & Lara 2009), makes the Andes an excellent case study for our review.

Employing a literature search, we find eight suitable studied Andean volcanoes, all of which are located within the Central and Southern volcanic zones. From north to south, they are: Paniri (Mancini et al. 2019), Uturuncu (Comeau et al. 2016), Láscar (Díaz et al. 2012), Lastarria (Díaz et al. 2015), Laguna del Maule (Cordell et al. 2018), Tinguiruirica (Pearce et al. 2020), Villarrica (Pavez et al. 2020), and Osorno (Díaz et al. 2020). All of these studies display good spatial coverage of the volcano, except for Villarrica, where only the northern flank was instrumented. The Paniri study area also covers the San Pedro - San Pablo and Cerro del Léon volcanoes, while the Tinguiruirica study area includes the Planchón-Peteroa volcano. For studies covering multiple volcanoes, we select the volcano closest to the imaged electrical conductivity anomalies as the representative volcano, although the anomalies themselves may be related to multiple different volcanoes.

Figure 2.1 shows a simplified summary of the electrical resistivity structures beneath the eight studied volcanoes, summarising the depths, magnitudes, and relative spatial relations of the imaged electrical conductivity anomalies, as well as any proposed interpretations. Where possible, the electrical conductivity and depth values are taken directly from the source publication text. Otherwise, these values are estimated from the available figures (Appendix A). For each anomaly, only the maximum electrical conductivity is shown, although in reality each anomaly is characterised by a range of electrical conductivities. The presence of these main electrical conductivity anomalies is confirmed by sensitivity testing in each study. Figure 2.1 highlights the wide range of magnitudes, depths, and locations of the imaged electrical conductivity anomalies. However, it is also important to recognise differing levels of recent activity, varied erupted products, and different morphologies of the studied volcanoes. For example, while most of the studied volcanoes are andesitic to dacitic stratovolcanoes typical of subduction zones, Villarrica and Osorno are dominated by more mafic basaltic to basaltic-andesite compositions, while the most recent lavas from the Laguna del Maule caldera are rhyolitic (Figure 2.1).

A prevalent feature of the Andean volcano magnetotelluric studies is a relatively thin but often laterally extensive electrical conductivity anomaly present at shallow depths (<3 km), imaged at all of the volcanoes except Tinguiruirica and Villarrica. These shallow anomalies generally have electrical conductivities of 0.1 to 1 S m^{-1}, although a stronger shallow anomaly is imaged at Uturuncu (1 to 10 S m^{-1}), while a weaker shallow anomaly is imaged at Osorno (0.01 S m^{-1}). The large lateral but limited vertical extent of these shallow anomalies is consistent with clay minerals produced by hydrothermal alteration, as electrically conductive smectite minerals break down at temperatures much above 200 °C (Beaufort et al. 2015, Stimac et al. 2015). However, hydrothermal fluids themselves are also proposed to directly contribute to the shallow high electrical conductivity anomalies at most of the studied volcanoes, perhaps reflecting the prevalence of hot springs and fumaroles. At Láscar, the shallow anomaly is interpreted exclusively as hydrothermal fluids. Tinguiruirica does not display a typical shallow anomaly, although a hydrothermal system is instead interpreted from a deeper anomaly located between 2 to 12 km depth, attributed to either fluids or clay minerals depending on whether the hydrothermal system is active or extinct.

At depths greater than a few kilometers, the electrical resistivity structures beneath volcanoes are highly variable, although many deeper anomalies also have maximum electrical conductivities of 0.1 to 1 S m^{-1}. Interestingly, the strongest anomalies (>1 S m^{-1}) are located beneath Uturuncu, Lastarria, and Laguna del Maule, which are among the least historically active of the studied volcanoes. Weaker anomalies (<0.1 S m^{-1}) are located beneath Villarrica and Osorno, which are the two studied volcanoes which display mafic compositions. Láscar displays both strong and weak deeper anomalies.

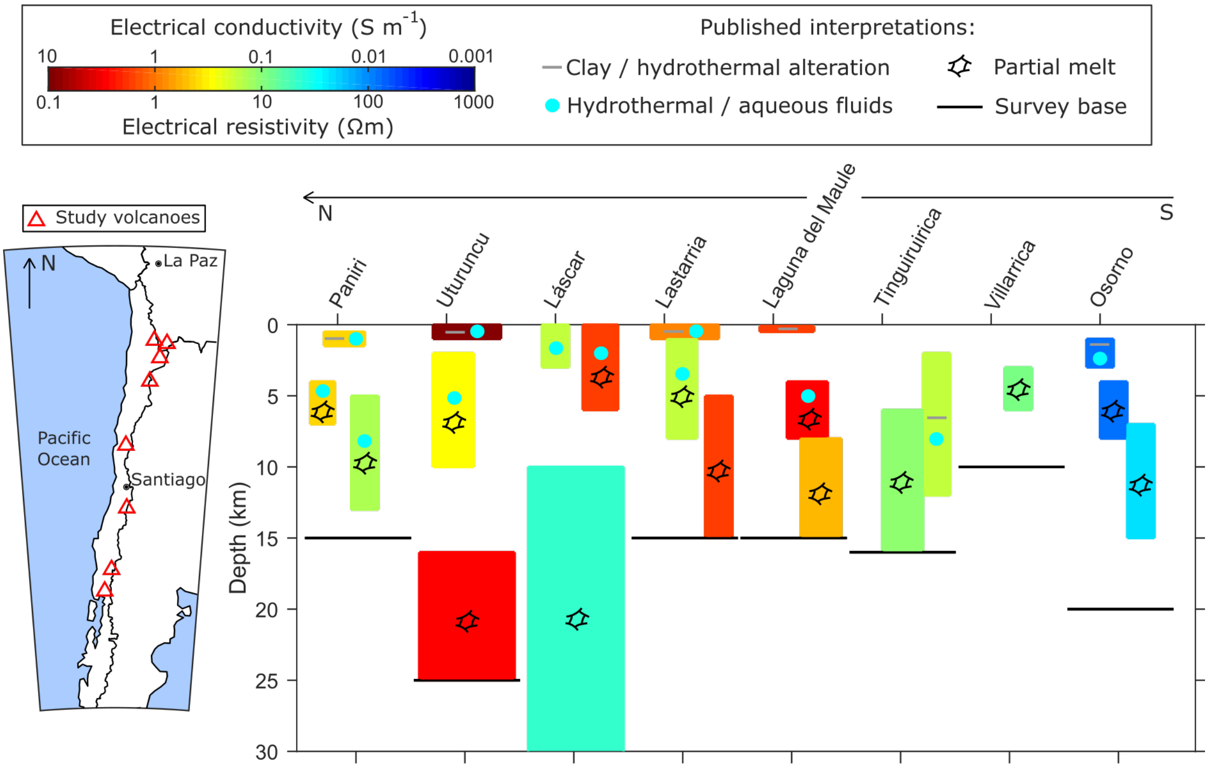

Other volcanoes in study	(San Pedro-San Pablo, Cerro del León)					(Planchón-Peteroa)		
Volcano morphology	Stratovolc (Stratovolc, domes)	Stratovolc	Stratovolc Domes	Stratovolc Domes	Caldera Stratovolc Domes	Stratovolc (Stratovolc, caldera)	Stratovolc Caldera	Stratovolc Domes Caldera
Last erupted	Pleistocene (1960?)	Pleistocene	2017	Holocene?	50 BC	1917 (2019)	2022	1869
Erupted products	And - Dac (BaA - Dac)	And - Dac	And - Dac	And - Dac	Bas - Rhy	Bas - And (Bas - Dac)	Bas - BaA	Bas - Dac

Bas = basalt; BaA = basaltic-andesite; And = andesite; Dac = dacite; Rhy = rhyolite.

Figure 2.1: Graphical representation of the electrical resistivity structures at the eight studied Andean volcanoes (see Appendix A for images). The imaged anomalies are shaded according to their maximum electrical conductivities, with their approximate spatial relationships also represented (lateral distances not to scale). The symbols show the interpretations given in each study. For studies covering multiple volcanoes, the characteristics of the other volcanoes are given in parentheses in the summary table.

All of the studied volcanoes except Villarrica display two deeper electrical conductivity anomalies (Figure 2.1). The first of these anomalies is located at intermediate depths (≈5 km), but can extend upwards towards the surface (e.g. Láscar) and downwards to depths >10 km (e.g. Tinguiruirica). The second of these anomalies is located deeper (>10 km), with its top generally at around 5-8 km depth. At Láscar and Uturuncu, the second anomaly is considerably deeper, beginning at 10 and 16 km depth respectively. The base of the deep anomaly is rarely imaged, only being resolved at Paniri and Osorno. The absence of a deep anomaly at Villarrica could reflect the poor station coverage around the volcano, or the shallow limit of the survey.

The geometry of the intermediate depth anomalies varies from spherical or sill-like at Paniri, Láscar, Villarrica, and Osorno, through dipping structures at Lastarria, Laguna del Maule, and Tinguiruirica, to vertical at Uturuncu. By contrast, the deep anomalies are more voluminous, reaching dimensions of 10's km at Láscar and Uturuncu. Both the intermediate and deep anomalies are often laterally offset from the volcanic edifice; only Uturuncu and Osorno have intermediate depth anomalies directly beneath the volcano, while at Láscar and Tinguiruirica, the intermediate depth anomalies reach >10 km from the edifice. Determining whether the deep and intermediate depth anomalies are connected is complicated due to smoothing during the inversion process. However, a connection is imaged at Laguna del Maule, Tinguiruirica, and Osorno, while at Uturuncu the two anomalies are partly connected through a region with slightly lower electrical conductivities.

The intermediate depth and deep anomalies are all attributed to the presence of partial melt, except for the intermediate depth anomaly at Tinguiruirica, which is interpreted as a hydrothermal system. However, the studies at Paniri, Uturuncu, and Laguna del Maule note that the observed electrical conductivities of the intermediate depth anomalies are difficult to explain with partial melt alone. Therefore, these studies suggest the additional presence of exsolved saline magmatic fluids, which are more electrically conductive than partial melt. The intermediate depth anomalies at Láscar and Lastarria are also interpreted as being caused by magma and/or magmatic fluids. The deep anomalies are generally uniquely interpreted as partial melt, although the presence of additional fluids is suggested at Paniri.

2.2.3 Complementary geophysical and petrological data

Complementary data are required to constrain the interpretation of volcano magnetotellurics, such as whether the intermediate depth electrical conductivity anomalies at Andean volcanoes (Figure 2.1) represent partial melt or saline magmatic fluids. For example, crystallisation depths calculated using geobarometry on volcanic products can be compared with the depths of electrical conductivity anomalies. Corresponding geobarometry depths are cited as evidence for partial melt generating the intermediate depth anomalies at Paniri (Cerro del León), Uturuncu, Laguna del Maule, and Villarrica (De Silva et al. 1994, Muir et al. 2014, Klug et al. 2020, Morgado et al. 2015), and in the deep anomalies at Paniri and Laguna del Maule (Godoy et al. 2018, Klug et al. 2020). However, geobarometry does not indicate the lateral location of melt reservoirs, and also might not represent the current location and state of melt reservoirs, depending on the age of the analysed material.

By contrast, complementary geophysical methods provide present-day sub-surface images, but suffer from the same non-uniqueness as magnetotellurics. For example, partial melt was interpreted at depths of approximately 20 km beneath Uturuncu and Láscar from a large region of reduced seismic shear wave velocities ($-\Delta V_s$ >30%) known as the Altiplano-Puna magma body, which coincides with the deep electrical conductivity anomalies (Chmielowski et al. 1999, Zandt et al. 2003, Ward et al. 2014). Similarly, slow compressional wave velocities ($-\Delta V_p \approx 9\%$) beneath Villarrica overlap with the intermediate depth electrical conductivity anomaly and were also inferred to be of magmatic origin (Mora-Stock 2015). However, slow wave velocities that coincide with the intermediate depth electrical conductivity anomalies at Uturuncu ($-\Delta V_s \approx 10\%$) and Tinguiruirica ($-\Delta V_p > 6\%$) were attributed to hydrothermal systems instead (Jay et al. 2012, Pavez et al. 2016). At Lastarria, slow shear wave velocities ($-\Delta V_s$ = 23-63%) match remarkably well with all three imaged electrical conductivity anomalies, and were interpreted as a shallow hydrothermal system overlying two deeper melt reservoirs (Spica et al. 2015).

Combining multiple geophysical datasets can reduce uncertainties in interpreting active magmatic systems. For example, at Laguna del Maule, compelling evidence for a shallow (4 km) melt reservoir is provided by overlapping slow shear and compressional wave velocities from seismic tomography ($-\Delta V_s$ = 12-28%, $-\Delta V_p$ = 9%), low densities from gravity surveys ($-\Delta\rho = 600$ kg m^{-3}), and a sill-like inflation source detected using InSAR (>25 cm / year uplift) (Bai et al. 2020, Wespestad et al. 2019, Miller et al. 2017, Feigl et al. 2014). However, no robust electrical conductivity anomaly is associated with this inferred melt reservoir (Cordell et al. 2018, 2020). Instead, a strong electrical conductivity anomaly (>1 S m^{-1}) is located some 5 km to the north, rooted at greater depths but converging upwards towards the inferred melt reservoir. At intermediate depths, the high electrical conductivity of this anomaly, combined with the lack of associated gravity and seismic velocity anomalies, is consistent with saline magmatic fluids (Wespestad et al. 2019). In contrast, the melt reservoir inferred from seismic tomography and gravity surveys could go undetected by magnetotellurics if it has low temperature or water content, especially as it is located beneath a highly electrically conductive clay cap (Cordell et al. 2020).

2.3 Electrical conductivity anomalies

Electrical conductivity anomalies beneath volcanoes are generally attributed to silicate melts, saline magmatic fluids, or electrically conductive minerals such as sulphides or certain clays. In magmatic environments, clay and sulphide minerals form by alteration or precipitation from magmatic-hydrothermal fluids (Sillitoe 2010), which in turn are derived from volatiles exsolved from silicate melts (Audétat & Edmonds 2020, Tattitch et al. 2021). Because of this genetic link, the phases responsible for generating electrical conductivity anomalies beneath volcanoes may be somewhat spatially coincident, although a general transition from deeper melt reservoirs, through overlying exsolved saline magmatic fluids, to shallower mineralisation and alteration might be expected. With magnetotelluric data alone, it is generally impossible to uniquely determine the cause of an electrical conductivity anomaly. However, it is possible to constrain the interpretation of electrical conductivity anomalies, by utilizing knowledge of the electrical conductivities displayed by common electrically conductive phases.

The electrical conductivity of common electrically conductive phases can be measured experimentally in the laboratory as a function of temperature, pressure, and composition (Laštovičková 1991, Ni et al. 2014). However, electrically conductive phases generally constitute only a proportion of a given rock mass, so the relevant parameter for magnetotelluric data interpretation is the effective electrical conductivity of the rock mass as a whole. The effective electrical conductivity depends on both the proportion and spatial connectivity of the electrically conductive phase(s) within the host rock. Different levels of spatial connectivity are represented by different geometrical mixing models, or can be characterised by empirically determined relationships (Table 2.1: Glover et al. (2000)). Depending on which mixing model is used, the calculated effective electrical conductivity can vary greatly. Here, we review the laboratory-determined electrical conductivities of clay and sulphide minerals, saline magmatic fluids, and silicate melts, and discuss the appropriate mixing models for each phase.

Table 2.1: Mixing models for effective electrical conductivity (σ_{Eff}) in two-phase media, in order of decreasing spatial connectivity and effective electrical conductivity. (Electrical conductivity is the inverse of electrical resistivity).

Name	$\sigma_{Eff} =$	Visualisation	Reference
Parallel model	$(1-X_2)\sigma_1 + X_2\sigma_2$	Layers arranged parallel to electric current direction.	(Guéguen & Palciauskas 1994)
Hashin-Shtrikman (HS) upper bound	$\sigma_2(1-\frac{3(1-X_2)(\sigma_2-\sigma_1)}{3\sigma_2-X_2(\sigma_2-\sigma_1)})$	Space-filling spheres with a core of host rock and rim of electrically conductive phase.	(Hashin & Shtrikman 1962)
Films model	$(1-X_2)\sigma_1 + \frac{2}{3}X_2\sigma_2$	Completely wetted films of electrically conductive phase along host rock grain boundaries.	(Waff 1974)
Tubes model	$(1-X_2)\sigma_1 + \frac{1}{3}X_2\sigma_2$	Tubes of electrically conductive phase along host rock triple junctions.	(Grant & West 1965)
Hashin-Shtrikman (HS) lower bound	$\sigma_1(1+\frac{3X_2(\sigma_2-\sigma_1)}{3\sigma_1+(1-X_2)(\sigma_2-\sigma_1)})$	Space-filling spheres with a core of electrically conductive phase and rim of host rock.	(Hashin & Shtrikman 1962)
Perpendicular model	$(\frac{1-X_2}{\sigma_1}+\frac{X_2}{\sigma_2})^{-1}$	Layers arranged normal to electric current direction.	(Guéguen & Palciauskas 1994)
Modified Archie's Law	$(1-X_2)^p\sigma_1 + X_2^m\sigma_2$ $p = \frac{log_{10}(1-X_2^m)}{log_{10}(1-X_2)}$	Empirical relationship with conductive phase connectivity defined by m.	(Glover et al. 2000)

σ_{eff} = Effective electrical conductivity; σ_1 = Host rock electrical conductivity; σ_2 = Conductive phase electrical conductivity; X_2 = Proportion of electrically conductive phase. Archie's Law is an empirical relationship, not a geometrical mixing model.

2.3.1 Clay and sulphide minerals

Based on drilling results, shallow laterally extensive electrical conductivity anomalies beneath volcanoes are coincident with smectite-rich layers within argillic alteration zones (Ryan et al. 2013, Bertrand et al. 2012, Lee et al. 2020). Argillic alteration is generated by low temperature hydrothermal fluids, and often forms an impermeable clay cap overlying hydrothermal systems (Stimac et al. 2015). The electrical conductivity of smectite itself is complex (Lévy et al. 2018), although smectite within the clay cap must display a high degree of spatial connectivity to explain the observed electrical conductivities of >0.1 S m^{-1} (Díaz et al. 2015, Lee et al. 2020). However, as smectite is only stable at temperatures <180-240 °C (Stimac et al. 2015), above which it is progressively replaced by less electrically conductive chlorite, electrical conductivity anomalies attributable to clays are restricted to shallow hydrothermal systems only and are not the main focus of our study.

In contrast, sulphide minerals are stable at much higher temperatures. Many common sulphide minerals are semiconductors, which have variable electrical conductivities controlled by impurities and defects within the crystal structure (Pridmore & Shuey 1976). Pyrite is the most abundant sulphide mineral and other common sulphide minerals are unlikely to have significantly greater electrical conductivities (Pridmore & Shuey 1976). At ambient conditions, the electrical conductivity of natural pyrite spans 1-10,000 S m^{-1} (Sasaki 1955). However, the electrical conductivity converges at higher temperatures, being on the order of 10^3 S m^{-1} at 400 °C and 10^4 S m^{-1} at >500 °C (Sasaki 1955). Furthermore, Pridmore & Shuey (1976) showed that pyrite of hydrothermal origin displays much higher electrical conductivity (typically 10^2-10^4 S m^{-1}) than pyrite of sedimentary origin (typically 10^1-10^2 S m^{-1}) at room temperature. In magmatic-hydrothermal environments, pyrite therefore likely has an extremely high electrical conductivity on the order of 10^3 S m^{-1} or greater. However, whether sulphide-bearing rocks display high electrical conductivities depends on the spatial connectivity of the sulphide mineralisation.

Conceptually, disseminated sulphide mineralisation may have very low spatial connectivity, whereas sulphide veins may display very high connectivity. Figure 2.2 shows the effective electrical conductivities of sulphide ores, taken from induced polarization measurements at open-pit porphyry mines (Nelson & Van Voorhis 1983) and laboratory measurements on drill core from a sulphide prospect (Johnson & Anderson 1981). Despite the difference in measurement method, both studies show consistent electrical conductivities. Assuming a hydrothermal sulphide electrical conductivity of 1000 S m^{-1} at ambient temperature, sulphide mineralisation displays poor spatial connectivity, falling between a thousandth and a hundredth of the Hashin-Shtrikman (HS) upper bound mixing model. Vella & Emerson (2012) obtained similar results for magnetite, with >0.4 volume fraction of magnetite needed to significantly increase the electrical conductivity.

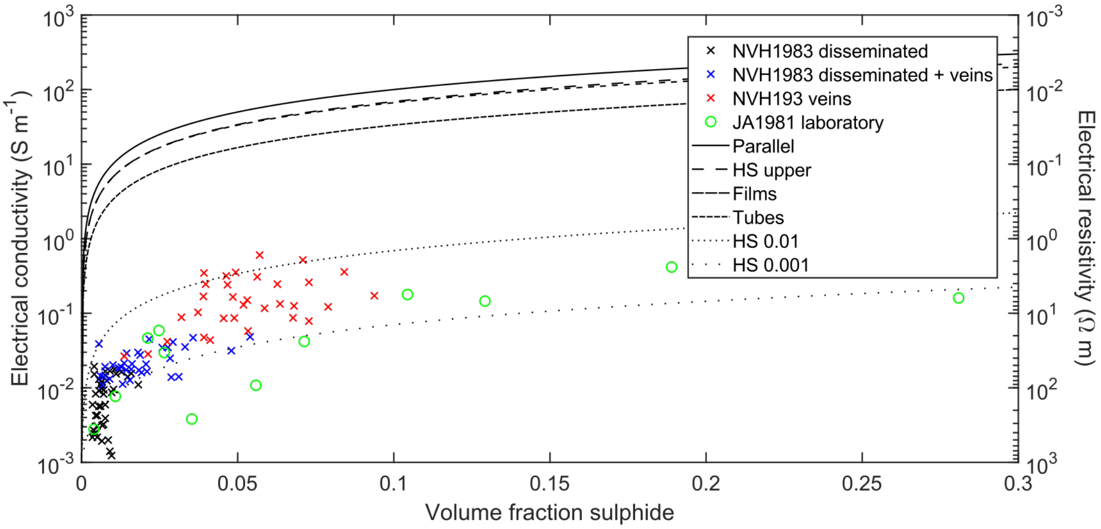

Figure 2.2: Electrical conductivity of sulphide ore as a function of sulphide volume fraction. NVH1983 is from Nelson & Van Voorhis (1983), with weight fraction sulphide divided by 2 to approximate volume fraction sulphide. JA1981 is from Johnson & Anderson (1981). The shown mixing models use an estimated pure sulphide electrical conductivity of 1000 S m^{-1} and are insensitive to the negligible host rock electrical conductivity. HS 0.01 and HS 0.001 refer to a hundredth and a thousandth of the Hashin-Shtrikman upper bound for electrical conductivity value respectively.

Electrical conductivity anomalies generated by sulphide veins therefore likely have electrical conductivities <1 S m^{-1}, while disseminated sulphide mineralisation, which is probably more relevant at the kilometers scale of transcrustal magnetotelluric surveys, likely has effective electrical conductivities <0.1 S m^{-1}. Higher temperatures at greater depths could increase these values, however, the poor spatial connectivity of sulphide mineralisation likely impedes the formation of strong electrical conductivity anomalies. Low density and seismic wave velocities associated with several electrical conductivity anomalies beneath volcanoes (Díaz et al. 2012, 2015, Comeau et al. 2016, Pearce et al. 2020) are also inconsistent with substantial sulphide mineralisation.

2.3.2 Saline magmatic fluids

Saline magmatic fluids conduct electricity through the movement of dissolved ions, so salinity is the greatest control on their electrical conductivity. Fluids exsolved from melt reservoirs are typically in a supercritical state with salinities in the range of 5-15 wt% $NaCl_{eq}$ (Heinrich 2005, Audétat & Edmonds 2020, Tattitch et al. 2021). However, as these fluids ascend to shallower depths, pressure decrease can trigger phase separation into coexisting hypersaline brine and low salinity vapour phases (Figure 2.3) (Driesner & Heinrich 2007). The dense brine, which is more likely to be retained within the host rock than the vapour, can be many times more saline than the initial magmatic fluid. Further pressure decrease may lead to the formation of coexisting vapour and halite phases.

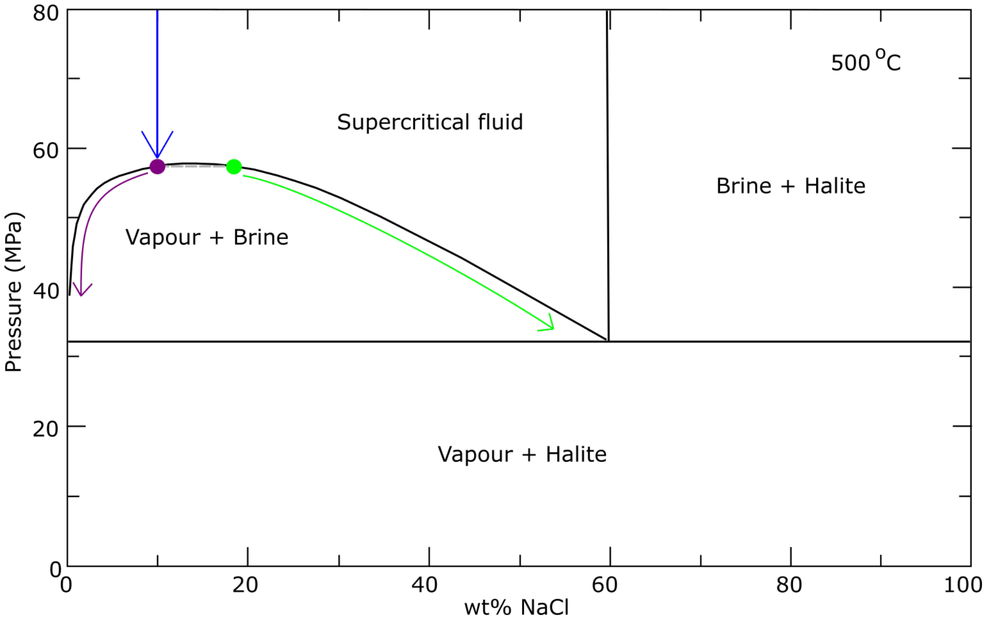

Figure 2.3: Phase changes for ascending supercritical saline magmatic fluids with a bulk salinity of 10 wt% NaCl (blue), under a constant fluid temperature of 500 °C. When pressure decreases to 57 MPa, the supercritical fluid separates into coexisting vapour (purple) and hypersaline brine (green), with salinities of 10 and 18 wt% NaCl respectively. Continued pressure decrease drives the vapour phase to progressively lower salinity, and the brine phase to progressively higher salinity. At 32 MPa, another phase transition occurs due to halite precipitation. Phase boundaries from Driesner & Heinrich (2007).

Taking NaCl solution as a proxy, the electrical conductivity of saline magmatic fluids under crustal pressure and temperature conditions can be calculated using the empirical relationship of Watanabe et al. (2021) (Table 2.2). Although no electrical conductivity measurements have been conducted on hypersaline brines, the relationship of Watanabe et al. (2021) can be extrapolated to estimate these electrical conductivities. By contrast, the relationship of Sinmyo & Keppler (2017) does not produce reasonable electrical conductivities if phase separation occurs, and Watanabe et al. (2021) state that extrapolation of the Sinmyo & Keppler (2017) model to higher salinities causes an underestimation of the electrical conductivity.

Table 2.2: NaCl solution empirical electrical conductivity relationships under crustal conditions.

Model	Fluid	Salinity (wt%)	Temperature (°C)	Pressure (GPa)
Sinmyo & Keppler (2017)	NaCl	0.058 - 5.63	100 - 600	0.0001 - 1
Watanabe et al. (2021)	NaCl	0.06 - 24.6	20 - 525	0.0025 - 0.2

Figure 2.4 shows how the electrical conductivity of NaCl solution increases with increasing salinity, due to higher concentrations of charge carrying ions. Typical supercritical fluids exsolved from magmas (5-15 wt% $NaCl_{eq}$) have electrical conductivities on the order of 10^1 S m^{-1}, whereas hypersaline brines (>20 wt% $NaCl_{eq}$) formed by phase separation of this fluid are predicted to have electrical conductivities on the order of 10^2 S m^{-1}. The effects of temperature and pressure on the electrical conductivity of NaCl solution are complex. For any given salinity, the electrical conductivity reaches a maximum at around 250-300 °C, independent of pressure, due to an increase in charge carrier mobility with temperature (Quist & Marshall 1968, Sinmyo & Keppler 2017, Watanabe et al. 2021). Above approximately 300 °C, pressure also becomes an important control. Under lower pressures, the electrical conductivity decreases above 300 °C, due to a combination of fluid expansion decreasing the number of ions per unit volume, and a decrease in the dielectric constant of water (Watanabe et al. 2021). Under higher pressure conditions, the peak electrical conductivity is maintained towards higher temperatures, as the increased pressure reduces fluid expansion while also increasing the dielectric constant of water (Sinmyo & Keppler 2017, Watanabe et al. 2021).

The spatial connectivity of saline fluids could vary with host rock lithology. However, studies on the electrical conductivity of fluid bearing rocks focus on potential hydrocarbon reservoir rocks. Figure 2.5a shows the effective electrical conductivities of clean sandstones saturated with 4 wt% NaCl solution, measured in the laboratory at ambient conditions (Gomez et al. 2010). Mixing models using the measured electrical conductivity of the saturating fluid (5.9 S m^{-1}) show that the fluid spatial connectivity increases with fluid fraction; at porosity below around 0.15, the effective electrical conductivity is around a tenth of the HS upper bound value, whereas the tubes model is appropriate at porosity above 0.15.

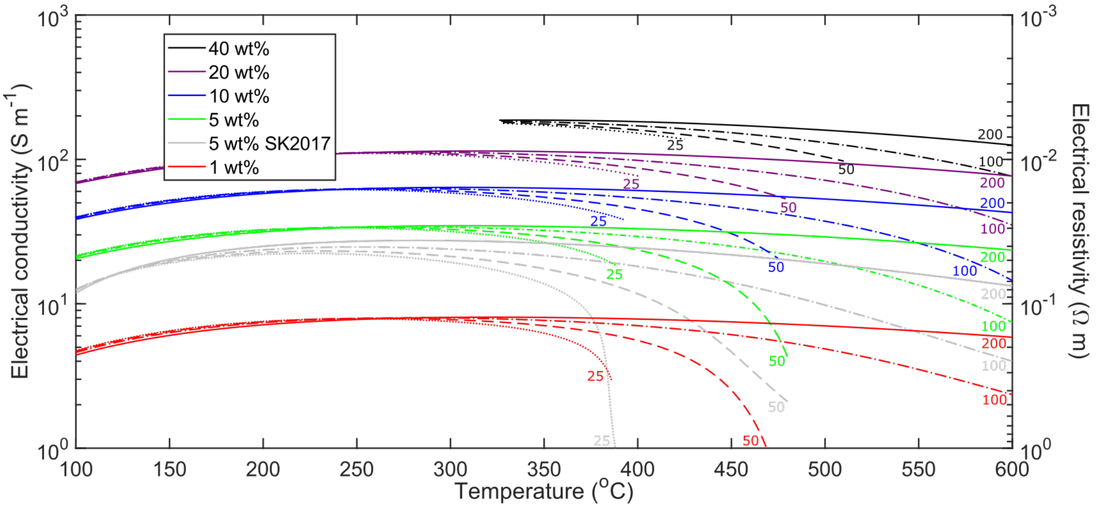

Figure 2.4: Electrical conductivity of NaCl solution as a function of temperature, calculated using Watanabe et al. (2021). Colour indicates salinity, while the numbers show pressure in MPa. The plots are calculated only where a liquid or supercritical fluid phase exists with the specified salinity. The electrical conductivity of 5 wt% NaCl solution calculated using Sinmyo & Keppler (2017) is also shown in grey.

Similarly, Figure 2.5b shows the effective electrical conductivities of sandstones with a variable clay content (0-28%) saturated with 3.5 wt% NaCl solution at 26 MPa and ambient temperature (Han et al. 2015). Despite the increased clay content and confining pressure, mixing models using the measured electrical conductivity of the saturating fluid (4.7 S m^{-1}) show similar spatial connectivities to that of clean sandstones, suggesting that saline fluid connectivity is relatively high under a variety of conditions. However, the data in Figure 2.5 are only for clastic sedimentary rocks, and fluid connectivity in magmatic systems could differ and requires further study. Conceptually, the typically lower permeability of igneous rocks may mean lower fluid connectivity and lower bulk conductivity. However, high fluid connectivity at low fluid fractions may be feasible if the fluid is wetting and forms films along grain boundaries.

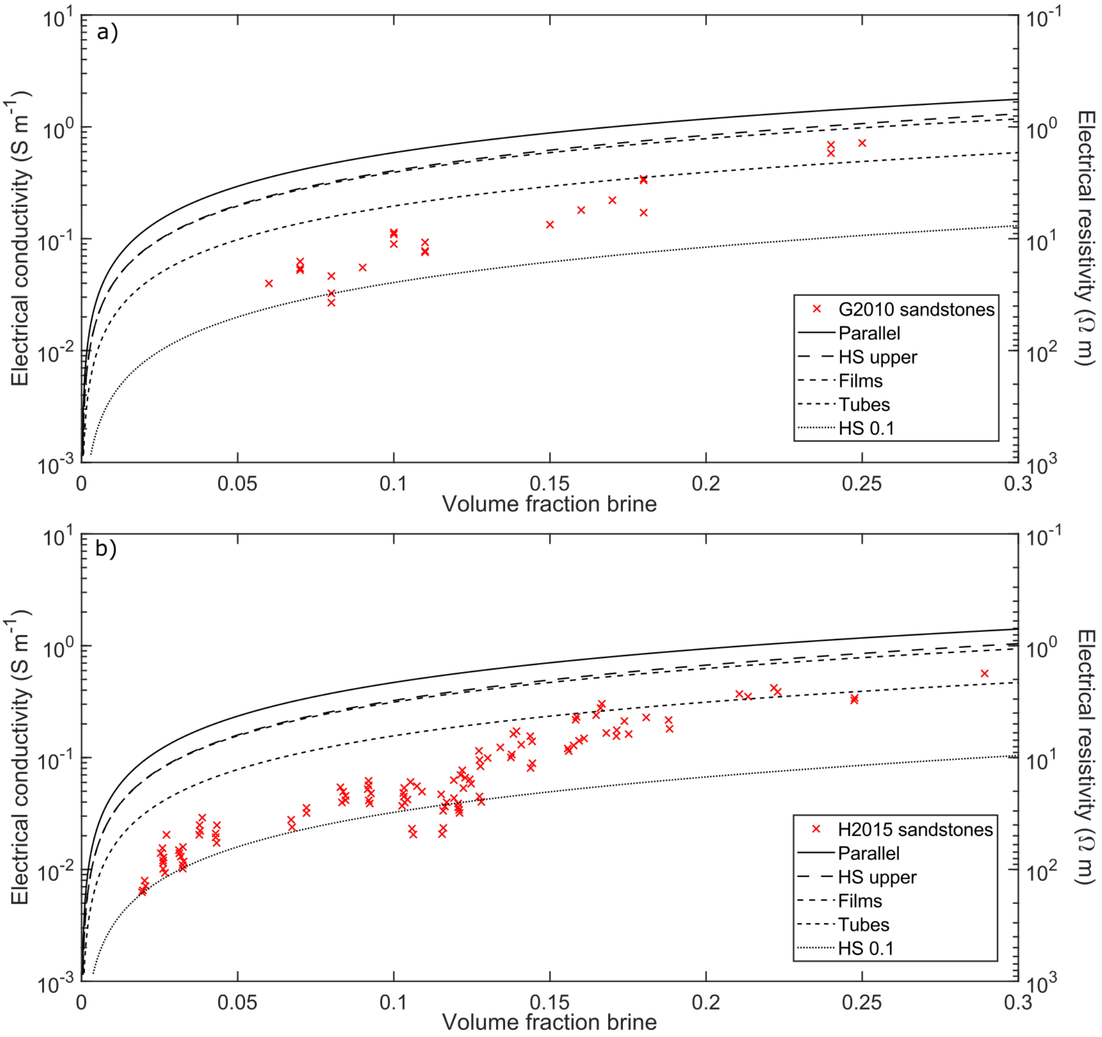

Figure 2.5: Electrical conductivity of sandstones saturated with NaCl solution as a function of porosity. a) Clean sandstones saturated with 4 wt % NaCl solution at ambient conditions, with fully-saturated electrical conductivity calculated from partially-saturated electrical conductivity using Archie's equation (Gomez et al. 2010). b) Sandstones with variable clay content (0-28%) fully-saturated with 3.5 wt % NaCl solution at 26 MPa and ambient temperature (Han et al. 2015). The shown mixing models use the measured electrical conductivity of the saturating fluid (5.9 S m^{-1} in a; 4.7 S m^{-1} in b) and are insensitive to the negligible host rock electrical conductivity. HS 0.1 refers to a tenth of the HS upper bound for electrical conductivity.

2.3.3 Silicate melts

Silicate melts are also ionic electrical conductors, with Na^+ the dominant charge carrier except in some hydrous mafic and intermediate melts (Gaillard 2004, Guo et al. 2016, 2017). The electrical conductivity of silicate melts is complex, being strongly dependent on temperature, composition, and water content, with pressure generally less important. Zhang et al. (2021) provide a complete review on melt electrical conductivity, albeit at mantle conditions. Overall, melt electrical conductivity increases with increasing temperature and water content, but decreases with increasing pressure (Guo et al. 2017). At mantle conditions, Zhang et al. (2021) state that melt electrical conductivity generally decreases with increasing silica content. However, in the crust, melt differentiation leads to silicic melts which are colder but also more water rich than their mafic parental melts, which complicates how silica content correlates with electrical conductivity.

Currently, the only generalised empirical melt electrical conductivity relationship is the SIGMELTS model of Pommier & Le-Trong (2011), which calculates melt electrical conductivity as a function of temperature, pressure, and SiO_2, Na_2O, and H_2O contents. However, more recent experiments have shown that SIGMELTS significantly overestimates electrical conductivities of melts with low water contents and significantly underestimates electrical conductivities for melts with high water contents (Guo et al. 2017, Zhang et al. 2021). Therefore, we prefer to use fixed melt composition empirical electrical conductivity relationships, which are available for a range of melt compositions as a function of temperature, pressure, and water content (Table 2.3). These relationships are calibrated at very high pressures only (>500 MPa), so they must be extrapolated to crustal pressures. Guo et al. (2016) state that extrapolation of their relationship for rhyolitic melts to lower pressures is likely valid, while pressure is less important for andesitic and basaltic melts (Zhang et al. 2021). Care must also be taken when applying these relationships to melts with different major oxide compositions, however, compositional differences can be partially mitigated by using the Nernst-Einstein equation to apply a correction proportional to the Na^+ concentration (Guo et al. 2016, 2017).

Figure 2.6 shows melt electrical conductivities calculated using the fixed composition relationships for basaltic, andesitic, and rhyolitic melts (Table 2.3) as a function of water content and at pressures of 2 GPa ($\approx$70 km) and 0.1 GPa ($\approx$4 km). We use representative temperatures of 700-900 °C for rhyolitic melts, 900-1100 °C for andesitic melts, and 1100-1300 °C for basaltic melts (Lesher & Spera 2015). The relationship of Ni et al. (2011)

for basaltic melts does not include a term to account for pressure, so we approximate basaltic melt electrical conductivity below 2 GPa by calculating and applying the relative increase in the electrical conductivity of andesitic melts between 2 GPa and the specified pressure, using the relationship of Laumonier et al. (2017) at the desired temperature. The relationship of Laumonier et al. (2017) is preferred to that of Guo et al. (2017) for andesitic melts because it is calibrated to a higher water content.

Table 2.3: Empirical silicate melt electrical conductivity relationships

Model	Composition	SiO_2 (wt%)	Na_2O (wt%)	Temperature (°C)	Pressure (GPa)	H_2O (wt%)
Pommier & Le-Trong (2011)	General	49.2 - 55.7	2.0 - 6.1	400 - 1300	0 - 0.4	0 - 5.6
Ni et al. (2011)	Basaltic	50.1	3.7	1200 - 1650	2.0	0 - 6.0
Laumonier et al. (2017)	Andesitic	60.9	2.1	910 - 1407	0.5 - 3.0	0 - 9.0
Guo et al. (2017)	Andesitic	60.8	3.2	890 - 1300	0.5 - 1.0	0 - 5.9
Laumonier et al. (2015)	Dacitic	67.9	2.1	400 - 1350	0.3 - 3.0	0 - 11.8
Guo et al. (2016)	Rhyolitic	75.7	4.7	595 - 1392	0.5 - 1.0	0.1 - 7.9

SiO_2 and Na_2O are wt% anhydrous.

Figure 2.6 shows that basaltic melts generally display the greatest electrical conductivity. This is mostly due to their higher temperature, rather than compositional differences. The importance of melt composition, in particular the sodium content, is illustrated by the lower electrical conductivities of andesitic melts compared with basaltic and rhyolitic melts, as the relationship of Laumonier et al. (2017) for andesite is based on data for a relatively sodium-poor composition (Table 2.3). Water content is also a very strong control on the melt electrical conductivities, which converge at very high water contents. Water content and temperature have a greater affect on electrical conductivity for basic melts compared to silicic melts. Conversely, pressure exerts a stronger control on electrical conductivity for rhyolitic melts compared to andesitic melts. At high water contents, the relationships of Laumonier et al. (2017) and Guo et al. (2016) imply a reversal of the negative pressure effect on andesite and rhyolite electrical conductivity (Figure 2.6b,c). However, this probably arises from extrapolation beyond the experimental ranges into melts that would be super-saturated with water. Overall, most crustal melts likely have electrical conductivities on the order of 10^0 S m^{-1} or less, with only very hot or very water-rich melts having electrical conductivities >10 S m^{-1}.

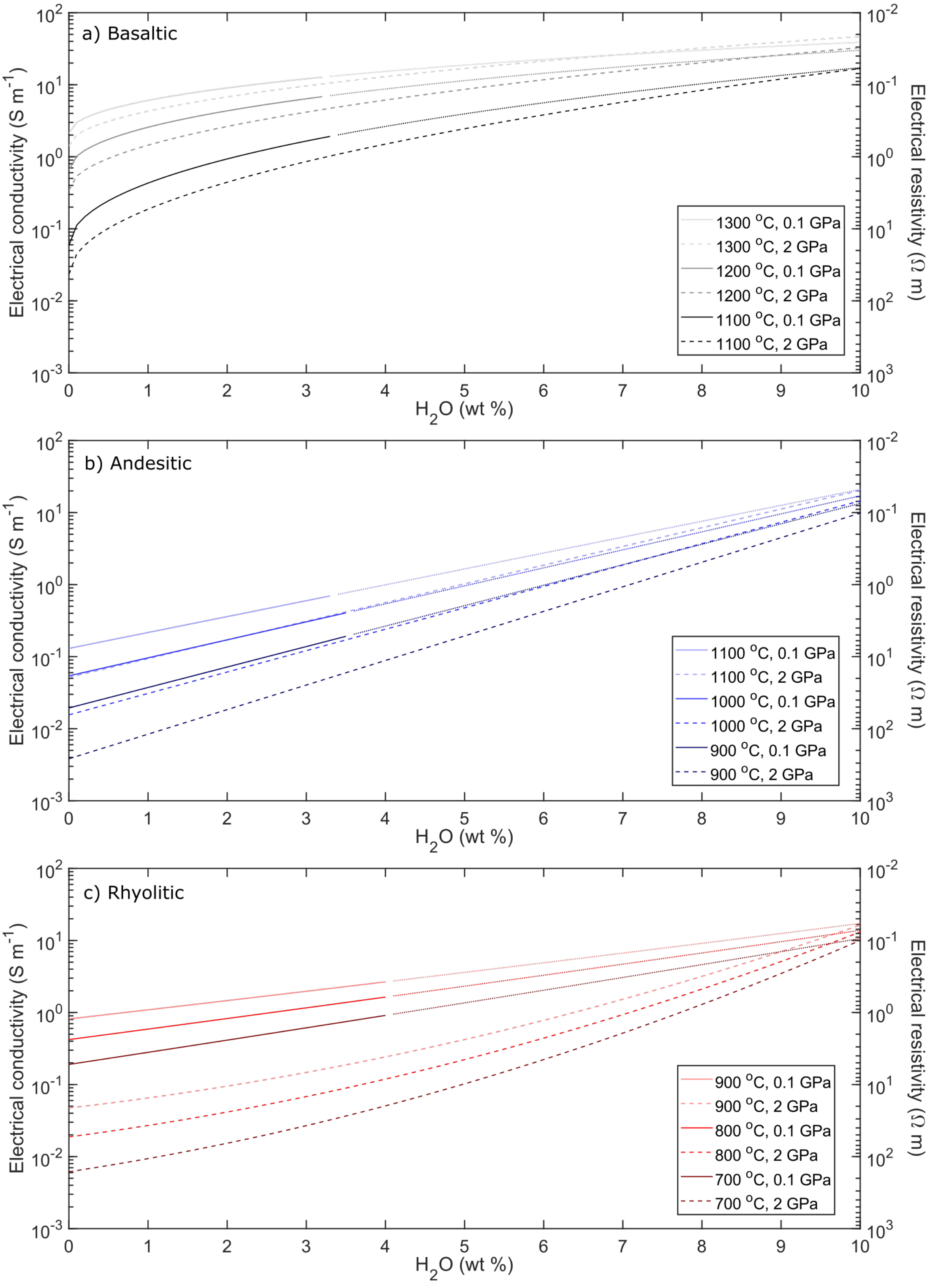

Figure 2.6: Silicate melt electrical conductivity calculated from the fixed melt composition relationships as a function of water content at a range of representative temperatures and 0.1 and 2 GPa. Dotted lines represent where water saturation is exceeded for the 0.1 GPa case. a) Basaltic (Ni et al. 2011), b) Andesitic (Laumonier et al. 2017), c) Rhyolitic (Guo et al. 2016) (Table 2.3.

In melt storage zones, melt spatial connectivity is a function of the interfacial energies at melt-grain boundaries (Daines & Pec 2015). Figure 2.7a shows the effective electrical conductivities of synthetic iron-free olivine rocks with added synthetic basaltic melt at 1475 °C and atmospheric pressure, measured in the laboratory (Ten Grotenhuis et al. 2005). Mixing models using the measured melt electrical conductivity (7.5 S m^{-1}) show that melt connectivity is extremely high. At low melt fractions, the effective electrical conductivity is well modelled by the tubes model, whereas at intermediate melt fractions the films or HS upper bound models are suitable, and at high melt fractions the parallel model is appropriate.

Likewise, Figure 2.7b shows the effective electrical conductivities of San Carlos olivine with added mid-ocean ridge basaltic melt at 1326 °C and 1.5 GPa (Yoshino et al. 2010). Despite the vastly increased pressure, mixing models using the defined melt electrical conductivity (10 S m^{-1}) show that the effective electrical conductivity is well represented by the HS upper bound or parallel models at all melt fractions studied. However, the data in Figure 2.7 are for olivine rocks only. Melt connectivity in more silicic rocks may be lower and requires further investigation, as more melt is needed to form an interconnected network in silicic rocks compared to mafic rocks (Vigneresse et al. 1996, Rosenberg & Handy 2005).

2.4 Electrical conductivity models

2.4.1 Silicate melt or saline magmatic fluids?

At depths greater than typical clay caps (>2-3 km), electrical conductivity anomalies of mostly 0.1 to 1 S m^{-1} beneath volcanoes are usually attributed to the presence of melt and/or fluids (Figure 2.1). However, whether an electrical conductivity anomaly is interpreted as silicate melt or as saline magmatic fluids has important implications. While some studies offer a preferred interpretation, often no such distinction is made (e.g. Díaz et al. (2012, 2015), Mancini et al. (2019)). Although distinguishing between melt and magmatic fluids from magnetotelluric data alone is difficult, we have shown that saline magmatic fluids generally have higher electrical conductivities (10^1-10^2 S m^{-1}) than typical crustal melts (10^{-2}-10^1 S m^{-1}). An important question therefore is whether partial melt can generate sufficiently high effective electrical conductivities, using appropriate mixing models and physical parameters, to explain the observed electrical conductivity anomalies beneath volcanoes. If partial melt cannot explain the observed anomalies, this would suggest that saline magmatic fluids generate the anomalies instead. This is particularly relevant for the intermediate depth electrical conductivity anomalies imaged beneath volcanoes, which could represent either potentially economically important saline magmatic fluids, or potentially hazardous shallow melt reservoirs.

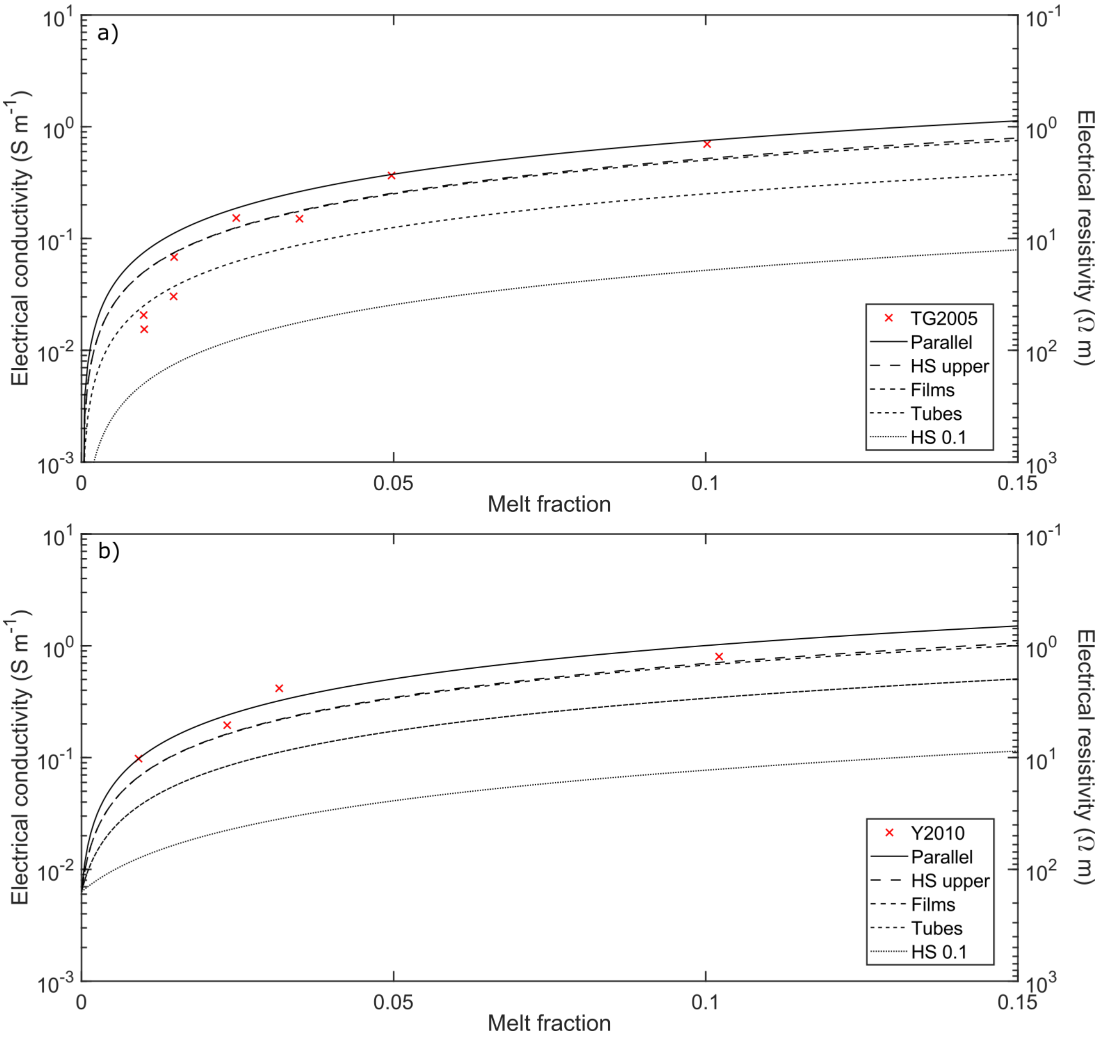

Figure 2.7: Electrical conductivity of melt-bearing rocks as a function of melt fraction. a) Synthetic iron-free olivine rocks with synthetic basaltic melt at 1475 °C and atmospheric pressure (Ten Grotenhuis et al. 2005). b) San Carlos olivine with mid-ocean ridge basaltic melt at 1326 °C and 1.5 GPa (Yoshino et al. 2010). The mixing models use the measured melt electrical conductivity of 7.5 S m^{-1} in a), and is defined as 10 S m^{-1} in b). The shown mixing models are insensitive to the host rock electrical conductivity. HS 0.1 refers to 1/10 of the HS upper bound for electrical conductivity.

To investigate this, we use the fixed melt composition electrical conductivity relationships to calculate the maximum electrical conductivity anomalies that could be generated by partial melt. The maximum electrical conductivity of silicate melts increases with depth, due to increasing water solubility in melts with increasing pressure. However, water solubility in melts also depends on the melt composition and temperature, which themselves affect the melt electrical conductivity. Therefore, we calculate the water solubility as a function of depth for a range of melt compositions and temperatures. For consistency, we use the major oxide melt compositions from the electrical conductivity relationships for basaltic, andesitic, and rhyolitic melts (Ni et al. 2011, Laumonier et al. 2017, Guo et al. 2016), with the same representative temperatures shown in Figure 2.6. We then input these values to the MagmaSat model (Ghiorso & Gualda 2015) within VESIcal software (Iacovino et al. 2021) to calculate saturation pressures for water contents up to 15 wt%. For each water content, we use the default 'fixed volatiles' normalisation, which maintains the specified water content and scales the major oxide contents so that the system as a whole totals 100 wt%. To convert the calculated saturation pressures to saturation depths, we define a lithostatic pressure gradient with a high crustal density of 2700 kg m^{-3}, thereby maximising water solubility as a function of depth (Figure 2.8).

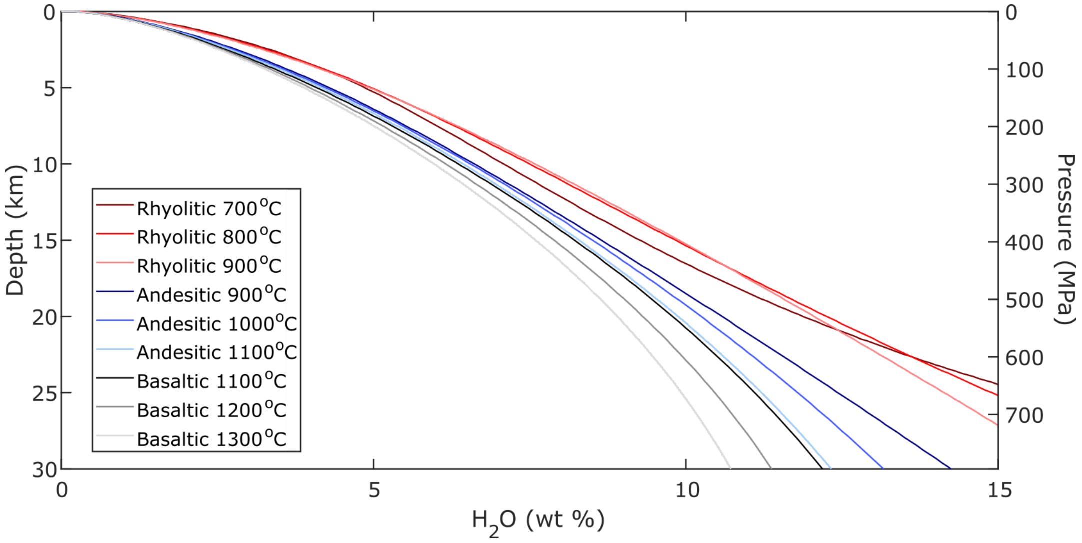

Figure 2.8: Water solubility in melts as a function of depth, calculated using MagmaSat (Ghiorso & Gualda 2015) and assuming a lithostatic pressure gradient with a high crustal density of 2700 kg m^{-3}.

For each melt composition and temperature, we then use the fixed melt composition electrical conductivity relationships to calculate the maximum melt electrical conductivities as a function of depth, by assuming water saturation in the melts (Figure 2.9a). Electrical conductivity anomalies generated by pure melt could in theory match those shown in Figure 2.9a, however, geophysical, geochemical, and geological observations suggest that crustal melts are generally stored as crystal-rich mushes (Bachmann & Huber 2016, Magee et al. 2018). Therefore, we calculate the maximum electrical conductivity anomalies for partial melts using the films mixing model, which we consider to give the highest reasonable melt spatial connectivity. We use a melt fraction of 0.1 to represent a typical mushy system, and a maximum melt fraction of 0.4 to represent a very melt-rich mush (Figure 2.9b).

Figure 2.9a shows that for depths <15 km, water-saturated basaltic melts have the highest electrical conductivities due to their higher temperatures, typically being on the order of 10^0 S m^{-1} at 1100 °C and 10^1 S m^{-1} at 1200 and 1300 °C. By contrast, the electrical conductivities of water-saturated andesitic and rhyolitic melts are generally on the order of 10^{-1}-10^0 S m^{-1}. However, with increasing depth, the greater water solubility in andesitic and rhyolitic melts (Figure 2.8) causes their maximum electrical conductivities to exceed those of basaltic melts. At depths >15 km, the electrical conductivities of water-saturated andesitic and rhyolitic melts are on the order of 10^1 S m^{-1}, potentially reaching 10^2 S m^{-1} at even greater depths (Figure 2.9a). Whether deep andesitic and rhyolitic melts can have electrical conductivities on the order of 10^2 S m^{-1} in reality is unclear, as this would require melts with water contents >12 wt%. Although some evidence exists for such superhydrous melts (e.g. Krawczynski et al. (2012), Goltz et al. (2020)), their widespread presence is unconfirmed. Additionally, the calculations for superhydrous melts exceed the calibrated water contents in both MagmaSat and the fixed composition electrical conductivity models, thereby introducing greater error.

Using the films mixing model, a mush with a high melt fraction of 0.4 has an electrical conductivity approximately half an order of magnitude lower (73%) than pure melt. Nonetheless, electrical conductivity anomalies of 0.1 S m^{-1} at any depth beneath volcanoes can be explained by basaltic, andesitic, or rhyolitic partial melts (Figure 2.9b). In contrast, anomalies of 1 S m^{-1} probably cannot be explained by andesitic or rhyolitic partial melts at depths <5 km, but could be explained by basaltic partial melt. For anomalies of 10 S m^{-1}, only very water-rich mushes at depths >20 km can produce the required electrical conductivities. We consider the electrical conductivity profiles in

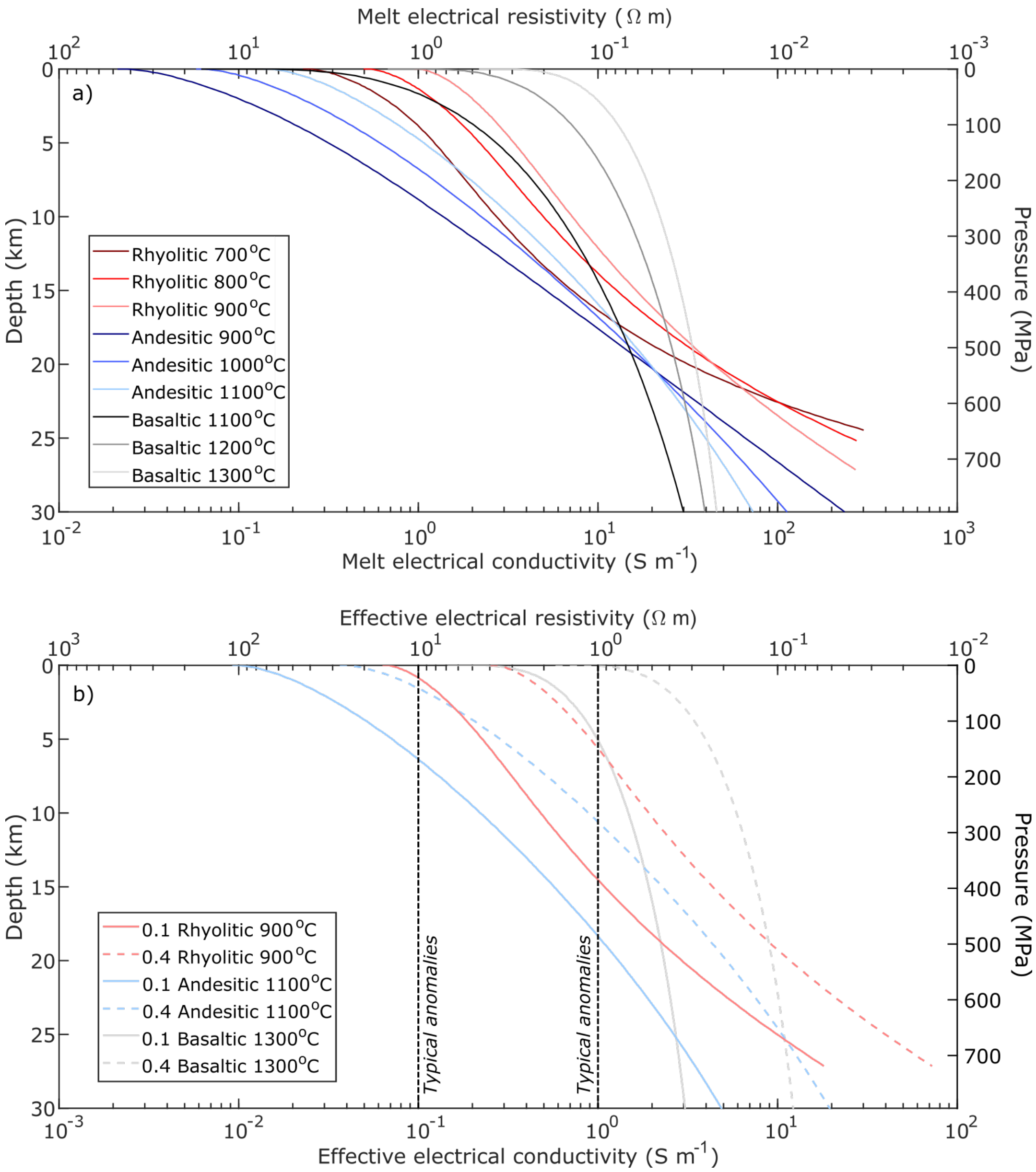

Figure 2.9: a) Maximum melt electrical conductivity as a function of depth, calculated using the fixed composition melt electrical conductivity models (Ni et al. 2011, Laumonier et al. 2017, Guo et al. 2016) and assuming water-saturated melts (up to a maximum of 15 wt% H_2O) under a lithostatic pressure gradient with a crustal density of 2700 kg m^{-3}. b) Maximum electrical conductivity anomalies generated by the presence of partial melt with the properties shown in a) for melt fractions of 0.1 and 0.4, assuming the films mixing model, a host rock with negligible electrical conductivity, and a lithostatic pressure gradient with a crustal density of 2700 kg m^{-3}. For clarity, only the hottest representative temperature is shown for each melt composition, as this has the greatest electrical conductivity. Note the different electrical conductivity scale from a) to b).

Figure 2.9b to represent the maximum reasonable values attributable to the presence of partial melt beneath most volcanoes. Only in exceptional circumstances, such as for highly sodic melts or melt fractions above 0.4, are these values likely to be exceeded.

In reality, electrical conductivity anomalies caused by melt may be significantly lower. For example, a more conservative melt fraction of 0.1 reduces the electrical conductivity by over an order of magnitude (93%) relative to pure melt, using the films mixing model. A melt fraction of 0.1 cannot explain electrical conductivity anomalies of 1 S m^{-1} at depths <5 km for basaltic melts, or at depths of <15 km for andesitic or rhyolitic melts (Figure 2.9b). This highlights the significance of strong ($\approx$1 S m^{-1}) intermediate depth electrical conductivity anomalies beneath arc volcanoes, such as at Láscar and Laguna del Maule (Figure 2.1). These strong anomalies are difficult to explain with partial melt, so they are most consistent with potentially economically important saline magmatic fluids (Blundy et al. 2021). Partial melt reservoirs with very high temperatures (>1200 °C) or high melt fractions (>0.3) cannot be discounted using magnetotellurics alone, but but no current additional geophysical or petrological data support these interpretations.

2.4.2 Simplified magmatic systems

To link the laboratory-derived electrical conductivity relationships for melt and saline magmatic fluids with the results of the volcano magnetotelluric studies, we present simplified models of magmatic systems and calculate their electrical resistivity structures. Detailed dynamic models of magmatic-hydrothermal systems are provided by Scott et al. (2017) and Afanasyev et al. (2018), however, our focus is to investigate the range of electrical resistivity structures beneath volcanoes and identify the main physical controls. Similar models to those presented here were also recently published by Watanabe et al. (2022), and we discuss where their models differ from ours.

In our models, we define a melt reservoir with 0.15 melt fraction between 8 km depth and the base of the model at 12 km, consistent with the deep electrical conductivity anomalies at Andean volcanoes (Figure 2.1). Here, we show both basaltic and rhyolitic melt reservoirs with a water content of 5 wt%, such that the top of the reservoir is close to water saturation. Overlying and derived from this melt, magmatic fluids with a bulk salinity of 5-15 wt% NaCl are are assumed to fill the existing porosity structure, which decays exponentially with depth. We apply magmatic fluid temperatures between 400-600°C and fluid pressure gradients between hydrostatic and lithostatic (i.e. densities between 1000 and 2700 kg m^{-3}) to investigate variations in the depths of phase changes within the magmatic fluid column and the effect on the electrical resistivity structure. Where vapour and hypersaline brine phases coexist, we assume that the vapour escapes upwards towards the surface, so the fluid salinity and electrical conductivity are given by the brine phase. Where vapour and halite phases coexist, the fluid salinity and electrical conductivity are given by the vapour phase, as halite is not electrically conductive. To calculate the model electrical resistivity structure, we compute effective electrical conductivities using the films mixing model for the partial melt (Figure 2.7), and a tenth of the HS upper bound for the saline magmatic fluids (Figure 2.5).

Figure 2.10 shows the electrical resistivity profiles generated by the simplified magmatic system models. Each model can be split into four depth domains, defined by the fluid phases present and their salinity. The deepest domain is associated with the melt reservoir, with Figure 2.10 showing water-saturated basaltic and rhyolitic melts. For these water-saturated melts, the electrical conductivity of the melt domain spans the range of 0.1 to 1 S m^{-1} typical for electrical conductivity anomalies beneath volcanoes. Water under-saturated melts would have lower electrical conductivities.

Directly above the melt reservoir, the magmatic fluid column is usually in a supercritical state and therefore has a salinity equal to that of the initial exsolved magmatic fluid. For particularly hot magmatic fluids under sufficiently low pressures, the supercritical domain may be absent (Figure 2.10d). The supercritical fluid domain generally has a relatively low electrical conductivity on the order of 10^{-2} S m^{-1}, although it occasionally reaches 10^{-1} S m^{-1} for high bulk salinities. Greater magmatic fluid pressures and salinities increase the electrical conductivity of the supercritical domain, whereas greater temperatures decrease the electrical conductivity.

Above the supercritical domain, lower pressure causes the magmatic fluid to separate into hypersaline brine and vapour phases. The high salinity of the brine causes this domain to have electrical conductivities mostly around 0.1 to 1 S m^{-1}, which are typical for observed electrical conductivity anomalies beneath volcanoes. The depth of the brine domain is highly dependent on the pressure and temperature conditions. For greater magmatic fluid temperatures, the brine domain exists over a greater depth range; for fluid temperatures of 300 °C, there is no significant brine lens. Greater fluid pressures shift the brine domain towards shallower depths. For our static models, the initial salinity of the exsolved magmatic fluid has little effect on the brine domain properties.

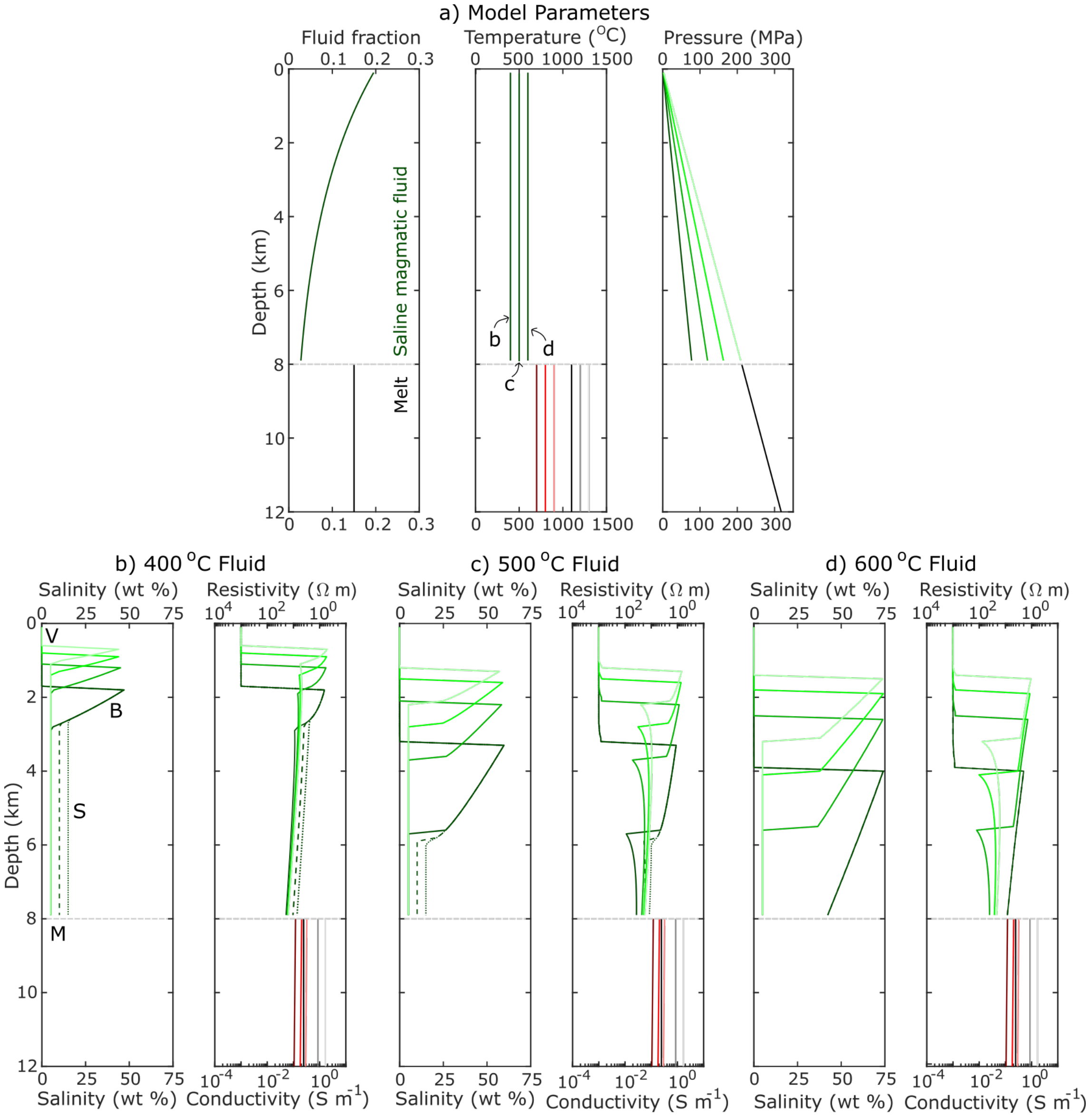

Figure 2.10: Simplified models of magmatic systems and their calculated electrical resistivity profiles. The models consist of a lower melt reservoir of basaltic (grey) or rhyolitic (red) composition with 5 wt% water, overlain by an exsolved magmatic fluid column (green). a) Model parameters as a function of depth. Variable magmatic fluid temperatures of 400 °C, 500 °C, and 600 °C correspond to the panels b), c), and d) respectively. Variable fluid pressures from hydrostatic (darkest green) to lithostatic (lightest green) are also shown. b-d) The calculated salinities of the magmatic fluid column and the calculated electrical conductivites of the whole magmatic system. The effects of increased bulk magmatic fluid salinities of 10 and 15 wt% are shown by dashed and dotted lines respectively, for the hydrostatic magmatic fluid pressure gradient only. In b), the locations of the domains for the hydrostatic fluid pressure case are indicated for visualisation (M = melt, S = supercritical, B = brine, V = vapour).

Above the brine domain, further pressure decrease causes a transition to coexisting vapour and halite phases. The vapour domain has negligible electrical conductivity, although clay caps could generate electrical conductivity anomalies at these depths. At greater depths, the electrical conductivity of the supercritical and brine domains increases towards shallower depths, due to increasing porosity and brine formation. By contrast, the electrical conductivity of the melt domain will probably decrease towards shallower depths, due to water exsolution and decreasing temperature (Figure 2.9).

Important differences between our models and those of Watanabe et al. (2022) arise from how the effective electrical conductivities are calculated in the magmatic fluid column. Firstly, our use of a tenth of the HS upper bound mixing model for saline magmatic fluids (Figure 2.5) means that intermediate depth electrical conductivity anomalies on the order of 0.1 to 1 S m^{-1} are best interpreted as hypersaline brine lenses; lower salinity primary magmatic fluids generally produce effective electrical conductivities <0.1 S m^{-1} in our models. By contrast, Watanabe et al. (2022) use the HS upper bound, which allows them to explain intermediate depth electrical conductivity anomalies of ≥0.1 S m^{-1} using fluids with a salinity as low as 0.5 wt% NaCl. Secondly, in the brine-vapour coexistence region, Watanabe et al. (2022) calculate the bulk fluid electrical conductivity of the mixed hypersaline brine and vapour phases, whereas we assume the vapour escapes upwards and use only the brine. Consequently, our electrical conductivities in the brine domain are greater than those of Watanabe et al. (2022).

While both approaches may be valid under different circumstances, we note that our models produce electrical resistivity profiles that can explain the diverse features of the Andean volcano magnetotelluric studies (Figure 2.1). For example, colder magmatic fluid temperatures result in a vertically extensive supercritical fluid domain with low electrical conductivities, which separates the shallower electrically conductive brine lens from the deeper electrically conductive melt reservoir (Figure 2.10b). Separated intermediate depth and deep anomalies are observed at Uturuncu, Láscar, and Lastarria. By contrast, hotter magmatic fluid temperatures result in a deeper and more vertically extensive brine lens, with less separation between the melt reservoir and the brine domain (Figure 2.10d). This may give the appearance of a continuous electrical conductivity anomaly with depth, as seen at Laguna del Maule and Tinguiririca. A continuous anomaly with depth could also occur for colder magmatic fluids with a very high bulk salinity (≥10 wt%: Figure 2.10a). However, the lack of sampling of magmatic fluids means these hypotheses are untested. The melt reservoir depth, which we do not investigate, is also important.

While our models can reproduce the observed electrical resistivity structures well, we also recognise alternative explanations. For example, whether the intermediate depth and deep anomalies are connected could relate to the current volume of fluid transfer between the melt reservoir and the overlying brine lens. Alternatively, depending on their electrical conductivity, some intermediate depth anomalies could be interpreted as shallow melt reservoirs. In this case, the connection between the intermediate depth and deep electrical conductivity anomalies would relate to melt transfer between the two reservoirs instead.

2.5 Discussion

2.5.1 Interpreting volcano magnetotellurics

Magnetotelluric studies reveal a range of electrical resistivity structures beneath Andean volcanoes (Figure 2.1). With the exception of shallow electrical conductivity anomalies attributable to clay minerals, interpretation of volcano magnetotellurics generally aims to ascertain the nature of the fluid responsible for the anomaly. At the first order, this means distinguishing between partial melt or saline magmatic fluids. More detailed analyses may comment on factors such as the fluid temperature, composition, and fraction. However, we have shown that even the distinction between partial melt and saline magmatic fluids is difficult using magnetotelluric data alone. The exception to this at arc volcanoes are relatively shallow anomalies (<10 km) with high electrical conductivities (≥ 1 S m^{-1}), which are difficult to explain with partial melt and so most likely represent saline fluids (Figure 2.11). These anomalies could also represent coexisting melt and saline fluids, although the saline fluids must have high spatial connectivity in order to increase the effective electrical conductivity; isolated bubbles of exsolved magmatic fluids within a partial melt will not significantly increase the electrical conductivity.

The deep electrical conductivity anomalies at the studied volcanoes are generally interpreted as partial melt (Figure 2.1). At large depths, the high water solubility in melts can explain the high electrical conductivities, while also reducing fluid exsolution and formation of saline magmatic fluids. However, whether the intermediate depth anomalies represent melt, saline magmatic fluids, or both, is less clear. To further investigate the origins of the intermediate depth and deep electrical conductivity anomalies, Table 2.4 shows the calculated volume fractions of representative melts and saline fluids required to explain the anomalies at the studied volcanoes. The representative melts are

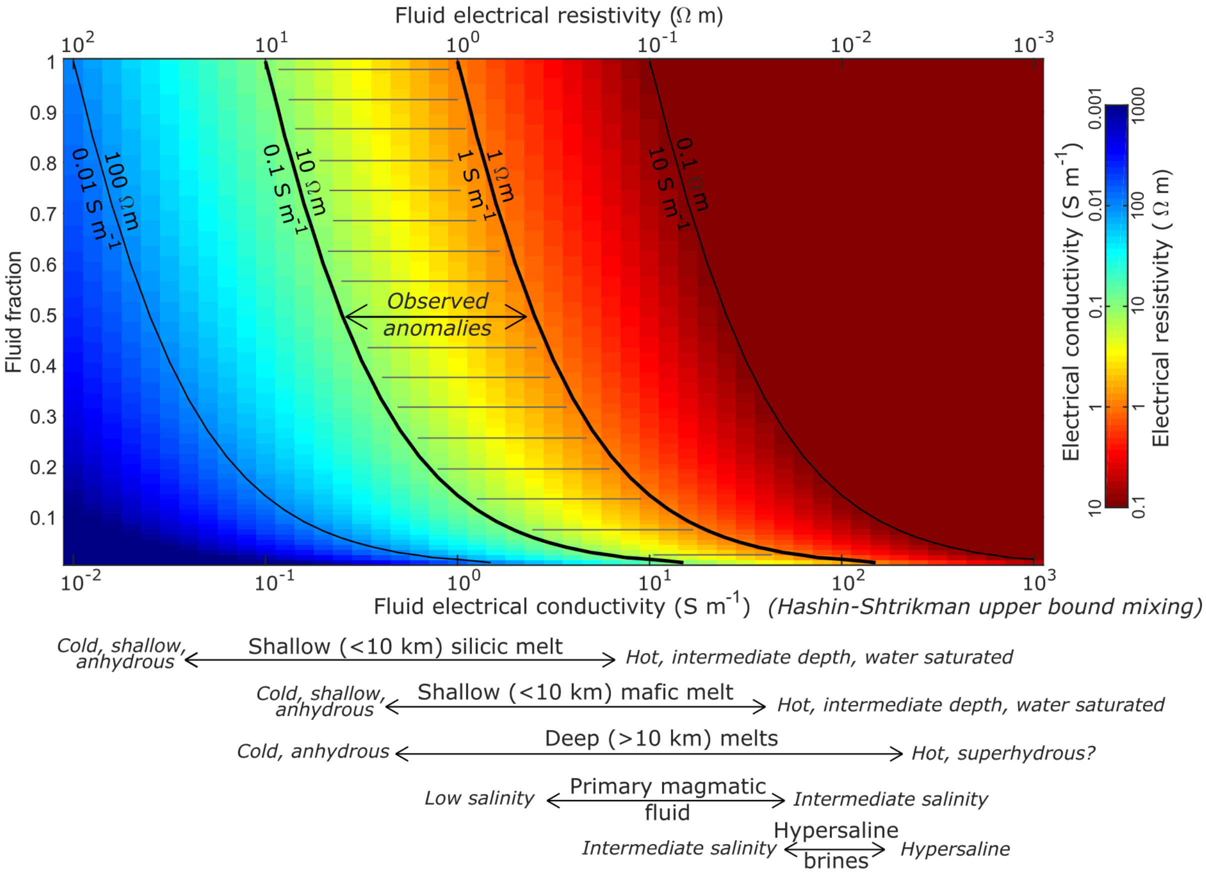

Figure 2.11: Effective electrical conductivities (colour shading) calculated using the HS upper bound (high spatial connectivity) mixing model, as a function of fluid electrical conductivity and fluid fraction. Representative values of fluid electrical conductivities are shown below the chart. The region corresponding to typical observed electrical conductivity anomalies on the order of 0.1 to 1 S m^{-1} is also indicated. Note that extremely high fractions of shallow silicic melt are required to explain typical anomalies, while only very low fractions of hypersaline brines are required. The chosen mixing model is also an important control.

andesitic melt at 1100 °C and rhyolitic melt at 900 °C (Figure 2.9), both assumed to be at water-saturation at the top of each anomaly. The electrical conductivity relationship for andesitic melts (Laumonier et al. 2017) has a relatively low sodium content, so we attempt to counteract this by using a high 1100 °C temperature instead. Basaltic melts are not considered, as hot mafic melt reservoirs are more consistent with deeper lower crustal reservoirs at subduction zones (Hildreth & Moorbath 1988). Additionally, although basaltic melts theoretically can display the highest electrical conductivities (Figure 2.9), the two studied basaltic volcanoes, Villarrica and Osorno, actually exhibit the lowest magnitude electrical conductivity anomalies. For saline fluids, we use 5 wt% NaCl solution to represent primary magmatic fluids and 40 wt% NaCl solution to represent hypersaline brines. To avoid defining fluid temperatures and pressures, we take the saline fluid electrical conductivities as the peak values in Figure 2.4 (34.7 S m^{-1} for 5 wt% NaCl, 187.2 S m^{-1} for 40 wt% NaCl). To calculate the required fluid fractions, we use the films mixing model for melts (Figure 2.7), and a tenth of the HS upper bound for saline fluid fractions < 0.15 and the tubes model for saline fluid fractions >0.15 (Figure 2.5).

Table 2.4 shows that hot water-saturated andesitic melt can explain all of the deep electrical conductivity anomalies except Lastarria, although very high melt fractions (≈ 0.5) are required at Uturuncu and Laguna del Maule. However, the representative andesitic melt cannot explain the intermediate depth anomalies at Uturuncu, Láscar, Lastarria, and Laguna del Maule. Additionally, extremely high andesitic melt fractions are required to explain the intermediate depth anomalies at Paniri (0.93) and Tinguiririca (0.7). As andesite is the typical composition of the studied Andean volcanoes, this casts doubt on the interpretation of the intermediate depth anomalies as partial melt. Moderate fractions of hot water-saturated rhyolitic melt can explain most of the intermediate depth anomalies, however, the intermediate depth anomalies at Láscar and Laguna del Maule cannot be explained by rhyolitic melt either. Therefore, we consider that saline magmatic fluids are the more likely explanation for at least some, if not most, of the imaged intermediate depth electrical conductivity anomalies. Despite using a lower spatial connectivity mixing model, only relatively low saline fluid fractions (<0.2) are required to explain the intermediate depth anomalies. For hypersaline brines, a fluid fraction of <0.05 can explain most of the intermediate depth anomalies, although higher fluid fractions are required at Láscar and Laguna del Maule.

Although this analysis provides useful generalised results, detailed analyses at individual volcanoes should incorporate melt and fluid compositions and temperatures from petrological constraints. For example, the low electrical conductivities at Osorno are thought to arise from the very low water contents in the melts (Tagiri et al. 1993), which reduces the melt electrical conductivity and limits magmatic fluid exsolution. However, a single volcano may exhibit several different melt compositions, while petrologically inferred melt storage temperatures can vary by several hundred degrees (e.g. Boschetty et al. 2022). The variability in electrical conductivity within anomalies with depth is also important; the increase in electrical conductivity with depth in the deep anomaly at Lastarria may explain why our results struggle to allow partial melt as an explanation.

Table 2.4: Silicate melt and saline magmatic fluid fractions required to explain the intermediate depth and deep electrical conductivity anomalies at the studied Andean volcanoes

Anomalies			Andesite 1100 °C		Rhyolite 900 °C		5 NaCl	40 NaCl
Volcano	Depth (km)	Conductivity (S m^{-1})	Conductivity (S m^{-1})	Melt fraction	Conductivity (S m^{-1})	Melt fraction	Fluid fraction	Fluid fraction
Paniri	4-7	0.50	0.81	0.93	2.89	0.26	*0.15*	0.04
	5-13	0.17	1.04	0.25	3.37	0.08	0.08	0.02
Uturuncu	2-10	0.33	0.43	>1	1.98	0.25	0.14	0.03
	>16	3.33	10.02	0.50	19.33	0.26	*0.29*	*0.15*
Láscar	0-6	2.00	0.15	>1	1.03	>1	*0.20*	*0.15*
	>10	0.05	3.26	0.03	6.99	0.02	0.03	0.01
Lastarria	1-8	0.20	0.29	>1	1.54	0.20	0.09	0.02
	>5	1.00	1.04	>1	3.37	0.45	*0.15*	0.08
Laguna del Maule	4-8	3.33	0.81	>1	2.89	>1	*0.29*	*0.15*
	>8	0.67	2.08	0.49	5.18	0.20	*0.15*	0.06
Tinguiruirica	2-12	0.20	0.43	0.70	1.98	0.16	0.09	0.02
	>8	0.13	2.08	0.10	5.18	0.04	0.06	0.02
Villarrica	3-6	0.10	0.60	0.25	2.43	0.07	0.05	0.01
Osorno	4-8	0.01	0.81	0.02	2.89	0.01	0.01	0.01
	7-15	0.03	1.70	0.03	4.51	0.01	0.02	0.01

Italics shows where the tubes mixing model has been used for saline fluids with fluid fractions >0.15.

2.5.2 Integrating complementary data

The interpretation of the intermediate depth electrical conductivity anomalies as saline magmatic fluids leads to a model of deeper melt reservoirs, overlain by saline magmatic fluids, and capped by a clay alteration layer. In general, this three layer model fits the studied Andean volcanoes well. However, previous studies often infer partial melt in the intermediate depth anomalies (Figure 2.1). Given the at best ambiguous evidence for intermediate depth partial melt from magnetotellurics, interpretation of partial melt in the intermediate depth anomalies must rely on further information. For the studied volcanoes, the most commonly cited evidence for intermediate depth partial melt comes from petrologic geobarometry analyses, as cited for Paniri (Cerro del León) Uturuncu, Laguna del Maule, and Villarrica (De Silva et al. 1994, Muir et al. 2014, Klug et al. 2020, Morgado et al. 2015). At the global scale, petrologically inferred melt storage depths also cluster around intermediate depths between 4-6 km (Rasmussen et al. 2022). Rasmussen et al. (2022) also cite geophysical evidence, mainly based on surface deformation and seismic tomography, for global melt storage depths commonly between 4-6 km. Taken together, these observations suggest that partial melt may also be present in the intermediate depth electrical conductivity anomalies, although our review generally favours saline magmatic fluids as the source of the enhanced electrical conductivities (e.g. Figure 2.11).

The coexistence of partial melt and saline magmatic fluids at intermediate depths, especially over the kilometer scale resolution of volcano geophysical surveys, may not be uncommon. For example, petrological evidence for melts ascending from 14 to 4 km depth at Laguna del Maule coincides with the electrical conductivity anomalies (Klug et al. 2020). This suggests that the intermediate depth anomaly attributed to saline magmatic fluids may also act as a conduit for melt transfer to the shallow melt reservoir that is not detected by magnetotellurics. From the geologic record, mixed melt and magmatic fluid systems at intermediate depths may be preserved as porphyry (copper) systems. In these systems, small (< 1 km across) porphyritic dykes derived from a deeper pluton act as sources and pathways for magmatic fluids, which produce characteristic halos of alteration and mineralisation surrounding the intrusion (Sillitoe 2010). Porphyry emplacement depths, typically in the upper 4 km but up to 9 km depth, match well with the intermediate depth electrical conductivity anomalies, while the underlying parental plutons are inferred to be located at 5-15 km depth, overlapping with the deep electrical conductivity anomalies (Cloos 2001, Singer et al. 2005).

Direct evidence for melt and fluid coexistence comes from Krafla, Iceland, where drilling attempting to reach supercritical geothermal reservoir conditions terminated upon intercepting rhyolitic melt at 2.1 km depth (Elders et al. 2014). Subsequent magnetotelluric investigation showed that this melt was encountered near the intersection of an intermediate depth electrical conductivity anomaly, interpreted as either partial melt or aqueous fluids, and an overlying chimney-like anomaly, associated with a permeable fault zone that acts as a conduit for aqueous fluids (Lee et al. 2020). Based on other wells in the area and geophysical constraints, the rhyolite melt was interpreted as a small sill rather than a major melt reservoir, and would not have been detected by the magnetotelluric surveys (Lee et al. 2020).

Complementary geophysical methods can help constrain whether an electrical conductivity anomaly is caused by melt or magmatic fluids. As previously noted for Laguna del Maule, considering multiple geophysical datasets together can reduce uncertainty. For example, to explain a given electrical conductivity anomaly, the melt fraction required may be several times greater than the required magmatic fluid fraction (Table 2.4). While a large melt fraction is likely to produce low gravity and slow seismic wave speed anomalies, a small fraction of saline fluid may be undetectable. However, this is complicated by the fact that saline fluids have lower densities than silicate melts, so produce greater density reductions for the same fluid fraction. For seismic wave velocities, the effects of melt and magmatic fluid also depend on their geometry in the rock mass, which is another unknown (Takei 2002, Brantut & David 2019). Nonetheless, seismic wave speeds can be used to review the fluid fraction inferred from magnetotellurics; in particular, high inferred melt fractions should correspond to significantly lower shear wave velocities. Similarly, the ratio of P-wave to S-wave velocities could be useful, with higher values potentially indicating melts and lower values indicative of fluids (Takei 2002, Lees 2007). The distribution of seismicity can be used to indicate the position of the brittle-ductile transition (BDT) (Ito 1993). Partial melt reservoirs are hotter than the BDT, so will be characterised by a lack of volcano-tectonic earthquakes, whereas magmatic fluid reservoirs could be cooler than the BDT and exhibit volcano-tectonic earthquakes or swarm seismicity (McNutt & Roman 2015).

Although the exact nature of the intermediate depth electrical conductivity anomalies remains ambiguous, there exists one instance of an intermediate depth anomaly being directly sampled by drilling. At Kakkonda, Japan, drilling penetrated the fringes of an intermediate depth anomaly at 3.7 km depth, where hypersaline fluids entered the well.

The fluid had a salinity of 39-55 wt% and temperature of 500 °C, while the host rock porosity was measured as 0.024 (Kasai et al. 1998, Fujimoto et al. 2000). If we use these values with a tenth of the HS upper bound, as suggested by laboratory data for low porosity (Figure 2.5), we obtain an effective electrical conductivity of 0.16-0.26 S m^{-1}, which is a reasonable match with the electrical conductivity of 0.10-0.16 S m^{-1} imaged using magnetotellurics (Uchida et al. 2000). For the same fluid, the central part of the intermediate depth anomaly at Kakkonda with an electrical conductivity of around 1 S m^{-1} would require a fluid fraction of 0.15.

2.5.3 Implications for magmatic systems

The large variety in electrical resistivity structures imaged at Andean volcanoes could reflect differences in the magnetotelluric methodology between studies, the diverse characteristics of the volcanoes, or the dynamic nature of magmatic systems. Overall, electrical conductivity anomalies imaged using magnetotellurics are consistent with a model consisting of a deep vertically-extensive melt reservoir, overlain by intermediate depth exsolved saline magmatic fluids, and finally a shallow clay cap (Figure 2.12). The exact nature of the intermediate depth anomalies is unclear; saline magmatic fluids are generally most consistent with the observed electrical conductivities, but localised regions of melt are probably also present, at least transiently. The coexistence of partial melt and saline magmatic fluids at intermediate depths suggests these anomalies may represent active porphyry (copper) systems.

The deep electrical conductivity anomalies, which are interpreted as melt reservoirs, are generally vertically-extensive (Figure 2.1), consistent with the transcrustal magmatic system model. Furthermore, the intermediate depth and deep anomalies are often connected, providing further evidence for the transcrustal model. However, smoothing and a lack of sensitivity at large depths during inversion blur the image. By contrast, where the deep and intermediate depth anomalies are not connected, this is consistent with models of a deep melt reservoir periodically supplying melt to a shallower reservoir (Gudmundsson 2006). Several of the intermediate depth anomalies are dipping, perhaps highlighting the importance of structures in controlling magma and magmatic fluid pathways. Both the intermediate depth and deep anomalies are also often laterally offset from the volcanic edifices, and recent eruptions do not always occur from the volcano located closest to the imaged reservoirs (e.g. Planchón-Peteroa, San Pedro).

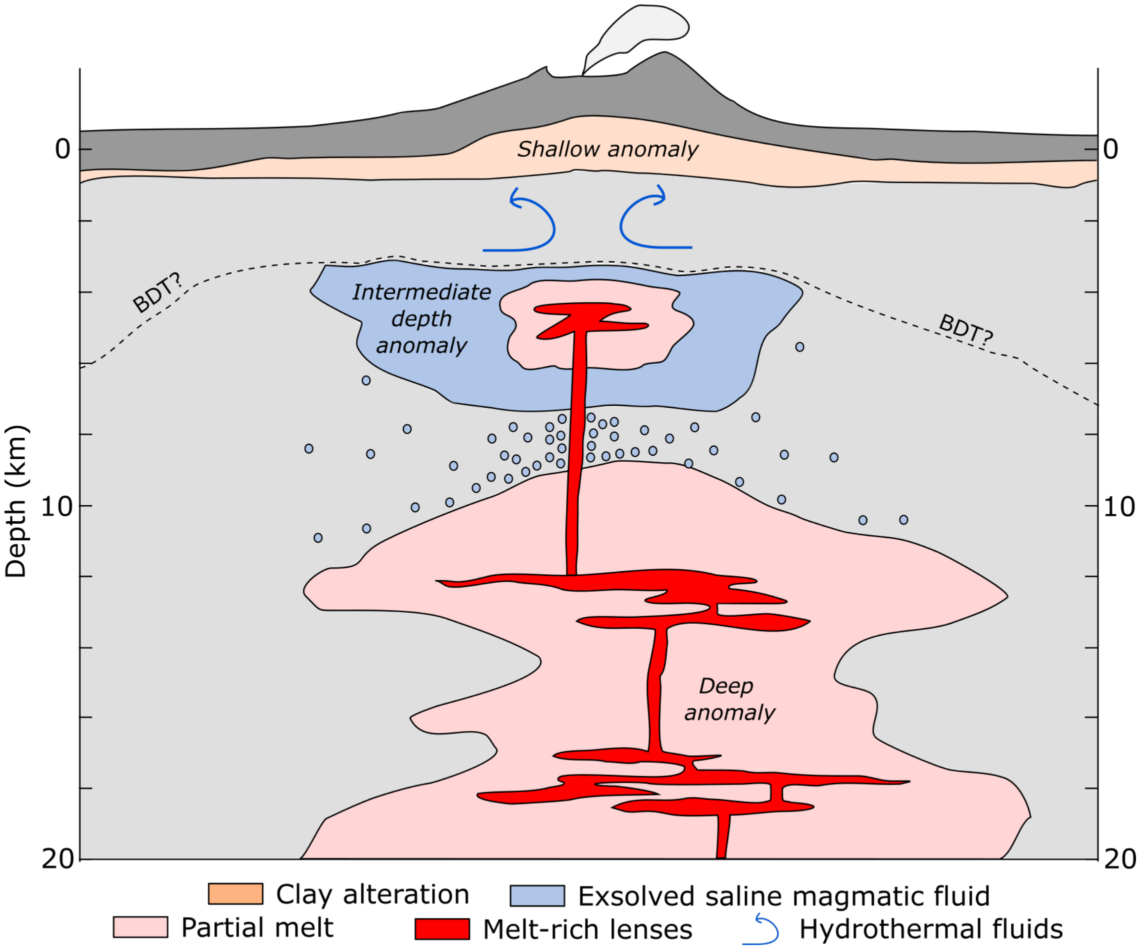

Figure 2.12: Summary of the generalised model proposed to explain electrical resistivity structures revealed by magnetotellurics at Andean volcanoes. Electrical conductivity anomalies at deep (>10 km), intermediate (≈5 km), and shallow (<3 km) depths are consistent with a model of deeper melt reservoirs, overlain by exsolved saline magmatic fluids, and capped by a clay alteration layer. Typical geothermal exploration targets hydrothermal fluids (meteoric or seawater, so low electrical conductivity) circulating beneath the clay cap but above the brittle-ductile transition (BDT). Interpretation of the deeper structure must therefore rely on indirect imaging such as magnetotellurics.

The nature of the intermediate depth anomalies is important from an economic perspective, for projects aiming to harness high enthalpy geothermal energy or extract metals from saline magmatic fluids. Metal content in magmatic fluids is strongly correlated to the fluid salinity (Blundy et al. 2021), but determining fluid salinity from magnetotellurics is extremely challenging; our simplified magmatic system models favour hypersaline brine lenses as the cause of intermediate depth electrical conductivity anomalies (Figure 2.10), but Table 2.4 shows that reasonable fluid fractions of low salinity primary magmatic fluids can also generate the observed anomalies. However, the scarcity of very strong ($\geq$1 S m^{-1}) intermediate depth electrical conductivity anomalies suggests that large hypersaline brine lenses are either uncommon, or are characterised by very low fluid fractions. This observation is consistent with the rarity of large well-mineralised porphyry copper deposits, despite porphyry-type alteration being common throughout volcanic arcs (Richards 2018). The very strong intermediate depth anomalies at Láscar and Laguna del Maule are exceptions to this, while Kakkonda provides direct evidence for the existence and mobility of hypersaline brines at low fluid fractions, and also hints at potential regions of higher fluid fractions. Alternatively, pockets of high fluid fraction hypersaline brines may be present beneath many volcanoes, but not detectable at the scale relevant to transcrustal magnetotelluric surveys. This would have the effect of smoothing out the electrical conductivity anomaly, a problem which also applies melt rich lenses existing within lower melt fraction mushes.

2.5.4 Future directions

Magnetotellurics provides useful insights into the sub-surface structure at volcanoes, although uncertainties remain in its interpretation. To constrain these uncertainties, observations at Kakkonda highlight the importance of accurate laboratory-derived electrical conductivity relationships and an understanding of the appropriate spatial connectivities. Opportunities exist to add to our knowledge in this area. For example, it would be useful to have more generalised electrical conductivity relationships for silicate melts, and for these to be constrained at crustal pressures. The electrical conductivity of hypersaline brines also requires further study. Most importantly, work investigating the spatial connectivity of melt and fluids depending on pressure, fluid and rock composition, and fluid fraction is also important, especially at low fluid fractions and in crystalline rocks. However, whether the spatial connectivity determined in the laboratory is applicable to transcrustal scale magnetotelluric surveys is also an important consideration.

Our review of Andean volcano magnetotelluric studies could be extended to other areas and tectonic settings. At other subduction zones, volcano magnetotelluric studies are generally consistent with the findings from the Andes. For example, spatially separate intermediate depth and deep electrical conductivity anomalies have been imaged beneath volcanoes in New Zealand (Bertrand et al. 2012), North America (Peacock et al. 2016), and Japan (Aizawa et al. 2022), while some subduction zone volcanoes display a single vertically-extensive electrical conductivity anomaly (Hill et al. 2009, Aizawa et al. 2014, Ogawa et al. 2014, Matsushima et al. 2020). By contrast, rift or hotspot volcanoes likely have hotter more mafic melt compositions but lower water contents than arc volcanoes, which may produce different electrical resistivity structures. At individual volcanoes, integrating petrological constraints on melt and fluid composition and temperature with improved electrical conductivity relationships would further constrain magnetotelluric interpretation. Repeat (4D) Magnetotelluric surveys could also shed light on the dynamic nature of magmatic systems.

2.6 Conclusions

The commonly observed electrical resistivity structure beneath Andean arc volcanoes of deep (>10 km), intermediate depth (≈5 km), and shallow (<3 km) electrical conductivity anomalies is consistent with a model of deeper melt reservoirs, overlain by saline magmatic fluids, and capped by a clay alteration layer (Figure 2.12). Although many previous studies attribute intermediate depth anomalies to the presence of partial melt, we show that saline magmatic fluids are generally more consistent with the observed electrical conductivities. However, the presence of partial melt at intermediate depths is also likely, suggesting that the intermediate depth anomalies may represent active porphyry (copper) systems. Incorporating other geophysical and petrological data is key for improving the interpretation of magnetotelluric data. To further constrain the interpretation of volcano magnetotelluric data, developments in laboratory-derived electrical conductivity relationships, especially investigating the spatial connectivity of partial melt and saline fluids in the upper crust, are also required.

CHAPTER

3

DECADAL TIMESCALE CORRELATIONS BETWEEN GLOBAL EARTHQUAKE ACTIVITY AND VOLCANIC ERUPTION RATES

At the global scale, large tectonic earthquakes and volcanic eruptions are believed to be random and independent events. Here, we compare global time-series of large earthquakes ($M_w \geq 7$) and explosive volcanic eruptions (VEI ≥ 2) spanning 1960-2019. Both time-series exhibit decadal timescale trends, over which annual earthquake and eruption rates vary by a factor of ~2. Moreover, global seismic moment release is positively correlated with global eruption rate, with Monte Carlo permutation tests showing that this correlation is significant with a P-value of <0.05. Although large earthquakes can trigger eruptions at nearby volcanoes, the magnitude of this effect is insufficient to cause the observed global correlation. Other mechanisms, such as triggering of distant eruptions (> 1000 km) by earthquake-induced dynamic stress changes, modulation of global earthquake and eruption rates by variations in Earth's rotational velocity, or natural synchronisation of events over repeating cycles, are therefore required to explain the correlation.

This chapter is previously published as (Jenkins, Biggs, Rust & Rougier 2021). See the note on previous publications for more detail (Page xvii).

3.1 Introduction

Earthquakes and volcanoes have long been associated with each other due to their occurrence near plate boundaries. However, whether the timings of large tectonic earthquakes and explosive volcanic eruptions are related is unclear. On one hand, several studies have investigated how stress changes generated by large earthquakes can trigger eruptions at nearby ($\lesssim$ 1000 km) volcanoes (e.g. Linde & Sacks 1998, Nishimura 2017, Sawi & Manga 2018). Although the exact findings of these studies differ, with eruption triggering associated with greatly increasing eruption rates over the first few days following earthquakes (Linde & Sacks 1998) to producing only minor increases in eruption rates over the following months to several years (Sawi & Manga 2018), it is now generally accepted that earthquakes can trigger volcanic eruptions (Hill et al. 2002, Seropian et al. 2021, see also Chapter 4). By contrast, at the global scale, large earthquakes and volcanic eruptions are generally believed to be random and independent events. For example, despite some apparent clustering of large earthquakes globally, such as the occurrence of six $M_w \geq 8.5$ events between 2004 and 2012 (Lay 2015), most authors agree that aftershock-removed catalogues of large earthquakes are consistent with random Poissonian behaviour (Michael 2011, Daub et al. 2012, Shearer & Stark 2012, Parsons & Geist 2012, Ben-Naim et al. 2013). Likewise, De la Cruz-Reyna (1991) showed that global explosive eruptions are well-represented by a Poisson point process, and several other studies assume that global eruptions show Poissonian behaviour (e.g. Deligne et al. 2010, Furlan 2010, Mead & Magill 2014, Rougier et al. 2016, Rougier, Sparks, Cashman & Brown 2018).

In this study, we investigate the relationship between seismicity and volcanism by comparing time-series of large earthquakes ($M_w \geq 7$) and explosive volcanic eruptions (VEI ≥ 2) spanning 1960 through 2019. Our focus is on earthquake and eruptive activity at the global scale, but we also consider regional time-series from subduction zones (Figure 3.1). To characterise the relationship between the earthquake and eruption time-series, we calculate their cross-correlation. We then use Monte Carlo permutation testing to quantify the significance of the observed correlations. Our novel methodology produces results that provide evidence for a relationship between global earthquake and eruption activity, and we discuss how eruption triggering and other physical processes contribute to this.

3.2 Data and Methods

3.2.1 Time-series generation

Systematic global recording of earthquakes and eruptions began during the 1950s and 1960s. Therefore, we choose a start year of 1960 to avoid including biased or incomplete data from before standard practises were adopted (Figure 3.2). To generate the global earthquake and eruption time-series, we divide global earthquake and eruption datasets into bins by calendar year, and then sum the events within each bin. For the regional time-series, only events located within the regions defined in Figure 3.1 are included.

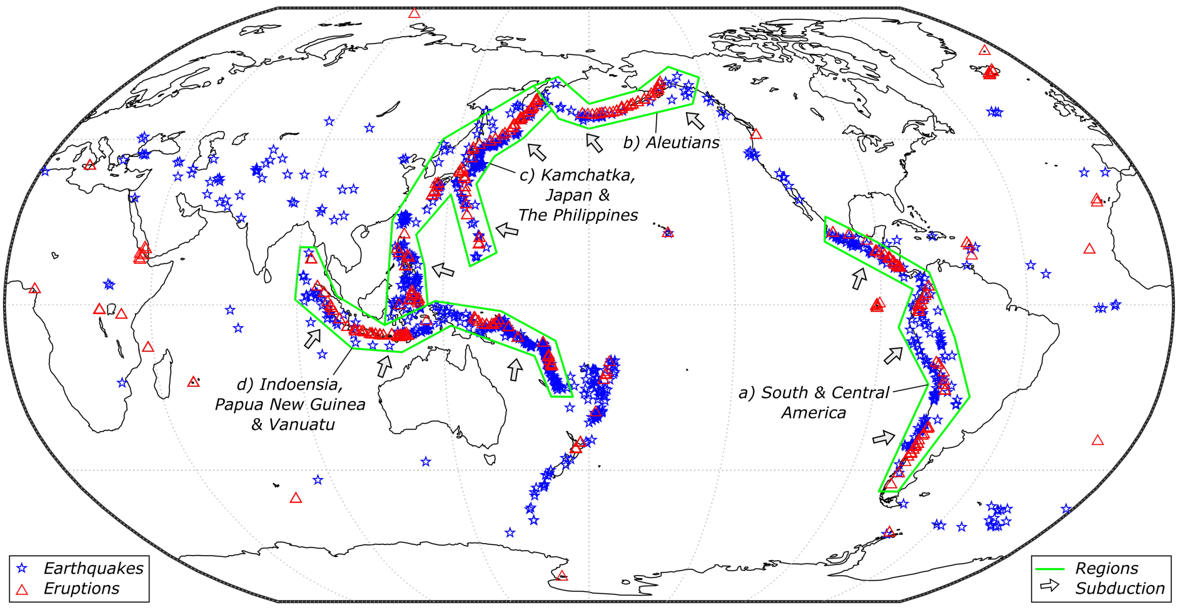

Figure 3.1: The locations of $M_w \geq 7$ earthquakes (blue stars) and VEI ≥ 2 eruptions (red triangles) during 1960-2019. Green outlines show the boundaries of the four regional time-series (Figure 3.14).

We use earthquake times, locations, and moment magnitudes (M_w) from the International Seismological Centre main catalogue for 1960 through 1975 (ISC: International Seismological Centre 2020), and from the Global Centroid Moment Tensor catalogue for 1976 through 2019 (CMT: Dziewonski et al. 1981). The ISC catalogue is calculated to be complete above approximately M_w 6 since 1960 (Storchak et al. 2013, 2015, Di Giacomo et al. 2018), while the CMT catalogue is reported complete above M_w 5.5 (Dziewonski et al. 1981, Ekström et al. 2012). Both catalogues are available for 1976 through

2016 and show good agreement (Figure 3.3). To account for earthquake magnitudes, we present the earthquake time-series in terms of seismic moment release per year, following the common practice of treating scalar seismic moments from individual earthquakes ($M_o = 10^{1.5M_w+9.09}$) as extensive (i.e. having the property of physical additivity. We also show results that use the number of earthquakes per year instead. For the global earthquake time-series, we include only $M_w \geq 7$ earthquakes, as smaller earthquakes do not greatly contribute towards global seismic moment release. For the regional time-series, we include $M_w \geq 6$ earthquakes, as some regions have years without any $M_w \geq 7$ events.

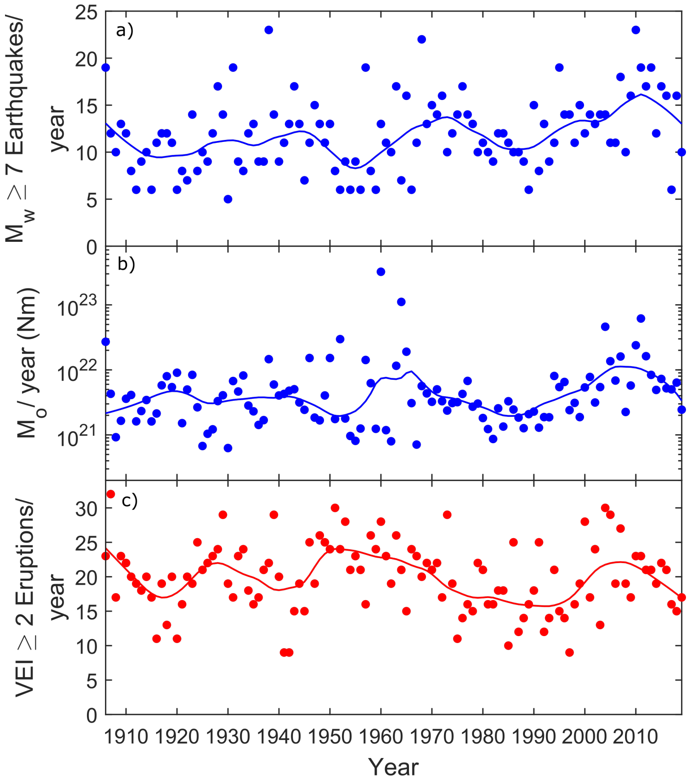

Figure 3.2: The combined global ISC-CMT earthquake catalogue and GVP eruption catalogue from 1906-2019, with 15% span parameter LOESS curves. Earthquake data prior to 1976 are from the ISC catalogue. a) Annual $M_w \geq 7$ earthquake rate; b) annual $M_w \geq 7$ seismic moment release; c) Annual VEI ≥ 2 eruption rate. The annual number of $M_w \geq 7$ earthquakes is generally lower prior the early 1960s, consistent with the greater number of earthquakes in the ISC-GEM supplementary catalogue (no or poor magnitude values; not included in our time-series) prior to 1964, and especially prior to 1960. Eruption numbers decrease noticeably during the two World Wars, so the earliest the eruption time-series can be reliably used is ~1950. Therefore, we choose 1960 as our start date, so as to include the 1960 Chile and 1964 Alaska M_w 9 earthquakes. We also show cross-correlation results for time-series starting at 1906 and 1948 in Figure 3.9.

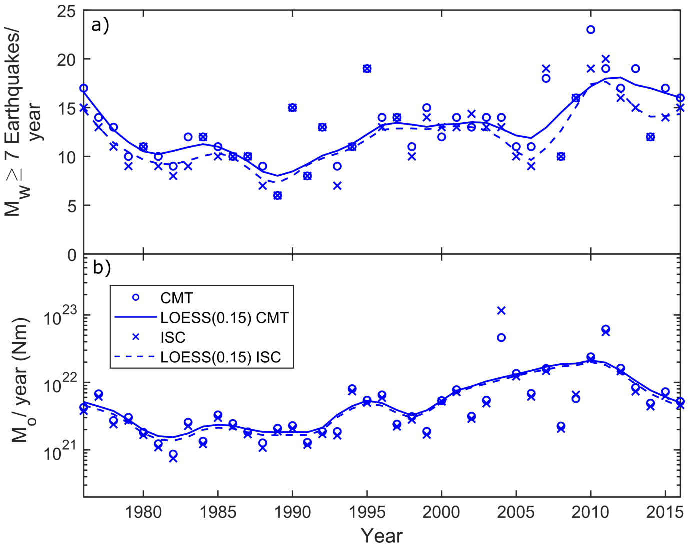

Figure 3.3: Comparison of the ISC (crosses) and CMT (circles) global earthquake catalogues for 1976-2016, with 15% span LOESS curves (lines). a) Annual $M_w \geq 7$ earthquake rate; b) annual $M_w \geq 7$ seismic moment release (the large disparity in 2004 is due to different M_w for the Boxing Day 2004 Sumatra earthquake).

We obtain eruption start dates, locations, and explosivity (VEI) from the Global Volcanism Program (GVP Global Volcanism Program 2013). There is no visually obvious under-recording of explosive eruptions (VEI ≥ 2) with age, so we assume the record is complete since 1960 (e.g. Newhall & Self 1982, Mead & Magill 2014, Papale 2018), although Rougier, Sparks & Cashman (2018) suggest that recording rates decrease prior to 1980. As the VEI scale is only semi-quantitative (Newhall & Self 1982), we do not account for eruption magnitudes, and instead present the eruption time-series in terms of the number of VEI ≥ 2 eruptions per year. The GVP lists the initiation of 1157 eruptions with VEI ≥ 2 from 1960 through 2019, including 87 eruptions with an uncertain start year and 64 cases of multiple eruptions from a single volcano within the same calendar year. Including or excluding these multiple and uncertain eruptions in the time-series does not greatly affect the results. The GVP also notes where eruption magnitude is uncertain, but we take the VEI values as given.

3.2.2 Cross-correlation analysis

To characterise the relationship between the earthquake and eruption times-series, we calculate their cross-correlation. The cross-correlation gives the correlation coefficient (ρ) between the earthquake time-series (E) and the eruption time-series (V) as a function of the timeshift (i, in years) applied to the eruption time-series

$$\rho_i = \rho(E, L^i V), \tag{3.1}$$

where L is the lag operator, which for a time-series $x = (x_1, \ldots, x_T)$ has the property

$$(L^i x)_j = \begin{cases} x_{j-i} & 1 \leq j - i \leq T \\ \texttt{NA} & \text{otherwise,} \end{cases} \tag{3.2}$$

where `NA` denotes ‘not available’. In other words, correlations at negative timeshifts ($i < 0$) correspond to changes in earthquake activity preceding changes in eruption activity, while correlations at positive timeshifts ($i > 0$) signify changes in eruption activity preceding changes in earthquake activity. The correlation coefficient we compute is the Spearman’s rank correlation coefficient, which quantifies the strength of the monotonic relationship between seismic moment release and eruption rate, with a value of 1 for a perfect positive correlation and -1 for a perfect negative correlation. The more common Pearson’s correlation coefficient only assesses linear relationships, but we have no reason to believe that the relationship between seismic moment release and eruption rate will be linear.

To determine the significance of the observed correlations, we define a null model in which there is no relationship between the timings of earthquakes and eruptions. The null model maintains the locations and magnitudes of the observed earthquakes and eruptions, with only their dates being changed. We apply two different methods to reassign event dates. In the first method (RAND), the earthquake and eruption dates are randomly generated within the time-series boundaries, simulating Poissonian behaviour. For the second method, we use a permutation test (PERM), in which the observed earthquake and eruption dates are first pooled together, then randomly reassigned back to the events. Unlike RAND, PERM accounts for the clustering of dates in the observed dataset, although the clustering in the individual time-series is not perfectly maintained as some earthquake dates become eruption dates and vice versa. The presence of clustering in PERM induces some degree of positive correlation on average at small timeshifts, which tends to decrease the significance of the observed correlations.

We use Monte Carlo simulation to calculate P-values for the observed correlations under the null model, for both the RAND and PERM methods. If ρ_i^{obs} is the observed correlation coefficient at timeshift i, $\rho_i^{(r)}$ is the r^{th} simulated correlation coefficient using

RAND or PERM at timeshift i, and there are R simulations altogether, then

$$p_i = \frac{1 + \sum_{r=1}^{R} 1(\rho_i^{(r)} \geq \rho_i^{\text{obs}})}{1 + R} \tag{3.3}$$

is a P-value (Davison 2003, section 7.3). p_i gives the probability of obtaining the observed correlation, or stronger, under the null model. For visualisation, our results plot ρ_i^{obs} over the percentiles of $\rho_i^{(1)}, \ldots, \rho_i^{(R)}$, which allows for approximation of the P-values according to the percentiles. Conventionally, a P-value of <0.05 (approximately the 95^{th} percentile) is considered to be a statistically significant result. However, as p_i is calculated for each timeshift, with a long enough sequence of timeshifts, some correlations will be significant purely by chance under the null model. Therefore, we must be careful not to over-interpret any one significant P-value over the whole sequence of applied timeshifts.

3.3 Results

3.3.1 Global time-series

Figure 3.4b shows the global seismic moment release time-series, while Figure 3.4c shows the global eruption time-series, including multiple and uncertain eruptions. As the time-series themselves show considerable variability from year-to-year, we fit locally-weighted polynomial regressions (LOESS) to help visualise multi-year trends in earthquake and eruption activity. From the LOESS curves, there is visually a correlation between seismic moment release and eruption rate, which is apparent over decadal timescales. In particular, periods of high seismic moment release and volcanic activity occurred during the 1960s and early 1970s, and then again from around 2000 until the early 2010s. By contrast, the 1980s and 1990s were characterised by relatively lower seismic and volcanic activity, and data since around 2015 suggest a trend towards another period of lower levels of global activity.

Figure 3.4d shows the cross-correlation between the (unsmoothed) global seismic moment release time-series and the (unsmoothed) global eruption time-series. The observed positive correlations at timeshifts between -10 and +6 years support the visual correlation evident from the LOESS curves, with peak correlation coefficients of 0.3 to 0.4 indicating a weak to moderate correlation between global seismic moment release and global eruption rate (Figure 3.5). Furthermore, the observed negative correlations at timeshifts longer than around ±10 years highlight the decadal timescale over which the correlation acts. Although the most positive correlation coefficient of 0.41 occurs at a timeshift of +5 years, overall there are more positive correlations at negative timeshifts than at positive timeshifts. This may suggest that changes in earthquake activity occur a few years before corresponding changes in eruption rate. However, this is poorly constrained, as the highest correlation coefficients occur at timeshifts ranging between -4 and +5 years. Interestingly, at 0 years timeshift, Figure 3.5 shows that years with low seismic moment release display a broad range of eruption rates, whereas years with high seismic moment release (>10^{22} Nm) always display high eruption rates. Therefore, while high eruption rates can occur regardless of the annual seismic moment release, years with high seismic moment release always display high eruption rates.

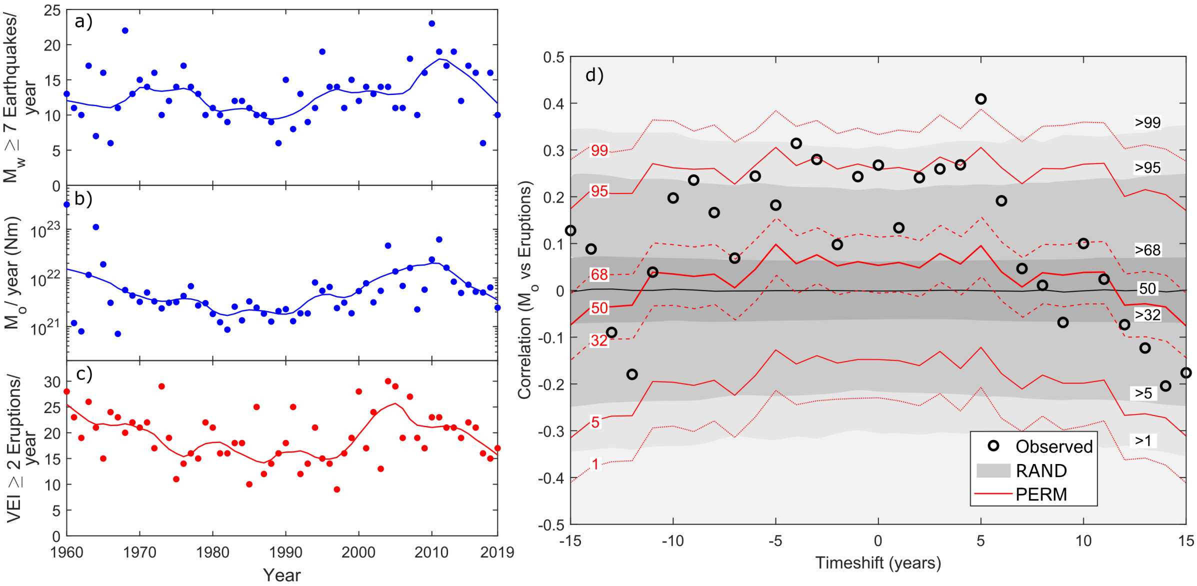

Figure 3.4: a-c) Global earthquake and eruption time-series 1960-2019 (circles), with 15% span parameter LOESS curves (lines) for visualisation. The eruption time-series includes multiple and uncertain eruptions. d) Cross-correlation between global seismic moment release time-series (b) and VEI ≥ 2 eruption time-series (c), with reference to the percentiles of the RAND (shading, black line, and black numbers) and PERM (red lines and numbers) null models. Negative timeshifts correspond to changes in earthquake activity preceding changes in eruption activity, and vice versa for positive timeshifts.

Under the null model, the observed global correlations are significant at $P < 0.05$ for timeshifts of -4, 0, 4, and 5 years using PERM, with additional significant correlations at timeshifts of -9, -6, -3, -1, 2, and 3 years using RAND (Figure 3.4d). From the Monte Carlo simulations, the probability of obtaining four or more timeshifts with significant correlations under PERM is 3%, while the chance of obtaining ten or more significant timeshifts under RAND is < 0.01% (Table 3.1). We therefore consider it unlikely that the observed global correlation occurs by chance. Similar results are achieved if the boundary date for the yearly binning is shifted (Figure 3.6), or if uncertain and multiple eruptions are excluded from the time-series (Figure 3.7), although the timeshifts which have significant correlations vary. Including VEI ≥ 0 eruptions likewise has little impact; however, using only VEI ≥ 3 eruptions, of which there are far fewer, reduces the number of timeshifts with significant correlations (Figure 3.8). Similarly, starting the time-series earlier, thereby incorporating potentially incomplete data, also decreases the correlation, with a greater affect the longer the time-series (Figure 3.9). More interestingly, using a 3-year bin duration for the time-series increases the peak observed correlation coefficients to 0.5 to 0.6, as well as further increasing their significance (Figure 3.10). However, using the Pearson correlation coefficient instead of the Spearman correlation coefficient causes a small decrease in the observed correlations and its significance, especially relative to RAND (Figure 3.11). This is because employing longer bin durations removes some of the annual variability in earthquake and eruption rates, instead giving more weight to the decadal timescale trends. Finally, we note that the global correlation depends more strongly upon the largest magnitude earthquakes, as shown by the lack of significant correlations under PERM if number of $M_w \geq 7$ earthquakes is used to measure earthquake activity instead of seismic moment release (Figures 3.12 and 3.13).

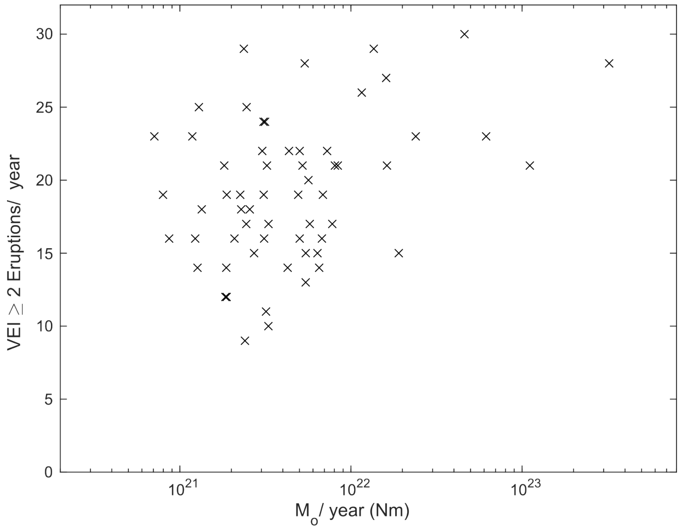

Figure 3.5: Cross-plot at zero timeshift for annual seismic moment release (Figure 3.4b) and VEI ≥ 2 volcanic eruption rate (Figure 3.4c), including multiple and uncertain eruptions. The corresponding correlation coefficient is 0.27, suggesting a weak to moderate correlation between annual seismic moment release and annual volcanic eruption rate.

Table 3.1: The probability of obtaining 'N' or greater number of timeshifts with a significant correlation ($P < 0.05$) under the null model from cross-correlation at short timeshifts ($-10 \leq i \leq 10$). This probability is calculated from 10000 RAND and PERM simulations (including multiple and uncertain eruptions). For reference, Figure 3.4 shows four significant observed correlations under PERM, corresponding to a probability of 0.0342. For RAND, there are ten significant correlations, which corresponds to a P-value of <0.0001.

Minimum number of timeshifts with $P < 0.05$	RAND	PERM
0	1.0000	1.0000
1	0.6734	0.6160
2	0.2832	0.2811
3	0.0755	0.1061
4	0.0149	0.0342
5	0.0025	0.0093
6	0.0004	0.0023
7	0.0001	0.0007
8	<0.0001	0.0003
9	<0.0001	<0.0001
10	<0.0001	<0.0001

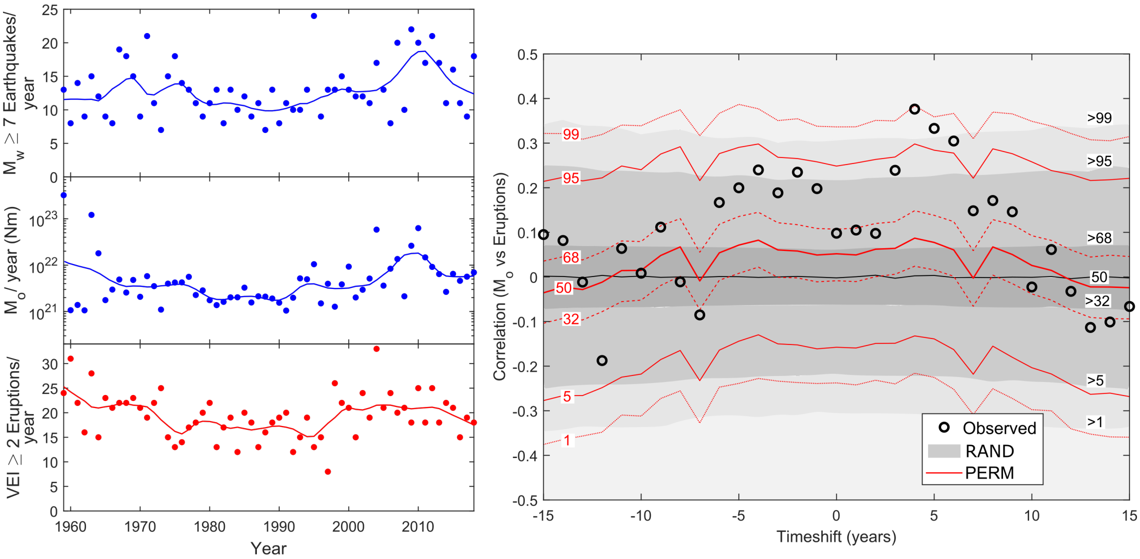

Figure 3.6: Time-series and cross-correlation as in Figure 3.4, but with the bin boundary data shifted by 6 months, to investigate the impact of the Western Calendar. The results are broadly similar to Figure 3.4, although the specific timeshifts with significant correlations vary.

a) Excluding multiple and uncertain eruptions

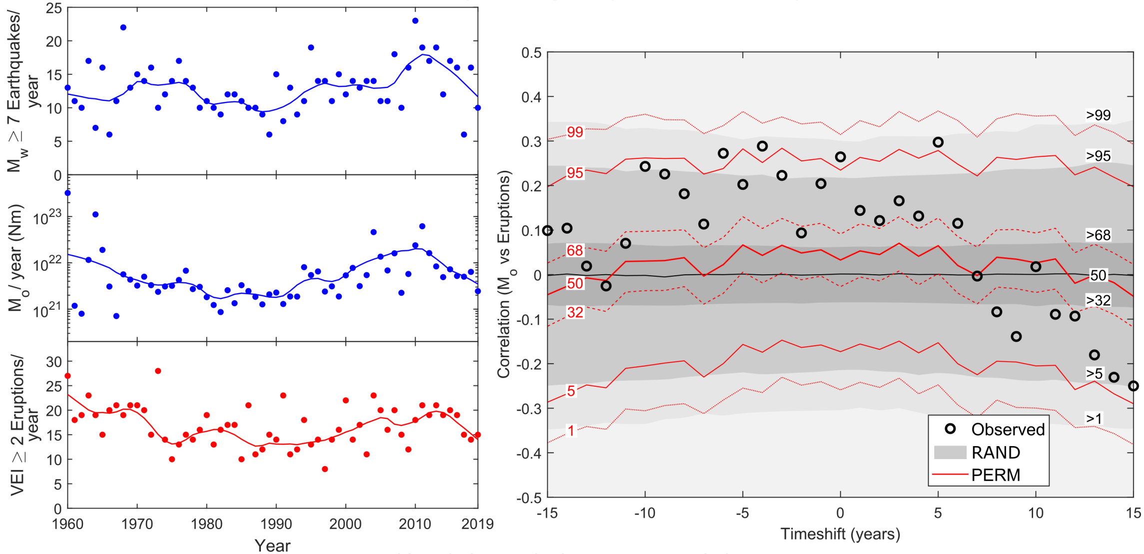

b) Including multiple eruptions, excluding uncertain eruptions

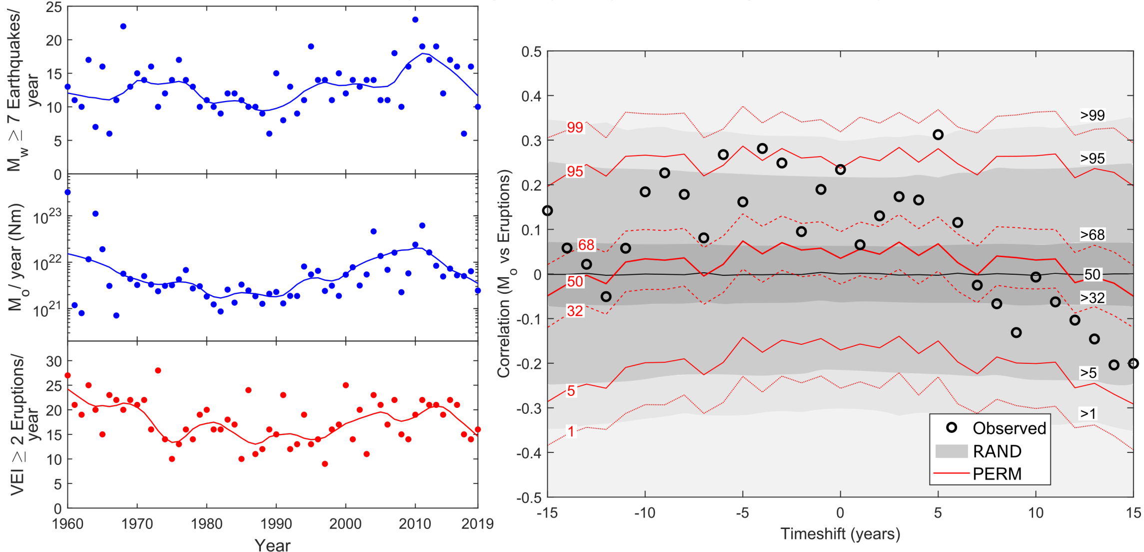

c) Excluding multiple eruptions, including uncertain eruptions

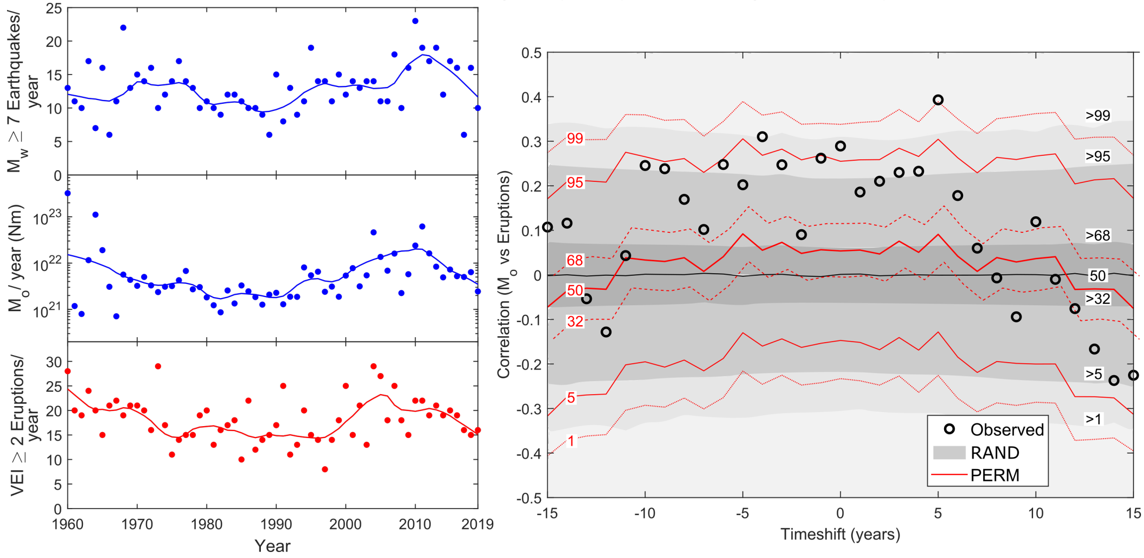

Figure 3.7: (Above) Time-series and cross-correlation as in Figure 3.4, but with the eruption time-series a) excluding multiple and uncertain eruptions; b) including multiple eruptions, excluding uncertain eruptions, and; c) excluding multiple eruptions, including uncertain eruptions. The results are broadly similar to Figure 3.4, although the exact timeshifts with significant correlations vary slightly.

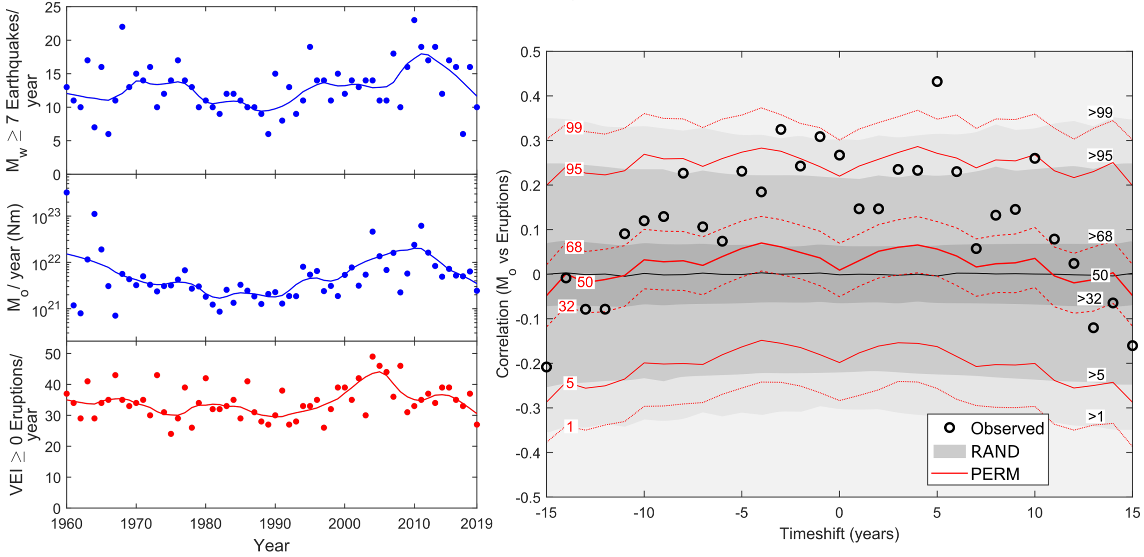

a) VEI ≥ 0 eruptions

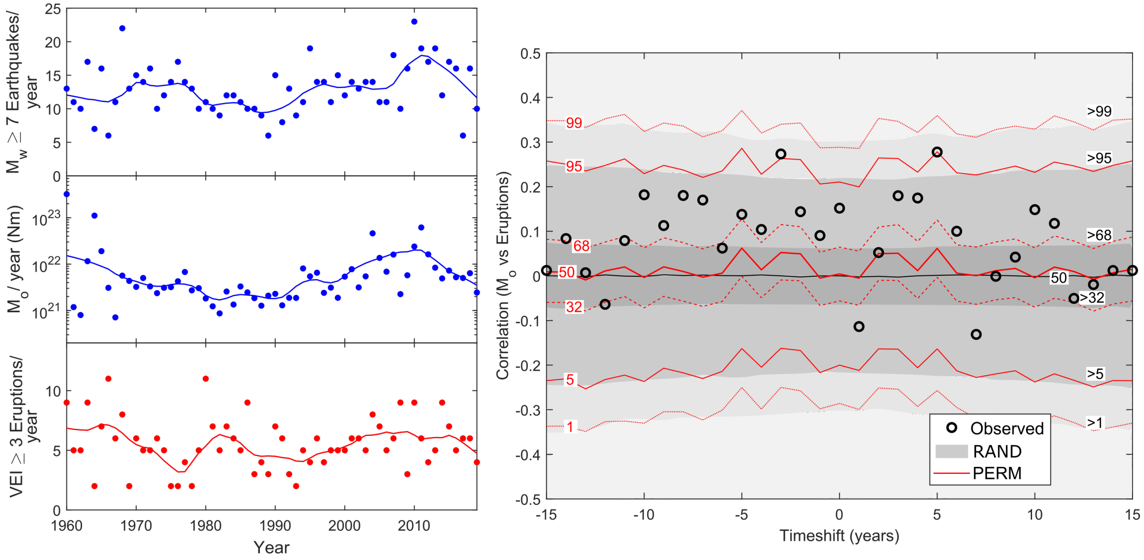

b) VEI ≥ 3 eruptions

Figure 3.8: Time-series and cross-correlation as in Figure 3.4, but with the eruption time-series a) including VEI ≥ 0 eruptions, and; b) only including VEI ≥ 3 eruptions. The results are broadly similar to Figure 3.4, although the statistical significance is lower for the VEI ≥ 3 time-series. However, we note that the VEI ≥ 0 eruption record is likely incomplete, while the number of VEI ≥ 3 eruptions is far lower than the number of VEI ≥ 2 eruptions, so decadal timescale trends are more difficult to identify.

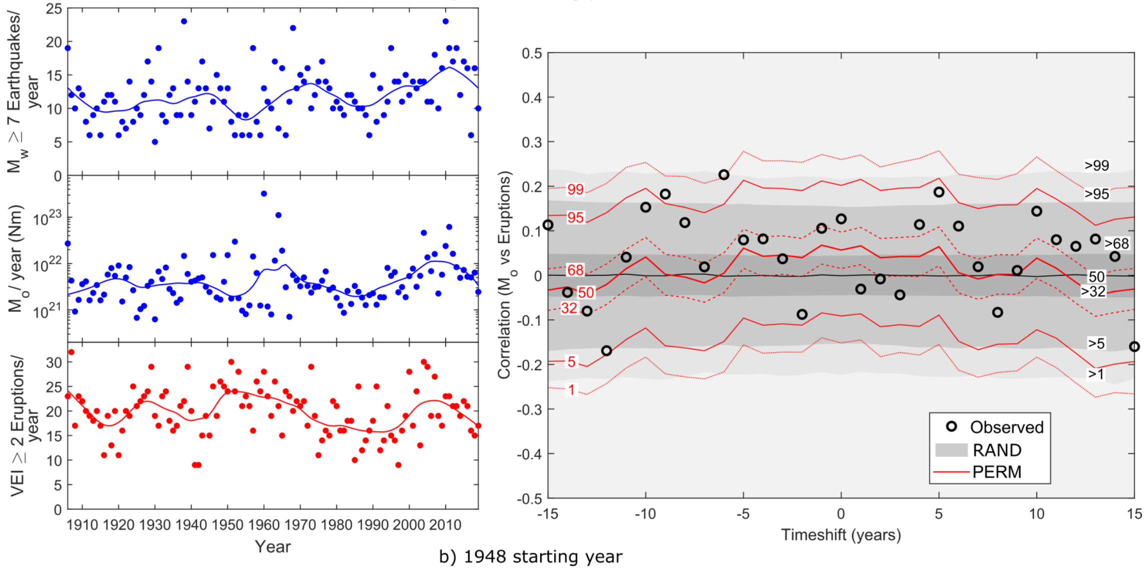

a) 1906 starting year

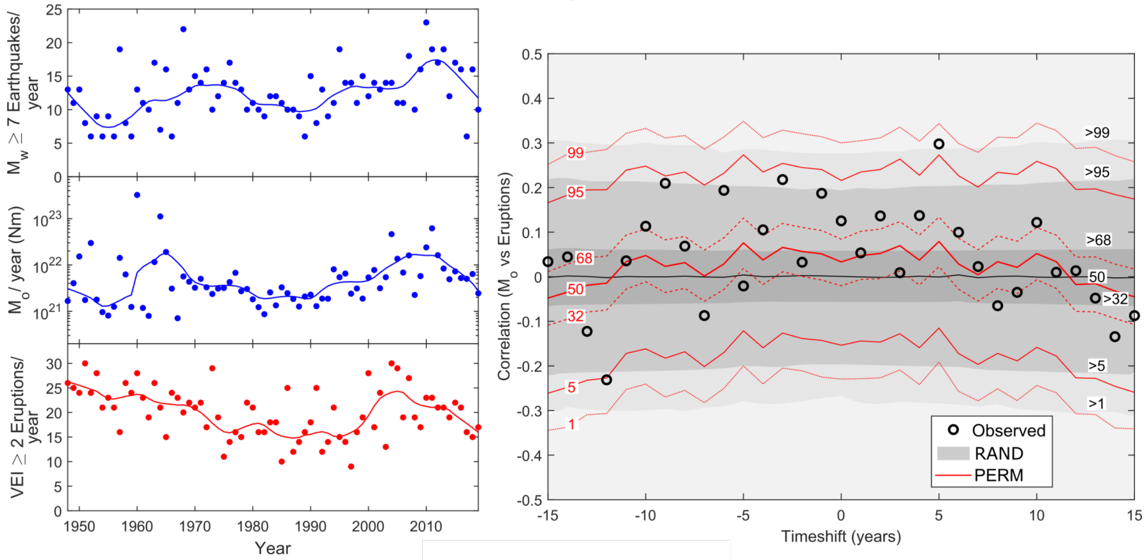

b) 1948 starting year

Figure 3.9: Time-series and cross-correlation as in Figure 3.4, but with the time-series starting at a) 1906, and b) 1948. For a starting year of 1948, there is some overall positive correlation, but this is greatly reduced relative to Figure 3.4. The correlation for a starting year of 1906 is reduced further still, possibly due to the incompleteness of earlier data.

a) 2-year bins

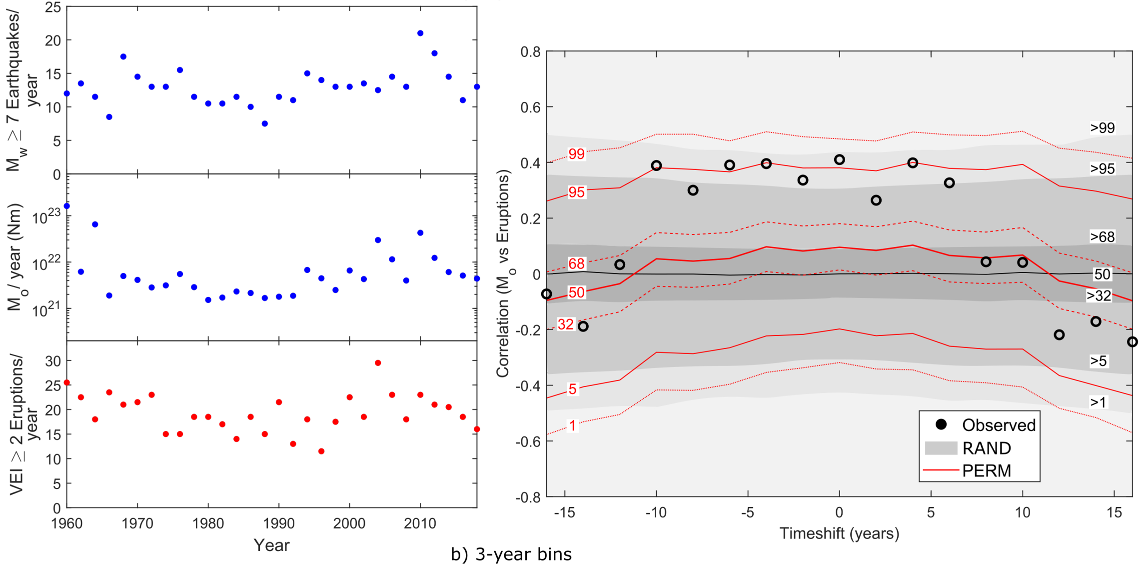

b) 3-year bins

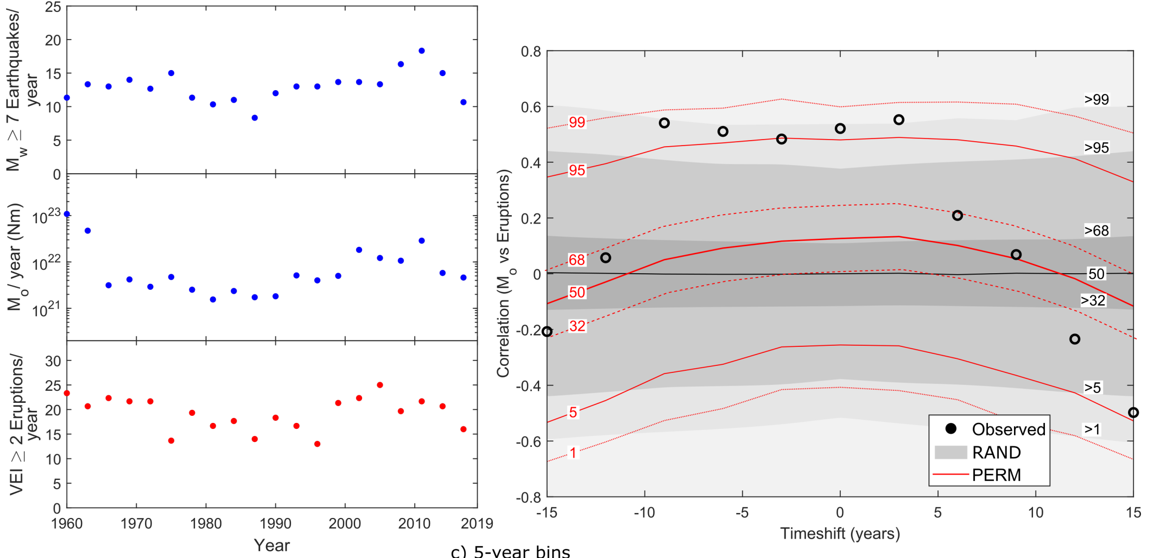

c) 5-year bins

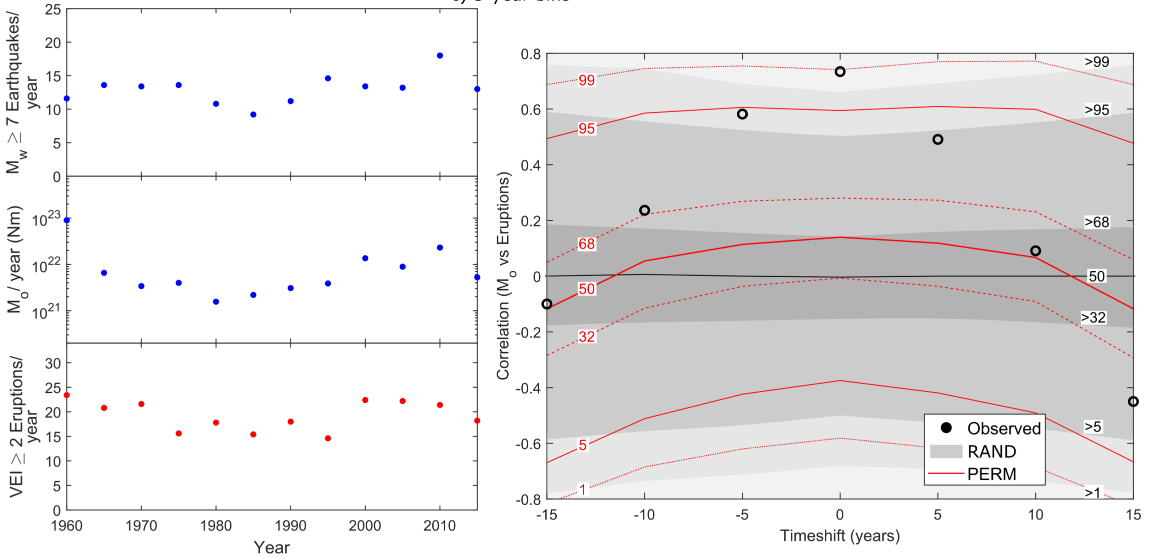

Figure 3.10: (Above) Time-series and cross-correlation as in Figure 3.4, but with bin durations of a) 2 years; b) 3 years, and; c) 5 years. The 3- and 5-year bin durations especially have more significant observed correlations. This is because the longer bin durations are better at capturing the decadal timescale variability in event rates, whereas the 1-year bin time-series are more impacted by shorter-term variability.

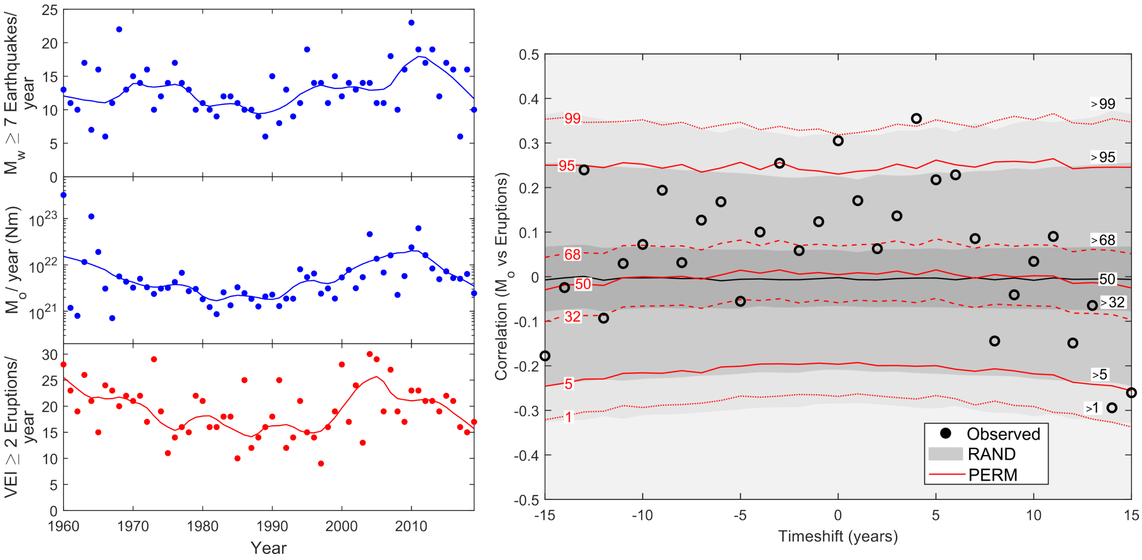

Figure 3.11: Time-series and cross-correlation as in Figure 3.4, but using the Pearson correlation coefficient instead of the Spearman correlation coefficient. The results are broadly similar to Figure 3.4, although the observed correlation coefficients are often slightly reduced and their statistical significance is lower, especially relative to RAND.

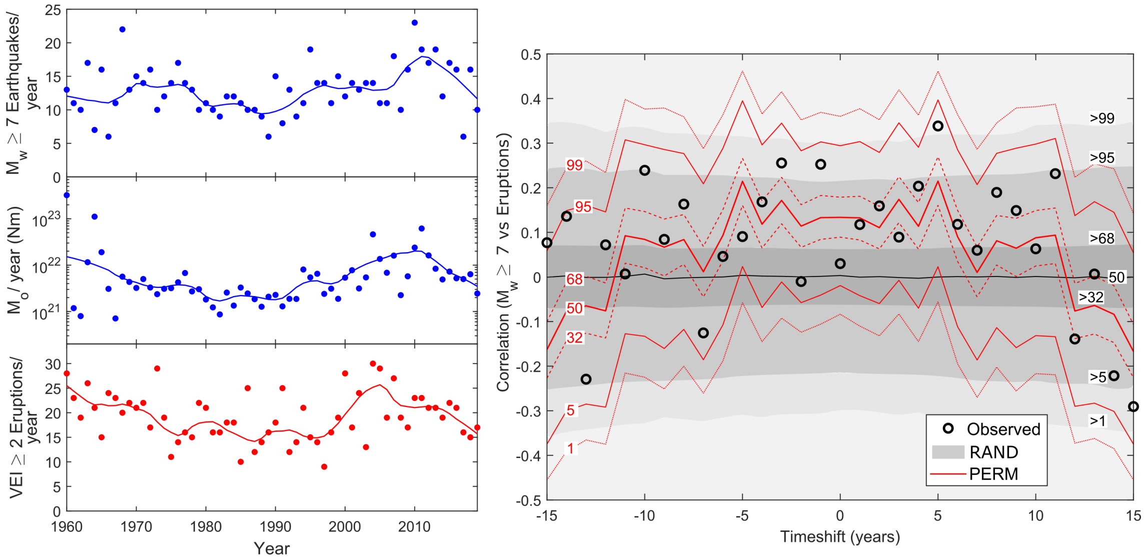

Figure 3.12: Time-series and cross-correlation as in Figure 3.4, but with number of $M_w \geq 7$ earthquakes used for cross-correlation, instead of seismic moment release. Although there is positive correlation at short timeshifts, this is not significant under PERM, which shows that the correlation depends more strongly on the largest magnitude earthquakes.

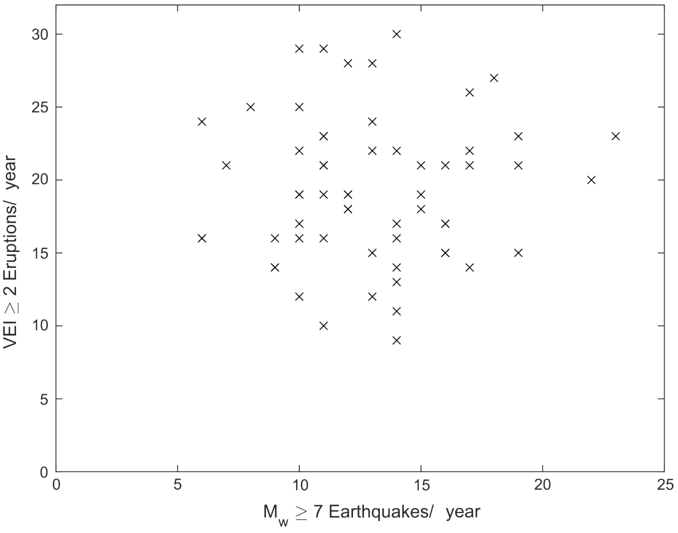

Figure 3.13: Cross-plot at zero timeshift for annual $M_w \geq 7$ earthquake rate (Figure 3.4a) compared with annual VEI ≥ 2 volcanic eruption rate (Figure 3.4c). The correlation coefficient at zero timeshift is 0.03, which suggests almost no correlation between annual earthquake rates and annual volcanic eruption rates.

3.3.2 Regional time-series

The majority of $M_w \geq 7$ earthquakes (66%) and VEI ≥ 2 eruptions (85%) are located along the subduction zones bordering the Pacific Ocean (Figure 3.1). Therefore, we generate four sets of regional time-series based on these plate boundaries (Figure 3.14). These regions are: a) eastward-directed subduction of the Nazca and Cocos plates below South and Central America; b) northward-directed subduction of the Pacific plate below the Aleutian arc; c) westward-directed subduction of the Pacific and Philippine Sea plates below the Kamchatka Peninsula, Japan, and the Philippines, and; d) northward-directed subduction of the Australian plate below Indonesia, Papua New Guinea, and Vanuatu. Of these, only the South and Central America region has easily-defined, non-overlapping boundaries.

Only the South and Central America region displays an obvious visual correlation, which is supported by positive correlations at timeshifts from -1 to +8 years, although these are not significant at $P < 0.05$ under PERM (Figure 3.14a). Indonesia, Papua New Guinea, and Vanuatu also shows mostly positive correlations at short timeshifts, which likewise do not reach the $P < 0.05$ threshold for PERM (Figure 3.14d). By contrast, the Aleutian arc has very little overall correlation (Figure 3.14b), while Kamchatka, Japan, and the Philippines displays negative correlations at short timeshifts and significant positive correlations at longer timeshifts (Figure 3.14c). However, we are cautious of over-interpreting these significant positive correlations for Kamchatka, Japan, and the Philippines due to the much lower correlations at the intervening timeshifts and the absence of significant correlations when using a 3-year bin size (Figure 3.15). Despite the generally low correlations for the regional time-series, the four $M_w > 9$ mega-earthquakes which dominate the global earthquake time-series are all associated with periods of high or increasing volcanic activity in their respective regional time-series (1960 Chile earthquake (Figure 3.14a); 1964 Alaska earthquake (Figure 3.14b); 2004 Sumatra earthquake (Figure 3.14d); 2011 Tohoku earthquake (Figure 3.14c)). The lack of regional correlation may therefore reflect the lack of large earthquakes in the regional time-series.

Figure 3.14: (Below) Regional earthquake and eruption time-series and cross-correlation. The time-series include $M_w \geq 6$ earthquakes, and multiple and uncertain eruptions. Colour scheme and symbols as in Figure 3.4. a) South and Central America; b) Aleutian arc; c) Kamchatka, Japan, and The Philippines; d) Indonesia, Papua New Guinea, and Vanuatu. See Figure 3.1 for region location maps.

a) South and Central America

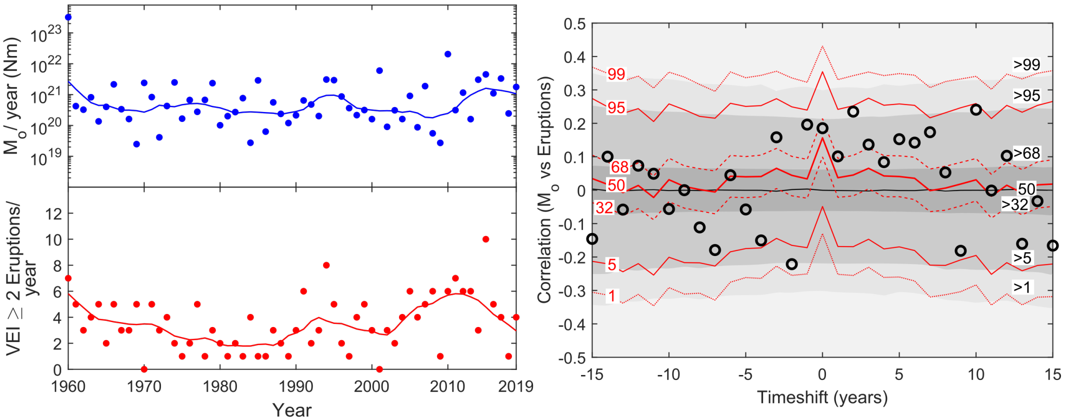

b) Aleutian Arc

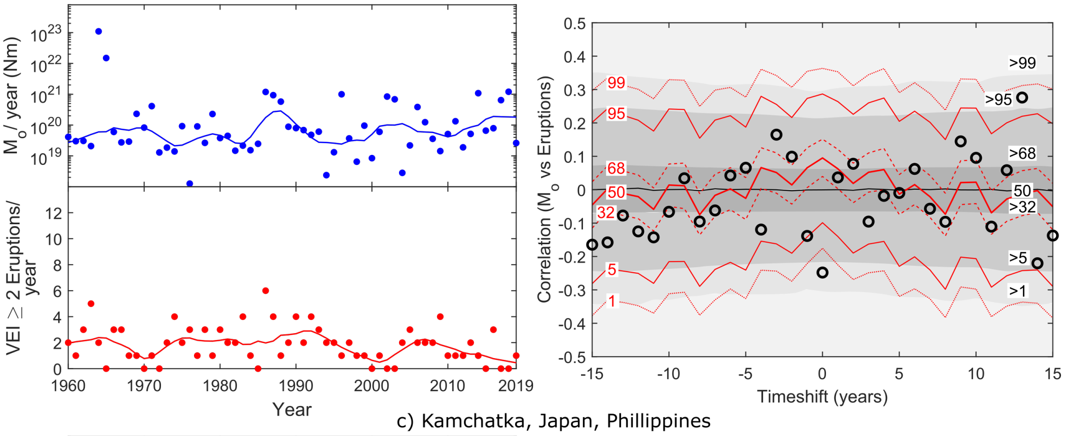

c) Kamchatka, Japan, Phillippines

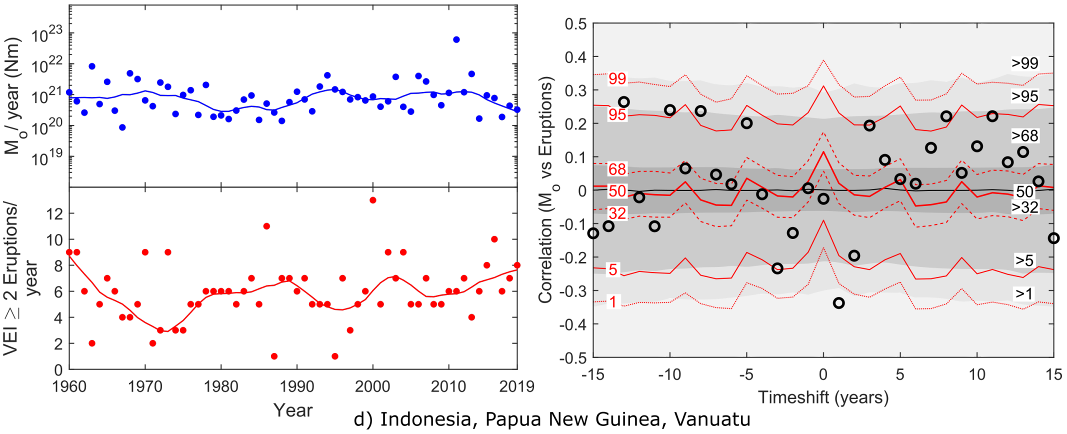

d) Indonesia, Papua New Guinea, Vanuatu

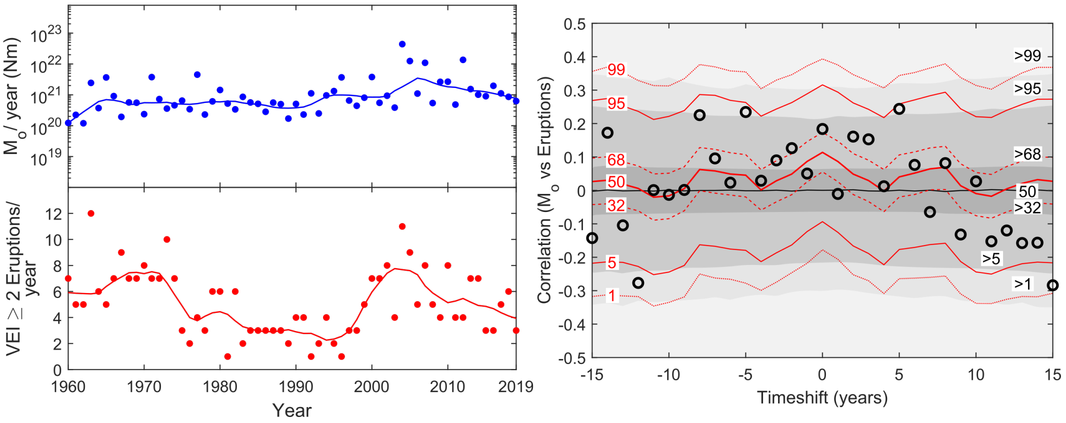

a) South and Central America

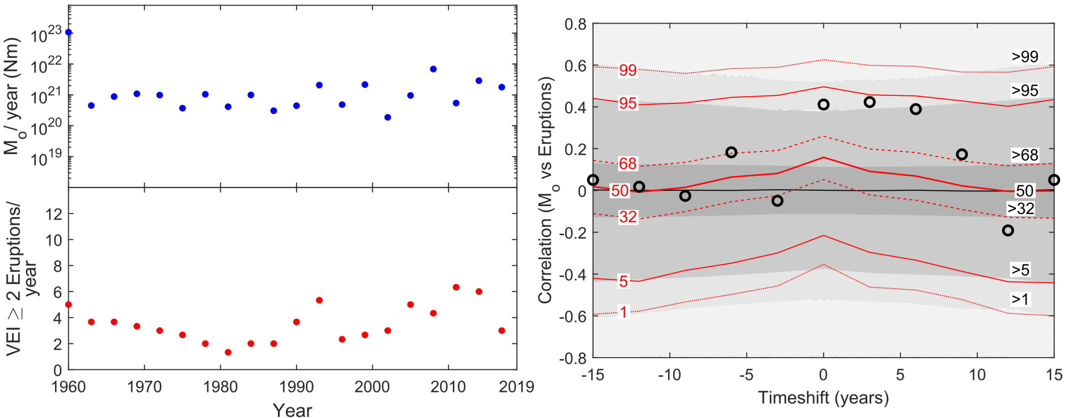

b) Aleutian Arc

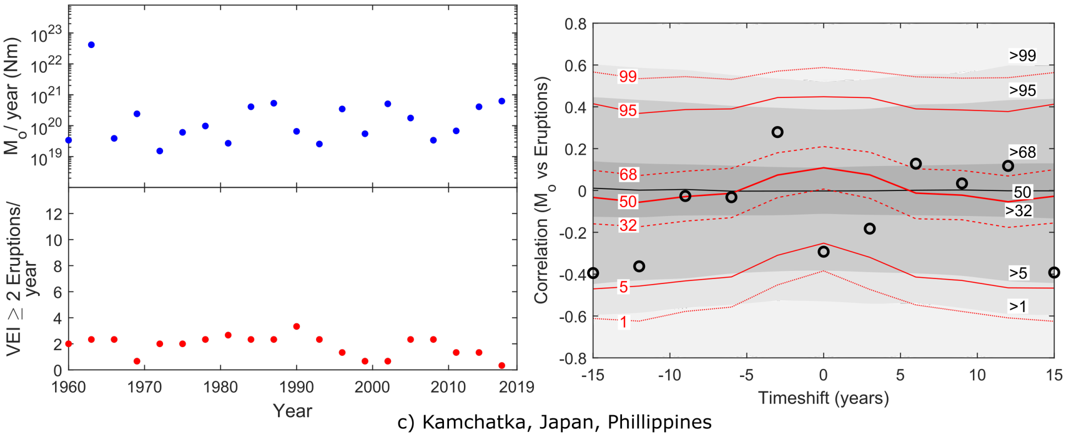

c) Kamchatka, Japan, Phillippines

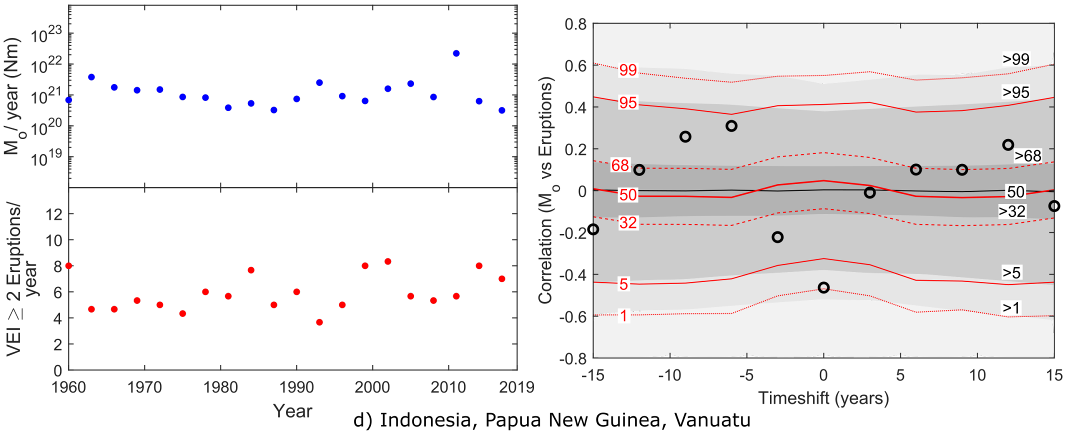

d) Indonesia, Papua New Guinea, Vanuatu

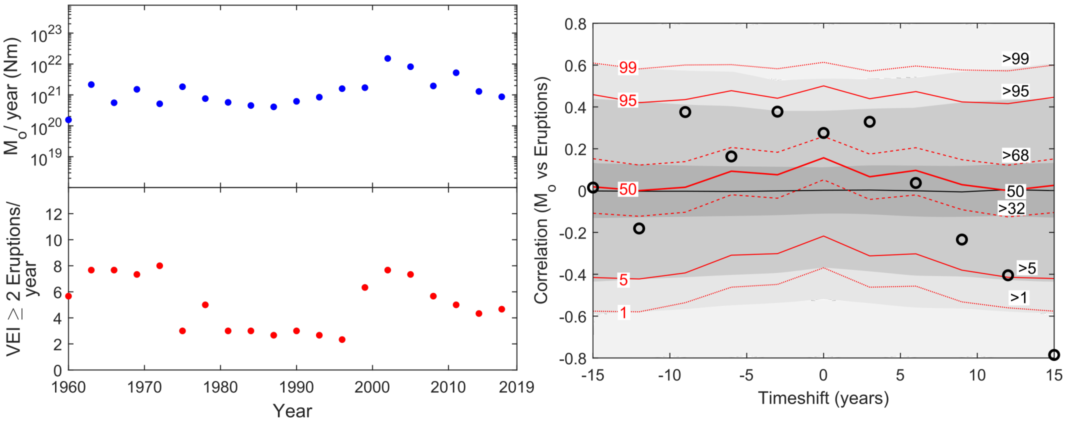

Figure 3.15: (Above) Regional earthquake ($M_w \geq 6$) and eruption (VEI ≥ 2, including multiple and uncertain eruptions) time-series 1960-2019, as in Figure 3.14 but with a 3-year bin duration. a) South and Central America; b) Aleutian arc; c) Kamchatka, Japan, and The Philippines; d) Indonesia, Papua New Guinea, and Vanuatu. See Figure 3.1 for region location maps.

3.4 Discussion

3.4.1 Implications

The correlation we observe between global seismic moment release and global eruption rate suggests that earthquake and eruption occurrences are not independent at the global scale. This is because Monte Carlo simulation shows that the probability of the correlation occurring by chance is low if earthquakes and eruptions are random and independent events. While our findings contrast with many previous studies (e.g. Michael 2011, De la Cruz-Reyna 1991), some more recent work does support the view that earthquake and eruptive activity is time-dependent. For example, several authors have reexamined the historic earthquake record and concluded that Poissonian behaviour cannot explain the temporal distribution of large earthquakes (Zaliapin & Kreemer 2017, Bendick & Bilham 2017, Rogerson 2018, Luginbuhl et al. 2018). Likewise, Gusev (2008, 2014) presented evidence for statistically significant clustering of global eruptions since 1900. To investigate whether our results support non-random time-dependent behaviour in earthquakes, eruptions, or both, we now explore causal mechanisms that could explain the observed correlation. As eruption triggering by earthquakes is the most obvious explanation, and is supported by the slight preference for positive correlations at negative timeshifts, we consider this mechanism first.

3.4.2 Eruption triggering

Earthquakes themselves display clustering at a local scale because earthquake-induced stress transfer causes aftershocks and earthquake sequences. However, evidence for earthquakes triggering other large earthquakes at distances much beyond 1000 km is limited, as stress changes decay with distance (Wyss & Toya 2000, Bufe & Perkins 2005, Parsons & Velasco 2011, Parsons et al. 2014, Johnson et al. 2015). Similarly, studies of earthquakes triggering volcanic eruptions focus on distances of 1000 km or less. For example, Linde & Sacks (1998) found that VEI ≥ 2 eruptions occurr four times more often than expected by chance within 5 days and 800 km of magnitude 8 or larger earthquakes, while Nishimura (2017) found a 50% increase in VEI ≥ 2 eruptions within 5 years and 200 km following $M_w \geq 7.5$ earthquakes. By contrast, Sawi & Manga (2018) found no significant increase in VEI ≥ 2 eruption rate within 5 days and 800 km of magnitude 6 or greater earthquakes, although they did find a 5-12% increase in eruptions in the following 2 to 24 months.

As eruption triggering is a relatively local scale phenomenon, the lower correlation between seismic moment release and eruption rate at the regional scale compared with the global scale argues against eruption triggering as the causal mechanism. However, the lower regional correlations may simply reflect the lower numbers of larger earthquakes in the regional time-series. Therefore, to investigate whether eruption triggering can explain the global correlation, we quantify the rate of eruption triggering by comparing the number of eruptions that occured after nearby large earthquakes with the number of eruptions that occured in the same time period before those earthquakes. Using the same datasets as for our correlation analysis, we find an increase of up to 10% in VEI ≥ 2 eruption rate within 1000 km and 1-5 years after $M_w \geq 7$ earthquakes. This corresponds to each $M_w \geq 7$ earthquake triggering, on average, an extra 0.01 to 0.1 eruptions within a few years and 1000 km (Table 3.2). We do not find strong evidence for eruption triggering with $M_w \geq 6$ earthquakes, nor for smaller or larger distances between the earthquakes and eruptions. Given that Figure 3.4a shows that the global rate of $M_w \geq 7$ earthquakes varies by around 20 earthquakes annually, the expected difference in global eruption rate due to triggering is at most around two eruptions per year. As this number is only a very small fraction of the actual annual variability in global eruption rate (Figure 3.4c), the global correlation likely cannot be explained by eruption triggering alone.

3.4.3 Alternative explanations

Various other physical processes have also been proposed to affect earthquake and eruption rates. However, for these to explain the global correlation, they would have to affect both earthquake and eruption rates in the same manner and with similar response times. For example, tidal stresses have been shown to influence earthquake rates and magmatic systems, although their twice-daily to fortnightly periodicities are too short for our time-series (Cochran et al. 2004, Métivier et al. 2009, Girona et al. 2018, Scholz et al. 2019). Climate change at both seasonal and long-term (i.e. glacial cycles) scales can affect earthquake and eruption rates by causing ice sheet unloading or groundwater changes (Larsen 2000, Mason et al. 2004, Bettinelli et al. 2008, Jull & McKenzie 1996,

Table 3.2: Eruption triggering calculated by comparing the number of eruptions that occurred before and after earthquakes with $M_w \geq$ Min M_w, within the specified distance and time period (see Chapter 4 for a more detailed eruption triggering investigation).

Triggering parameters				Results				
Min M_w	Aftershock filter[a]	Distance (km)	Time (yrs)	# of Eqs.[b]	Eruptions before[c]	Eruptions after[c]	% change[d]	Triggered per Eq.[e]
6	No	1000	1	7543	5232	5188	-0.8	-0.01
6	Yes	1000	1	1397	499	527	5.6	0.02
6	No	1000	5	7025	24520	24058	-1.9	-0.07
6	Yes	1000	5	383	486	495	1.9	0.02
7	No	1000	1	768	507	552	8.9	0.06
7	Yes	1000	1	445	261	287	10.0	0.06
7	No	1000	5	713	2489	2527	1.5	0.05
7	Yes	1000	5	174	434	451	3.9	0.10
7	No	200	1	768	55	59	7.3	0.01
7	No	2000	1	768	1284	1301	1.3	0.02
7	No	200	5	713	318	328	3.1	0.01
7	No	2000	5	713	6187	6078	-1.7	-0.02
8	No	1000	1	48	35	45	28.6	0.21
8	Yes	1000	1	42	27	31	14.8	0.10
8	No	1000	5	45	168	174	3.6	0.13
8	Yes	1000	5	34	121	123	1.7	0.06

[a] Exclusion of earthquakes within the specified distance and time period of a larger earthquake. [b] Earthquakes occurring within 'Time' years of the end of the time-series are excluded. [c] Includes multiple and uncertain eruptions, note that a single eruption may be counted for multiple earthquakes. [d] Percentage change in number of eruptions from before to after the earthquakes. [e] The mean number of eruptions triggered per earthquake, calculated by (Eruptions after - Eruptions before)/# of Eqs..

Huybers & Langmuir 2009, Kutterolf et al. 2013, Rawson et al. 2016, Olivieri & Spada 2015). However, only a few authors have proposed that climate change over decadal timescales may also alter event rates (Rampino et al. 1979, Pagli & Sigmundsson 2008). Furthermore, the observed periodicity in earthquake and eruption activity is difficult to explain with the ever-increasing temperatures due to anthropogenic climate change. More promisingly, periods of deceleration of the Earth's rotational velocity have been linked with increased rates of both earthquakes (Anderson 1974, Shanker et al. 2001, Bendick & Bilham 2017) and eruptions (Palladino & Sottili 2014, Tuel et al. 2017, Levin et al. 2019). However, the feedback and interactions between earthquakes and eruptions and the solid Earth, atmospheric, and astronomic processes that control the rotation of the Earth are far from clear.

Although our analysis showed that triggering of eruptions by nearby earthquakes occurs too infrequently to explain the global correlation, related mechanisms may play a role. For example, there is emerging evidence that seismic waves produced by large earthquakes can trigger aftershocks, and potentially other large earthquakes, at global distances (Pollitz et al. 2012, Parsons et al. 2014). Fluid-rich areas, such as magmatic-hydrothermal systems, are particularly susceptible to such dynamic stress changes (Hill et al. 2002). This suggests that eruption triggering at great distances is a possibility, although identifying such triggering is difficult due to the vast numbers of earthquakes and eruptions involved at large scales. While dynamic stress changes at great distances are likely to be low magnitude, over repeated earthquake cycles, this process could lead to a natural synchronisation of global earthquake and eruption events (Romanowicz 1993, Bendick & Bilham 2017). Furthermore, viscoelastic relaxation following large earthquakes could modulate these cycles of activity over decadal timescales (Marzocchi 2002, Zaliapin & Kreemer 2017). These mechanisms appeal because only the very largest earthquakes would produce significant effects at large time and length scales, consistent with the dependence of the observed correlation upon the largest magnitude earthquakes.

3.5 Conclusions

Annual global earthquake and eruption rates have varied by a factor of around two over decadal timescales since 1960. Moreover, global seismic moment release is positively correlated with global eruption rate, with Monte Carlo permutation tests showing that this correlation is significant at $P < 0.05$ for timeshifts up to ±5 years. Understanding the potential causes of this correlation is important for seismic and volcanic hazard assessment. We find that eruption triggering by nearby large earthquakes occurs too infrequently to fully explain the correlation in the global data, which suggests that other mechanisms, such as triggering of distant eruptions by earthquake-induced dynamic stress changes, modulation of global earthquake and eruption rates by variations in the Earth's rotational velocity, or natural synchronisation of events over many repeated cycles, are responsible.

While we demonstrate that the observed correlation is robust since 1960, the analysis of decadal timescale processes is inherently limited by the relatively short length of the available earthquake and eruption time-series (Figure 3.2). For some regions (e.g. Japan), it might be possible to extend the time-series backwards beyond 1960, although our results suggest that the correlation is reduced at the regional scale. Therefore, further global earthquake and eruption data acquired over the coming decades remains the most promising way to shed more light on the relationship between earthquakes and eruptions, as well as the cause of any potential correlation.

CHAPTER 4

THE RELATIONSHIP BETWEEN LARGE EARTHQUAKES AND VOLCANIC ERUPTIONS: A GLOBAL STATISTICAL STUDY

It is now generally accepted that large earthquakes can promote eruptions at nearby volcanoes. However, the prevalence of 'triggered' eruptions, as well as the distances and timescales over which triggering occurs, remain unclear. Here, we use modern global earthquake and eruption records to compare volcanic eruption rates both before and after large earthquakes with time-averaged background eruption rates. Importantly, we systematically vary the earthquake magnitudes we consider, as well as the distances and timescales used to calculate eruption rates. We also investigate the effects of earthquake depth and slip orientation. Overall, we find that post-earthquake eruption rates are around 1.25 times the average rate within 750 km and 1 year, and possibly 2 to 4 years, following $M_w \geq 7$ earthquakes. By contrast, pre-earthquake eruption rates are around 0.9 times the average rate within 750 km and 182 days, and possibly 1 year, before $M_w \geq 7$ earthquakes. Furthermore, deep earthquakes (≥70 km) appear to more strongly affect eruption rates than shallow earthquakes, while earthquake slip orientation is also important. Additionally, earthquakes with above average pre-earthquake eruption rates tend to have post-earthquake eruption rates that are relatively further above average, compared with earthquakes with below average pre-earthquake eruption rates. Further study of the relationships reported here represents a good opportunity to improve our understanding of tectono-magmatic relationships.

4.1 Introduction

The potential for large earthquakes to trigger eruptions at nearby volcanoes has long been noted (e.g. Darwin 1840). However, systematic global recording of earthquakes and eruptions only began in the mid-twentieth century (Storchak et al. 2015, Siebert et al. 2010), therefore limiting detailed statistical analyses of the relationships between earthquakes and eruptions until more recently. Since the 1990s, numerous studies have investigated how earthquakes affect volcanic eruption rates (i.e. the number of eruptions per unit time), at scales from individual volcanoes (Nostro et al. 1998, Walter & Amelung 2006), through regional correlations (Watt et al. 2009, Eggert & Walter 2009, Bebbington & Marzocchi 2011, Bonali et al. 2013), to globally (Linde & Sacks 1998, Marzocchi 2002, Manga & Brodsky 2006, Nishimura 2017, Sawi & Manga 2018). These studies generally find that volcanic eruptions occur more often than expected following nearby large earthquakes. Consequently, it is now mainly accepted that earthquakes can trigger volcanic eruptions, and various physical mechanisms have been proposed to explain this (see reviews by Hill et al. 2002, Seropian et al. 2021).

However, the prevalence of triggered eruptions, as well as the distances and timescales over which eruption triggering occurs, remain unclear. Although previous studies have considered these factors, their findings vary markedly; eruption triggering has been associated with greatly increasing eruption rates over the first few days following earthquakes (Linde & Sacks 1998), to producing only minor increases in eruption rates over the following months to several years (Sawi & Manga 2018). These variable findings are probably attributable to each study using different earthquake and eruption records and different definitions for triggered eruptions in terms of the minimum earthquake magnitude required and the maximum distances and timescales between earthquakes and triggered eruptions. On the other hand, potentially important factors such as earthquake depth and slip orientation have not yet been studied. Addressing these issues in quantifying how earthquakes affect eruption rates is important for assessing volcanic risk, as well as for understanding the processes which lead to volcanic eruptions.

Determining definitively whether an earthquake triggered a given volcanic eruption is challenging, as most earthquakes and eruptions occur in regions with high background rates of seismic and volcanic activity, predominantly at subduction zones. Furthermore, it is widely believed that earthquakes can only trigger eruptions at volcanoes that are already close to erupting anyway (Barrientos 1994, Manga & Brodsky 2006, Walter

& Amelung 2007, Nishimura 2017). Therefore, we prefer to avoid the term eruption triggering. Instead, we use modern global earthquake and eruption records to investigate how earthquakes promote, or perhaps sometimes inhibit, volcanic eruptions (e.g. Marzocchi 2002). To achieve this, we calculate volcanic eruption rates both before and after nearby large earthquakes and compare these against the time-averaged background eruption rate. We then use Monte Carlo simulations with randomised eruption dates to quantify the significance of observed deviations from the time-averaged eruption rate. To thoroughly characterise how earthquakes affect eruption rates, we systematically vary the earthquake magnitudes we consider and the distances and timescales used to calculate eruption rates. We also investigate the effects of earthquake depth and slip orientation and the implications of using different methods to calculate eruption rates.

4.2 Summary of previous studies

As there is now a wealth of literature concerning the relationship between earthquakes and eruptions, we restrict this review to studies investigating the statistical relationship between large earthquakes and volcanic eruptions at the global scale. Perhaps the first attempt at this was provided by Carr (1977), who produced time-series for great thrust earthquakes and volcanic eruptions along the circum-Pacific subduction zones from 1820 to 1976. Using these time-series, Carr (1977) suggested that subduction zones often exhibit a period of low volcanic eruption rates for several years to a few decades before great earthquakes, followed by a period of increased eruption rates beginning a few years before or after great earthquakes. In contrast to subsequent studies, Carr (1977) highlighted the decrease in eruption rates prior to large earthquakes as the most characteristic finding, although the statistical significance of this result was not tested.

The first truly global eruption triggering study was performed by Linde & Sacks (1998), using earthquake records from the USGS National Earthquake Information Centre compendium (NEIC) and eruption records from the Smithsonian Global Volcanism Program (GVP) for the past several hundred years. Investigating both great ($M \geq 8$) and large ($7 \leq M < 8$) magnitude earthquakes, Linde & Sacks (1998) identified a peak in VEI ≥ 2 eruption rates lasting for a few days within 750 km following great earthquakes and within 250 km following large earthquakes. Simulations using randomised earthquake catalogues showed that the probability of the observed eruption rate peaks occurring by chance was $\ll 1\%$. No enhanced eruption rates were identified beyond 750 km, or for timescales longer than a few days following earthquakes. Manga & Brodsky (2006) later recreated the study of Linde & Sacks (1998) using an updated earthquake catalogue and observed a similar peak in VEI ≥ 2 eruption rates within 5 days and 800 km following $M > 8$ earthquakes. While this provided further evidence for short-term eruption triggering, Manga & Brodsky (2006) also highlighted the conspicuous absence of short-term triggered eruptions following the most recent large earthquakes.

By contrast, Marzocchi (2002) found that the eight largest explosive eruptions (VEI ≥ 5) of the twentieth century were significantly correlated with earthquakes that occurred 0-5 and 30-35 years prior to the eruptions, at distances up to 1000 km away. This evidence for longer-term eruption triggering was calculated using a perturbation function to model the effects of $M_s \geq 7$ earthquakes on future erupting volcanoes. Marzocchi (2002) attributed the 0-5 and 30-35 year time gaps between the earthquakes and eruptions to the effects of coseismic and postseismic stress changes respectively. Similarly, Walter & Amelung (2007) investigated how the four historically recorded $M > 9$ megathrust earthquakes (1952 Kamchatka, 1960 Chile, 1964 Alaska, 2004 Sumatra) affected eruption rates at volcanoes up to 1500 km away. By comparing the 3-year post-earthquake eruption rates with the average eruption rates calculated over the previous fifty years, Walter & Amelung (2007) found significant increases in eruption rates associated with the earthquakes, with rarely erupting volcanoes showing the greatest increase.

More recently, Sawi & Manga (2018) also recreated the study of Linde & Sacks (1998) but using only earthquakes and eruptions from 1964 through 2016, taken from the Advanced National Seismic System composite catalogue (ANSS) and the GVP respectively. To offset the decrease in the number of earthquakes and eruptions caused by removing all events prior to 1964, Sawi & Manga (2018) expanded their definition of a triggered eruption to include eruptions within 5 days and 800 km following $M \geq 6$ earthquakes. To quantify eruption triggering, Sawi & Manga (2018) compared VEI ≥ 2 eruption rates over 5 days following earthquakes with VEI ≥ 2 eruption rates over 5 days before earthquakes. Monte Carlo simulations with randomised eruption dates showed that eruption rate changes within 5 days of earthquakes were in agreement with those expected by random chance, suggesting that the short-term eruption triggering reported by Linde & Sacks (1998) may have been an artefact caused by the historical records. However, Sawi & Manga (2018) also investigated eruption rate changes over longer timescales and found a 5-12% increase in eruption rates for periods of 2 months to 2 years following earthquakes, significant at the 1 sigma level.

By contrast, Nishimura (2017) investigated in greater detail how longer-term eruption triggering depends on earthquake magnitude and the distance from earthquakes. Using earthquake records from the Global Centroid Moment Tensor catalogue (CMT) from 1976 to 2010 and eruption records from the GVP from 1966 to 2015, Nishimura (2017) used a similar method to Sawi & Manga (2018) to compare pre-earthquake and post-earthquake eruption rates. Investigating distances up to 1000 km from earthquakes in increments of 200 km, Nishimura (2017) found that VEI ≥ 2 eruption rates increased by approximately 50% within 200 km and 5 years following $M_w \geq 7.5$ earthquakes. Monte Carlo simulations using randomised earthquake dates showed that the probability of this occurring by chance was <1%. However, no significant increases in eruption rate were found at larger distances or greater timescales, or for earthquakes with $7 \leq M_w < 7.5$. Additionally, of the 52 triggered volcanic eruptions within 200 km and 5 years following $M_w \geq 7.5$ earthquakes, 20 came from only two volcanoes (Bezymianny and Ulawun), although excluding repeat eruptions from the results still produced 20-60% increases in eruption rate.

Overall, the studies of Linde & Sacks (1998), Nishimura (2017), and Sawi & Manga (2018) highlight the different conclusions reached by global statistical studies investigating eruption triggering. First, Linde & Sacks (1998) used historical records to show the importance of short-term eruption triggering within hundreds of kilometers and a few days following $M > 7$ earthquakes. This was subsequently disputed by Sawi & Manga (2018), who found no evidence for eruption triggering within a few days of earthquakes but did identify an approximately 10% increase in eruption rates within 800 km and longer timescales of 2 months to 2 years following $M > 6$ earthquakes. By contrast, Nishimura (2017) investigated the importance of earthquake magnitude and distance in more detail, reporting more significant eruption rate increases of approximately 50% within 200 km and 5 years following $M_w \geq 7.5$ earthquakes. Further contrasting results were also provided by Jenkins, Biggs, Rust & Rougier (2021), who found moderate increases of around 10% in VEI ≥ 2 eruption rates within 1000 km and 1-5 years following $M_w \geq 7$ earthquakes but no strong evidence for eruption triggering for distances of 200 or 2000 km, or for $M_w \geq 6$ earthquakes. Except for the earlier study of Linde & Sacks (1998), these studies all used relatively similar data and methods, suggesting that the different parameter ranges investigated, or at least the ranges reported, are likely responsible for the variable conclusions (Table 4.1).

Table 4.1: Reported parameter ranges investigated by previous global statistical studies of eruption triggering.

Study	Earthquake magnitude	Distance from earthquake (km)	Timescale following earthquakes (days)
Linde & Sacks (1998)	$M > 8$	0 - 250	1000, in daily bins
	$7 \leq M < 8$	0 - 500	
		0 - 750	
Manga & Brodsky (2006)	$M > 8$	0 - 800	1000, in daily bins
Nishimura (2017)	$M_w \geq 7.5$	0 - 200	0 - 1826
	$(7 \leq M_w < 7.5)$	(200 - 400)	(1826 - 3652)
		(400 - 600)	
		(600 - 800)	
		(800 - 1000)	
Sawi & Manga (2018)	$M > 6$	0 - 800	(0 - 5)
			(0 - 30)
			0 - 60
			0 - 120
			0 - 365
			0 - 730
			(0 - 1825)
Jenkins, Biggs, Rust & Rougier (2021)	$(M_w \geq 6)$	(0 - 200)	0 - 365
	$M_w \geq 7$	0 - 1000	0 - 1826
	$M_w \geq 8$	(0 - 2000)	

(Parentheses show parameters without significant evidence for eruption triggering.)

4.3 Data and method

4.3.1 Data

Following recent global statistical studies on eruption triggering (Nishimura 2017, Sawi & Manga 2018, Jenkins, Biggs, Rust & Rougier 2021), we use only modern global earthquake and eruption records compiled since the mid-twentieth century. In doing this, we aim to minimise the impact of potentially biased data; specifically, the possibility that eruption triggering can be attributed to large earthquakes inducing a state of temporarily heightened awareness in local populations, resulting in increased reporting of volcanic eruptions (Manga & Brodsky 2006). While we consider this unlikely for our data, we note that volcanic eruptions can have uncertain start dates, even during the late-twentieth and early-twenty-first centuries. Only since around 2010 has the number of uncertain start date eruptions fallen dramatically, probably due to increased remote sensing.

We use earthquake times, locations, and moment magnitudes (M_w) from the Global Centroid Moment Tensor catalogue, from its inception in 1976 through 2020 (CMT: Dziewonski et al. 1981). The CMT catalogue is reported to be complete above M_w 5.5 (Dziewonski et al. 1981, Ekström et al. 2012), so we use a minimum M_w of 6 to obtain a total of 5418 earthquakes over the 45 year catalogue. We further divide these events into 4885 M_w 6 earthquakes, 506 M_w 7 earthquakes, and 27 $M_w \geq 8$ earthquakes. We also classify earthquakes by their hypocentral depth and slip orientation. For depth, we use a threshold depth of 70 km to separate shallower crustal earthquakes from deeper earthquakes within subducted slabs. For slip orientation, we analyse the slip rake angles from the CMT focal mechanism solutions, using both nodal planes as the true fault plane is generally unknown. We define normal faulting earthquakes as those with at least one rake between -70° and -110°, reverse earthquakes as those with at least one rake between 70° and 110°, and strike-slip earthquakes as those with at least one rake either between -20° and 20°, >160°, or $< -160°$. Visual inspection of the focal mechanism solutions reveals that this method classifies slip orientations well and few earthquakes cannot be classified due to satisfying multiple categories (Table 4.2).

Table 4.2: Classification of the earthquakes extracted from the 1976-2020 CMT catalogue used in this study.

M_w	Depth	Reverse	Normal	Strike-slip	Oblique	Unclassified	
$6 \leq M_w < 7$	<70	1635	388	1337	449	13	3822
	≥70	214	290	197	325	37	1063
$7 \leq M_w < 8$	<70	213	32	87	37	2	371
	≥70	28	43	23	38	3	135
$M_w \geq 8$	<70	12	3	5	4	0	24
	≥70	0	3	0	0	0	3
		2102	759	1649	853	55	5418

Oblique refers to earthquakes that do not satisfy any slip category; unclassified refers to earthquakes which satisfy multiple slip categories.

We use volcanic eruption start dates, locations, and explosivity (VEI) from the Global Volcanism Program (GVP: Global Volcanism Program 2013). In order to calculate how eruption rates vary up to 5 years before and after nearby earthquakes, we consider eruptions from 1971 through 2020. The completeness of the GVP for smaller eruptions is unclear, but for explosive eruptions (VEI ≥ 2) we assume that the eruption record is complete since 1971 (e.g. Newhall & Self 1982, Mead & Magill 2014, Papale 2018, Jenkins, Biggs, Rust & Rougier 2021). The GVP notes where eruption magnitudes are uncertain, but we take the VEI value for each eruption as given. The GVP lists the initiation of 924 eruptions with VEI ≥ 2 over the 50 years from 1971 through 2020, including 182 eruptions with an uncertain start date (Table 4.3). We experiment with including or excluding uncertain start date eruptions in our analysis, as well as with using different minimum VEI thresholds.

Table 4.3: Classification of the volcanic eruptions extracted from the 1971-2020 GVP catalogue used in this study.

VEI	Certain date eruptions	Uncertain date eruptions
0	118	55
1	467	145
2	510	142
3	191	38
4	36	2
≥5	5	0

4.3.2 Methods

4.3.2.1 Eruption rates before and after earthquakes

To calculate volcanic eruption rates both before and after large earthquakes, we first define the desired earthquake parameters (M_w, depth, slip orientation) and eruption parameters (VEI, start date certainty) to study. We also specify the distance and timescale from the earthquakes over which to calculate the eruption rates. Here, we investigate surface distances of up to 1000 km from the earthquake centroid locations in increments of 250 km, over timescales of 30, 91, 182, 365, 730, 1096, 1461, and 1826 days (1 month to 5 years). We primarily treat these distances and timescales cumulatively (i.e. 1000 km and 1826 days represents the eruption rates within 0 to 1000 km and 1 to 1826 days either before or after each earthquake), but they can also be considered as individual bins (i.e. 1000 km and 1826 days represents the eruption rates within 750-1000 km and 1461-1826 days either before or after each earthquake). Cumulative eruption rates are more meaningful as they sample more eruptions over longer distances and timescales. However, eruption rate changes at short distances or timescales could become smeared out over longer distances and timescales when using cumulative eruption rates.

Once the desired input parameters are defined, we select all of the earthquakes and eruptions in our database that meet the specified criteria. Earthquakes that occurred less than the specified timescale before the end date of the database (31^{st} December 2020) are automatically rejected, and potential foreshocks and aftershocks can optionally be filtered out. For simplicity, we use a variation of the aftershock filtering method described by Nishimura (2017), whereby earthquakes that occurred within a certain distance and time period of a larger earthquake are deemed to be foreshocks or aftershocks and are discarded.

For each selected earthquake ($E_i = E_1 ... E_n$), we search the selected volcanic eruptions to determine the number of eruptions that occurred within the specified distance and timescale before the earthquake (B_i), as well as the number of eruptions that occurred within the specified distance and timescale after the earthquake (A_i). Eruptions that occurred on the same day as the earthquake are not counted; the GVP does not list eruption times, so it is generally unknown whether an eruption initiated before or after the earthquake. Repeat eruptions from a single volcano within the specified timescale can be either included or excluded. As B_i and A_i give the numbers of eruptions over the specified timescale, they therefore represent the pre-earthquake and post-earthquake eruption rates respectively for each earthquake.

4.3.2.2 Time-averaged eruption rates

Recent global statistical studies have quantified eruption triggering by comparing post-earthquake eruption rates with pre-earthquake eruption rates calculated over the same distance and timescale (Nishimura 2017, Sawi & Manga 2018, Jenkins, Biggs, Rust & Rougier 2021). However, we use an alternative approach, whereby we compare post-earthquake eruption rates with long-term time-averaged eruption rates (e.g. Walter & Amelung 2007). Using time-averaged eruption rates provides a more stable reference to compare post-earthquake eruption rates with. Additionally, this method also allows us to compare pre-earthquake eruption rates with time-averaged eruption rates (e.g. Carr 1977).

Ideally, we would calculate the time-averaged eruption rate within the specified distance of each earthquake using a long eruption record prior to the eruption record used to determine B_i and A_i. However, the completeness of the global eruption record much before to 1971 is unclear (e.g. Jenkins, Biggs, Rust & Rougier 2021). Therefore, we instead calculate the time-averaged eruption rate for each earthquake by determining the number of eruptions that occurred within the specified distance of that earthquake over our entire eruption record (N_i: 1971 through 2020), excluding the 5 years either side of the earthquake. Excluding the 5 years either side of the earthquake helps to ensure that the time-averaged eruption rate is independent of any changes to eruption rates caused by the earthquake itself. For cases where repeat eruptions from a single volcano within the specified timescale are excluded, this restriction also applies to the time-averaged eruption rate calculation. The time-averaged eruption rate (N_i) can then be used to express the average eruption rate within the specified distance and timescale of each earthquake,

$$\mu_i = t\frac{N_i}{T}, \tag{4.1}$$

where t is the specified timescale and T is the timescale used to calculate N_i (40 years, except for earthquakes between 2016-2020).

A potential issue with using long-term time-averaged eruption rates is that time-averaging could smooth out inherently clustered underlying eruption rates. To investigate this, Figure 4.1 shows the distribution of inter-eruption times within 750 km of $M_w \geq 7$ earthquakes, compared with simulated distributions of inter-eruption times calculated using randomised eruption dates (see section 4.3.2.5 for simulation methods). The observed distribution of inter-eruption times deviates slightly from the average simulated distribution of inter-eruption times over inter-eruption times of around 1 to 2 years, showing that there is some clustering in the observed eruptions at inter-eruption times of 1 to 2 years. However, the observed distribution of inter-eruption times is not vastly different from a distribution that would be expected for random eruption dates, suggesting that this clustering effect is only minor. Therefore, we consider that our averaging method is likely suitable. Further evidence of the suitability of our averaging method is shown by the fact that observed eruption rates tend towards the average eruption rate over long timescales of 1826 days before and after earthquakes (e.g. Figure 4.2).

4.3.2.3 Combined relative eruption rates

For any given individual earthquake, the eruption rates B_i and A_i are generally low (<10 eruptions) over our timescales of up to 5 years. Statistical analyses on such small sample sizes are limited, so evidence for eruption triggering is unlikely to be found by analysing individual earthquakes. Therefore, to provide more meaningful results, we follow the approach of previous studies by summing the eruption rates from all of the

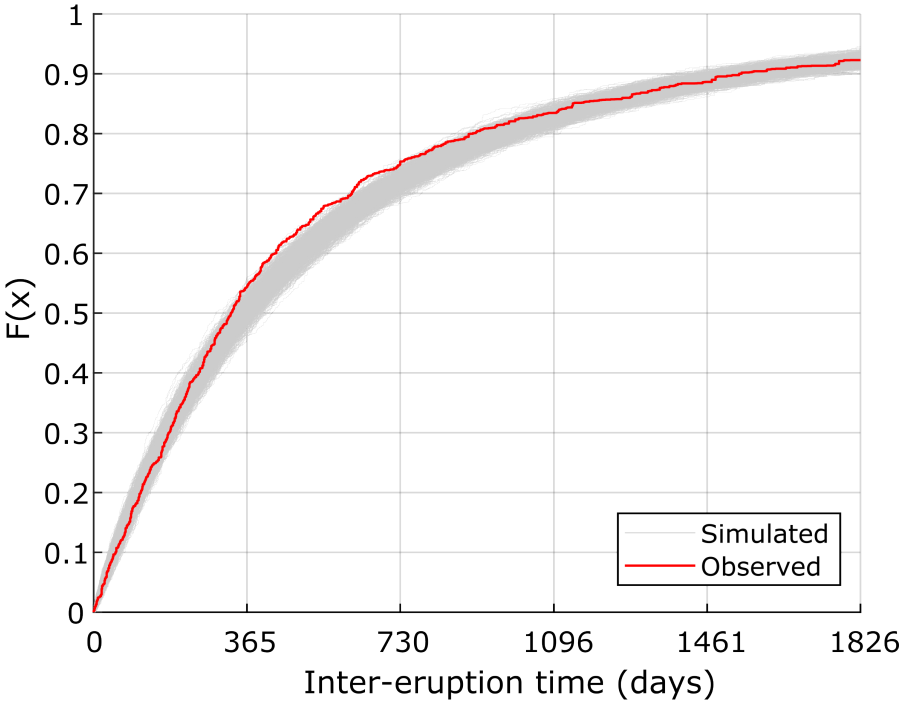

Figure 4.1: Cumulative distribution of inter-eruption times within 750 km of $M_w \geq 7$ earthquakes, compared with simulated cumulative distributions of inter-eruption times calculated using randomised eruption dates. The inter-eruption times are taken from the long-term time-average eruption rate calculation for each earthquake, which identifies all of the eruptions within the specified distance of each earthquake, before calculating the time between subsequent eruptions. To calculate these inter-eruption times, we allow repeat eruptions from a single volcano but exclude eruptions with an uncertain start date; for the inter-eruption times calculation, we also do not exclude the 5 years either side of the earthquake.

selected earthquakes (Nishimura 2017, Sawi & Manga 2018, Jenkins, Biggs, Rust & Rougier 2021). For n selected earthquakes, the combined eruption rates associated with those earthquakes are therefore given by

$$B = \sum_{i=1}^{n} B_i, \tag{4.2}$$

$$A = \sum_{i=1}^{n} A_i, \tag{4.3}$$

$$\mu = \sum_{i=1}^{n} \mu_i, \tag{4.4}$$

from which the combined pre-earthquake (ΔB) and combined post-earthquake (ΔA) eruption rates relative to the average eruption rate are given by

$$\Delta B = \frac{B}{\mu}, \tag{4.5}$$

$$\Delta A = \frac{A}{\mu}, \tag{4.6}$$

where values of ΔB and $\Delta A < 1$ represent below average eruption rates and values of ΔB and $\Delta A > 1$ represent above average eruption rates. We use ΔB and ΔA as our main measures of how earthquakes affect eruption rates, and hereafter we refer to ΔB and ΔA simply as 'relative eruption rates'.

4.3.2.4 Relative eruption rates for individual earthquakes

Information about each individual earthquake is lost using the combined relative eruption rates approach, and a single volcanic eruption may be counted for several different earthquakes. Therefore, we further investigate our results using an alternative approach, whereby we calculate the pre-earthquake (ΔB_i) and post-earthquake (ΔA_i) eruption rates relative to the average eruption rate for each individual earthquake,

$$\Delta B_i = \left(\frac{B_i}{\mu_i}\right), \tag{4.7}$$

$$\Delta A_i = \left(\frac{A_i}{\mu_i}\right), \tag{4.8}$$

and calculate the proportion of individual earthquakes (f) which display values of ΔB_i and ΔA_i above a given threshold value (x),

$$f(B_i) = \left(\frac{\sum_{i=1}^{n} 1(\Delta B_i > x)}{n}\right), \tag{4.9}$$

$$f(A_i) = \left(\frac{\sum_{i=1}^{n} 1(\Delta A_i > x)}{n}\right). \tag{4.10}$$

To avoid skewing the results by earthquake location, only earthquakes which occur near active volcanoes (i.e. μ_i and/or B_i and/or $A_i > 0$) are included in the eruption rate analysis for each individual earthquake.

4.3.2.5 Quantifying statistical significance

To quantify the significance of pre-earthquake or post-earthquake eruption rates from average eruption rates, we use 1000-run Monte Carlo simulations. In each simulation, we calculate the eruption rates associated with large earthquakes using the same parameters and method as for the real data but with randomised eruption dates instead. The simplest way to randomise the eruption dates is to assign each selected eruption a completely random date within the catalogue boundaries (e.g. Sawi & Manga 2018). However, this generates simulated eruption catalogues with different time distributions of eruptions compared to the observed eruption catalogue. Therefore, we use a more robust approach whereby we randomly permutate the selected eruption dates instead (i.e. pool together the selected eruption dates and then randomly redistribute them back to the selected eruptions). Random permutation maintains the time distribution of the observed eruption catalogue and therefore accounts for any global eruption rate variations unrelated to eruption triggering (e.g. Jenkins, Biggs, Rust & Rougier 2021). A potential issue with both randomly permutating the eruption dates and completely randomising the eruption dates is that the time distributions of eruptions at any given volcano are not maintained, which could result in unrealistically clustered simulated eruptions (e.g. two eruptions recorded on consecutive days at the same volcano, which in reality would be classified as a single eruption). However, by imposing limits on the recurrence of eruptions at any one volcano, we show that this does not significantly affect the results.

Using randomised simulations, the significance of an observed relative eruption rate (ΔObs) is shown by its percentile score (P) relative to the $j = 1000$ simulated eruption rates (ΔSim_j),

$$P = 100\left(\frac{\sum_{j=1}^{1000} 1(\Delta Obs \geq \Delta Sim_j)}{1000}\right), \tag{4.11}$$

where a percentile score of 100 represents the case where the observed relative eruption rate is greater than or equal to all of the simulated relative eruption rates, and a percentile score of 0 represents the case where the observed relative eruption rate is lower than all of the simulated relative eruption rates.

Similarly, the significance of an observed proportion of individual earthquakes with a relative eruption rate above a given threshold ($f(Obs_i)$) is shown by its percentile score relative to the $j = 1000$ simulated proportions of individual earthquakes with relative eruption rates above the same threshold ($f(Sim_i)_j$),

$$P = 100\left(\frac{\sum_{j=1}^{1000} 1(f(Obs_i) \geq f(Sim_i)_j)}{1000}\right), \tag{4.12}$$

where a percentile score of 100 represents the case where the observed proportion of earthquakes with a relative eruption rate above the threshold is greater than or equal to all of the simulated proportions of earthquakes with relative eruption rates above the threshold, and a percentile score of 0 represents the case where the observed proportion of earthquakes with a relative eruption rate above the threshold is lower than all of the simulated proportions of earthquakes with relative eruption rates above the threshold.

Relative eruption rates associated with earthquakes can be >1 (above average eruption rates) or <1 (below average eruption rates), so percentile scores close to either 100 (significantly above average eruption rates) or 0 (significantly below average eruption rates) are considered significant. As we test a range of parameters and timescales, it is expected that some percentile scores will be significant purely by chance, so we focus on cases where the percentile scores consistently indicate a significant result across a range of timescales or parameter choices.

4.4 Results

4.4.1 Principal results

Overall, we find that volcanic eruption rates deviate significantly from average eruption rates within 750 km and up to several years of earthquakes with a minimum M_w of 7 (Figure 4.2: see section 4.4.2 for a systematic investigation of these parameters and Table 4.4 for detailed results). This primarily consists of above average post-earthquake eruption rates, with Figure 4.2a showing combined relative eruption rates of 1.64 within 750 km and 30 days following $M_w \geq 7$ earthquakes, decaying to 1.27 at 1 year, and 1.19 to 1.12 at 3 to 5 years. However, there are also below average pre-earthquake eruption rates, with relative eruption rates of 0.87 to 0.91 within 750 km and 30 to 182 days before $M_w \geq 7$ earthquakes. For timescales of ≥ 1 year before $M_w \geq 7$ earthquakes, relative eruption rates within 750 km are close to 1.

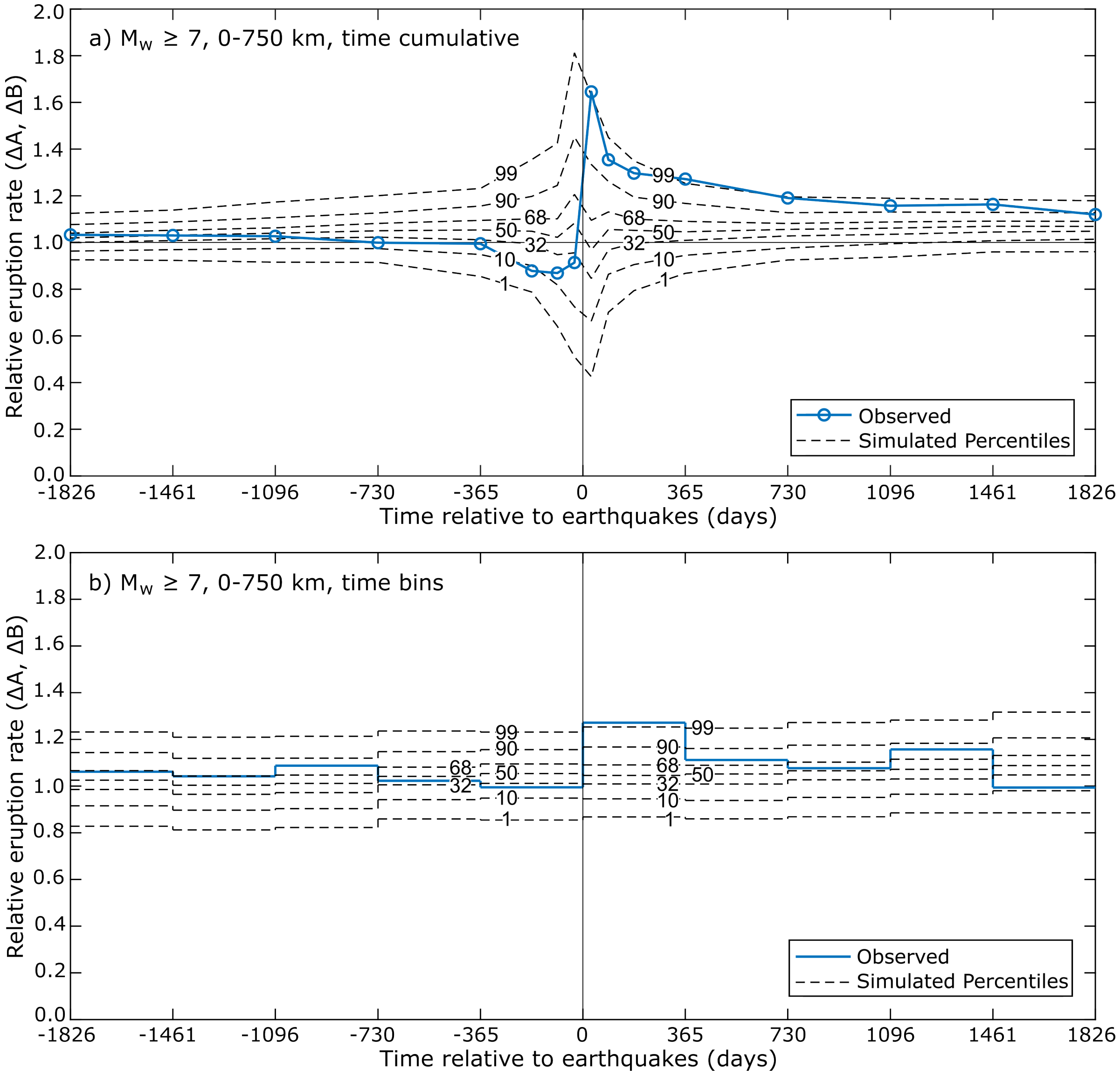

Figure 4.2: Combined VEI ≥ 2 eruption rates within 750 km and up to 5 years before and after $M_w \geq 7$ earthquakes, relative to average eruption rates. This includes repeat eruptions from a single volcano but excludes eruptions with an uncertain start date. No foreshock or aftershock filtering is applied. The percentiles of the simulated eruption rates calculated using random permutation of the observed eruption dates are also shown. a) Relative eruption rates over cumulative timescales. b) Relative eruption rates over yearly binned timescales.

To understand the significance of the observed eruption rates, Figure 4.2a also shows the percentiles of the simulated eruption rates calculated by randomly permutating the eruption dates. Compared to the simulations, the above average post-earthquake eruption rates have percentile scores of >99% over timescales of 30 days and 1 year, suggesting that it is very unlikely that these above average post-earthquake eruption rates occur by chance. The above average post-earthquake eruption rates over all of the other timescales also have percentile scores of >95%, except at 5 years where the percentile score is 87%. For the below average pre-earthquake eruption rates, the percentile score over a timescale of 182 days is 7%, suggesting that there is a reasonably low chance that this below average eruption rate occurs by chance. However, the below average pre-earthquake eruption rates over timescales of 30 days, 91 days, and 1 year have percentile scores of 31%, 17%, and 25% respectively, suggesting that these below average eruption rates are more consistent with those expected by chance.

Figure 4.2a shows eruption rates over cumulative timescales, so deviations from the average eruption rate over short timescales before or after earthquakes may become smeared out over longer timescales. Therefore, Figure 4.2b shows eruption rates in 1 year bins instead. Over timescales of 1 to 4 years, the binned post-earthquake relative eruption rates are 1.08 to 1.15, while over timescales of 4 to 5 years, the binned post-earthquake relative eruption rates are close to 1. However, compared to the simulations, the binned post-earthquake eruption rates over 1 to 4 years have percentile scores of 76%, 56%, and 81%, suggesting that these eruption rates are more comparable with those expected by chance. Similarly, the binned pre-earthquake eruption rate has a percentile score of 40% over a timescale of 1 to 2 years, suggesting that pre-earthquake eruption rates over timescales of 1 to 2 years are also comparable with those expected by chance.

4.4.2 Effects of M_w, distance, and time

The main parameters considered by previous eruption triggering studies were earthquake magnitude and the distance and timescale between earthquakes and eruptions. As previous studies have produced contrasting results, we now provide a systematic investigation into how these key parameters affect eruption rates associated with earthquakes (Table 4.4). Figure 4.3 shows eruption rates over cumulative timescales of up to 5 years before and after earthquakes as a function of earthquake magnitude (M_w 6, M_w 7, and $M_w \geq 8$) and the distance from earthquakes (0-250 km, 250-500 km, 500-750 km, and 750-1000 km). Within 5 years of M_w 6 earthquakes, relative eruption rates are generally between 1 and 1.10, regardless of distance and timescale, although there is more variability over timescales of <1 year. However, the eruption rates associated with M_w 6 earthquakes have few very high or very low percentile scores compared to the simulated eruption rates; at distances of 0-250 km, the percentile scores alternate between positive and negative, while distances of 250-500 km have positive percentile scores and distances of 500-750 km have negative percentile scores. Due to the lack of consistently significant percentile scores, the eruption rates associated with M_w 6 earthquakes are likely comparable with those expected by random chance.

By contrast, post-earthquake eruption rates within 750 km and 1 to 5 years of M_w 7 earthquakes are consistently above average, with relative eruption rates between 1.10 to 1.35. Likewise, post-earthquake eruption rates within 750 km and <1 year of M_w 7 earthquakes are also mostly above average, including very high relative eruption rates of 2.44 within 30 days and 250-500 km and 1.59 within 30 days and 500-750 km. However, the relative eruption rate within 0-250 km and 30 days following M_w 7 earthquakes is 0.56. The generally above average post-earthquake eruption rates within 750 km of M_w 7 earthquakes have consistently high percentile scores relative to the simulations, being >95% within 0-250 km over 182 days to 2 years, >95% within 250-500 km over 30 to 91 days, and >95% within 500-750 km over 1 to 4 years. Therefore, it is unlikely that these above average post-earthquake eruption rates within 750 km of M_w 7 earthquakes occur by chance. By contrast, pre-earthquake eruption rates for M_w 7 earthquakes are more variable as a function of distance and timescale, generally alternating between slightly above average and slightly below average. Exceptions to this are relative eruption rates of 0.48-0.68 within 500-750 km and 30 to 182 days before M_w 7 earthquakes, with low percentile scores of <10%. Beyond 750 km, eruption rates associated with M_w 7 earthquakes are generally close to average, although pre-earthquake eruption rates within 750-1000 km and 2 to 5 years before M_w 7 earthquakes do have relatively low percentile scores of <20%.

$M_w \geq 8$ earthquakes exhibit variable post-earthquake eruption rates as a function of distance and timescale, with relative eruption rates ranging from 0.71 to 1.78 within 1 to 5 years and 750 km. Likewise, for timescales of ≤1 year, post-earthquake eruption rates following $M_w \geq 8$ earthquakes are above average at distances of 250-750 km but below average at distances of 0-250 km and 750-1000 km. The variable post-earthquake eruption rates following $M_w \geq 8$ earthquakes are reflected by variable percentile scores relative to the simulations. By contrast, pre-earthquake eruption rates within 500 km

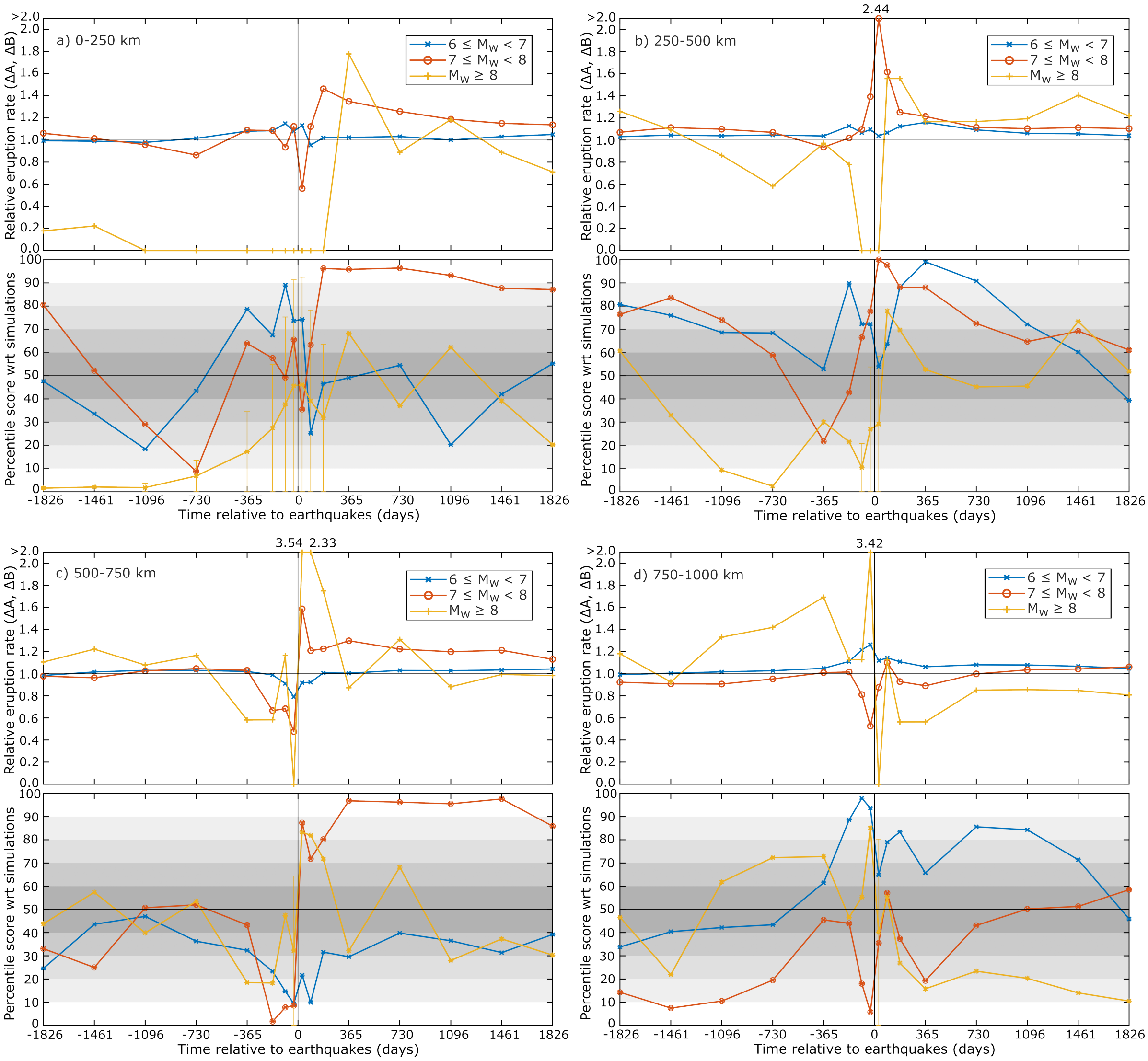

Figure 4.3: Top panels: Observed combined VEI ≥ 2 eruption rates over cumulative timescales up to 5 years before and after earthquakes as a function of earthquake magnitude, relative to average eruption rates. This includes repeat eruptions from a single volcano but excludes eruptions with an uncertain start date. No foreshock or aftershock filtering is applied. Relative eruption rates of >2 are indicated by labelling. Bottom panels: the corresponding percentile scores for the observed eruption rates with respect to simulations using random permutation of the observed eruption dates. Lighter shading for percentile scores near 0% or 100% suggests significant deviations from average eruption rates. Error bars show where the observed eruption rate is equal to the simulated eruption rates across multiple percentiles. Each pair of panels shows a different distance range from earthquakes over which eruption rates are calculated: a) 0-250 km, b) 250-500km, c) 500-750km, and d) 750-1000 km.

of $M_w \geq 8$ earthquakes are generally below average, especially within 0-250 km, where relative eruption rates are 0 to 0.22. The below average pre-earthquake eruption rates within 500 km of $M_w \geq 8$ earthquakes have low percentile scores, being <10% within 0-250 km and 2 to 5 years and <10% within 250-500 km and 2 to 3 years. Therefore, it is relatively unlikely that these below average pre-earthquake eruption rates within 500 km of $M_w \geq 8$ earthquakes occur by chance. Pre-earthquake eruption rates within 500-750 km of $M_w \geq 8$ earthquakes alternate between above and below average, while within 750-1000 km, $M_w \geq 8$ earthquakes generally have above average pre-earthquake eruption rates and below average post-earthquake eruption rates.

Table 4.4: Numbers of eruptions associated with earthquakes for different input parameters (see Figures 4.2 and 4.3 for visualisation)

	Input parameters								Output								
										Eruption numbers over timescale							
Figure	M_w	Distance (km)	Depth (km)	Slip type	Min VEI	Eq. filtering	Repeat erups.	Uncert. erups.	Earthquakes[a]	-30 30	-91 91	-182 182	-365 365	-730 730	-1096 1096	-1461 1461	-1826 1826
4.2a	≥7	0-750	all	all	2	n/a	Yes	No	533-481	15 27	43 67	86 127	194 248	381 454	574 647	752 849	915 992
4.2b	≥7	0-750	all	all	2	n/a	Yes	No	533-481				194 248	195 212	203 201	190 211	188 176
4.3a	6-7	0-250	all	all	2	n/a	Yes	No	4876-4332	40 42	129 107	240 226	474 449	859 873	1204 1230	1592 1659	1953 2064
4.3a	7-8	0-250	all	all	2	n/a	Yes	No	506-456	4 2	10 12	23 31	46 57	70 102	116 144	163 185	208 223
4.3a	≥8	0-250	all	all	2	n/a	Yes	No	27-25	0 0	0 0	0 0	0 2	0 2	0 4	1 4	1 4
4.3b	6-7	250-500	all	all	2	n/a	Yes	No	4876-4332	57 54	168 168	352 351	642 718	1255 1311	1827 1867	2416 2443	2879 2906
4.3b	7-8	250-500	all	all	2	n/a	Yes	No	506-456	8 14	19 28	35 43	64 83	143 149	214 215	284 284	325 335
4.3b	≥8	250-500	all	all	2	n/a	Yes	No	27-25	0 0	0 2	2 4	5 6	6 12	13 18	21 27	30 29
4.3c	6-7	500-750	all	all	2	n/a	Yes	No	4876-4332	43 50	150 152	323 329	662 652	1284 1284	1869 1864	2391 2433	2825 2995
4.3c	7-8	500-750	all	all	2	n/a	Yes	No	506-456	3 10	13 23	25 46	77 97	154 180	220 257	267 336	333 385
4.3c	≥8	500-750	all	all	2	n/a	Yes	No	27-25	0 1	1 2	1 3	2 3	8 9	11 9	16 13	18 16
4.3d	6-7	750-1000	all	all	2	n/a	Yes	No	4876-4332	70 62	204 192	370 369	692 701	1320 1389	1909 2025	2456 2609	2962 3132
4.3d	7-8	750-1000	all	all	2	n/a	Yes	No	506-456	3 5	14 19	35 32	68 60	125 131	170 194	224 257	274 315
4.3d	≥8	750-1000	all	all	2	n/a	Yes	No	27-25	1 0	1 1	2 1	6 2	10 6	14 9	12 11	19 13

[a] Number of earthquakes decreases with increasing specified timescales, as earthquakes with dates between 2016-2020 have to be progressively removed.

4.4.3 Effects of earthquake depth, slip orientation, and VEI

4.4.3.1 Earthquake depth

The effects of earthquake depth, slip orientation, and eruption VEI on eruption rates associated with earthquakes remain understudied. Therefore, we investigate how these parameters affect our principal results (Table 4.5), beginning with earthquake hypocentral depth. Figure 4.4 compares eruption rates within 750 km of shallow (<70 km) and deep (≥70 km) $M_w \geq 7$ earthquakes. While shallow and deep earthquakes show generally similar eruption rates, deep earthquakes exhibit both greater magnitude deviations from the average eruption rate and more significant percentile scores than shallow earthquakes. In particular, below average pre-earthquake eruption rates within 30 to 182 days before deep earthquakes have percentile scores of <5% relative to the simulations, while all other timescales also have percentile scores of <20%. Therefore, these below average pre-earthquake eruption rates before deep earthquakes are unlikely to occur by chance. The above average post-earthquake eruption rates following deep earthquakes also generally have more significant percentile scores than the shallow earthquakes, although the post-earthquake eruption rate percentile scores are most significant when all earthquakes are included.

4.4.3.2 Earthquake slip orientation

Figure 4.5 shows the eruption rates within 750 km of $M_w \geq 7$ earthquakes with different slip orientations. Overall, all of reverse, normal, and strike-slip earthquakes display above average post-earthquake eruption rates, all with similar percentile scores generally between 80%-100%, relative to the simulations. By contrast, only normal and strike-slip earthquakes exhibit below average pre-earthquake eruption rates. However, Figure 4.4 shows that below average pre-earthquake eruption rates are primarily associated with deep earthquakes, which mainly occur within subducted slabs. The focal mechanisms of deep slab events might not represent the crustal stress regime. Therefore, to investigate the effects of different crustal stress regimes, Figure 4.6 shows the eruption rates associated within 750 km of shallow (<70 km) $M_w \geq 7$ earthquakes depending on their slip orientation. Figure 4.6 shows that, over all timescales, shallow reverse earthquakes generally display above average eruption rates with high percentile scores, while shallow normal earthquakes generally display below average eruption rates with low percentile scores. By contrast, shallow strike-slip earthquakes generally show below average pre-earthquake eruption rates but above average post-earthquake eruption rates.

4.4.3.3 Eruption VEI

By default, we use a minimum eruption threshold of VEI ≥ 2, as this is the lowest VEI for which we are confident that the eruption record is complete. However, Figure 4.7 shows that removing the VEI threshold (i.e. VEI ≥ 0) does not greatly alter the principal results, with the exception of a lower percentile score for the above average post-earthquake eruption rates over a timescale of 182 days. By contrast, increasing the threshold to VEI ≥ 3 greatly reduces the percentile scores for the above average post-earthquake eruption rates and also completely removes the below average pre-earthquake eruption rates.

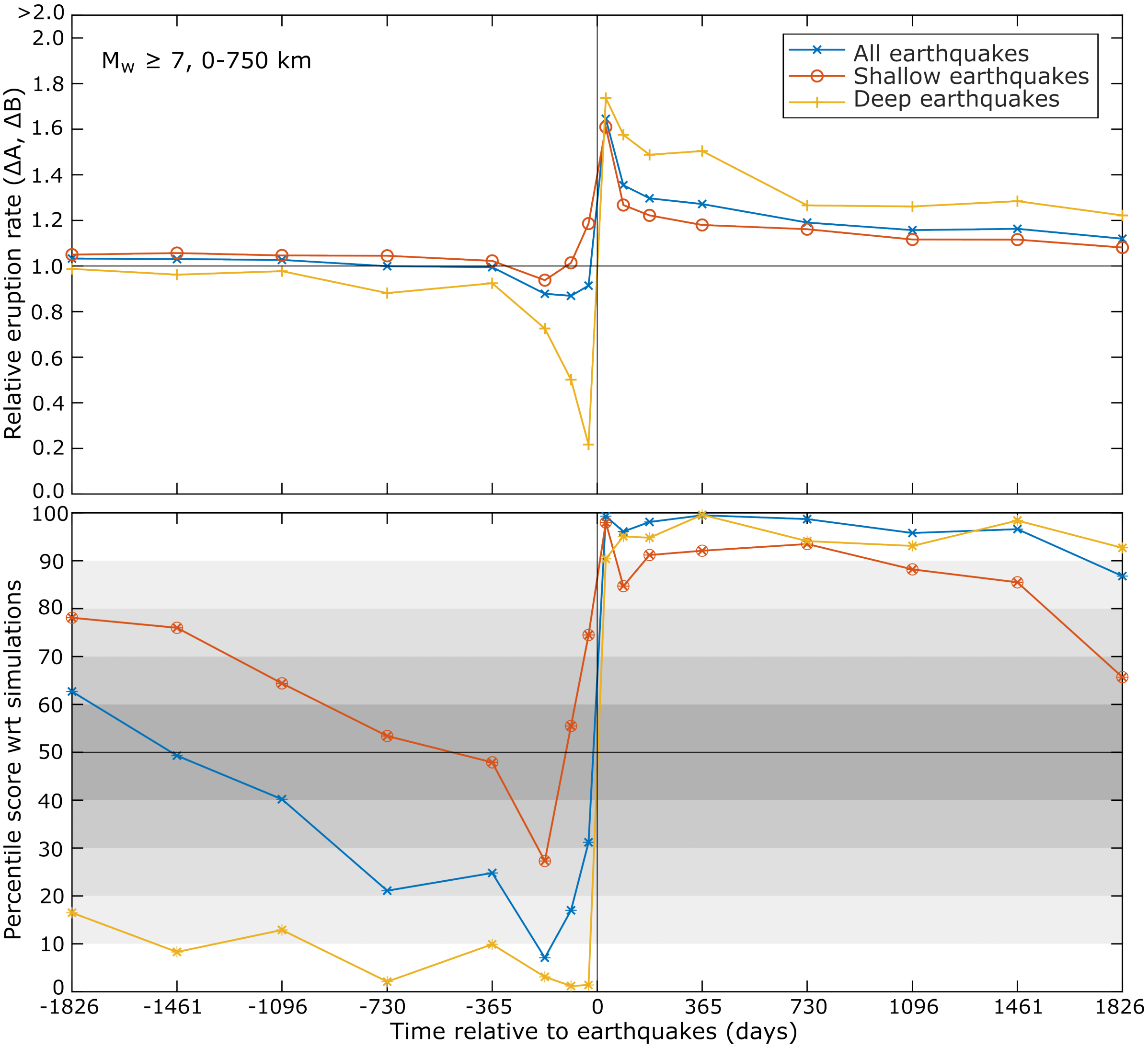

Figure 4.4: Top panel: Observed combined VEI ≥ 2 eruption rates within 750 km and cumulative timescales of up to 5 years before and after $M_w \geq 7$ earthquakes, relative to average eruption rates. Eruption rates are shown for all earthquakes, shallow earthquakes (<70 km), and deep earthquakes (≥70 km). This includes repeat eruptions from a single volcano but excludes eruptions with an uncertain start date. No foreshock or aftershock filtering is applied. Bottom panel: the corresponding percentile scores for the observed eruption rates with respect to simulations using random permutation of the observed eruption dates. Lighter shading for percentile scores near 0% or 100% suggests significant deviations from average eruption rates.

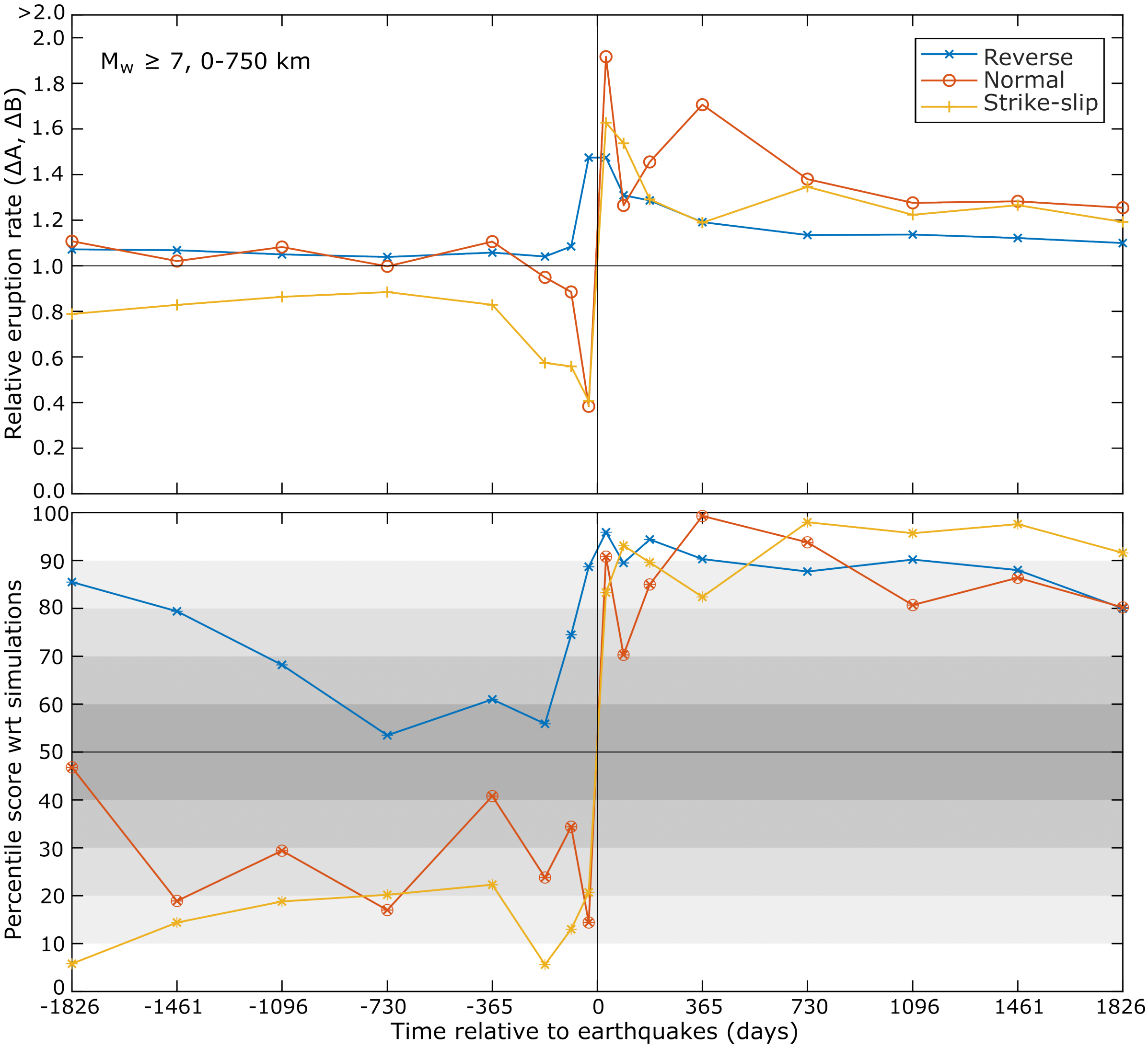

Figure 4.5: Top panel: Observed combined VEI ≥ 2 eruption rates within 750 km and cumulative timescales of up to 5 years before and after $M_w \geq 7$ earthquakes, relative to average eruption rates. The eruption rates are shown for reverse, normal, and strike-slip earthquakes. This includes repeat eruptions from a single volcano but excludes eruptions with an uncertain start date. No foreshock or aftershock filtering is applied. Bottom panel: the corresponding percentile scores for the observed eruption rates with respect to simulations using random permutation of the observed eruption dates. Lighter shading for percentile scores near 0% or 100% suggests significant deviations from average eruption rates.

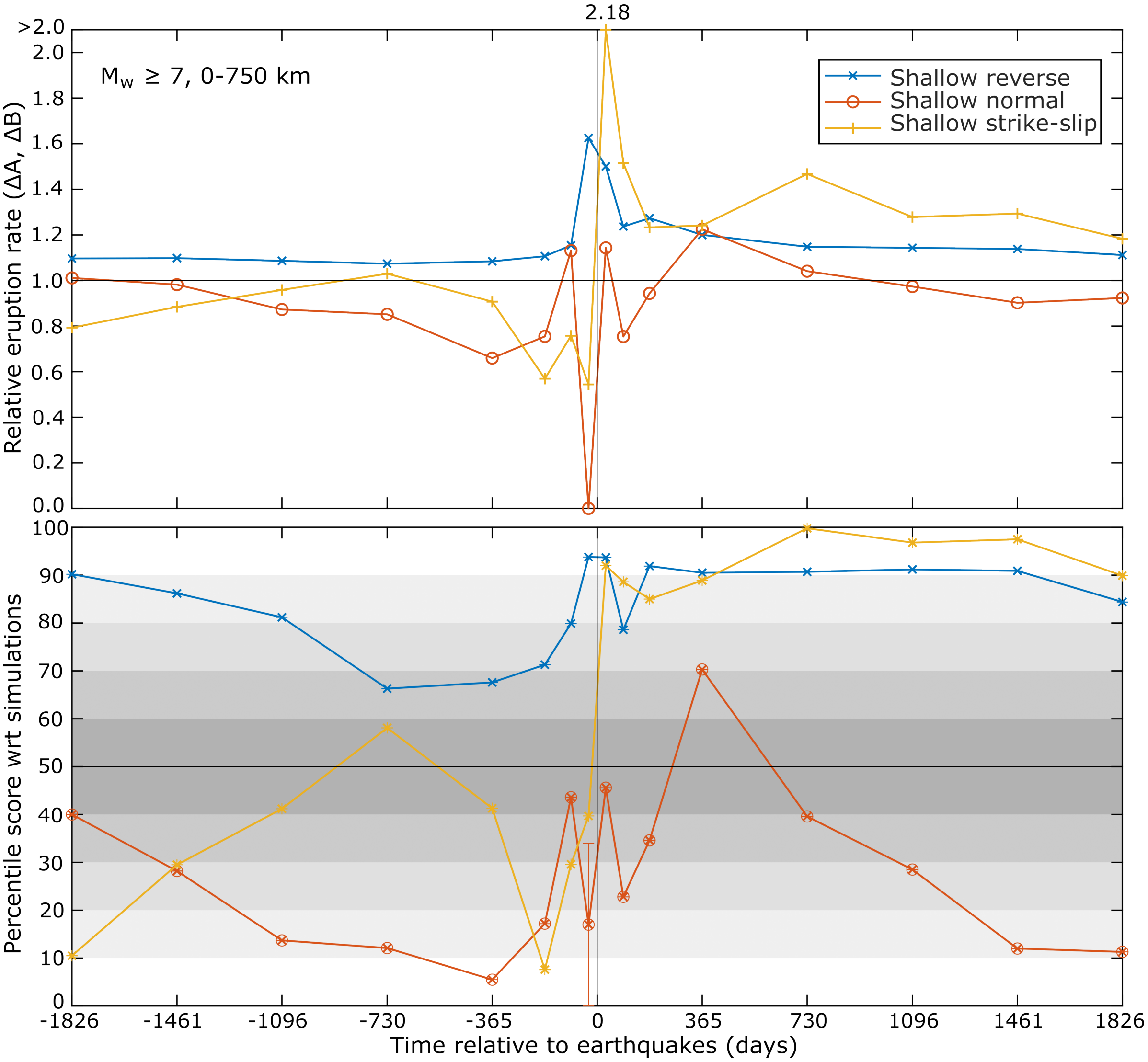

Figure 4.6: Top panel: Observed combined VEI ≥ 2 eruption rates within 750 km and cumulative timescales of up to 5 years before and after $M_w \geq 7$ earthquakes, relative to baseline eruption rates. The eruption rates are shown for reverse, normal, and strike-slip earthquakes with shallow (< 70 km) hypocentral depths. This includes repeat eruptions from a single volcano but excludes eruptions with an uncertain start date. No foreshock or aftershock filtering is applied. Relative eruption rates of >2 are indicated by labelling. Bottom panel: the corresponding percentile scores for the observed eruption rates with respect to simulations using random permutation of the observed eruption dates. Lighter shading for percentile scores near 0% or 100% suggests significant deviations from average eruption rates.

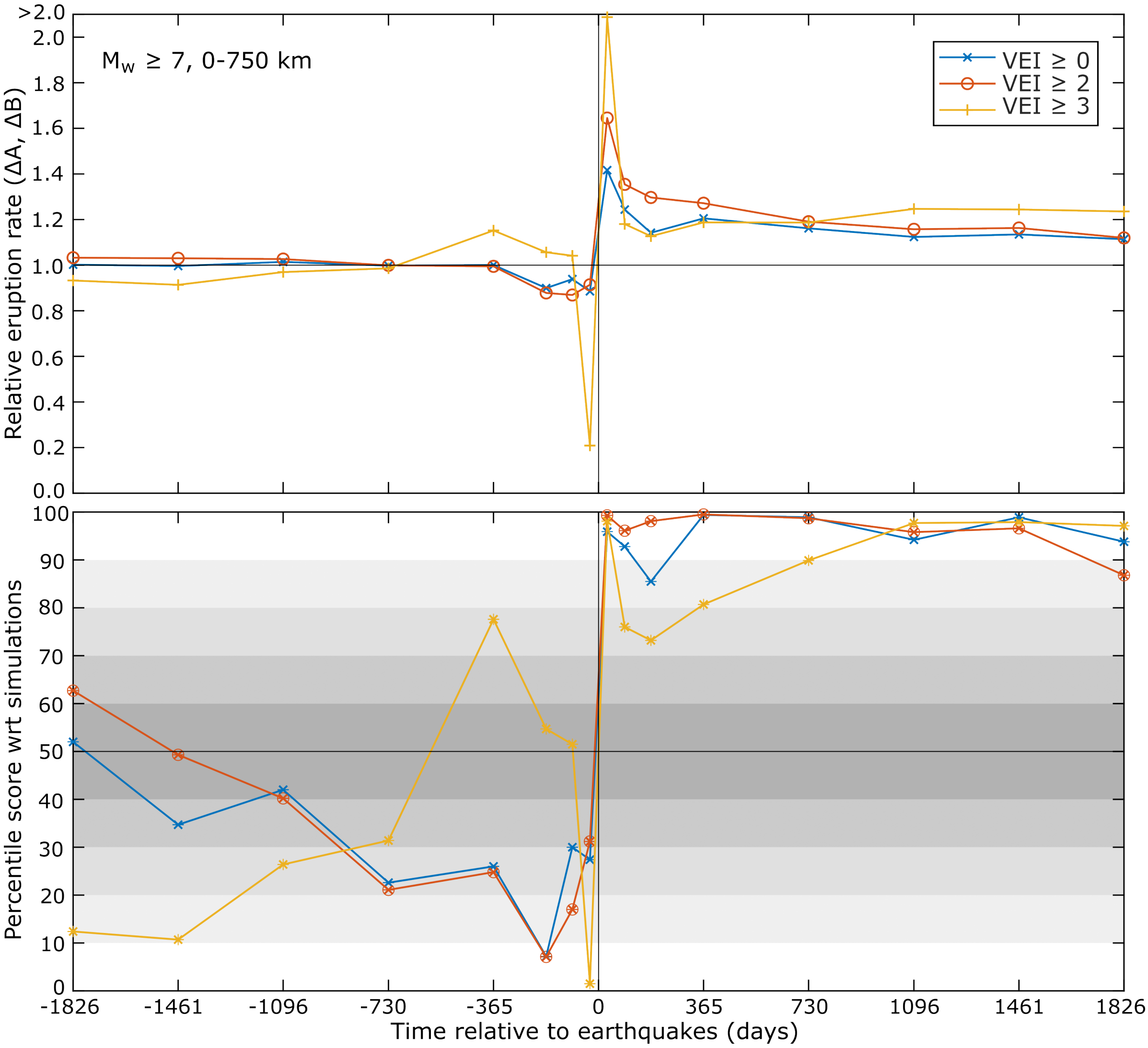

Figure 4.7: Top panel: Observed combined VEI ≥ 2 eruption rates within 750 km and cumulative timescales of up to 5 years before and after $M_w \geq 7$ earthquakes, relative to average eruption rates. The eruption rates are shown for eruptions within a minimum VEI of 0, 1, and 2. This includes repeat eruptions from a single volcano but excludes eruptions with an uncertain start date. No foreshock or aftershock filtering is applied. Bottom panel: the corresponding percentile scores for the observed eruption rates with respect to simulations using random permutation of the observed eruption dates. Lighter shading for percentile scores near 0% or 100% suggests significant deviations from average eruption rates.

Table 4.5: Numbers of eruptions associated with earthquakes for different input parameters (see Figures 4.4, 4.5, 4.6 and 4.7 for visualisation)

	Input parameters								Output								
										Eruption numbers over timescale							
Figure	M_w	Distance (km)	Depth (km)	Slip type	Min VEI	Eq. filtering	Repeat erups.	Uncert. erups.	Earthquakes[a]	-30	-91	-182	-365	-730	-1096	-1461	-1826
										30	91	182	365	730	1096	1461	1826
4.4	≥7	0-750	all	all	2	n/a	Yes	No	533-481	15	43	86	194	381	574	752	915
										27	67	127	248	454	647	849	992
4.4	≥7	0-750	0-70	all	2	n/a	Yes	No	395-359	14	36	66	143	287	419	555	675
										19	45	86	165	319	447	586	695
4.4	≥7	0-750	≥70	all	2	n/a	Yes	No	138-122	1	7	20	51	94	155	197	240
										8	22	41	83	135	200	263	297
4.5	≥7	0-750	all	reverse	2	n/a	Yes	No	253-239	13	29	55	111	216	326	439	542
										13	35	68	125	236	353	461	556
4.5	≥7	0-750	all	normal	2	n/a	Yes	No	81-69	1	7	15	35	60	95	113	151
										5	10	23	54	83	112	142	171
4.5	≥7	0-750	all	strike-slip	2	n/a	Yes	No	115-96	1	4	8	23	46	60	72	84
										4	11	18	33	70	85	110	127
4.6	≥7	0-750	0-70	reverse	2	n/a	Yes	No	225-212	13	28	53	103	202	305	410	503
										12	30	61	114	216	321	425	510
4.6	≥7	0-750	0-70	normal	2	n/a	Yes	No	35-30	0	3	4	7	18	26	37	46
										1	2	5	13	22	29	34	42
4.6	≥7	0-750	0-70	strike-slip	2	n/a	Yes	No	92-77	1	4	6	19	40	48	54	59
										4	8	13	26	57	64	79	88
4.7	≥7	0-750	all	all	0	n/a	Yes	No	533-481	25	80	152	337	658	983	1265	1545
										40	106	193	406	766	1089	1441	1717
4.7	≥7	0-750	all	all	2	n/a	Yes	No	533-481	15	43	86	194	381	574	752	915
										27	67	127	248	454	647	849	992
4.7	≥7	0-750	all	all	3	n/a	Yes	No	533-481	1	15	30	65	108	154	188	231
										10	17	32	67	130	198	256	306

[a] Number of earthquakes decreases with increasing specified timescales, as earthquakes with dates between 2016-2020 have to be progressively removed.

4.4.4 Sensitivity to method choices

4.4.4.1 Simulation method

To ensure that our findings are robust, we also test the sensitivity of the principal results to our methodology choices (Table 4.6), beginning with the choice of simulation method. By default, we use random permutation of the selected eruption dates with no limit on the recurrence of eruptions from a single volcano. However, this could potentially generate unrealistically clustered simulated eruptions at individual volcanoes, which could affect the percentile scores. Therefore, we modify our random permutation algorithm to impose a limit on the recurrence of eruptions from a single volcano within either 91 days or 1 year. To ensure successful permutation of all of the selected eruption dates while conforming with the recurrence limits, we reassign eruption dates to the volcanoes that have the most eruptions first; if a randomly chosen eruption date would violate the recurrence limit given the eruption dates already reassigned to a volcano, then the chosen date is returned to the pool and another eruption date is randomly chosen instead. Figure 4.8 shows that using eruption recurrence limits does not significantly affect the percentile scores of the observed eruption rates, suggesting that random permutation of the selected earthquake dates without a recurrence limit is appropriate.

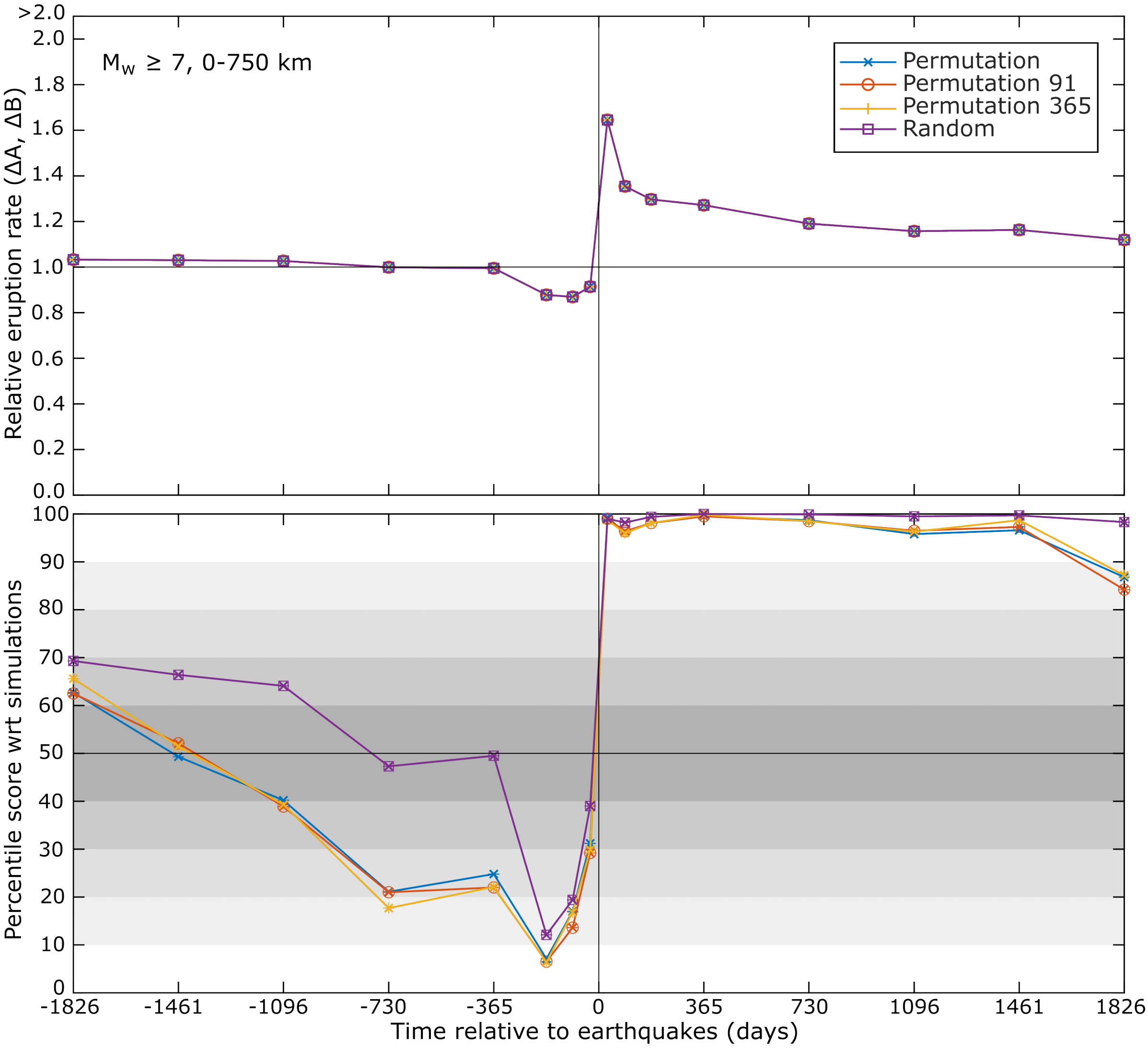

Figure 4.8: Top panel: Observed combined VEI ≥ 2 eruption rates within 750 km and cumulative timescales of up to 5 years before and after $M_w \geq 7$ earthquakes, relative to average eruption rates. This includes repeat eruptions from a single volcano but excludes eruptions with an uncertain start date. No foreshock or aftershock filtering is applied. Bottom panel: the corresponding percentile scores for the observed eruption rates with respect to different simulation methods: random permutation of the observed eruption dates; random permutation of the observed eruption dates with a recurrence limit on eruptions at a single volcano of 91 or 365 days; and completely random eruption dates. Lighter shading for percentile scores near 0% or 100% suggests significant deviations from average eruption rates.

Figure 4.8 also shows the percentile scores for the observed eruption rates calculated using completely randomised eruption dates instead of randomly permutated eruption dates (e.g. Sawi & Manga 2018). Using completely randomised eruption dates increases the percentile scores for the observed eruption rates. This decreases the significance of the below average pre-earthquake eruption rates, although not considerably for timescales of ≤182 days. By contrast, using completely randomised eruption dates increases the significance of the above average post-earthquake eruption rates, generating percentile scores of >99% for all timescales between 182 days and 4 years. Using completely randomised eruption dates produces higher percentile scores than random permutation of eruption dates because observed global rates of earthquakes and eruptions are correlated, due to either eruption triggering or external factors (Jenkins, Biggs, Rust & Rougier 2021). Consequently, with random permutation of eruption dates, above average eruption rates associated with earthquakes are expected by chance to some degree. This is shown by the median percentile of the random permutation simulations exhibiting slightly above average eruption rates within 5 years of earthquakes (Figure 4.2). By contrast, with completely random eruption dates, earthquakes are associated with average eruption rates by chance.

4.4.4.2 Foreshock and aftershock filtering

Large earthquakes trigger aftershocks, while large earthquakes themselves can occur in sequences (Freed 2005). By default, we do not filter potential foreshocks or aftershocks from the selected earthquakes. However, because we calculate eruption rates for each selected earthquake, including multiple related earthquakes could skew the results. Therefore, we use a simple method described by Nishimura (2017) to identify earthquakes that occur within a specified distance and time period of a larger earthquake as potential foreshocks and aftershocks. Figure 4.9 shows that removing potential foreshocks and aftershocks using the same distance and timescale as used for calculating eruption rates, or using the same distance and a timescale of 14 days, does not significantly affect the principal results.

4.4.4.3 Repeat and uncertain eruptions

By default, we allow repeat eruptions from a single volcano within the specified timescale, but we exclude eruptions with an uncertain start date. Figure 4.10 shows that over short timescales, excluding repeat eruptions does not greatly affect the percentile scores of the observed below average pre-earthquake eruption rates or the observed above average

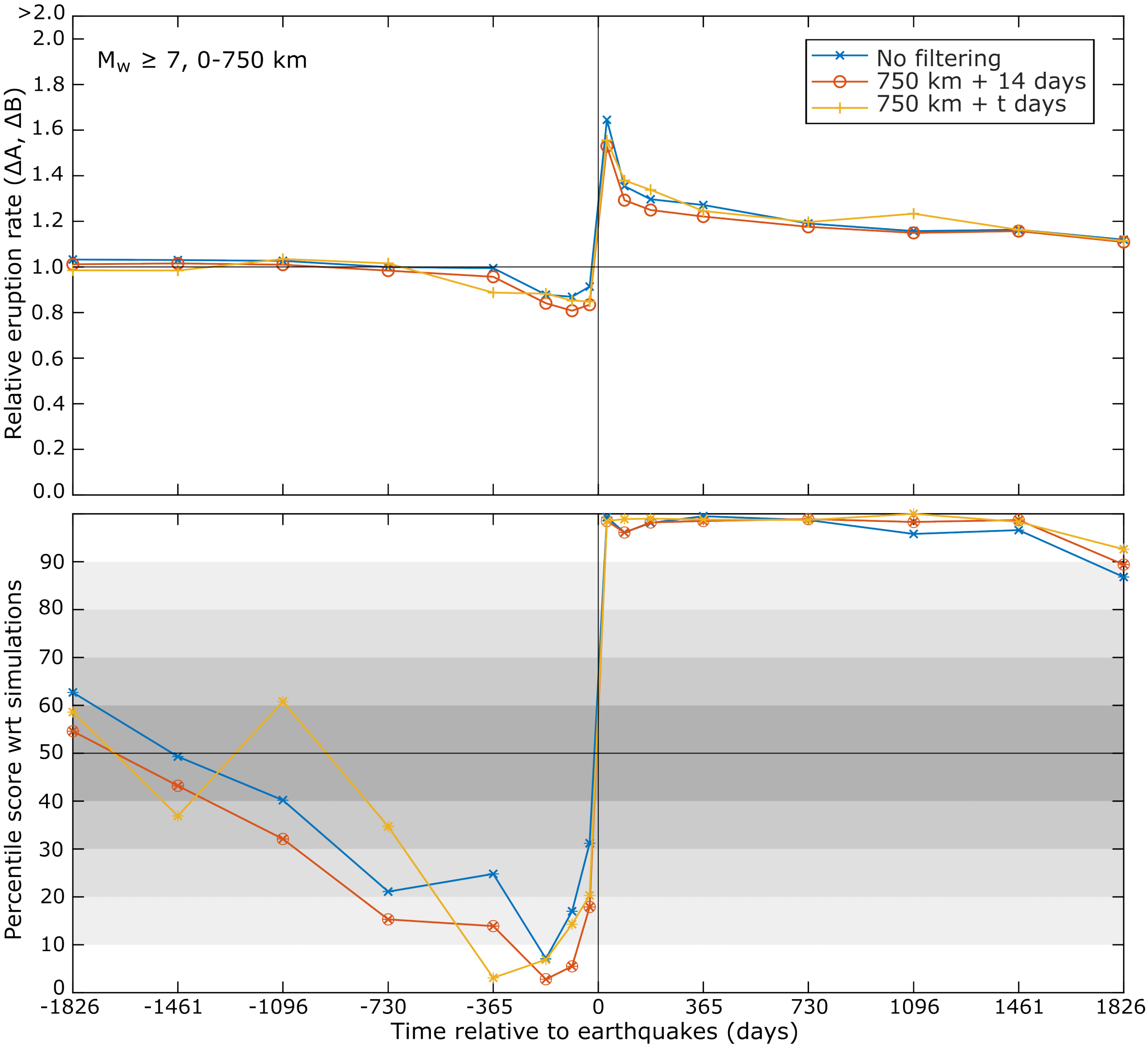

Figure 4.9: Top panel: Observed combined VEI ≥ 2 eruption rates within 750 km and cumulative timescales of up to 5 years before and after $M_w \geq 7$ earthquakes, relative to average eruption rates. The eruption rates are shown for different foreshock and aftershock filtering methods. Potential foreshocks and aftershocks are filtered using the method of (Nishimura 2017), whereby earthquakes occurring within 750 km and either 14 days, or the same timescale as used for calculating eruption rates, from a larger earthquake are discarded. This includes repeat eruptions from a single volcano but excludes eruptions with an uncertain start date. Bottom panel: the corresponding percentile scores for the observed eruption rates with respect to simulations using random permutation of the observed eruption dates. Lighter shading for percentile scores near 0% or 100% suggests significant deviations from average eruption rates.

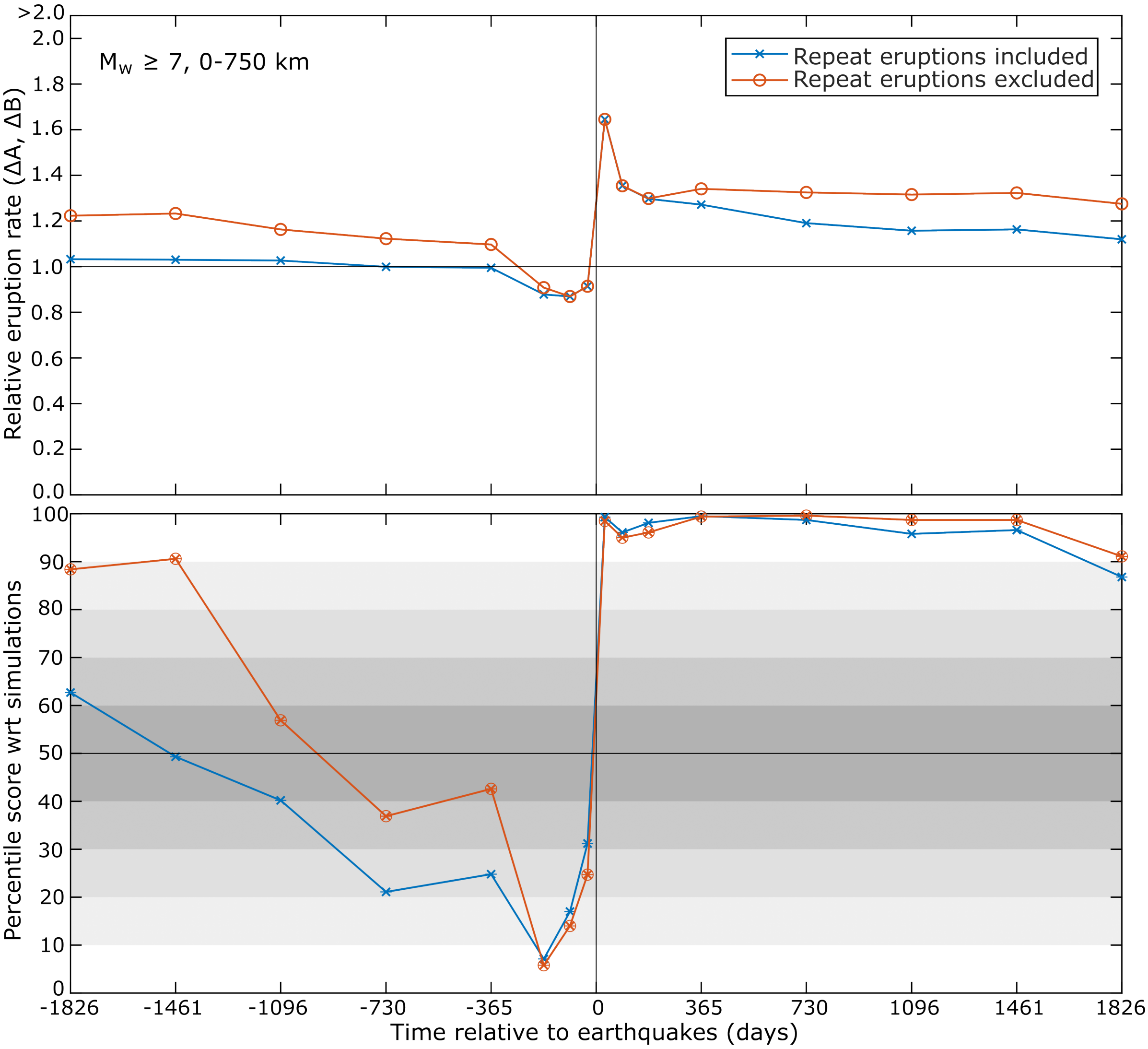

Figure 4.10: Top panel: Observed combined VEI ≥ 2 eruption rates within 750 km and cumulative timescales of up to 5 years before and after $M_w \geq 7$ earthquakes, relative to average eruption rates. The eruption rates are shown both including and excluding repeat eruptions from a single volcano within the specified timescale. This excludes eruptions with an uncertain start date. No foreshock or aftershock filtering is applied. Bottom panel: the corresponding percentile scores for the observed eruption rates with respect to simulations using random permutation of the observed eruption dates. Lighter shading for percentile scores near 0% or 100% suggests significant deviations from average eruption rates.

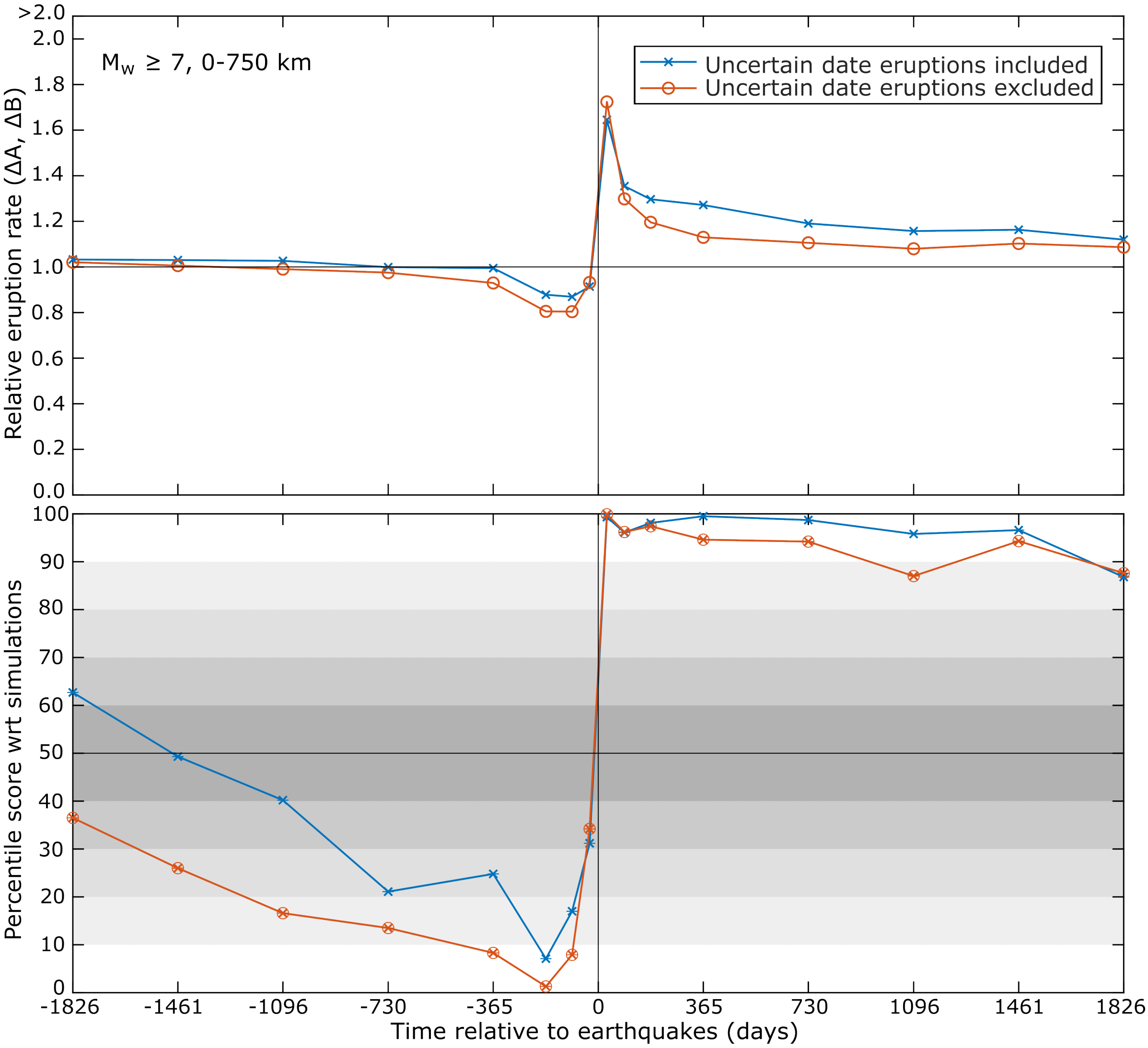

Figure 4.11: Top panel: Observed combined VEI ≥ 2 eruption rates within 750 km and cumulative timescales of up to 5 years before and after $M_w \geq 7$ earthquakes, relative to average eruption rates. The eruption rates are shown both including and excluding eruptions with an uncertain start date. This includes repeat eruptions from a single volcano. No foreshock or aftershock filtering is applied. Bottom panel: the corresponding percentile scores for the observed eruption rates with respect to simulations using random permutation of the observed eruption dates. Lighter shading for percentile scores near 0% or 100% suggests significant deviations from average eruption rates.

post-earthquake eruption rates. For timescales ≥1 year, excluding repeat eruptions causes the percentile scores to be higher, but this does not impact our principal findings. By contrast, Figure 4.11 shows that including eruptions with an uncertain start date causes the percentile scores to be lower, but again this does not affect our principal findings.

Table 4.6: Numbers of eruptions associated with earthquakes for different input parameters (see Figures 4.8, 4.9, 4.10 and 4.11 for visualisation)

	Input parameters								Output								
										Eruption numbers over timescale							
Figure	M_w	Distance (km)	Depth (km)	Slip type	Min VEI	Eq. filtering	Repeat erups.	Uncert. erups.	Earthquakes[a]	-30 30	-91 91	-182 182	-365 365	-730 730	-1096 1096	-1461 1461	-1826 1826
4.8	≥7	0-750	all	all	2	n/a	Yes	No	533-481	15 27	43 67	86 127	194 248	381 454	574 647	752 849	915 992
4.9	≥7	0-750	all	all	2	n/a	Yes	No	533-481	15 27	43 67	86 127	194 248	381 454	574 647	752 849	915 992
4.9	≥7	0-750	all	all	2	750km, 14d	Yes	No	477-427	12 22	35 56	72 107	163 208	328 392	492 560	645 735	777 852
4.9	≥7	0-750	all	all	2	750km, xd	Yes	No	468-166	12 22	34 55	64 97	114 160	185 218	224 267	237 280	245 277
4.10	≥7	0-750	all	all	2	n/a	Yes	No	533-481	15 27	43 67	86 127	194 248	381 454	574 647	752 849	915 992
4.10	≥7	0-750	all	all	2	n/a	No	No	533-481	15 27	43 67	86 123	189 231	327 386	449 508	574 616	658 686
4.11	≥7	0-750	all	all	2	n/a	Yes	No	533-481	15 27	43 67	86 127	194 248	381 454	574 647	752 849	915 992
4.11	≥7	0-750	all	all	2	n/a	Yes	Yes	533-481	20 37	52 84	103 153	237 288	485 550	721 786	956 1048	1176 1252

[a] Number of earthquakes decreases with increasing specified timescales, as earthquakes with dates between 2016-2020 have to be progressively removed.

4.4.5 Alternative methods

4.4.5.1 Eruption rates for individual earthquakes

To further investigate the above average post-earthquake eruption rates within 1 year and 750 km of $M_w \geq 7$ earthquakes (Figure 4.2), we classify $M_w \geq 7$ earthquakes by their depth and slip orientation then calculate the proportion of earthquakes in each class with above average post-earthquake eruption rates ($\Delta A_i > 1$) and greatly above average post-earthquake eruption rates ($\Delta A_i > 3$) (Figure 4.12a). Only earthquakes that occurred within 750 km of an active volcano (i.e. μ_i and/or B_i and/or $A_i > 0$) are included in this analysis. Figure 4.12a shows that shallow earthquakes more often have above average post-earthquake eruption rates than deep earthquakes. The proportion of shallow earthquakes with above average post-earthquake eruption rates is also greater than in 89% of the simulations, compared to 74% for deep earthquakes. However, Figure 4.12a also shows that deep earthquakes more often display greatly above average post-earthquake eruption rates than shallow earthquakes, which likely explains the higher combined post-earthquake eruption rates following deep earthquakes (Figure 4.4). The proportions of deep and shallow earthquakes with greatly above average post-earthquake eruption rates both have high percentile scores of 98% and 94% respectively compared to the simulations. For earthquake slip orientations, Figure 4.12a shows that shallow reverse earthquakes and shallow strike-slip earthquakes more often have above average post-earthquake eruption rates than shallow normal earthquakes, in agreement with the combined post-earthquake eruption rates (Figure 4.6). The proportions of shallow strike-slip and shallow reverse earthquakes with greatly above average post-earthquake eruption rates both have relatively high percentile scores of 93% and 88% respectively compared to the simulations. Although Figure 4.12a shows that shallow normal earthquakes more often have greatly above average post-earthquake eruption rates, the corresponding percentile score of 60% shows that this result is not significant,

To further investigate the below average pre-earthquake eruption rates within 182 days and 750 km of $M_w \geq 7$ earthquakes (Figure 4.2), Figure 4.12b shows the proportion of earthquakes in each class with above average pre-earthquake eruption rates ($\Delta B_i > 1$). Figure 4.12b shows that above average pre-earthquake eruption rates are more frequently associated with shallow earthquakes generally and especially shallow reverse earthquakes. Therefore, Figure 4.12b shows that deep earthquakes and shallow normal and shallow strike-slip earthquakes more often have below average pre-earthquake eruption rates, in agreement with the combined relative eruption rates (Figure 4.4 and Figure 4.6). Compared to the simulations, this result is more significant for deep earthquakes and shallow strike-slip earthquakes, which have relatively low percentile scores of 6% and 13% respectively. We do not calculate the proportion of individual earthquakes with greatly below average pre-earthquake eruption rates; this is because μ_i is generally <1 over a short timescale of 182 days, meaning that most earthquakes with below average pre-earthquake eruption rates have a relative eruption rate of 0.

4.4.5.2 Eruption rates after versus before earthquakes

We also use the eruption rates for each individual earthquake method to investigate whether earthquakes with above average post-earthquake eruption rates also exhibit any deviations in their pre-earthquake eruption rates. Within 750 km and 1 year of $M_w \geq 7$ earthquakes, Figure 4.13 shows that earthquakes with above average pre-earthquake eruption rates more often also display above average or greatly above average post-earthquake eruption rates, compared to earthquakes with below average pre-earthquake eruption rates. More importantly, the proportions of earthquakes with above average pre-earthquake eruption rates that also display above average or greatly above average

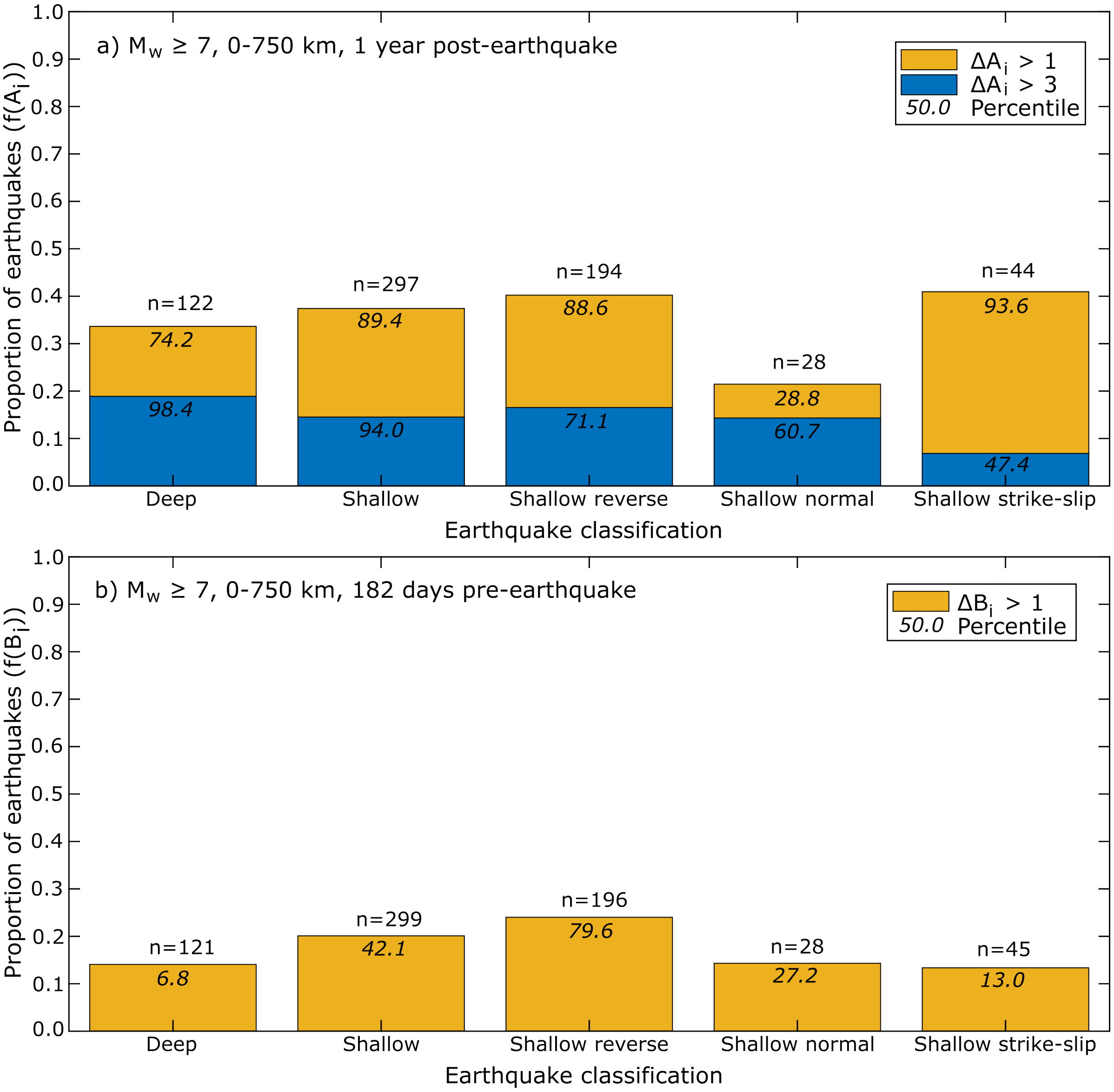

Figure 4.12: Proportion of $M_w \geq 7$ earthquakes within each classification that have a) post-earthquake relative eruption rates of >1 and >3 within 750 km and 1 year, and b) pre-earthquake relative eruption rates of >1 within 750 km and 182 days. Note that the proportion of earthquakes with $\Delta A_i > 1$ also includes all the earthquakes with $\Delta A_i > 3$. The numbers in italics give the percentile scores relative to the simulated proportions of earthquakes with relative eruption rates exceeding the threshold values, using random permutation of the observed eruption dates. n gives the number of earthquakes in each class. Only earthquakes which occur within 750 km of an active volcano (i.e. μ_i and/or B_i and/or $A_i > 0$) are included in this analysis.

post-earthquake relative eruption rates have percentile scores of 99.1% and >99.99% respectively relative to the simulations. Therefore, it very unlikely that earthquakes with above average pre-earthquake eruption rates also have above average post-earthquake eruption rates by chance.

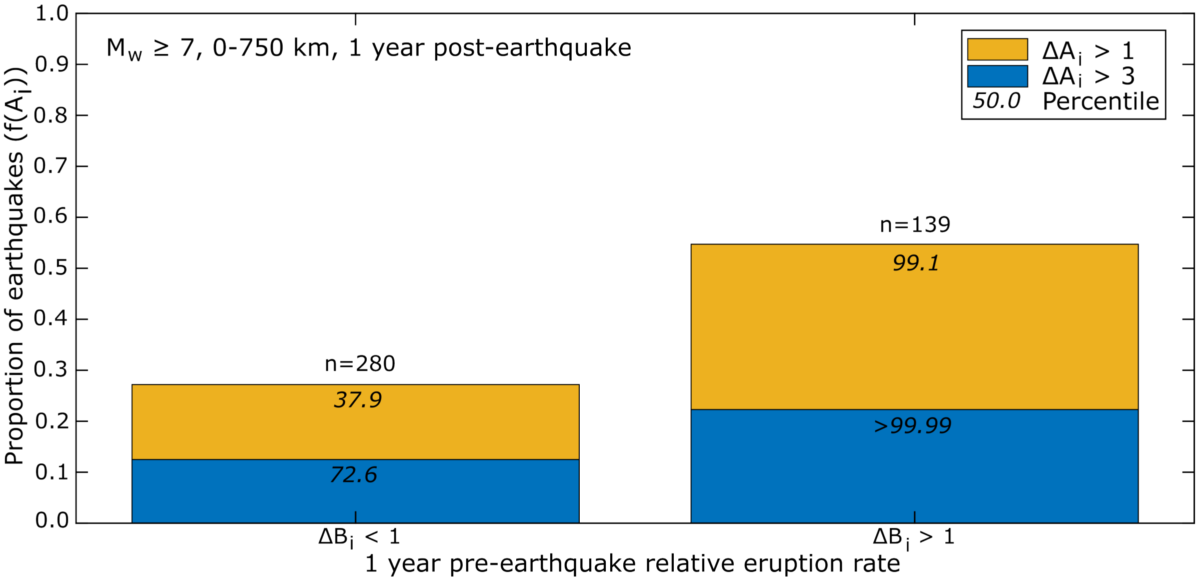

Figure 4.13: Proportion of $M_w \geq 7$ earthquakes that have post-earthquake relative eruption rates of >1 and >3 within 750 km and 1 year, as a function of their pre-earthquake relative eruption rates within 750 km and 1 year. Note that the proportion of earthquakes with $\Delta A_i > 1$ also includes all the earthquakes with $\Delta A_i > 3$. The numbers in italics give the percentile scores relative to the simulated proportions of earthquakes with relative eruption rates exceeding the threshold values, using random permutation of the observed eruption dates. n gives the number of earthquakes in each class. Only earthquakes which occur within 750 km of an active volcano (i.e. μ_i and/or B_i and/or A_i > 0) are included in this analysis.

In more detail, Figure 4.14 shows the proportion of earthquakes within each class with above average and greatly above average post-earthquake eruption rates as a function of their pre-earthquake eruption rates, within 750 km and 1 year. Figure 4.14 shows that each class of earthquake more often displays above average or greatly above average post-earthquake eruption rates when the pre-earthquake eruption rates are also above average. The exception to this are shallow strike-slip earthquakes, which have a greater proportion of earthquakes with greatly above average post-earthquake eruption rates when the pre-earthquake eruption rate is below average. By contrast, shallow normal earthquakes display the strongest relationship between above average pre-earthquake eruption rates and greatly above average post-earthquake eruption rates, with a percentile score of 99.95% relative to the randomised simulations. However, there are only four shallow normal earthquakes with above average pre-earthquake eruption rates, so the sample size for this relationship is very small.

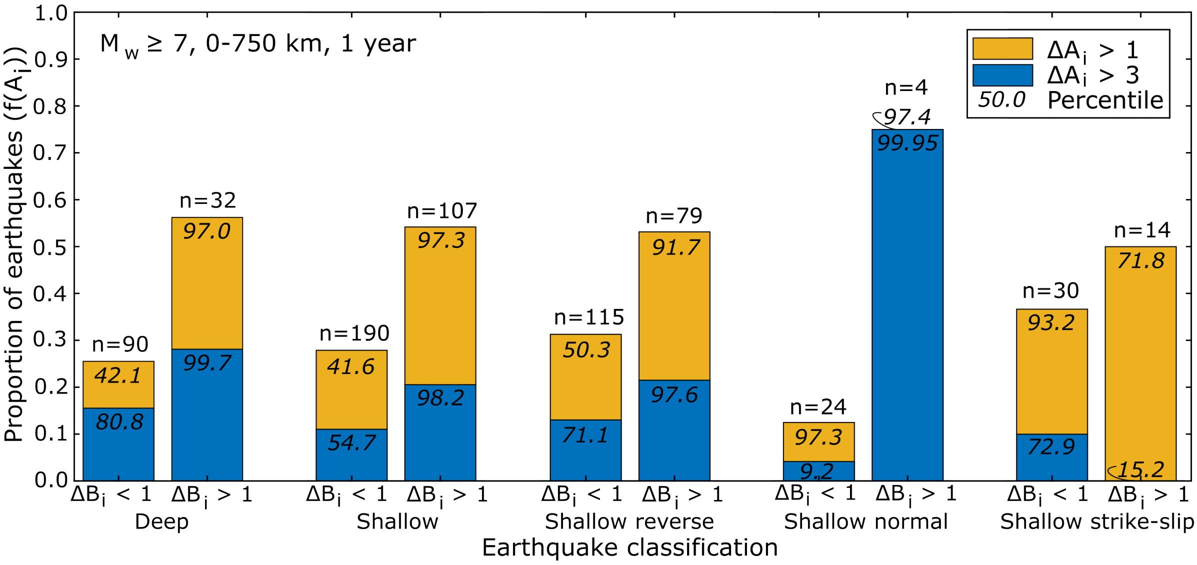

Figure 4.14: Proportion of $M_w \geq 7$ earthquakes that have post-earthquake relative eruption rates of >1 and >3 within 750 km and 1 year, as a function of both their class and pre-earthquake relative eruption rates within 750 km and 1 year. Note that the proportion of earthquakes with $\Delta A_i > 1$ also includes all the earthquakes with $\Delta A_i > 3$. The numbers in italics give the percentile scores relative to the simulated proportions of earthquakes with relative eruption rates exceeding the threshold values, using random permutation of the observed eruption dates. n gives the number of earthquakes in each class. Only earthquakes which occur within 750 km of an active volcano (i.e. μ_i and/or B_i and/or $A_i > 0$) are included in this analysis.

Figure 4.15 compares the pre-earthquake and post-earthquake eruption rates within 750 km and 1 year for each individual earthquakes. As with Figure 4.13 and Figure 4.14, Figure 4.15 shows that earthquakes with above average pre-earthquake eruption rates more often have above average post-earthquake eruption rates. However, Figure 4.15 also shows that, when both pre-earthquake and post-earthquake eruption rates are above average, the post-earthquake eruption rates tend to exceed the pre-earthquake eruption rates. Specifically, there are 20 earthquakes with above average post-earthquake eruption rates exceeding their above average pre-earthquake eruption rates, while there are only 12 earthquakes with above average pre-earthquake eruption rates exceeding their above average post-earthquake eruption rates. The same is true across all eruption rates; there are 105 earthquakes where the post-earthquake eruption rate exceeds the pre-earthquake eruption rate, while there are 81 earthquakes where the pre-earthquake eruption rate exceeds the post-earthquake eruption rate.

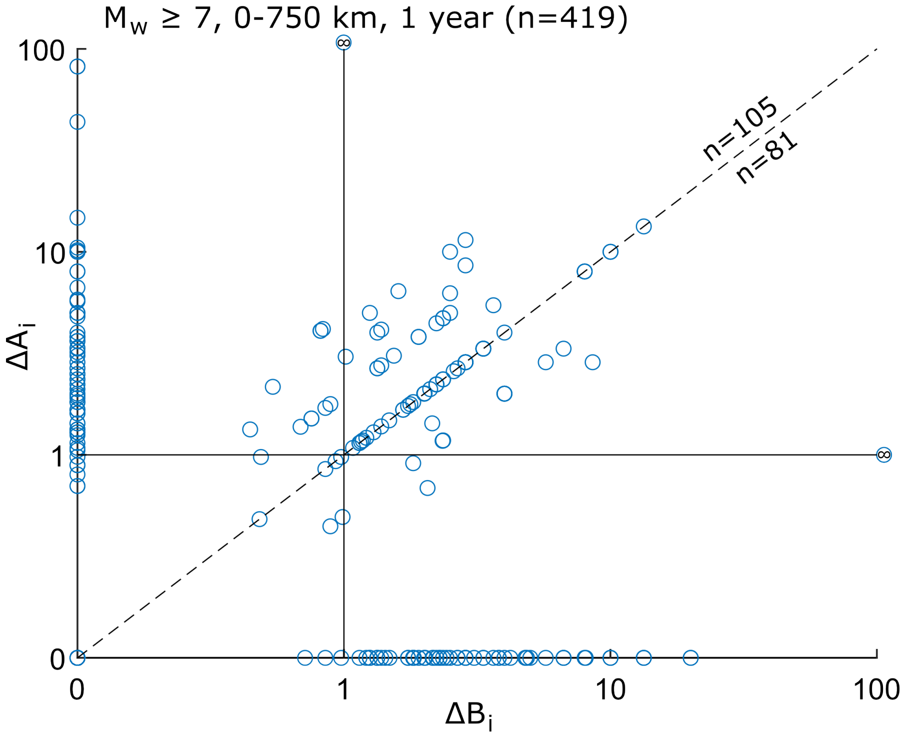

Figure 4.15: Observed VEI ≥ 2 pre-earthquake eruption rates compared with observed VEI ≥ 2 post-earthquake eruption rates, both within 750 km and 1 year of each individual $M_w \geq 7$ earthquake. The solid black lines divide areas of above average and below average eruption rates. Above the dashed black line, post-earthquake eruption rates are greater than pre-earthquake eruption rates; below the dashed black line, pre-earthquake eruption rates are greater than post-earthquake eruption rates. Only earthquakes which occur within 750 km of an active volcano (i.e. μ_i and/or B_i and/or $A_i > 0$) are included in this analysis (419 earthquakes in total, including 1 earthquake with $M_i = 0$, $B_i = 1$, and $B_i = \infty$, and 1 earthquake with $M_i = 0$, $A_i = 1$, and $A_i = \infty$). This includes repeat eruptions from a single volcano but excludes eruptions with an uncertain start date. No foreshock or aftershock filtering is applied.

To allow more direct comparison with previous eruption triggering studies (Nishimura 2017, Sawi & Manga 2018, Jenkins, Biggs, Rust & Rougier 2021), we also compare combined post-earthquake eruption rates (ΔA) with combined pre-earthquake eruption rates (ΔB) calculated over the same timescale. Figure 4.16 shows that, within 750 km and up to 5 years of $M_w \geq 7$ earthquakes, the post-earthquake eruption rates relative to pre-earthquake eruption rates show similar values to the post-earthquake eruption rates relative to average eruption rates (Figure 4.2). In particular, post-earthquake eruption rates are 1.28 times the pre-earthquake eruption rates within 750 km and 1 year, with a percentile score of 98% relative to simulations with randomly permutated eruption dates. For comparison, post-earthquake eruption rates are 1.27 times the average eruption rate within 750 km and 1 year, with a percentile score of 99%. Overall, comparing post-earthquake and pre-earthquake eruption rates (Figures 4.13-4.16) therefore shows that earthquakes with above average pre-earthquake eruption rates more often display above average post-earthquake eruption rates, and post-earthquake eruption rates are relatively greater than pre-earthquake eruption rates.

4.4.5.3 Global distribution of eruption rates

The eruption rates for each individual earthquake can also be used to investigate whether there are any spatial patterns in the eruption rates associated with earthquakes. Figure 4.17a shows the global distribution of eruption rates within 750 km and 1 year following $M_w \geq 7$ earthquakes, while Figure 4.17b shows the global distribution of eruption rates within 750 km and 182 days before $M_w \geq 7$ earthquakes. It is noticeable that earthquakes which occur near eruptions are restricted to subduction zones. Although it is difficult to identify any spatial patterns in the eruption rates, the similarity between Figure 4.17a and Figure 4.17b further highlights how post-earthquake and pre-earthquake eruption rates are correlated.

4.5 Discussion

4.5.1 Comparison with previous studies

Figure 4.2 and Figure 4.3 show that volcanic eruption rates deviate significantly from average eruption rates within 750 km of earthquakes with a minimum M_w of 7. This consists primarily of post-earthquake eruption rates that are around 1.25 times the average eruption rate over timescales of at least 1 year, and possibly to a lesser extent over 2 to 4 years, mainly following M_w 7 earthquakes. We also identify pre-earthquake eruption rates that are around 0.9 times the average eruption rate over timescales of at least 182 days, and possibly to a lesser extent over 1 year, mainly before $M_w \geq$

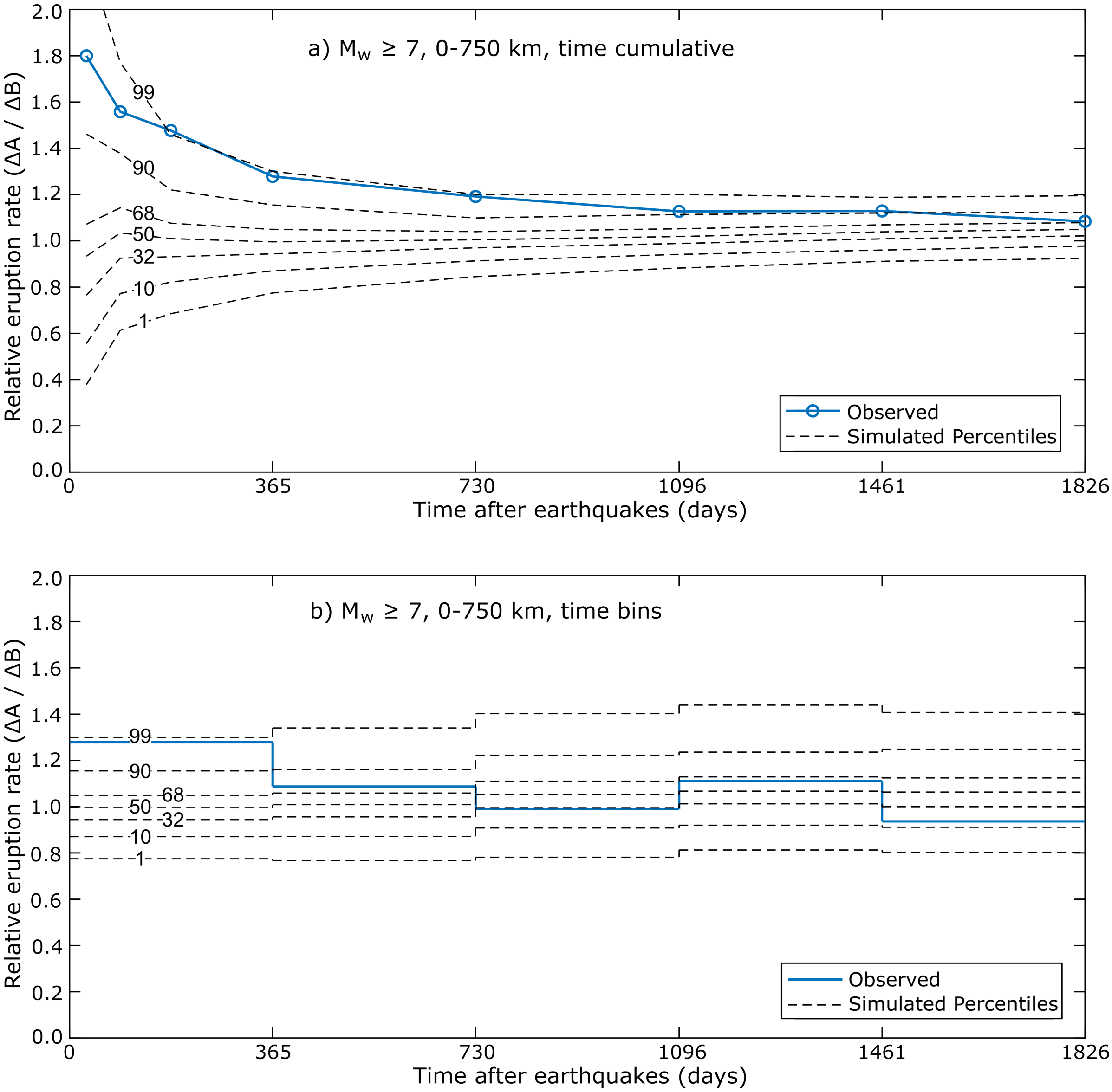

Figure 4.16: Combined VEI ≥ 2 post-earthquake eruption rates within 750 km and up to 5 years after $M_w \geq 7$ earthquakes, relative to combined pre-earthquake eruption rates calculated over the same distance and timescale. This includes repeat eruptions from a single volcano but excludes eruptions with an uncertain start date. No foreshock or aftershock filtering is applied. The percentiles of simulated eruption rates calculated using random permutation of the observed eruption dates are also shown. a) Relative eruption rates over cumulative timescales. b) Relative eruption rates over yearly binned timescales.

a) $M_w \geq 7$, 0-750 km, 182 days (time cumulative)

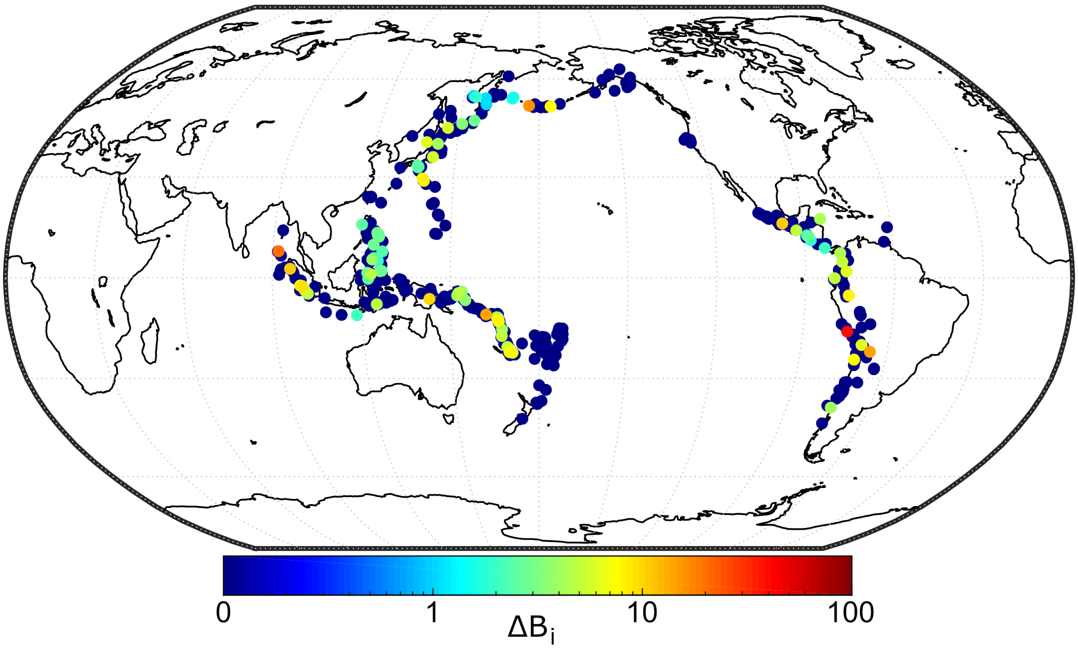

b) $M_w \geq 7$, 0-750 km, 1 year (time cumulative)

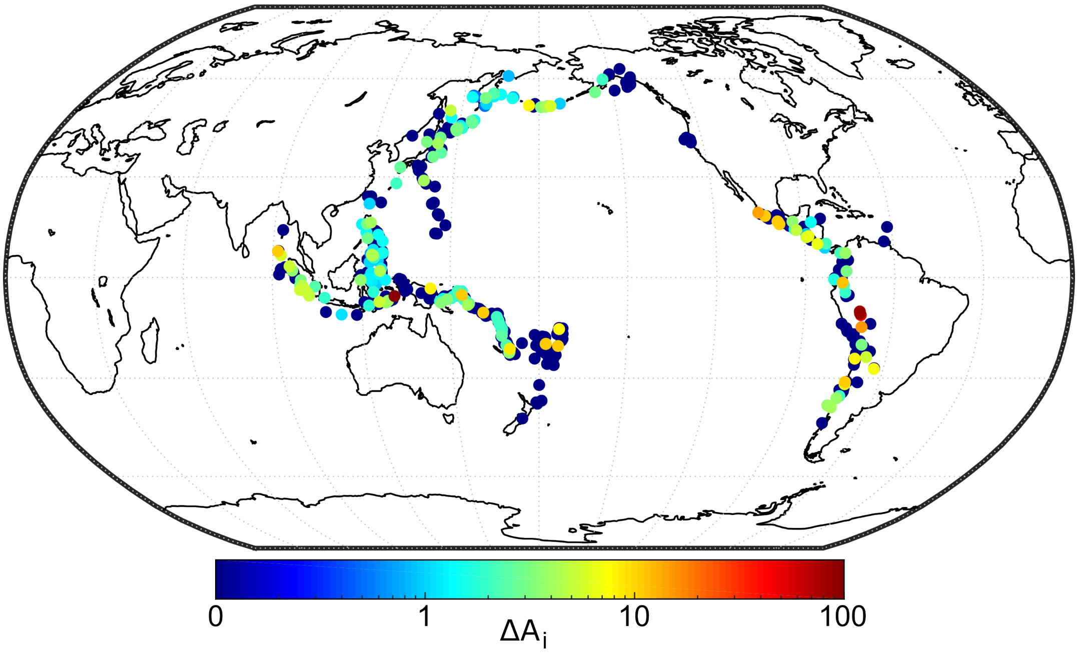

Figure 4.17: Spatial distribution of observed VEI ≥ 2 eruption rates within 750 km of $M_w \geq 7$ earthquakes for each individual earthquake. a) Pre-earthquake relative eruption rates within 182 days and b) Post-eruption relative eruption rates within 1 year. This includes repeat eruptions from a single volcano but excludes eruptions with an uncertain start date. No foreshock or aftershock filtering is applied. Only earthquakes which occur within 750 km of an active volcano (i.e. μ_i and/or B_i and/or $A_i > 0$) are shown. Note that the earthquakes are plotted in order from lowest to greatest relative eruption rate.

8 earthquakes and possibly also before M_w 7 earthquakes. Our study is the first to quantify borderline statistically significant below average pre-earthquake eruption rates, although this phenomenon was first proposed by Carr (1977). By contrast, Lemarchand & Grasso (2007) suggested that eruption rates increase during the 6 to 10 days both before and after earthquakes, within a distance of up to 10 times the earthquake rupture length. However, Lemarchand & Grasso (2007) used a minimum earthquake magnitude of 4.8, which is far smaller than our minimum M_w of 6. Therefore, the small earthquakes included by Lemarchand & Grasso (2007) may likely represent volcanotectonic events, for which a short-term correlation between earthquakes and eruptions is expected. For larger earthquakes, quantifying relative eruption rates over short timescales is challenging due to the small sample sizes available in the current modern global records (Figure 4.3 and Table 4.4). However, we do find some preliminary evidence for short-term (30 to 182 days) increases in eruption rates following nearby large earthquakes (Figure 4.2).

Compared with recent global statistical studies on eruption triggering, our post-earthquake eruption rates of around 1.25 times the average eruption rates (i.e. 25% above the average eruption rate) are greater than the approximately 10% increase found by Sawi & Manga (2018) but lower than the 50% increase suggested by Nishimura (2017). However, the parameter ranges investigated by Sawi & Manga (2018) and Nishimura (2017) are more restricted than we present here. Using our methodology and datasets but with the parameters investigated by Sawi & Manga (2018) (minimum M_w of 6, maximum distance between earthquakes and eruptions of 800 km, and timescales of 2 months and 2 years), we find that post-earthquake eruption rates are 6-7% above average. This is consistent with the 5-12% increase in eruption rates reported by Sawi & Manga (2018). However, when comparing post-earthquake and pre-earthquake eruption rates using the parameters used by Sawi & Manga (2018), we find eruption rate increases of only 3-4%.

Using our methodology and datasets but with the parameters reported by Nishimura (2017) (minimum M_w of 7.5, maximum distance between earthquakes and eruptions of 200 km, and a timescale of 5 years), we find that post-earthquake eruption rates are 23% below average. We also find that post-earthquake eruption rates decrease by 4% relative to pre-earthquake eruption rates over the same distance and timescale. These values differ vastly from the 50% increase in post-earthquake eruption rates reported by Nishimura (2017). Manual inspection of our results reveals that this discrepancy is primarily caused by differences in the earthquake locations used by up to half a degree of latitude and longitude; we obtain these values from the earthquake centroid location, whereas Nishimura (2017) used the earthquake epicentre location. For a small distance of 200 km from each earthquake, these variations of several tens of kilometers significantly alter which eruptions are associated with each earthquake.

Overall, we do not disagree with the findings of Nishimura (2017) and Sawi & Manga (2018), although our results argue for post-earthquake eruption rates intermediate between those reported by Nishimura (2017) and Sawi & Manga (2018). However, by only investigating a small parameter range, Nishimura (2017) and Sawi & Manga (2018) were not able to fully characterise the effects that large earthquakes have on volcanic eruption rates. In particular, we show that the calculated eruption rates can differ significantly as a function of the earthquake magnitudes, distances, and timescales considered (Figure 4.3). The vast difference between our results and those of Nishimura (2017), caused by using slightly different reported earthquake locations, also illustrates this point well and shows the importance of considering the whole parameter space.

4.5.2 Effects of different parameters

4.5.2.1 M_w, distance, and timescale

Given the differences in the calculated eruption rates across the studied parameters, we now consider how the eruption rates associated with earthquakes depend on these parameters. If eruption rates show expected behaviours based on physical principles, this would increase our confidence that the relationships we report do not simply occur by chance. For example, greater deviations from average eruption rates are expected for larger earthquake magnitudes and smaller distances from earthquakes. Figure 4.3 shows that post-earthquake eruption rates deviate significantly from average eruption rates within 750 km and several years of M_w 7 earthquakes, whereas post-earthquake eruption rates following M_w 6 earthquakes do not show significant deviations from average eruption rates. However, post-earthquake eruption rates following $M_w \geq 8$ earthquakes do not show significant deviations from average eruption rates. The lack of consistently above average post-earthquake eruption rates following $M_w \geq 8$ earthquakes therefore decreases our confidence in the above average post-earthquake eruption rates following M_w 7 earthquakes, although the low number of $M_w \geq 8$ earthquakes in our record (27) could explain this as statistical analyses on smaller sample sizes are limited (Table 4.4). Additionally, $M_w \geq 8$ earthquakes do exhibit consistently below average pre-earthquake eruption rates, suggesting that a relationship between the largest earthquakes and eruption rates does exist.

Above average post-earthquake eruption rates associated primarily with M_w 7 earthquakes are observed for all distances up to 750 km but not beyond 750 km (Figure 4.3). Similarly, below average pre-earthquake eruption rates associated mainly with $M_w \geq 8$ earthquakes are observed up to 500 km, and possibly up to 750 km, but not beyond 750 km (Figure 4.3). A limit to the distance over which significant deviations from background eruption rates occur is expected from physical principles, and our study suggests that this limit occurs at around 750 km. However, we note that the above average post-earthquake eruption rates following M_w 7 earthquakes do not show any clear relationship with distance up to 750 km; the relative eruption rates following M_w 7 earthquakes are generally greatest at 0-250 km, but the relative eruption rates at 500-750 km are generally both greater and more significant than those at 250-500 km. By contrast, the below average pre-earthquake eruption rates before $M_w \geq 8$ earthquakes do progressively weaken with increasing distance.

In general, deviations from average eruption rates are expected to decrease as the timescale between earthquakes and eruptions increases. However, the timescales over which eruptions initiate are also important and likely variable (Chamberlain et al. 2014, Kilgour et al. 2014, Metcalfe et al. 2021), while earthquake-related processes such as afterslip and visco-elastic relaxation can produce effects over timescales far longer than the actual seismic rupture (Copley 2014, Wang et al. 2012). Nonetheless, Figure 4.2 shows that, within 750 km of $M_w \geq 7$ earthquakes, pre-earthquake eruption rates are below average over timescales of 30 to 182 days, while post-earthquake eruption rates progressively decay from a high of 1.64 times the average eruption rate within 30 days to 1.12 times the average eruption rate within 5 years. This is consistent with the greatest deviations from average eruption rates occurring within the shortest timescale of earthquakes. However, we note that similar patterns are not observed across all distances and magnitudes (Figure 4.3). Furthermore, the low numbers of eruptions associated with earthquakes at shorter timescales (Table 4.4) makes it relatively easier to generate large deviations from the average eruption rate by chance. This explains why large deviations from the average eruption rate at short timescales do not always correspond to significant percentile scores relative to the random simulations.

4.5.2.2 Earthquake depth and slip orientation

Figure 4.4 shows that earthquake depth exerts a very strong control on eruption rates associated with earthquakes, with deep earthquakes (≥70 km) displaying greater deviations from average eruption rates than shallow earthquakes. This is the case for both the above average post-earthquake eruption rates and especially for the below average pre-earthquake eruption rates. The reasons for this are unclear, although we note that these deep earthquakes mainly occur within subducted slabs. Therefore, there appears to be some link between deep subduction earthquakes and subduction zone magmatism; this could relate to the location of deep earthquakes, which may lie underneath the volcanic arc, or deep subduction earthquakes may be more directly related to magma genesis at subduction zones, which occurs due to the release of fluids from the subducted slab into the mantle wedge (Tatsumi 1989) (Figure 4.18).

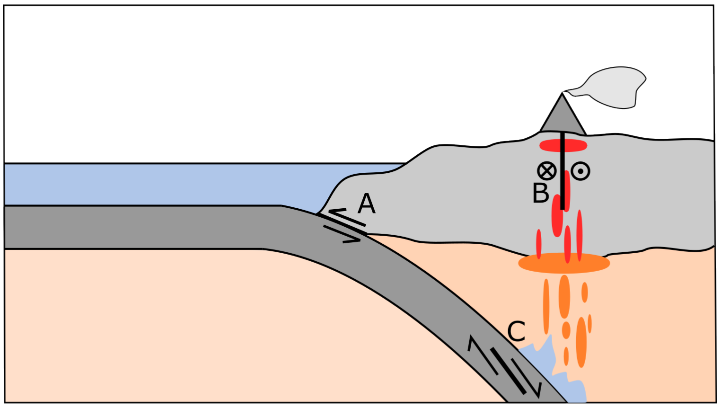

Figure 4.18: Schematic representation of the locations of earthquakes with different depths and slip orientations within subduction zones. For example, A represents shallow megathrust earthquakes at the plate interface, B shows earthquakes within volcanic arcs, such as along major arc-parallel strike-slip faults, while C shows deep slab earthquakes, which often have normal or strike-slip focal mechanisms. These earthquake distributions may provide clues regarding the distinct relative eruption rates associated with different earthquakes.

Likewise, Figure 4.6 hints at a potential relationship between the slip orientation of shallow earthquakes and the eruption rates associated with earthquakes. Overall, Figure 4.6 shows that post-earthquake eruption rates are generally greater than pre-earthquake eruption rates for earthquakes of all slip orientations. However, it is noticeable that eruption rates are generally above average within several years of shallow reverse earthquakes and generally below average within several years of shallow normal earthquakes. Only shallow strike-slip earthquakes show the below average pre-earthquake eruption rates and above average post-earthquake eruption rates displayed by considering all earthquakes (Figure 4.2). As all of the $M_w \geq 7$ earthquakes that occurred near active volcanoes between 1976-2020 were located in subduction zones (Figure 4.17), there appears to be some relationship between the local to regional tectonic setting (within the broader subduction zone environment) and the eruption rates associated with large earthquakes (Figure 4.18). The reasons for this are again unclear, although it could relate how the crustal stress field evolves over the seismotectonic cycle in different tectonic stress regimes.

4.5.2.3 Pre-earthquake eruption rate

Figures 4.13-4.16 show that pre-earthquake eruption rates are also a very strong control on the post-earthquake eruption rates following large earthquakes. Specifically, the above average post-earthquake eruption rates are more statistically significant when pre-earthquake eruption rates are also above average. The reasons for this are again unclear; however, this suggests that volcanoes that have recently erupted, or are close to other volcanoes that have recently erupted, are more easily affected by nearby large earthquakes. This implies that many eruptions do not completely release the built up magmatic pressures, either at the individual volcano or across the volcanic region more generally, so that earthquakes which occur during times of high volcanic activity coincide with more volcanoes in near critical states.

4.5.3 Implications

Assuming a causative relationship between earthquakes and the observed deviations from average eruption rates, we find that $M_w \geq 7$ earthquakes promote eruptions at volcanoes up to 750 km away within the following year to several years, while eruptions are also inhibited for several months within 750 km before $M_w \geq 7$ earthquakes. Consequently, at the regional scale, below average volcanic eruption rates correspond to an increased likelihood of a large earthquake occurring, while a large earthquake increases the likelihood of volcanic eruptions, especially when the pre-earthquake eruption rates are already high. However, the scope for using these observations predictively is limited. For context, our finding that volcanic eruption rates are 1.27 times the average eruption rate within 750 km and 1 year of $M_w \geq 7$ earthquakes corresponds to 248 observed eruptions between 1976 and 2020 compared to an average eruption rate of only 195 eruptions (Supplementary Material 2). Expressed differently, there were 53 extra or 'triggered' VEI ≥ 2 eruptions within 750 km and 1 year of $M_w \geq 7$ earthquakes between 1976 and 2020. Given that there were 526 $M_w \geq 7$ earthquakes over this period, of which 419 occurred within 750 km of an active volcano, this corresponds to an extra 0.13 eruptions within 1 year following each M_w 7 earthquake. Therefore, on average, around 1 in 8 $M_w \geq 7$ earthquakes that occur near active volcanoes will promote an eruption within 750 km and 1 year. As around 10 $M_w \geq 7$ earthquakes occur near active volcanoes annually at the global scale, on average there will be 1 or 2 eruptions promoted by earthquakes each year, compared with annual global VEI ≥ 2 eruption rates of 20-40.

The fact that earthquakes with different slip orientations affect eruption rates differently presents an opportunity to better our understanding of tectono-magmatic interactions. This also applies to the importance of deep earthquakes, while the complex spatiotemporal relationships between earthquakes and eruptions in general also requires further study. For example, at the global scale, there is a positive correlation between large earthquakes and volcanic eruption rates, as shown by Jenkins, Biggs, Rust & Rougier (2021) and illustrated here by how simulations with completely random eruption dates and simulations with randomly permutated eruption dates generate different percentile scores (Figure 4.8). By contrast, at the local to regional scale (<750 km), there are generally fewer eruptions before large earthquakes and more eruptions following large earthquakes (Figure 4.2).

4.6 Conclusions

Overall, we find that $M_w \geq 7$ earthquakes are associated with post-earthquake eruption rates of around 1.25 times the average eruption rate within 750 km and 1 year, as well as pre-earthquake eruption rates of around 0.9 times the average eruption rate within 750 km and half a year (Figure 4.2a). Randomised simulations show that the probability of the observed above average post-earthquake eruption rates occurring by chance is very low (<1%), while the probability of the below average pre-earthquake eruptions rates occurring by chance is also low (<10%). Post-earthquake eruption rates may also remain above average for 2 to 4 years following earthquakes, while pre-earthquake eruption rates may be below average for up to 1 year before earthquakes, although these deviations are less significant (Figure 4.2b). However, we note that eruption rates can vary significantly as a function of the earthquake magnitudes, distances and timescales considered (Figure 4.2). Additionally, determining eruption rates over shorter timescales relative to earthquakes is challenging, although we do find some preliminary evidence for above average post-earthquake eruption rates within 30 to 91 days (Figure 4.2a).

By assuming a causative relationship between earthquakes and the observed deviations from average eruption rates, we conclude that large earthquakes promote eruptions at nearby volcanoes, while eruptions also appear to be inhibited shortly before nearby large earthquakes. However, this general observation may not apply to individual earthquakes, as we find that deep earthquakes more strongly affect eruption rates than shallow earthquakes, while earthquakes with different slip orientations affect eruption rates differently. Further study of these relationships represents a good opportunity to further our understanding of tectono-magmatic processes. Similarly, reliable and modern earthquake and eruption records gathered over the coming decades will help to clarify the statistical relationships described here, especially where the sample sizes are currently low, such as for $M_w \geq 8$ earthquakes and short (<1 year) timescales. This is particularly important for the volcanic record, where increased remote sensing will provide more complete eruption records and also enable investigation of the potential links between earthquakes and non-eruptive volcanic phenomena (e.g. Takada & Fukushima 2013, Hill-Butler et al. 2020).

CHAPTER 5

A SYSTEMATIC APPROACH TO MAPPING REGIMES OF EARTHQUAKE-INDUCED STATIC STRESS CHANGES ACTING ON MAGMATIC PATHWAYS

Large earthquakes alter the crustal stress field across great distances (hundreds to thousands of kilometers) over geologically short timescales (seconds to years). These stress changes can affect magmatic systems, triggering (or suppressing) volcanic unrest and eruption, along with other deeper processes. We use simple kinematic source models in an isotropic elastic half-space to assess earthquake-induced static stress changes (>1 kPa) over the entire thickness of the lithosphere and consider the implications for magma ascent and storage. Modelling subduction zone earthquakes, we calculate static normal stress changes with depth on three mutually-perpendicular end-member magma pathways: vertical arc-parallel, vertical arc-perpendicular, and horizontal. From this, we define seven stress change regimes within the adjacent volcanic arc. Three of these regimes may strongly encourage magma ascent in dykes by inducing unclamping (decreased compressive normal stress) of vertical pathways which increases in magnitude towards the surface and clamping of horizontal pathways. Two of the regimes may encourage stalling and storage of magma in sills near the base of the crust by inducing unclamping of horizontal pathways at depth. The spatial distribution of the regimes is largely dependent on earthquake magnitude, but also varies with slip distribution and interface dip. We show how the responses of magmatic systems to earthquakes also depends on the stress change magnitude and the state of the magmatic system, with a greater impact expected for larger stress changes acting on weaker, more thermally mature systems.

This chapter is previously published as (Jenkins, Biggs, Rust & Jara 2021). See the note on previous publications for more detail (Page xvii).

5.1 Introduction

5.1.1 The crustal stress field

Rapid magma transfer through the Earth's crust occurs by flow in self-propagating sheet intrusions such as dykes (Clemens & Mawer 1992, Petford et al. 1993, Rubin 1995, Petford et al. 2000, Ruprecht & Plank 2013). Magmatic intrusions are generally mode I fractures and so preferentially open parallel to the minimum principal stress direction (σ_3), although they may be influenced by structures or weaknesses in the host rock such as faults, fractures, or layering (Anderson 1951, Nakamura 1977, Ziv et al. 2000, Gudmundsson 2002, 2020, Magee et al. 2013, Rivalta et al. 2015, Drymoni et al. 2020). At the regional level, crustal stress and structure is primarily controlled by plate tectonics (Zoback et al. 1989, Zoback 1992, Kearey et al. 2009). However, measurement of the present-day crustal stress field provides abundant evidence for spatiotemporal variations unrelated to plate motions (Heidbach et al. 2018). These variations, caused by factors such as topography, recent earthquakes, and crustal heterogeneities (e.g. layering, structure, previous magmatic activity) can have important implications for magmatic systems (e.g. Pinel & Jaupart 2005, Maccaferri et al. 2014, Lupi et al. 2020, Gudmundsson 2011, Cembrano & Lara 2009).

We investigate the impact of large earthquakes on magmatism. Large earthquakes alter the crustal stress field over hundreds to thousands of kilometers at timescales from seconds or minutes due to the elastic response of the crust, to years or tens of years for deeper postseismic processes (Piersanti et al. 1995, Pollitz et al. 1998, Heidbach et al. 2018, Levandowski et al. 2018, Becker et al. 2018). Earthquake-driven stress changes can be substantial, such as the near-complete stress drop, or even reversal of the stress field, observed following the 2011 M_w 9.0 Tohoku megathrust earthquake (Hardebeck & Okada 2018). Numerical models of magmatic systems generally do not consider these stress changes, often assuming a lithostatic stress state or a constant tectonic stress such as extension in rifts or compression at subduction zones (e.g. Roman & Heron 2007, Maccaferri et al. 2010, Menand et al. 2010, Chaussard & Amelung 2014). However, the fast rates of magma transport (cm or m s^{-1}) relative to tectonic loading (cm yr^{-1}) may give magmatic systems some degree of independence from the tectonic setting (De Saint Blanquat et al. 2011), whereas earthquake-driven stress changes may occur over timescales more likely to influence magma transport.

Several studies have investigated the triggering of volcanic eruptions by earthquakes. Both dynamic stress changes (due to the passage of seismic waves: Linde & Sacks 1998, Hill et al. 2002, Manga & Brodsky 2006) and static stress changes (due to the elastic relaxation of the crust: Hill et al. 2002, Walter & Amelung 2007, Watt et al. 2009, Bonali et al. 2013, 2015, Nishimura 2017) have been postulated as causative mechanisms for eruption triggering. However, volcanic eruption is only one possible response of the magmatic system and changes induced by a large earthquake may not culminate in an eruption. Recent work has identified non-eruptive responses to large earthquakes, including seismicity and surface deformation (De la Cruz-Reyna et al. 2010, Pritchard et al. 2013, Takada & Fukushima 2013, Hill-Butler et al. 2020) and static stress changes have also been implicated in inhibiting eruption (Ebmeier et al. 2016). Further, volcanoes represent only the upper, most easily observable parts of the magmatic system. New views on the architecture of magma reservoirs envisage a transcrustal system containing variable melt fractions, extending from the surface to the magma source in the mantle (Cashman et al. 2017, Sparks et al. 2019). Therefore, we consider the potential effects of earthquake-driven stress changes across the entire crust. While dynamic stress changes may be important, particularly in the shallow, bubble-rich parts of the system, we consider only static stress changes.

5.1.2 3D static stress change

We model coseismic static stress changes caused by (mega)thrust earthquakes at subduction zones and consider how they will affect magma ascent and storage in the adjacent volcanic arc. Megathrust earthquakes are the most powerful on Earth, generating the largest stress changes, and have frequently been implicated in eruption triggering (e.g. Walter & Amelung 2007). In general, subduction interface earthquakes relax horizontal compressional stresses within the volcanic arc and so are expected to encourage magma ascent (Walter & Amelung 2007). Evidence for the relaxation of horizontal compressional stresses following subduction interface earthquakes was provided by the 2011 Tohoku earthquake, following which some aftershocks displayed unusual faulting types, including many normal faulting earthquakes in regions usually dominated by reverse faulting (Asano et al. 2011, Nettles et al. 2011, Hardebeck & Okada 2018). Geodetic observations also show the importance of static stress changes following subduction interface earthquakes, with static stress changes driving afterslip on the subduction interface generating post-seismic surface displacements (Wang et al. 2012, Bürgmann 2018, Churchill et al. 2022). However, static stress changes cannot explain the evolution of surface displacements with time, indicating that other stress transfer mechanisms such as viscous relaxation are also important (Sun & Wang 2015, Freed 2005).

Although static stress changes are small ($<\approx 1$ MPa: Stein 1999) compared to the theoretical strength of the crust ($\sigma_1 - \sigma_3$ = 10's-100's MPa: Byerlee 1978, Brace & Kohlstedt 1980), evidence from earthquake aftershocks and induced seismicity shows that these small stress changes are sufficient to trigger brittle failure (King et al. 1994, Stein 1999, Ellsworth 2013). This leads to the contention that much of the Earth's crust is in a critically stressed state, within around one earthquake stress drop of failure (typically 3-10 MPa: Kanamori & Anderson 1975, Townend & Zoback 2000, McGarr 2014, Sibson 2017). Therefore, magmatic systems likely also exist in a critically stressed state, at least transiently, whereby small stress changes may possibly lead to observable effects such as unrest or eruption. This critically stressed state is evidenced by the high number of actively deforming volcanoes (Biggs & Pritchard 2017), theoretical studies suggesting that only relatively small magma overpressures may be sustained before failure (Gudmundsson 2012), and evidence that even tidal stresses can affect how magmatic systems deform (Scholz et al. 2019).

Previous studies investigating static stress changes on volcanic systems calculated either the mean stress change on the inferred sub-volcanic magma chamber (Hill et al. 2002, Walter & Amelung 2007), or the normal stress change on the inferred volcanic conduit (Bonali et al. 2013). Nostro et al. (1998) considered how the shape and orientation of the magma plumbing system affects the calculated stress changes following nearby large normal faulting earthquakes. Building on these concepts, we present a method for assessing static stress changes to more fully capture their magnitude, orientation, and gradient with depth over the entire lithosphere. Modelling subduction zone earthquakes as rectangular uniform-slip dislocations in an homogenous elastic halfspace, we calculate static normal stress changes on three mutually-perpendicular end-member magma pathways: vertical arc-parallel and arc-perpendicular pathways (dykes) and horizontal pathways (sills), where ‘arc’ refers to the volcanic arc, which strikes parallel to subduction zone interface (Figure 5.1a). These pathways represent current or potential magma conduits, which may be influenced by existing crustal weaknesses such as faults, fractures, or layering. We use the normal stress changes on these pathways (clamping/ unclamping) as a proxy for the magma response. Analysing the normal stress changes as a function of depth, we define a set of stress change regimes produced by typical subduction interface earthquakes and map out their spatial distributions. These regimes simplify the otherwise complex stress field changes and facilitate interpretation and discussion of the potential implications for magma ascent and storage. The results presented here represent the first fully three-dimensional analysis of static stress changes from a magmatic perspective and are therefore necessarily simplified. Future work should build on this, most notably through the inclusion of layered models and explicit calculation of the magmatic response.

5.2 Background and theory

5.2.1 Dislocation theory

Slip during an earthquake changes the elastic strain and stress fields in the surrounding rock. We model this computationally using elastic dislocation theory, where a finite rectangular dislocation is embedded into an initially unstrained elastic halfspace. Slip across the dislocation generates a displacement field (u_{ij}) in the surrounding halfspace, the spatial derivatives of which give the elastic strain tensor field (ϵ_{ij})

$$\epsilon_{ij} = \frac{1}{2}\left(\frac{\delta u_i}{\delta x_j} + \frac{\delta u_j}{\delta x_i}\right) \quad , \tag{5.1}$$

where i and j correspond to the three mutually perpendicular axes x, y, and z, and contractional deformation causes negative strain. We define the y-axis as parallel to the strike of the subduction zone interface, the x-axis as horizontal and parallel to the dip direction of the subduction interface, and the z-axis as vertical (Figure 5.1a).

Considering a pure thrust earthquake along a shallowly dipping subduction interface, most slip will occur in the x-direction, with a small component of slip in the z-direction and no slip in the y-direction. Induced normal strains in the x-direction (ϵ_{xx}) will therefore generally be larger than normal strains in the z-direction (ϵ_{zz}), which will generally be larger than normal strains in the y-direction (ϵ_{yy}). As there is no slip in the y-direction, any displacements in the y-direction must be induced in response to displacements in the x- and z-directions.

5.2.2 Normal stress changes on end-member pathways

Hooke's Law in three dimensions states that the normal stress on a structure depends on both the strain normal to that structure and the volumetric strain

$$\Delta\sigma_{ij} = 2\mu\epsilon_{ij} + \lambda\epsilon_{kk}\delta_{ij} \quad , \tag{5.2}$$

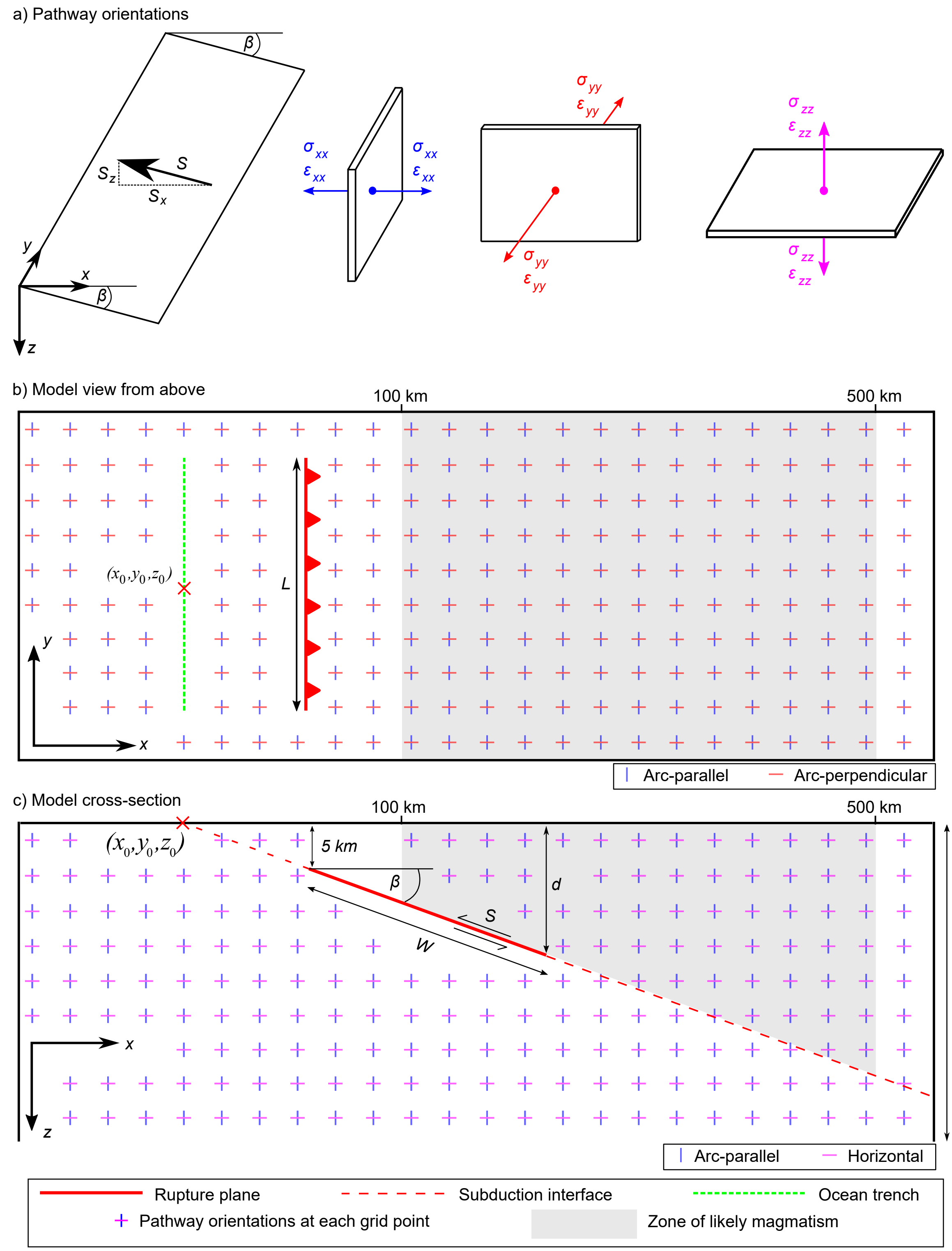
a) Pathway orientations
β
S
S_z
S_x
y
x
z
β
σ_{xx}
ε_{xx}
σ_{xx}
ε_{xx}
σ_{yy}
ε_{yy}
σ_{yy}
ε_{yy}
σ_{zz}
ε_{zz}
σ_{zz}
ε_{zz}
b) Model view from above
100 km
500 km
(x_0,y_0,z_0)
L
y
x
Arc-parallel
Arc-perpendicular
c) Model cross-section
100 km
500 km
(x_0,y_0,z_0)
5 km
β
d
S
W
x
z
100 km
Arc-parallel
Horizontal
Rupture plane
Subduction interface
Ocean trench
Pathway orientations at each grid point
Zone of likely magmatism

Figure 5.1: (Above) a) Orientation of the subduction interface and the end-member pathways within the defined coordinate system. β is the dip of the subduction interface, S shows the slip vector, with S_x and S_z the components of slip in the x- and z-directions respectively. The end-member pathways are: arc-parallel and vertical (blue), arc-perpendicular and vertical (red), and horizontal (pink). b) Plan and, c) cross-section views of the idealised model. L- rupture length, W- down-dip rupture width, S- slip magnitude, d- depth to bottom of rupture. The oceanic trench marks the intercept of the subduction interface with the model surface at $z = 0$. The portrayed grid spacing is not indicative of actual model grid size.

where σ_{ij} is the stress tensor, μ is the shear modulus, λ is Lamé's first parameter, δ_{ij} is the Kronecker delta, and ϵ_{kk} is the induced volumetric strain. The normal stress changes acting on arc-parallel ($\Delta\sigma_{xx}$), arc-perpendicular ($\Delta\sigma_{yy}$), and horizontal ($\Delta\sigma_{zz}$) pathways (Figure 5.1a) are therefore given by

$$\Delta\sigma_{xx} = 2\mu\epsilon_{xx} + \lambda(\epsilon_{xx} + \epsilon_{yy} + \epsilon_{zz}) \tag{5.3}$$

$$\Delta\sigma_{yy} = 2\mu\epsilon_{yy} + \lambda(\epsilon_{xx} + \epsilon_{yy} + \epsilon_{zz}) \tag{5.4}$$

$$\Delta\sigma_{zz} = 2\mu\epsilon_{zz} + \lambda(\epsilon_{xx} + \epsilon_{yy} + \epsilon_{zz}) \quad , \tag{5.5}$$

where $\epsilon_{xx} + \epsilon_{yy} + \epsilon_{zz}$ is the induced volumetric strain, tensile stresses are positive, and

$$\mu = \frac{E}{2(1+\nu)} \tag{5.6}$$

$$\lambda = \frac{E\nu}{(1+\nu)(1-2\nu)} \quad , \tag{5.7}$$

where E is the Young's modulus and ν is Poisson's ratio. The mean stress change ($\Delta\sigma_{kk}$) is given by the mean of the normal stress changes on the three end-member pathways

$$\Delta\sigma_{kk} = \frac{\Delta\sigma_{xx} + \Delta\sigma_{yy} + \Delta\sigma_{zz}}{3} \quad . \tag{5.8}$$

The normal stress changes on the end-member pathways (hereafter 'stress changes') are not independent of one another as they all depend on the volumetric strain. The importance of the induced volumetric strain depends on Poisson's ratio; the greater Poisson's ratio, the larger λ becomes relative to μ and therefore the volumetric strain contribution becomes larger.

5.2.3 Clamping and unclamping of pathways

Magma pathways exhibit many forms and geometries and can be modelled using a variety of methods (Dahm 2000, Taisne & Jaupart 2009, Rivalta et al. 2015). The expansion and propagation of intrusions is driven by magma overpressure (P_o), which is controlled by magma buoyancy, the host rock stress acting normal to the intrusion (σ_n), and, if the pathway is connected to the magma source, the excess pressure in the source region (P_e) (Gudmundsson 2012). Earthquakes potentially alter all three of these factors, however, we model only changes to the normal stress ($\Delta\sigma_n$) on the basis that $\Delta\sigma_n$ is generally much larger than changes to magma buoyancy and P_e for the following two reasons. Firstly, magma buoyancy will only change significantly if the earthquake induces volatile exsolution. Secondly, P_e is only a factor if the magma pathway is connected to the magma source region, in which case the source region will likely be located deeper and further from the earthquake and so will experience smaller stress changes. Furthermore, any stress changes acting on the magma source region will be opposed by changes to the internal magma pressure governed by the magma compressibility, suppressing changes to P_e (Albino et al. 2010). We therefore make the simplifying assumption that changes to the magma overpressure caused by an earthquake (ΔP_o) depend only on $\Delta\sigma_n$.

At the walls of an intrusion, the overpressure, P_o, acts outwards against σ_n in the host rock. We use the term 'clamping' (e.g. Freed 2005, Bonali et al. 2015, Bonini 2019) to refer to an increase in the compressive normal stress on a pathway caused by an earthquake ($\Delta\sigma_n$ is negative for clamping as tensile stresses are positive). For a magmatic pathway, clamping will decrease magma overpressure (ΔP_o is negative). Conversely, the term 'unclamping' refers to a decreasing compressive normal stress on a pathway (positive $\Delta\sigma_n$), which increases P_o (positive ΔP_o). In our model, the vertical arc-parallel and arc-perpendicular pathways represent potential pathways for dykes, generally favouring upward magma transport (Rubin 1995). Conversely, horizontal pathways represent potential pathways for sills and favour magma storage (Menand 2008, Canales et al. 2009, Gudmundsson 2011, 2012, Jaxybulatov et al. 2014). We use $\Delta\sigma_n$ on these pathways as a proxy for the magmatic response and present six mechanisms showing how clamping and unclamping may impact the end-member pathways (Figure 5.2).

Clamping of pathways decreases P_o, effectively acting as a stress barrier to magma transport. This inhibits intrusion propagation and decreases intrusion thickness and therefore magma flow rate (Gudmundsson 1986, 2020). However, clamping of existing

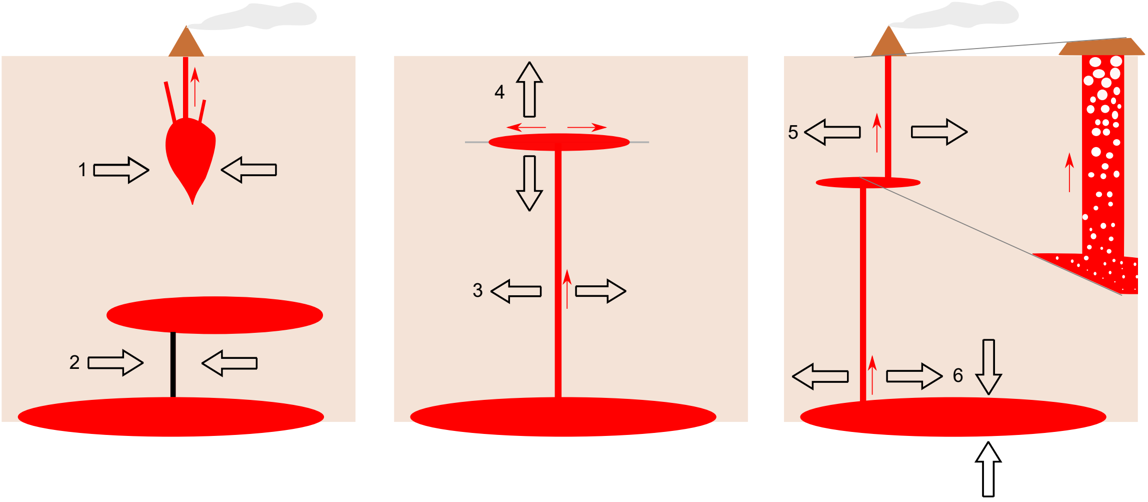

Figure 5.2: Simplified, not-to-scale diagram showing the mechanisms for static normal stress changes affecting planar magma bodies. (1) Clamping expels magma upwards from existing intrusions whilst (2) impeding magma from entering new or existing pathways. (3) Unclamping of vertical pathways encourages magma ascent in dykes, while (4) unclamping of horizontal pathways favours magma storage in sills. (5) Unclamping or volumetric expansion at shallow depths may encourage volatile exsolution and increase magma buoyancy. (6) Intersections of clamped horizontal magma reservoirs with unclamped vertical pathways may be especially favourable for upwards magma transport.

vertical intrusions may initially cause some magma ascent if the intrusion is connected to shallower parts of the system. This is because narrowing of the intrusion will be opposed by an increase in the internal magma pressure, which may subsequently dissapate by magma flow up and out of the intrusion (Figure 5.2, mechanism 1: Rikitake & Sato 1989, Feuillet et al. 2011). However, clamping of vertical pathways is generally expected to discourage magma ascent in dykes (Figure 5.2, mechanism 2), while clamping of horizontal pathways (increasing compressive vertical stress) is expected to discourage magma storage by inhibiting sill formation.

Conversely, unclamping of pathways increases P_o, favouring intrusion propagation and causing intrusion opening thickness to increase. Unclamping of vertical pathways therefore favours magma ascent in dykes, perhaps especially so when the magnitude of unclamping increases towards shallower depths as this generates a favourable pressure gradient for magma ascent (Figure 5.2, mechanism 3: Nostro et al. 1998, Hill et al. 2002, Bonali et al. 2013, Dahm 2000). Unclamping of horizontal pathways (decreasing compressive vertical stress) favours magma storage in sills. Unclamping of horizontal pathways also encourages dyke deflection into sills, as the decreased vertical stress makes it easier for the tensile stress ahead of a propagating dyke tip to open up mechanically weak horizontal structures such as layering (Figure 5.2, mechanism 4: Gudmundsson 2011). However, unclamping of sills increases P_o which may lead to failure of the sill walls. Depending on the local stress field, dyke injection upon failure is possible which will lead to magma ascent, although injection of further sills and growth of the magma storage zone may occur instead (Grosfils 2007, Albino et al. 2010).

At shallower depths, unclamping of intrusions (or expansion in σ_{kk}) may trigger volatile exsolution and thereby decrease the density of the magma, favouring magma ascent due to buoyancy (Figure 5.2, mechanism 5: Hill et al. 2002, Walter & Amelung 2007). Intersections between intrusions may also be important. Clamping of sill-like (horizontal) magma reservoirs may encourage flow of magma out of those reservoirs, potentially upwards into intersecting unclamped vertical intrusions, greatly favouring magma ascent (Figure 5.2, mechanism 6). Considering these six mechanisms, we suggest that, in general, magma ascent is favoured by clamping of horizontal pathways and unclamping of vertical pathways, while magma stalling and storage is favoured by clamping of vertical pathways and unclamping of horizontal pathways. However, it should be noted that, while these mechanisms are plausible and intuitive, observational evidence of their operation is currently unclear.

The response of the magmatic system depends on both the static stress change and the background stress field. Subduction zone interface earthquakes relax compressional stresses accumulated perpendicular to the plate boundary. Unclamping of arc-parallel pathways is therefore expected to be the main response, which will favour magma ascent, but the previously uninvestigated stress changes on arc-perpendicular and horizontal pathways may also be important. Coseismic unclamping has previously been invoked to explain magmatism occurring along arc-parallel structures that are unfavourably orientated within a compressive stress field with σ_1 perpendicular to the plate boundary (Sepúlveda et al. 2005, Lara et al. 2006, Walter & Amelung 2007, Mpodozis & Cornejo 2012, Bonali et al. 2013, Lupi & Miller 2014, Acocella 2014, Acocella et al. 2018).

5.3 Model setup

5.3.1 Earthquake ruptures

We use Coulomb 3 to calculate static stress changes caused by earthquake ruptures in an isotropic elastic halfspace (Lin & Stein 2004, Toda et al. 2005). Coulomb 3 uses the equations of Okada (1992) to calculate the displacement field surrounding a finite rectangular dislocation, from which the stress change tensor field is calculated using Hooke's Law. We model subduction interface earthquakes: thrust earthquakes that occur along the seismogenic boundary between the subducting slab and the overriding continental crust. We begin with an idealised moment magnitude (M_w) 8 model earthquake to illustrate the general static stress changes associated with subduction interface events, before presenting idealised earthquakes with M_w from 6 to 9. The effects of altering the dip of the subduction interface, the rupture scaling laws, the slip distribution, and Poisson's ratio are also investigated. We also present an example using a slip distribution model from a real subduction interface earthquake.

The source characteristics of subduction zone interface earthquakes vary between and within subduction zones due to heterogeneity in subduction geometry, mechanical properties of the interface, and stress distribution, amongst others (Schellart & Rawlinson 2013). The idealised models consider the simple case of a pure thrust earthquake with zero along-strike displacement and a uniform slip distribution. Pure thrust earthquakes may occur during orthogonal subduction, where the plate convergence vector is perpendicular to the plate boundary. Oblique convergence may also produce pure thrust earthquakes where strain is partitioned into thrusting and strike-slip faulting domains.

To generate the idealised models, we use global datasets of subduction zones (Pacheco et al. 1993, Tichelaar & Ruff 1993, Heuret et al. 2011, Hayes et al. 2018) to define a typical subduction zone interface on which the model thrust earthquakes occur. We find a mean interface dip of 20 degrees and choose an upper boundary of the seismogenic zone of 5 km (Table 5.1). Above 5 km, stable sliding is assumed to occur due to the presence of non-seismogenic sediment layers (Vrolijk 1990, Moore & Saffer 2001). We chose a shallower depth to the top of the seismogenic zone than suggested by the global datasets as large earthquakes often rupture far into the upper stable zone (Kanamori & Kikuchi 1993).

Table 5.1: Global dip and depth to top of the seismogenic zone data for subduction zones. The mean value is the average of all subduction zone segments in each study, without weighting for segment length.

Dataset - Interface dip	Min. dip	Mean dip	Max. dip
Tichelaar & Ruff (1993)	12	14	19
Pacheco et al. (1993)	17	25	32
Heuret et al. (2011)	9	20	33
Hayes et al. (2018)	9	20	33

Dataset - Upper seismogenic zone	Min. depth	Mean depth	Max. depth
Heuret et al. (2011)	1	11	35
Hayes et al. (2018)	10	11	14

Many scaling relationships exist for subduction zone earthquake rupture dimensions (e.g. Strasser et al. 2010, Blaser et al. 2010, Murotani et al. 2013, Skarlatoudis et al. 2016, Thingbaijam et al. 2017, Allen & Hayes 2017). The along-strike rupture length (L) versus M_w relationship is relatively well-defined and consistent, but there is more variability in the down-dip rupture width (W) versus M_w relationships (Allen & Hayes 2017). We use the scaling relationships derived by Strasser et al. (2010), which are empirically-derived, linear, non-self-similar, and lie roughly in the middle of existing scaling relationships (Allen & Hayes 2017). Although there is sound empirical and theoretical evidence for width-saturation of the seismogenic zone for larger subduction earthquakes (Hyndman et al. 1997, Tajima et al. 2013, Allen & Hayes 2017), disregarding this helps preserve the simplicity of our model.

For each idealised model earthquake magnitude, L and W are obtained from the relationships of Strasser et al. (2010), before the amount of reverse slip (S) on the interface is calculated by

$$S = \frac{10^{\frac{3}{2}(M_w+6.06)}}{\mu W L} \quad , \tag{5.9}$$

where μ is the shear modulus (all parameters in SI units). As the rupture dimensions are fixed and the model space is isotropic, the resulting static stress changes are independent of the Young's modulus; any increase to the Young's modulus is cancelled out by a corresponding decrease to the applied slip. Although the scaling relationships of Strasser et al. (2010) do not enforce self-similar scaling, we initially use the stress field changes produced by the M_w 8 idealised model earthquake as an example, under the assumption that the spatial patterns of stress field changes produced by the other idealised models will be generally similar, only acting over correspondingly different spatial scales and magnitudes (Wells & Coppersmith 1994).

5.3.2 Model geometry

The geometries of the model and end-member pathways are as previously described (Figure 5.1). The oceanic trench marks where the up-dip projection of the rupture plane intersects the surface $z = 0$; the midpoint of the trench defines the point [0 0 0] within the model wireframe. The x-axis is positive away from the oceanic trench in the direction of dip. Parameter values for each idealised model earthquake magnitude are shown in Table 5.2.

Table 5.2: Parameter values for the idealised model earthquakes of M_w 6 to 9, using the scaling relationships of Strasser et al. (2010).

M_w	L (km)	W (km)	d (km)	S (m)
6.0	11	17	11	0.2
7.0	42	38	18	0.8
8.0	160	84	34	2.9
9.0	610	190	70	10.5

Although magmatic intrusions may occur in any orientation, we use the arc-parallel and arc-perpendicular end-members as these are easily defined relative to the subduction zone tectonics. Further, intrusions may exploit pre-existing stuctures that act as planes of weakness in the orientations defined by our end-member pathways (Tosdal & Richards 2001, Richards et al. 2001, Cembrano & Lara 2009). Arc-parallel pathways may represent dykes formed in volcanic arcs undergoing extension due to slab rollback, or intrusions which exploit strike-slip faults or shear zones commonly found within volcanic arcs that accommodate any oblique convergence (e.g. Cembrano et al. 1996). Arc-perpendicular pathways may represent the path of least resistance for dykes formed under compressional subduction tectonics, or intrusions which exploit tear faults or so-called cross-arc lineaments of unclear nature (Salfity 1985, Salfity & Gorustovich 1998). Horizontal pathways may represent sills or magma bodies formed under strongly compressional settings, or due to the presence of rheological or density layering within the crust which create suitable conditions for sill formation in other tectonic environments (Gudmundsson 2011, Rivalta et al. 2015).

The normal stress changes on the end-member pathways are calculated at every point within the 3D model wireframe, however, it is important to consider the location of potential magmatic activity. Dickinson (1973) states that the distance between oceanic trenches and associated volcanic arcs ranges from 100 to 300 km. However, several present-day volcanic arcs lie towards the upper end of, or beyond, this range (e.g. Chile and Sumatra: Walter & Amelung 2007, Acocella et al. 2018). An analysis using the Smithsonian Global Volcanism database found a global mean trench-to-arc distance of 287 ± 161 km (Pall et al. 2018). This analysis suggests ≈84% of global subduction zone volcanoes should be located within 448 km of the oceanic trench. We therefore refer to the area between 100 and 500 km from the oceanic trench in the x-direction as the zone of likely magmatism (ZLM) and focus our interpretation and discussion on this area (Figure 5.1).

5.4 Modelled normal stress changes

The normal stress changes on the three end-member pathways and the mean stress change are shown for the M_w 8 model earthquake in map view at 5 km depth (Figure 5.3e-h) and in cross-section through the centre of the rupture (Figure 5.4e-h). Except where noted, all figures use an isotropic Poission's ratio of 0.25. The normal stress change depends on both the strain normal to the pathway and the volumetric strain. As ϵ_{xx} is the dominant strain component (Figures 5.3a, 5.4a), the volumetric strain (ϵ_{kk}: Figures 5.3d, 5.4d) strongly resembles ϵ_{xx}. The normal stress change on arc-parallel pathways ($\Delta\sigma_{xx}$: Figures 5.3e, 5.4e), therefore strongly resembles the induced strain ϵ_{xx}. Arc-parallel pathways are generally unclamped within the ZLM, although clamping occurs beyond the lateral rupture tips (Figure 5.3e). Beyond the down-dip rupture tip, the magnitude of unclamping increases towards the surface, whereas closer to and above the rupture itself, the magnitude of unclamping generally increases with depth towards the rupture (Figure 5.4e).

Figure 5.3: (Below) a-c) The three components of normal strain, and d) the volumetric strain induced by the M_w 8 model earthquake, shown in map view at 5 km depth (depth to top of rupture). The arrows show the displacement field projected onto the xy plane at 5 km depth in a) and b) to show how the strains ϵ_{xx} and ϵ_{yy} arise. e-g) The three components of normal stress change on end-member pathways, and h) the mean stress change for the M_w 8 model earthquake model. The ZLM is located in the area x = 100-500 km.

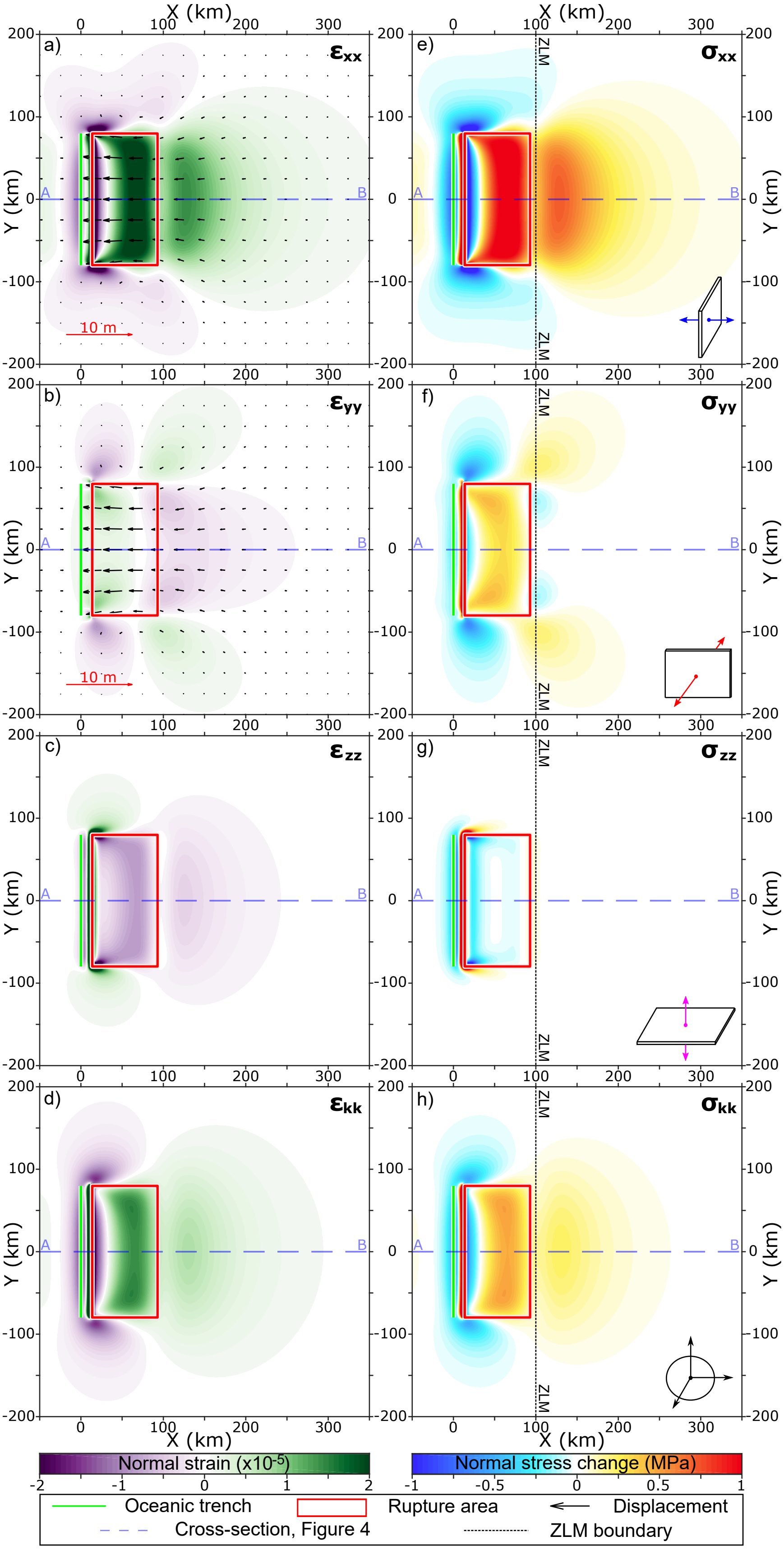
X (km)
Y (km)
a)
ε_{xx}
b)
ε_{yy}
c)
ε_{zz}
d)
ε_{kk}
e)
σ_{xx}
f)
σ_{yy}
g)
σ_{zz}
h)
σ_{kk}
10 m
A
B
ZLM
0
100
200
300
-100
-200
Normal strain (x10^{-5})
-2
-1
0
1
2
Normal stress change (MPa)
-1
-0.5
0
0.5
1
Oceanic trench
Rupture area
Displacement
Cross-section, Figure 4
ZLM boundary

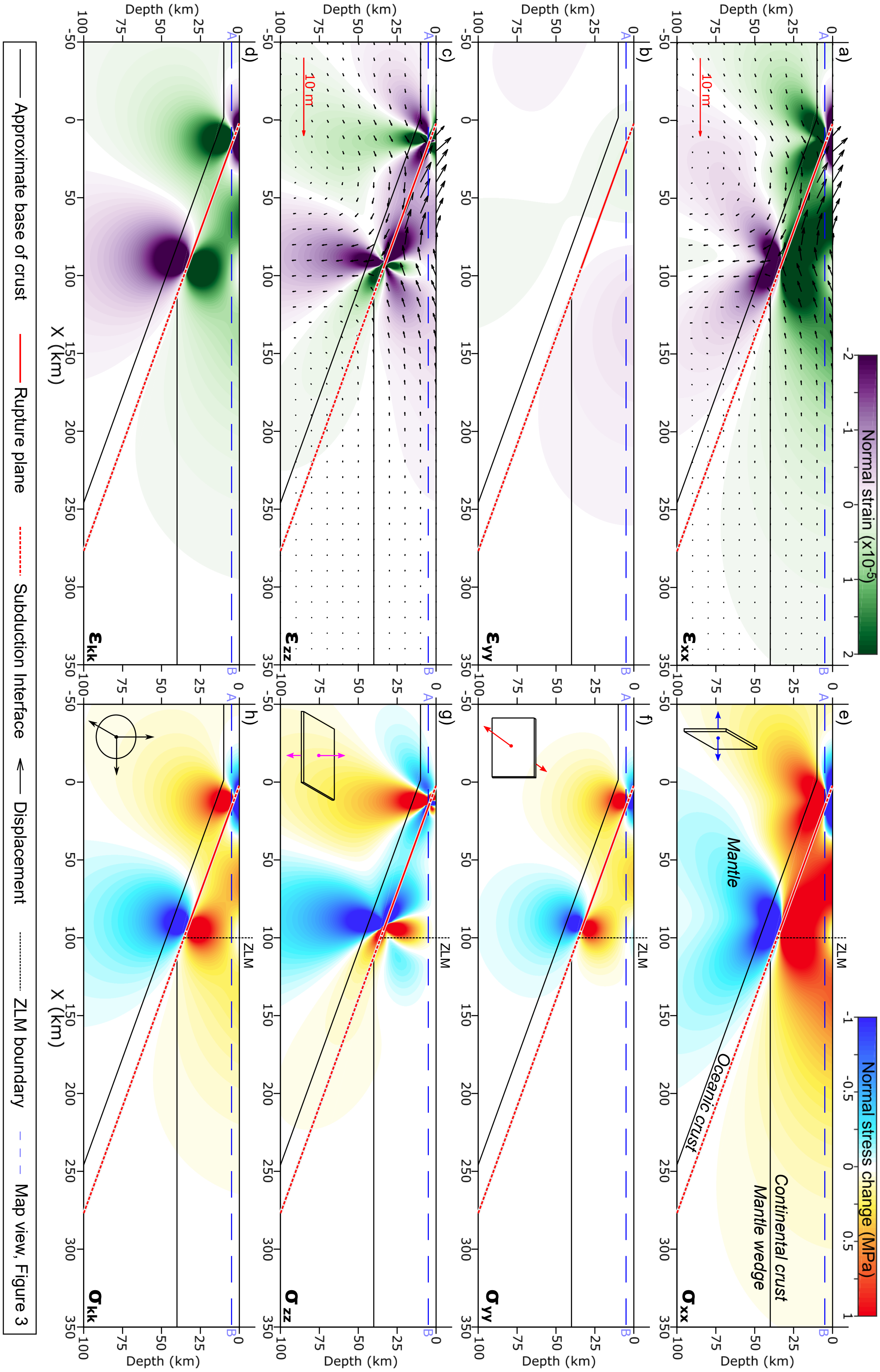
a)
b)
c)
d)
e)
f)
g)
h)
ε_{xx}
ε_{yy}
ε_{zz}
ε_{kk}
σ_{xx}
σ_{yy}
σ_{zz}
σ_{kk}
Normal strain (x10^{-5})
-2
-1
0
1
2
Normal stress change (MPa)
-1
-0.5
0
0.5
1
Depth (km)
X (km)
10 m
A
B
ZLM
Mantle
Oceanic crust
Continental crust
Mantle wedge
Approximate base of crust
Rupture plane
Subduction Interface
Displacement
ZLM boundary
Map view, Figure 3

Figure 5.4: (Above) a-c) The three components of normal strain, and d) the volumetric strain induced by the M_w 8 model earthquake, shown in cross-section through the centre of the rupture along the line $y = 0$. The arrows show the displacement field projected onto the xz plane at $y = 0$ in a) and c) to show how the strains ϵ_{xx} and ϵ_{zz} arise. e-g) The three components of normal stress change on end-member pathways, and h) the mean stress change for the M_w 8 model earthquake model. The ZLM is located above the subduction interface at x = 100-500 km.

As there is no slip on the rupture plane in the y-direction, ϵ_{yy} is largely induced to counteract stress changes resulting from displacements in the x-direction, as well as directly counteracting ϵ_{xx} due to the non-zero Poisson's ratio; where there is extension in ϵ_{xx} adjacent to the rupture plane (Figure 5.3a), there is a corresponding contraction in ϵ_{yy} (Figure 5.3b) and where there is contraction in ϵ_{xx} beyond the lateral rupture tips there is a corresponding extension in ϵ_{yy}. As ϵ_{yy} is the smallest component of induced strain, the stress changes on arc-perpendicular pathways ($\Delta\sigma_{yy}$: Figures 5.3f, 5.4f) are most strongly influenced by ϵ_{kk}. Contraction in ϵ_{yy} in the ZLM is counteracted by volumetric expansion, resulting in very small stress changes in σ_{yy} over much of the ZLM. However, arc-perpendicular pathways are unclamped above the down-dip rupture tip, with the magnitude of unclamping increasing with depth. Beyond the along-strike rupture tips, extension in ϵ_{yy} (Figure 5.3b) causes unclamping of arc-perpendicular pathways, with the magnitude of unclamping increasing towards the surface (Figure 5.3f).

The induced normal strain ϵ_{zz} depends on the relative magnitudes of slip in the z-direction on the rupture plane and the movement of the free-surface in the z-direction. Above the rupture plane, vertical (upwards) displacement on the rupture surface dominates over the uplift of the free surface, thus causing contraction in ϵ_{zz} (Figure 5.4c); this causes clamping of horizontal pathways above the rupture plane ($\Delta\sigma_{zz}$: Figure 5.4g). Beyond the down-dip rupture tip, subsidence is largest at the free surface and decays with depth, therefore also causing contraction in ϵ_{zz} (Figure 5.4c). However, contraction beyond the down-dip rupture tip is largely counteracted by volumetric expansion (Figure 5.4d), resulting in only a small lobe of clamping of horizontal pathways beyond the down-dip rupture tip, which transitions to unclamping at greater distances away from the rupture (Figure 5.4g). Above the down-dip rupture tip, there is a lobe of extension in ϵ_{zz} which combines with volumetric expansion in the same area (Figure 5.4d) to produce a strong lobe of unclamping of horizontal pathways (Figure 5.4g). By definition, the normal stress change on horizontal pathways at $z = 0$ is zero.

5.5 Stress change regimes

5.5.1 Motivation and method

At each model grid point, we generate profiles of normal stress change on the end-member pathways versus depth. By analysing those profiles that lie within the ZLM, we identify stress change regimes that display specific combinations of stress change on the end-member pathways with depth (e.g. Figure 5.5b-i). Defining these regimes simplifies the otherwise complex stress change field, allowing the patterns in stress change to be mapped out spatially (Figure 5.5a) and facilitating interpretation of whether each regime will favour magma storage or ascent. The regimes were originally defined using the M_w 8 idealised model and then refined using the different idealised models as well as real earthquake models. In total, we identify seven stress change regimes and two sub-regimes (Table 5.3).

Stress change regime assignment is automatically computed using the regime requirements as listed in Table 5.3. The stress change profiles are analysed to the depth of the subduction interface or 100 km, whichever is shallowest. Regime assignment requires ≥10 depth intervals above the subduction interface; for the z-increment of 2 km used here, this corresponds to a minimum depth to the subduction interface of 18 km for stress regime allocation. Additionally, the maximum normal stress change in each profile must exceed a minimum stress change threshold value of 10^{-3} MPa, which is on the order of solid Earth tidal stress changes (Cochran et al. 2004), with any smaller stress changes assumed to be insignificant.

Figure 5.5: (Below) Stress change regimes based on the stress changes with depth on end-member pathways for the M_w 8 idealised model earthquake. a) Spatial distribution of the stress change regimes. Regimes are not calculated at x <50 km, due to shallowing of the subduction interface towards lower x values. Contours show the maximum normal stress change on any end-member pathways above the subduction interface. b-i) Stress changes on end-member pathways versus depth profiles for the M_w 8 idealised model earthquake. The locations of the profiles are shown by the triangles in a). Note the different horizontal scale for each profile.

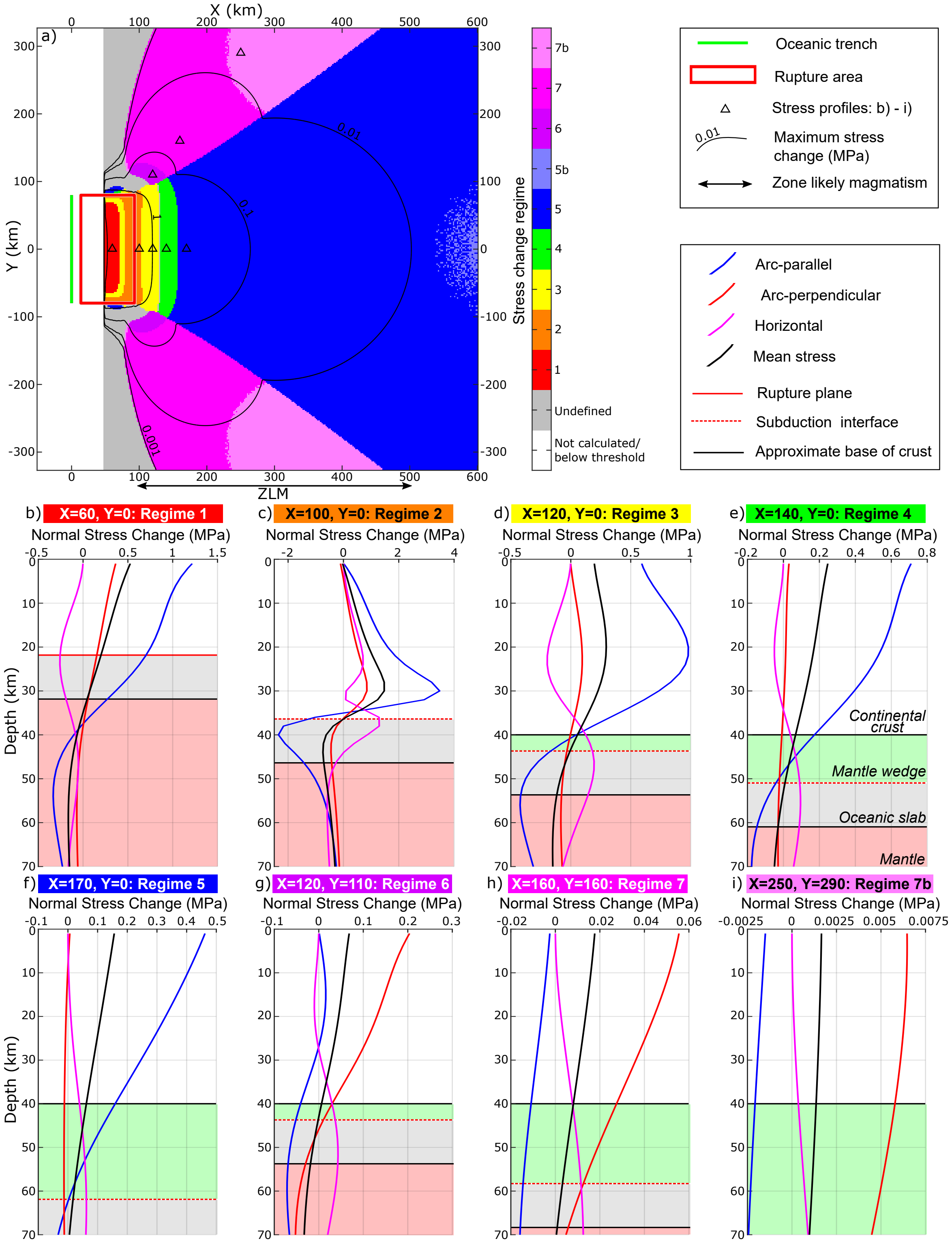
a)
X (km)
0
100
200
300
400
500
600
Y (km)
300
200
100
0
-100
-200
-300
0.01
0.1
0.001
1
ZLM
Stress change regime
7b
7
6
5b
5
4
3
2
1
Undefined
Not calculated/ below threshold
Oceanic trench
Rupture area
Stress profiles: b) - i)
Maximum stress change (MPa)
Zone likely magmatism
Arc-parallel
Arc-perpendicular
Horizontal
Mean stress
Rupture plane
Subduction interface
Approximate base of crust
b) X=60, Y=0: Regime 1
c) X=100, Y=0: Regime 2
d) X=120, Y=0: Regime 3
e) X=140, Y=0: Regime 4
Normal Stress Change (MPa)
Depth (km)
Continental crust
Mantle wedge
Oceanic slab
Mantle
f) X=170, Y=0: Regime 5
g) X=120, Y=110: Regime 6
h) X=160, Y=160: Regime 7
i) X=250, Y=290: Regime 7b
-0.5
0
0.5
1
1.5
-2
2
4
-0.2
0.2
0.4
0.6
0.8
-0.1
0.1
0.3
-0.02
0.02
0.04
0.06
-0.0025
0.0025
0.005
0.0075
10
20
30
40
50
60
70

Table 5.3: Summary of Stress Change Regimes

Regime	Arc-parallel	Arc-perpendicular	Horizontal	Location and notes
1	**Unclamping:** Maximum value at surface	(Unclamping: Increasing towards surface)	Clamping: Peak at subduction interface	Above the rupture plane
2	**Unclamping:** Increasing with depth*	(Unclamping: Increasing with depth*)	(Unclamping: Increasing with depth*)	Above the down-dip rupture tip. *Peak unclamping occurs at ≥75% depth to subduction interface. May transition to clamping very near the subduction interface
3	**Unclamping:** Peak in mid continental crust	(Unclamping: Peak in mid continental crust)	Clamping: Peak in mid continental crust	Either side of the down-dip rupture tip.
4	**Unclamping:** Increasing towards surface	(Unclamping/ clamping: Increasing towards surface)	Clamping: Peak in mid-continental crust*	Beyond down-dip rupture tip. *May transition to unclamping at greater depths
5	**Unclamping:** Increasing towards surface*	(Unclamping/ clamping: Increasing towards surface)	Unclamping: Increasing with depth	Further beyond the down-dip rupture tip. *Regime 5b where the value at the surface is not the largest, but still ≥90% maximum value
6	(Variable)	**Unclamping:** Increasing towards surface	Clamping: Peak in mid-continental crust	Beyond the lateral rupture tips.
7	(Variable)	**Unclamping:** Increasing towards surface*	Unclamping: Increasing with depth	Beyond the lateral rupture tips. *Regime 7b where the value at the surface is not the largest, but still ≥90% maximum value.

Note: Parentheses indicate a typical stress change for that regime, but not a requirement. Bold text indicates the largest magnitude stress change in each regime. The stress change on arc-perpendicular pathways in regimes 3-5 is typically very low magnitude, with clamping or unclamping determined by the rupture aspect ratio.

5.5.2 Regime definitions

Regimes 1-5 occupy the area roughly adjacent to the earthquake rupture and are characterised by unclamping of arc-parallel pathways as the largest magnitude stress change. The gradient with depth of this unclamping, as well as the stress changes on horizontal pathways, differ between these regimes. The stress changes on arc-perpendicular pathways in Regimes 1-5 depend strongly on the rupture aspect ratio but are generally very low magnitude and are not used in the assignment of these regimes. The spatial distribution of Regimes 1-5 relates to the location of the down-dip rupture tip, where stress change is concentrated. Near the down-dip rupture tip, stress changes increase downwards towards the subduction interface (Regime 2). Moving away from the rupture tip, the peak stress changes on arc-parallel pathways occur at progressively shallower levels, moving from the mid-continental crust (Regime 3), to the surface (Regimes 1, 4, and 5). Regimes 6 and 7 are located beyond the lateral faults tips and are characterised by unclamping of arc-perpendicular pathways as the largest stress change. Regimes 6 and 7 are differentiated by the stress change on horizontal pathways. Regimes 5 and 7 cover the greatest spatial extent, while regimes 1-4 and 6 occupy a much smaller area closer to the rupture itself. The undefined region in Figure 5.5a is an area of highly variable stress changes, due to proximity to both the down-dip and lateral rupture tips.

Regime 1 occurs in the region around the centre of the rupture. The maximum unclamping on arc-parallel pathways occurs at the shallowest depth, reaching values of >1 MPa at 1 km depth in the M_w 8 example (Figure 5.5b). The magnitude of unclamping generally increases upwards from the subduction interface towards the surface. Horizontal pathways are clamped in Regime 1, with peak clamping occurring at the subduction interface at values of <0.5 MPa for the M_w 8 model. Arc-perpendicular pathways are generally increasingly unclamped towards the surface, although with lower magnitudes (<0.5 MPa for the M_w 8 model) than the arc-parallel pathways.

Regime 2 has the largest stress change magnitudes of any regime, with up to several MPa of unclamping on arc-parallel pathways for the M_w 8 model. These high stress change values occur as Regime 2 is located near the down-dip rupture tip. The peak unclamping of arc-parallel pathways occurs near the base of the continental crust ($\geq$75% of the depth to the subduction interface), with a magnitude more than twice that at the shallowest depth (Figure 5.5c). All three end-member pathways are generally increasingly unclamped with depth towards the subduction interface, although below the depth of peak unclamping there may be a sharp reduction in the stress change and perhaps even a transition to clamping, especially for the horizontal pathways. Arc-perpendicular pathways show the same unclamping pattern as the arc-parallel pathways, suggesting that $\Delta\sigma_{yy}$ is mainly controlled by the volumetric expansion dominated by ϵ_{xx}.

Regime 3 occurs either side of Regime 2 at the down-dip rupture tip. The maximum unclamping of arc-parallel pathways is at intermediate depths, at less than 75% of the depth to the subduction interface but below the surface (Figure 5.5d). Horizontal pathways are clamped, with peak clamping also occurring at an intermediate depth between the surface and the subduction interface. The stress changes on arc-perpendicular pathways again match those on arc-parallel pathways, but with lower magnitudes. In the M_w 8 model, peak unclamping on arc-parallel pathways reaches around 1 MPa, while the stress changes on horizontal and arc-perpendicular pathways are lower.

Regimes 4 and 5 are located beyond the down-dip rupture tip and are characterised by increasing magnitudes of unclamping on arc-parallel pathways towards the surface. Peak unclamping values at 1 km depth are around 0.7 MPa in Regime 4 (Figure 5.5e) and 0.5 MPa in Regime 5 (Figure 5.5f) for the M_w 8 model. Horizontal pathways are clamped in Regime 4, with peak clamping at intermediate depths. The magnitude of clamping of horizontal pathways is lower in Regime 4 than in Regime 3, and there may be a transition to unclamping at greater depths closer to the subduction interface. In Regime 5, horizontal pathways are unclamped, with the magnitude of unclamping increasing with depth towards the subduction interface. The stress changes on arc-perpendicular pathways are more than an order of magnitude smaller than those on arc-parallel pathways in Regimes 4 and 5. At especially great distances from the rupture, there is a reduction in the magnitude of unclamping on arc-parallel pathways at shallow depths in Regime 5. Hence, we define Regime 5b, which is the same as Regime 5 but with an allowance for up to 10% reduction in unclamping at the surface, relative to the maximum unclamping value.

In Regimes 6 and 7, the maximum stress change occurs on arc-perpendicular pathways. Regimes 6 and 7 are located beyond the lateral rupture tips, with Regime 6 adjacent to the near-fault regimes 1-4, whereas Regime 7 occupies large areas adjacent to Regime 5. Unclamping of arc-perpendicular pathways increases towards the surface in both Regimes 6 and 7, reaching up to 0.2 MPa in the M_w 8 example in Regime 6 (Figure 5.5g), but an order of magnitude lower in Regime 7 (Figure 5.5h). In Regime 6, horizontal pathways are clamped with peak clamping at intermediate depths. In Regime 7, horizontal pathways are unclamped, with the magnitude of unclamping increasing with depth towards the subduction interface. Across Regimes 6 and 7, the stress changes on arc-parallel pathways are more variable, showing both clamping and unclamping depending on depth and the distance from the rupture. At large distances from the rupture, Regime 7b is defined where, as with Regime 5b, there is up to a 10% reduction in unclamping of arc-perpendicular pathways at the surface relative to the peak unclamping value.

5.5.3 Controls on regime distribution

5.5.3.1 Earthquake moment magnitude

Large earthquakes are assumed to be fundamentally similar to small earthquakes (e.g. Kanamori & Anderson 1975), so similar stress field changes are expected for different magnitude idealised subduction interface earthquakes, only acting over spatial scales corresponding to their rupture dimensions. The stress regime maps in Figure 5.6 show similar spatial distributions of stress change regimes for idealised earthquake models of M_w of 6 to 9. With increasing M_w, more of the ZLM is covered by the defined stress change regimes; larger earthquakes exhibit greater slip magnitudes and therefore generate larger stress changes at comparable distances. Further, stress change amplitude decays as a power law with distance away from the rupture plane and so large earthquakes generate strong stress changes over a larger crustal volume. The increased down-dip rupture width of larger earthquakes also causes the down-dip rupture tip to move to greater depths. With a deeper source of stress concentration, the width of the stress change regimes at the surface therefore increases with increasing earthquake magnitude. The contours in Figure 5.6 show the maximum value of unclamping on any end-member pathway above the subduction interface. While the orientation and gradient with depth of stress changes within a particular regime are the same regardless of earthquake magnitude, the magnitude of the stress changes varies with earthquake magnitude and distance to the rupture (Figures 5.7-5.9). For example, in the M_w 7 model, only Regimes 5, 7, and 7b are located within the ZLM with stress change magnitudes of <0.1 MPa (Figure 5.8). In the M_w 9 model, every stress change regime is located within the ZLM, with magnitudes commonly >1 MPa (Figure 5.9).

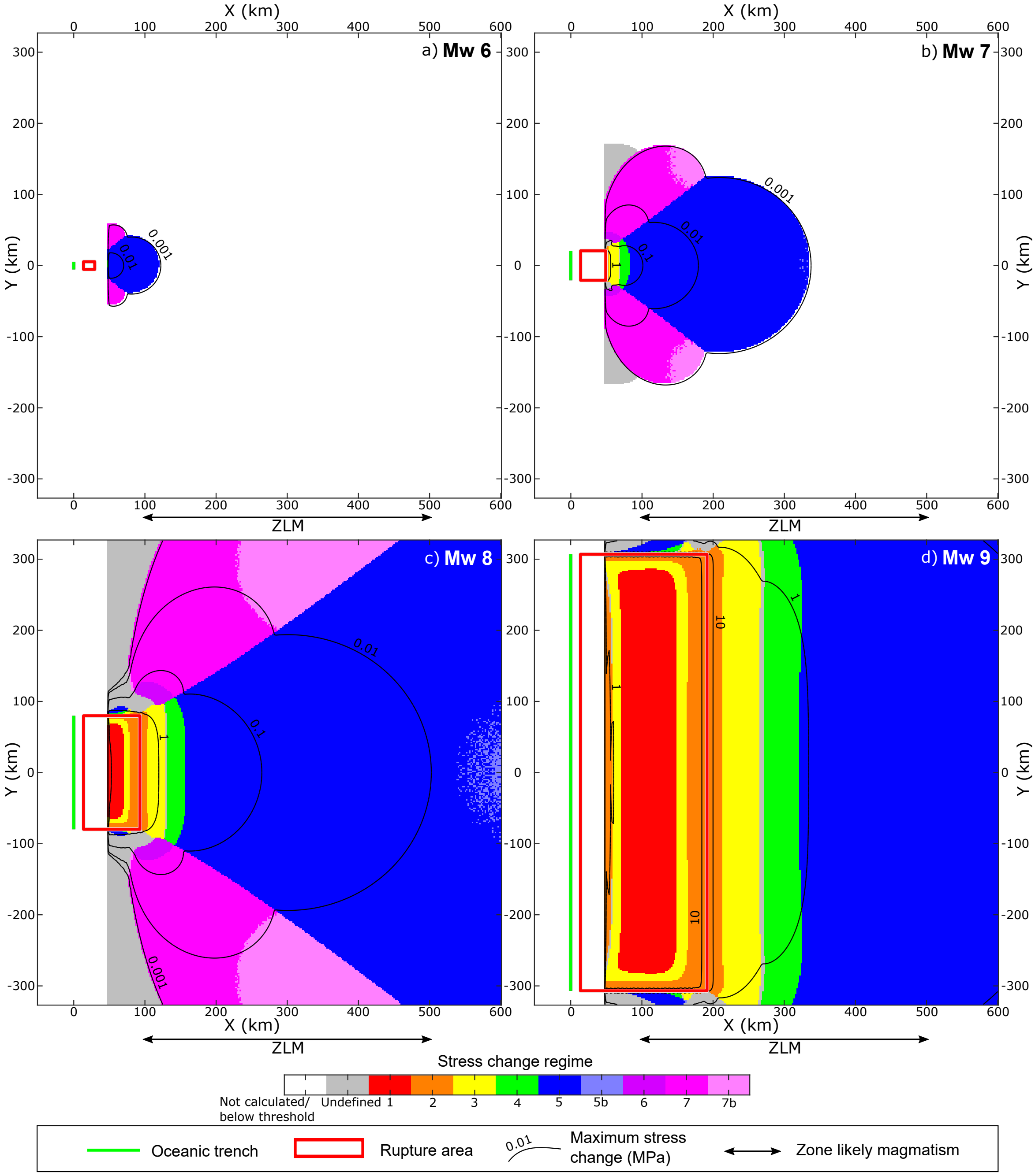

Figure 5.6: Spatial distributions of stress change regimes for different magnitude idealised earthquake models: a) M_w 6, b) M_w 7, c) M_w 8, and d) M_w 9. Regimes are not calculated at x <50 km, due to shallowing of the subduction interface towards lower x values. Contours show the maximum normal stress change on any end-member pathway above the subduction interface.

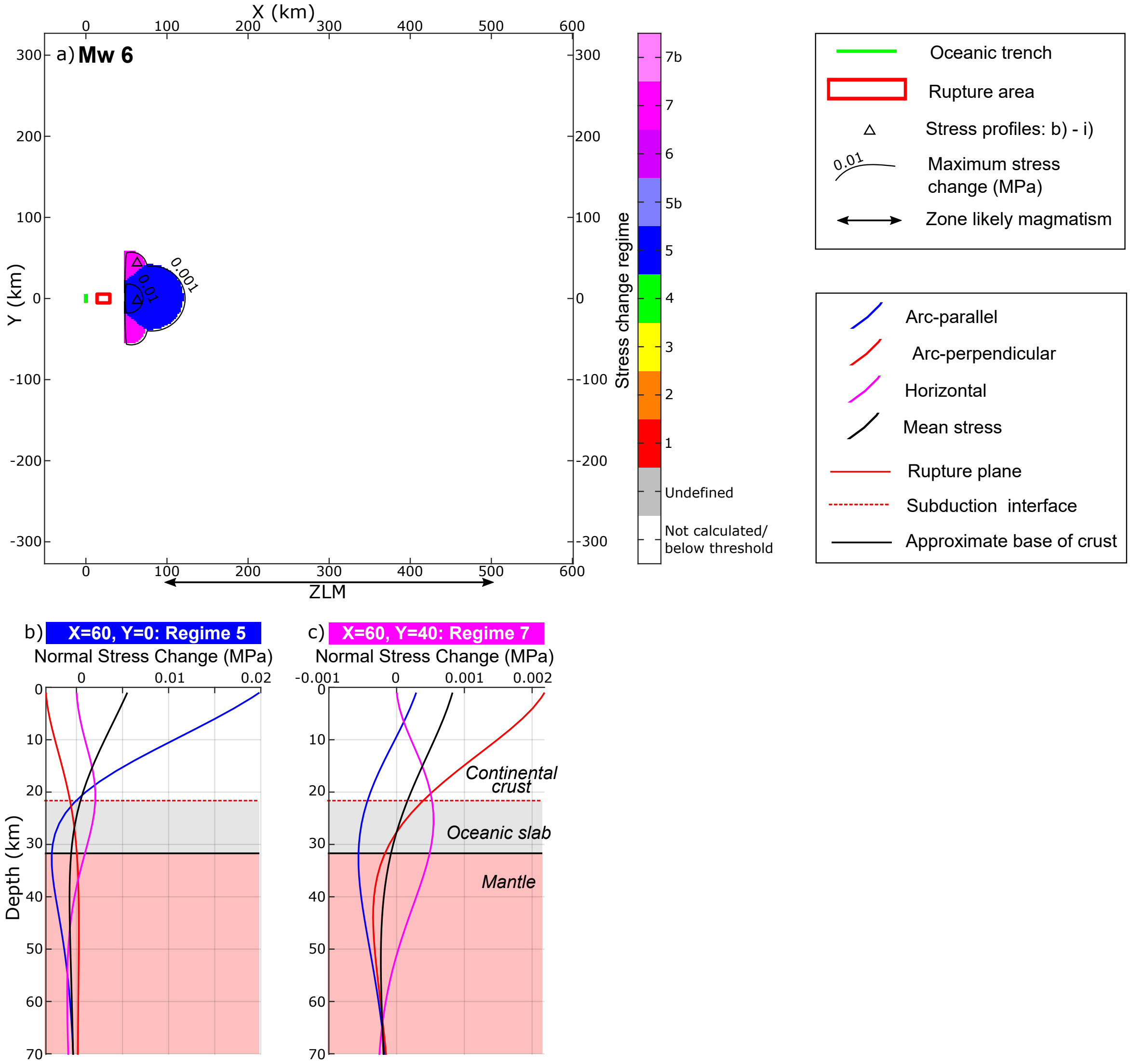

Figure 5.7: Stress change regimes based on the stress changes with depth on end-member pathways for the M_w 6 idealised model earthquake. a) Spatial distribution of the stress change regimes. b-c) Stress changes on end-member pathways versus depth profiles.

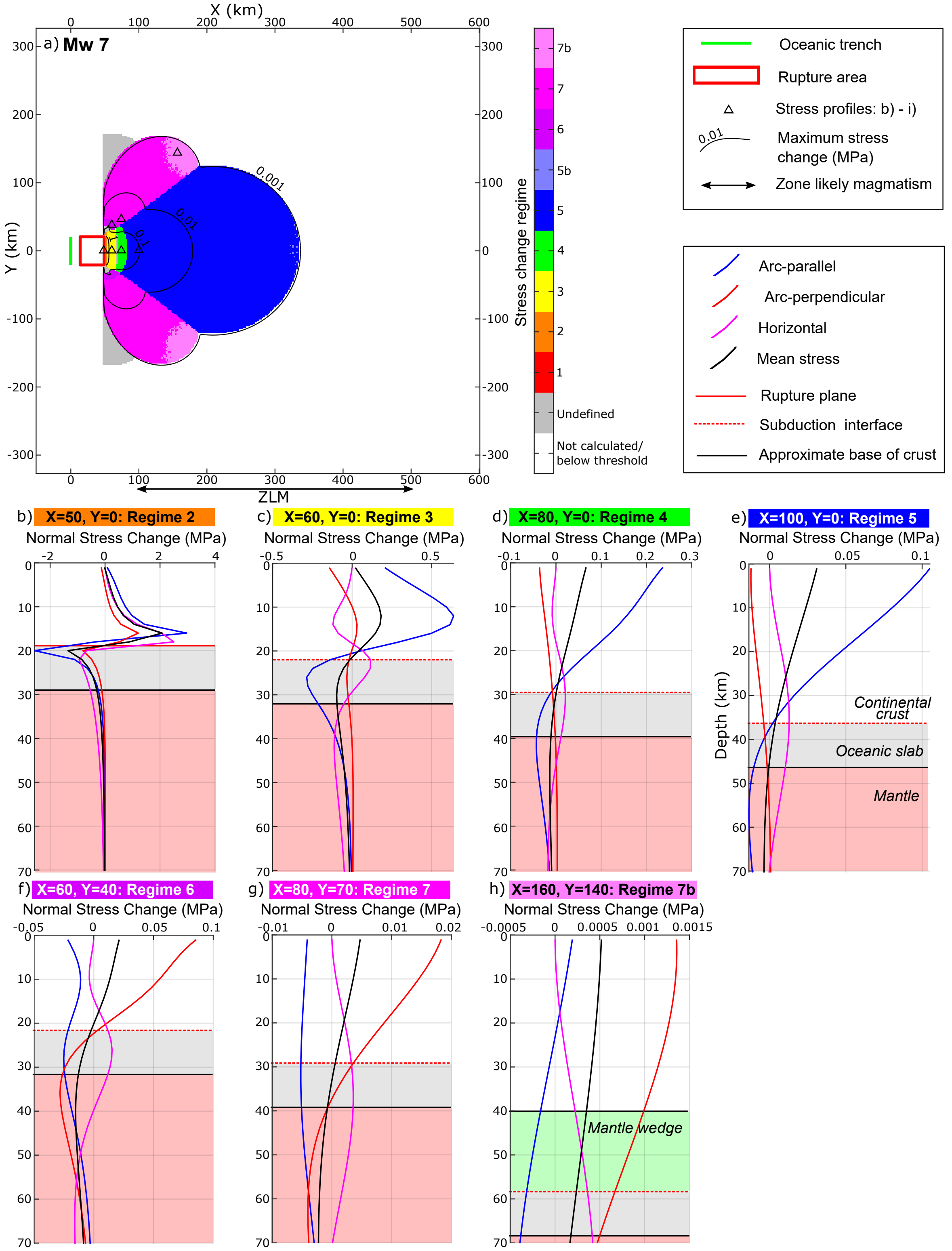

Figure 5.8: Stress change regimes based on the stress changes with depth on end-member pathways for the M_w 7 idealised model earthquake. a) Spatial distribution of the stress change regimes. b-c) Stress changes on end-member pathways versus depth profiles.

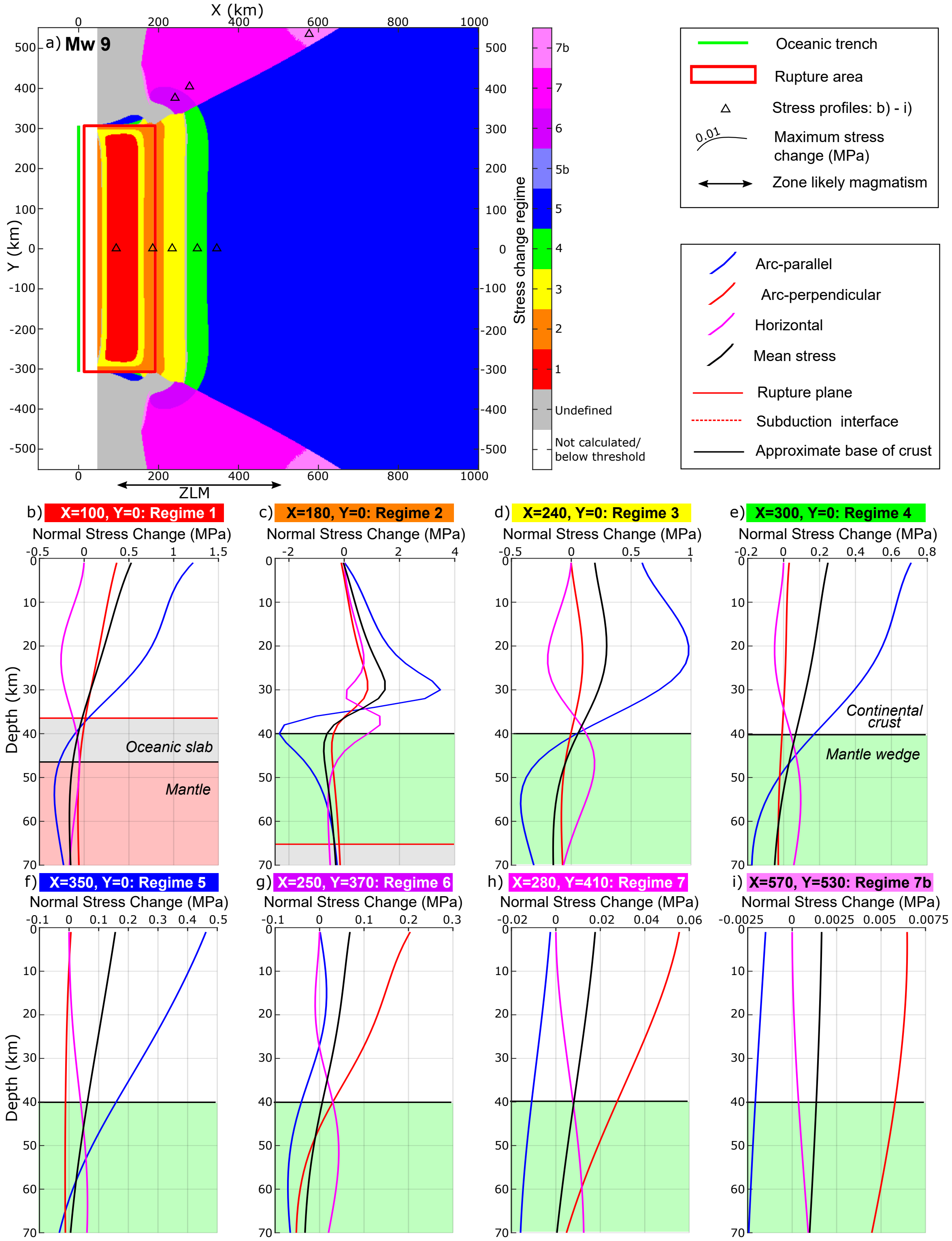

Figure 5.9: Stress change regimes based on the stress changes with depth on end-member pathways for the M_w 9 idealised model earthquake. a) Spatial distribution of the stress change regimes. b-c) Stress changes on end-member pathways versus depth profiles.

5.5.3.2 Subduction interface dip

We use a minimum interface dip of 9 degrees and a maximum dip of 35 degrees (Table 5.1) to investigate the effects of changing interface dip on the stress change regimes. Varying the interface dip considerably alters the near-fault distribution of the stress change regimes (Figure 5.10). Increasing the interface dip shifts the down-dip rupture tip to greater depths, thus causing wider regimes at the surface. This also means the magnitude of unclamping of arc-parallel pathways is larger for more steeply dipping subduction interfaces than more shallowly dipping ones at large trench-arc distances, even though there is less slip in the x-direction for more steeply dipping interfaces. The normal stress change on horizontal pathways is less affected.

5.5.3.3 Other parameters

Using different earthquake scaling laws to generate the idealised earthquake models alters the near-fault stress change regime distribution (Figrue 5.11). This is mainly due to variation in the depth of the down-dip rupture tip, caused by the varying down-dip rupture widths. Similarly, applying tapered slip to the idealised models, such that the magnitude of slip increases towards the centre of the fault plane, also causes minor changes to the near-fault stress change regime distributions (Figure 5.12). Changing the Poisson's ratio from the default value of 0.25 to a lower value of 0.1 or a higher value of 0.33 does not alter the stress change regime distributions, although the magnitude of $\Delta\sigma_{yy}$ increases with increasing Poisson's ratio (Figure 5.13).

5.5.3.4 Slip distribution - real earthquakes

Finite fault models inverted from real earthquakes typically include variability in the slip distribution by dividing the rupture plane into patches with variable rake and slip magnitude. The resulting stress changes are therefore more complex than those produced by the uniform slip models, although they likely still underestimate the real-world complexity. Figure 5.14 shows an example of the stress regimes produced from a finite fault model of the 2010 M_w 8.8 Maule, Chile earthquake. Overall, the stress regime distribution is similar to the idealised earthquakes, although there is significant complexity introduced in the near-fault area (Figure 5.15).

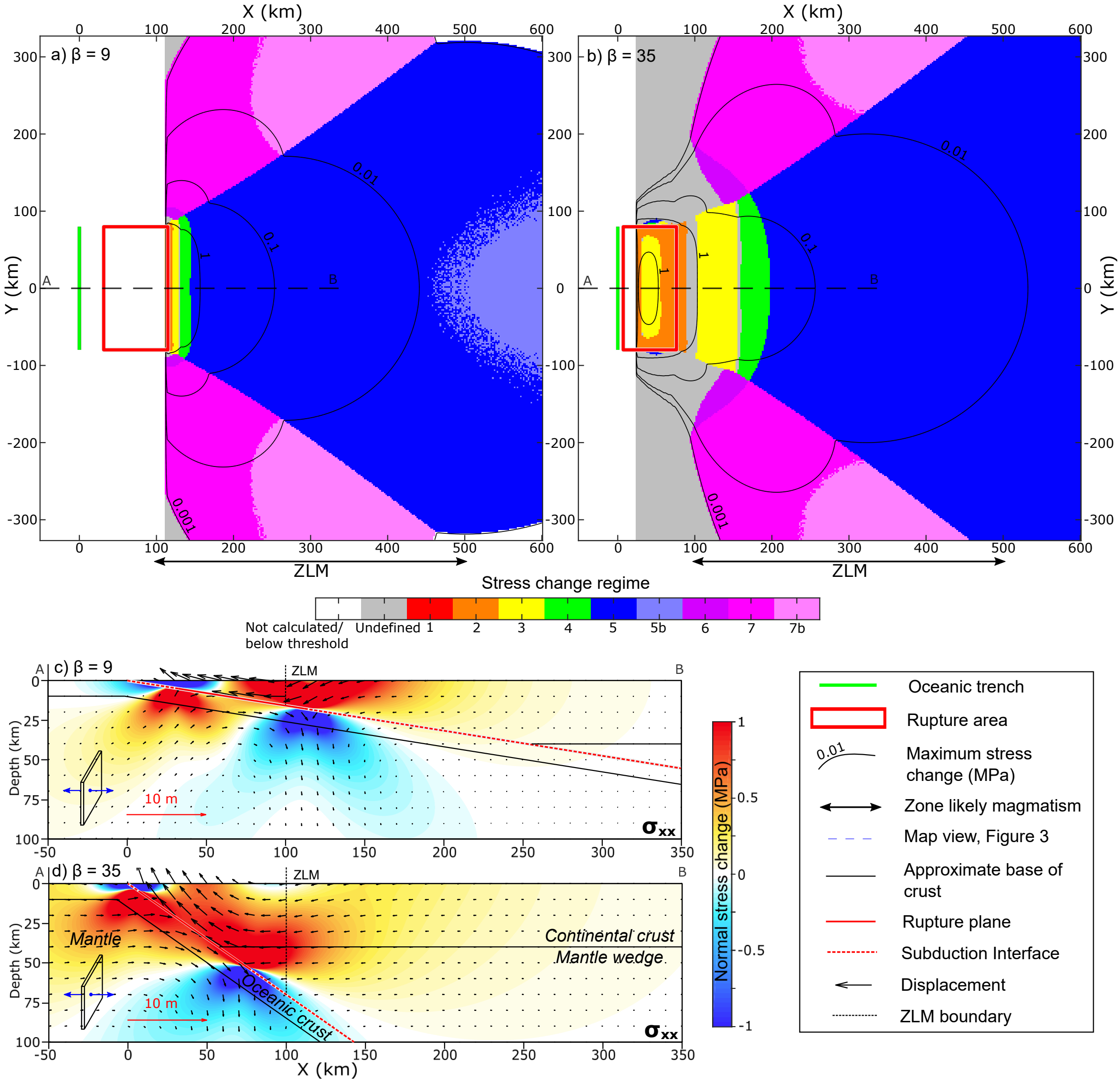

Figure 5.10: Spatial distribution of stress change regimes for the M_w 8 model earthquake on an interface with dip of a) 9 degrees and, b) 35 degrees. Contours show the maximum normal stress change on any end-member pathway above the subduction interface. Cross sections along the line A-B, showing the normal stress change on arc-parallel structures and the displacements projected onto the xz plane are shown in c) for the 9° interface and d) for the 35° interface.

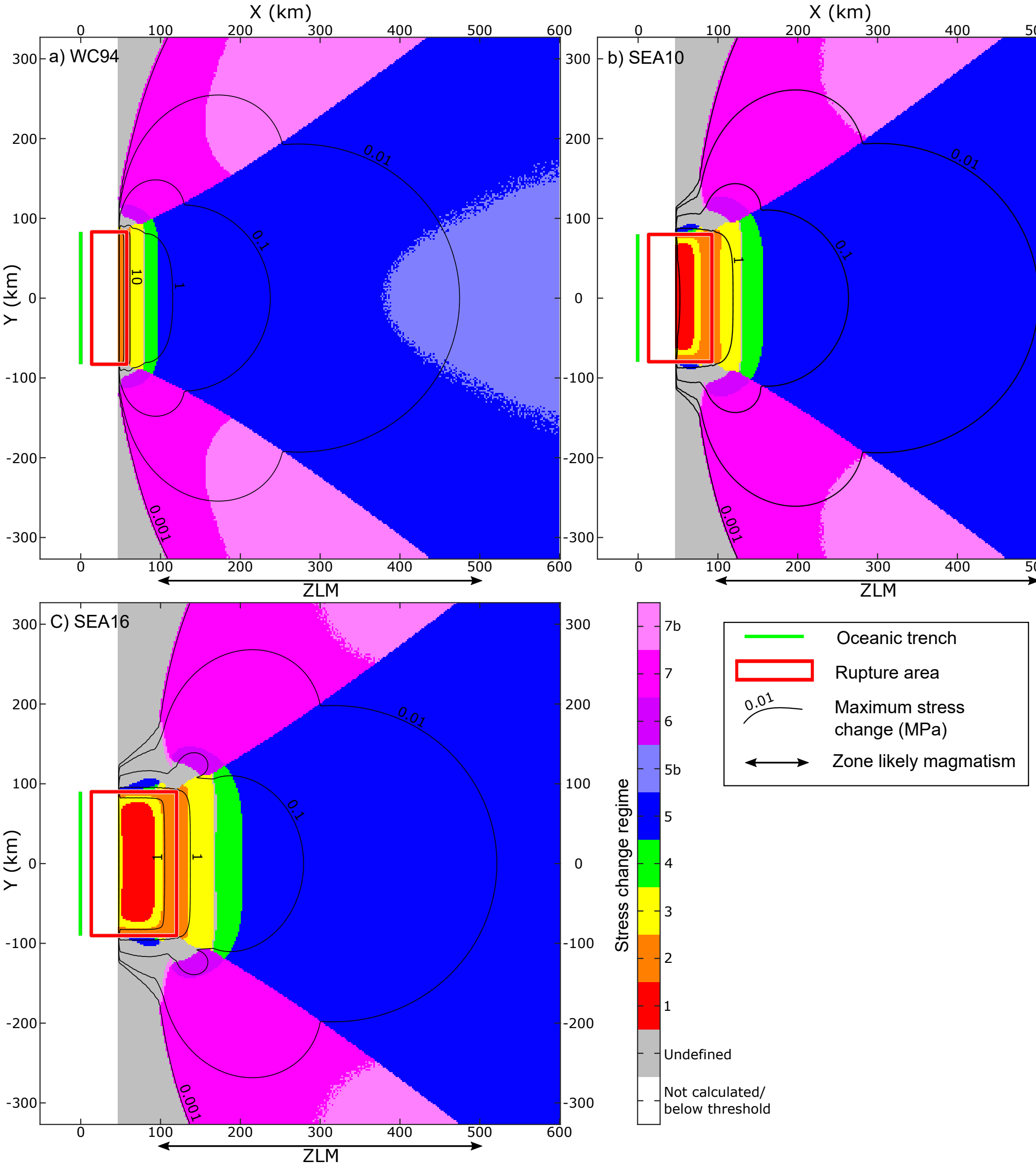

Figure 5.11: Spatial distribution of stress change regimes based on the stress changes on end-member pathways with depth for the M_w 8 idealised earthquake model, using scaling laws of a) Wells & Coppersmith (1994), b) Strasser et al. (2010), and c) Skarlatoudis et al. (2016). The changes to the spatial distribution of the stress change regimes are mainly caused by the varying down-dip rupture width, which alters the depth of the down-dip rupture tip, as in Figure 5.10.

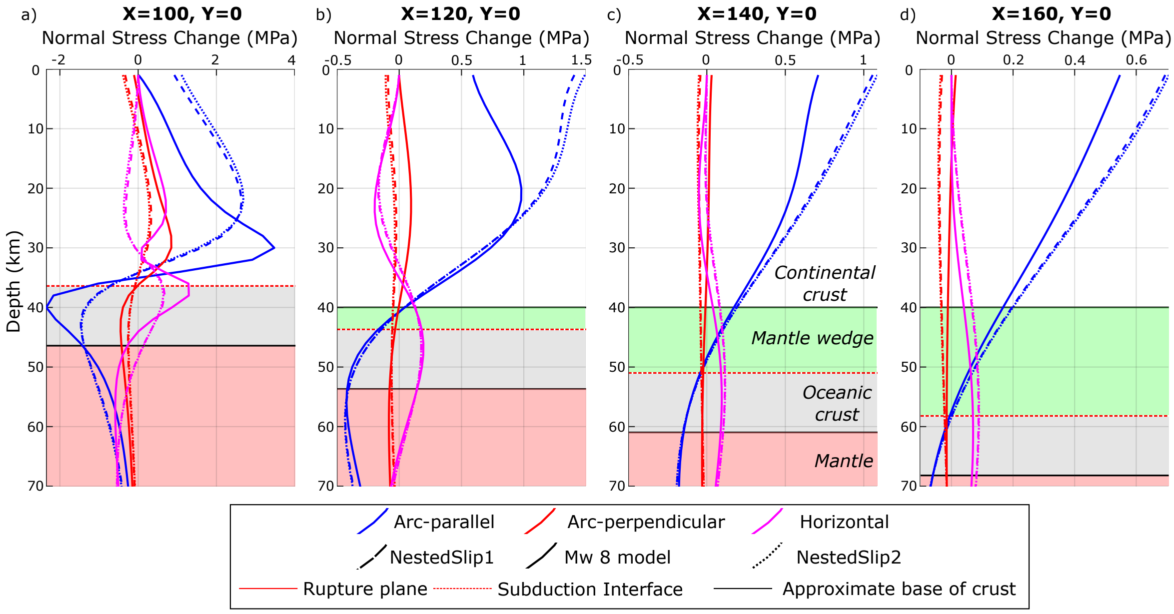

Figure 5.12: (Above) Stress change on end-member pathways versus depth profiles for the M_w 8 idealised earthquake model (Figure 5.5), with changing slip distribution shown by line shading. NestedSlip models were produced using the tapered slip option in Coulomb 3: NestedSlip1 has 10 nested patches of slip 50 km along-strike by 25 km down-dip while NestedSlip2 has 10 nested patches of slip of 70 km along-strike by 35 km down-dip. Note the different stress change scale for each profile. There are small differences in the near-fault stress change regime distribution; at x=120 km (b), the uniform slip model produces Regime 3 stress changes whereas the tapered slip models give Regime 4.

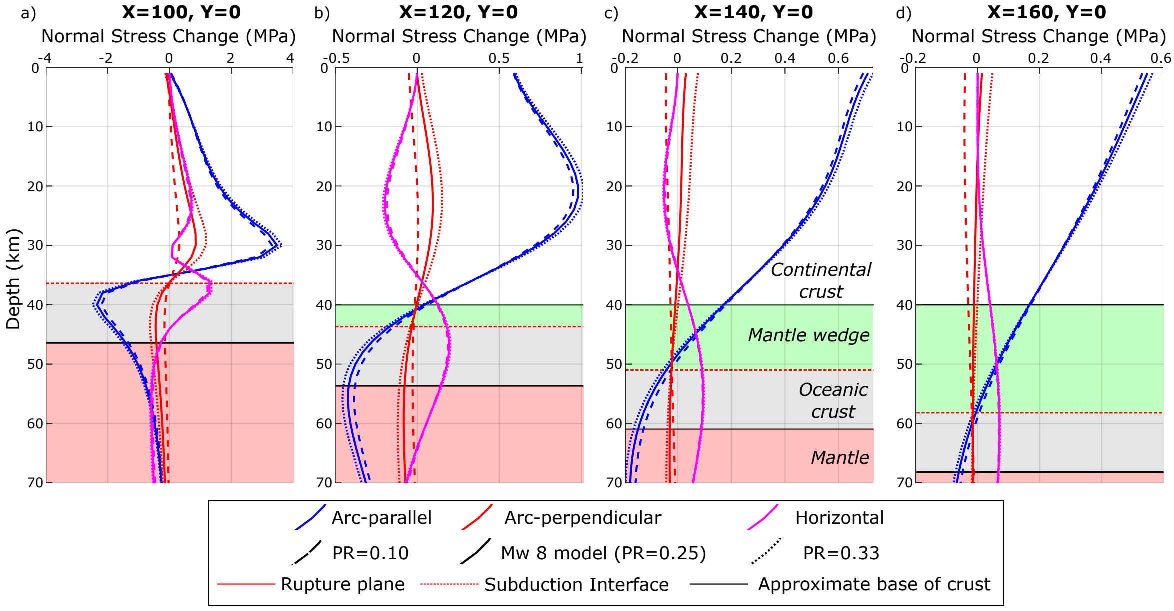

Figure 5.13: (Above) Stress change on end-member pathways versus depth profiles for the M_w 8 idealised earthquake model (Figure 5.5), with varying Poisson's ratio shown by line shading. Each profile shows a different stress change regime. Note the different stress change scale for each profile. Changing Poisson's ratio does not affect the stress change regime distribution, although $\Delta\sigma_{yy}$ increases with increasing Poisson's ratio.

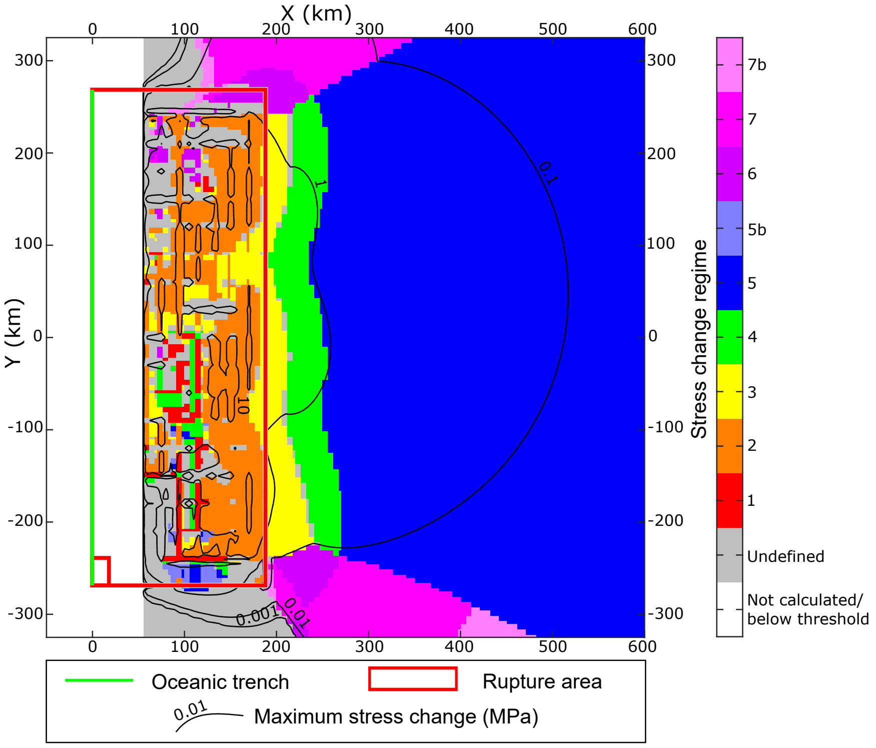

Figure 5.14: Stress change regimes for the 2010 M_w 8.8 Maule Chile earthquake, using the finite fault model of Hayes (2010) from the NEIC (http://earthquake.usgs.gov/earthquakes/eventpage/official20100227063411530_30/finite-fault). The size of each individual slip patch is shown by the slip patch in the bottom left corner of the rupture plane, the other slip patches have been removed for clarity. Note the near fault complexity in the stress change regimes, especially in Regime 1 and 2, with Regime 1 especially poorly produced. This complexity is also shown by the 10 MPa stress change contour within the rupture area. Young's modulus of model is 80 GPa.

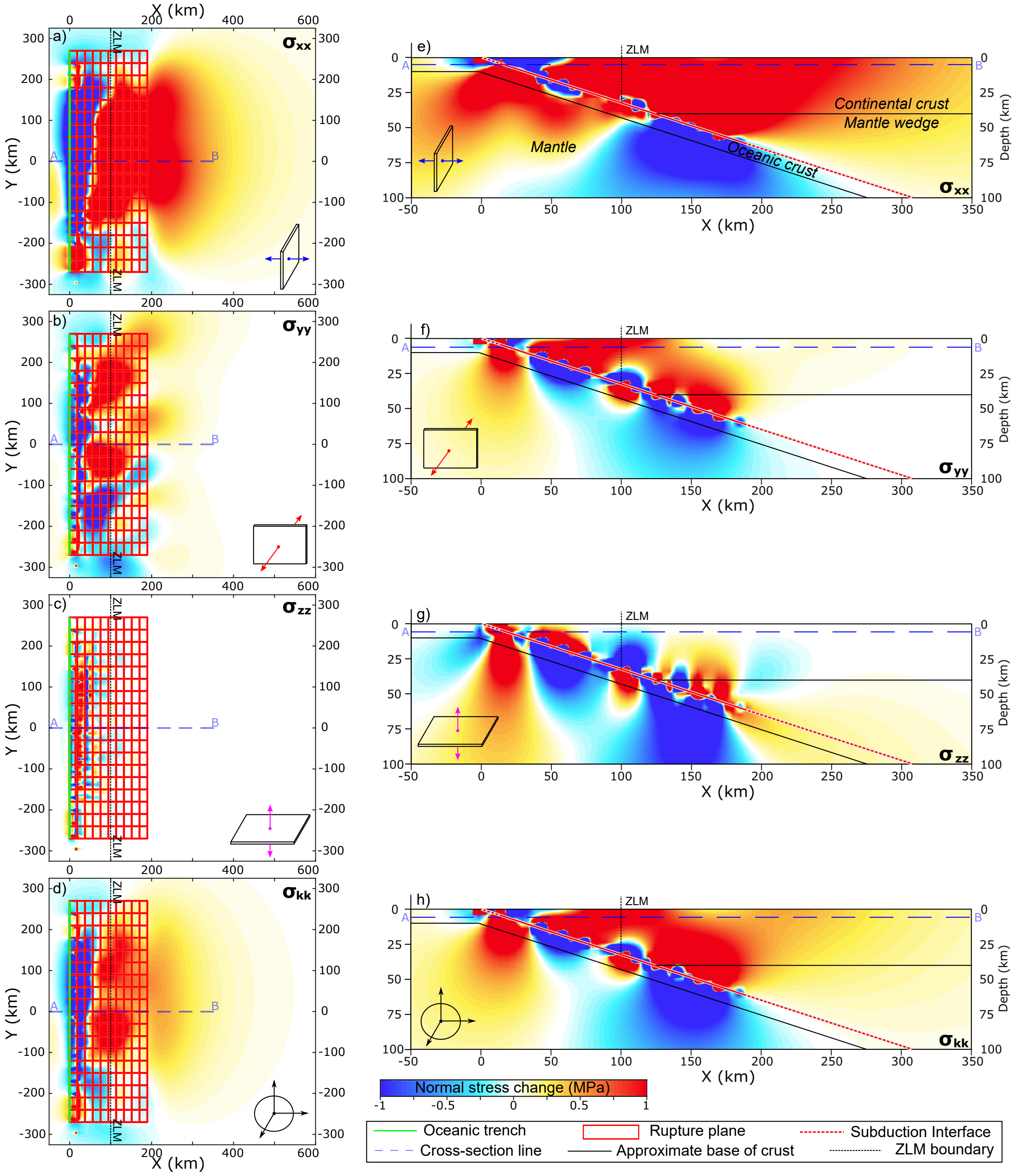

Figure 5.15: a-c) Plan view maps at 5 km depth of the three components of normal stress change and d) the mean stress change induced by the 2010 M_w 8.8 Maule Chile earthquake, using the finite fault model of Hayes 2010 from the NEIC (http://earthquake.usgs.gov/earthquakes/eventpage/official20100227063411530_30/finite-fault). e-g) Cross-sections along the line A-B through the centre of the model, showing the three components of normal stress change and h) the mean stress change. Young's modulus of model is 80 GPa. earthquake. The ZLM is located in the area x = 100-500 km.

5.6 Discussion

5.6.1 Regime implications for magmatic systems

We have defined a set of stress change regimes produced by typical subduction interface earthquakes, based on the magnitude, orientation, and gradient with depth of static stress changes within the ZLM. All three of these components of the static stress change may have implications for any potential impact on magmatic systems. We focus our discussion on how the different stress change regimes may favour either magma storage or ascent. Regimes which favour magma ascent are more likely to lead to volcanic unrest and possibly eruption. In general, clamping of vertical pathways and unclamping of horizontal pathways is expected to favour magma storage, whereas clamping of horizontal pathways and unclamping of vertical pathways will favour magma ascent. Unclamping of vertical pathways which increases in magnitude towards the surface may also generate a favourable pressure gradient for magma ascent.

Larger earthquakes produce strong static stress changes over the greatest crustal volume and so have greater potential to affect magmatic systems. However, we also highlight the importance of the spatial distribution of the stress changes regimes. For a given earthquake magnitude, the greatest stress changes occur in Regime 2 near the base of the continental crust. The peak stress changes in the relatively narrow Regime 2 are around an order of magnitude greater than in any other regime. In Regime 2, peak unclamping of all pathways generally occurs near the base of the continental crust, producing a large positive mean stress change with high potential to disturb magmatic bodies accumulated near the base of the crust (e.g. Hildreth & Moorbath 1988, Annen et al. 2006). However, due the narrowing of the lobe of unclamping of horizontal pathways above the down-dip rupture tip (Figure 5.4g), some areas in Regime 2 display a reduction in unclamping or a transition to clamping of horizontal structures near the subduction interface (e.g. Figure 5.5c). While this causes a reduction in the overall expansion, the combination of very high magnitude unclamping of vertical pathways and clamping or low magnitude unclamping of horizontal pathways may create favourable conditions for ascent of magmas from the lower crust.

Regimes 1, 4, and 6 also display characteristics which may strongly favour magma ascent. Regime 4 combines clamping of horizontal pathways with unclamping of arc-parallel pathways that increases in magnitude towards the surface. This combination of stress changes may be especially favourable for encouraging flow of magma out of horizontal reservoirs and upwards into vertical dykes. Regime 1 stress changes are very similar to Regime 4, however, Regime 1 stress changes may not be very widespread in real-world scenarios (Figure 5.14). Regime 6 combines clamping of horizontal pathways with unclamping of arc-perpendicular pathways that increases in magnitude towards the surface. Although the magnitudes of stress change are lower in Regime 6 than in Regime 4, unclamping of arc-perpendicular pathways may be important in compressive volcanic arcs where pre-existing cross-arc structures are more favourably orientated for fluid flow than arc-parallel structures (e.g. Lara et al. 2006, Cembrano & Lara 2009).

Regime 3 combines moderate magnitude clamping of horizontal pathways and unclamping of arc-parallel pathways in the mid-crust, which may encourage magma ascent. Regime 5 exhibits unclamping of arc-parallel pathways which increases in magnitude towards the surface, while Regime 7 displays unclamping of arc-perpendicular pathways which increases towards the surface, both of which may encourage magma ascent. However, horizontal pathways are unclamped at depth in Regimes 5 and 7, which may encourage accumulation of magma near the base of the crust, favouring magma storage at depth. Although the magnitudes of stress change are lowest in Regimes 5 and 7, they cover the largest area. Thus, while subduction thrust earthquakes generally encourage magma ascent by unclamping vertical pathways, large areas of the volcanic arc may experience unclamping of horizontal pathways at depth.

5.6.2 Threshold stress changes

In studies of earthquake triggering, a Coulomb static stress change value of 0.1 MPa is sometimes used as a threshold value, above which the triggering of earthquakes might be expected (Grasso & Sornette 1998, Freed 2005, Mulargia & Bizzarri 2014). Adopting this as a threshold for affecting magmatic systems, $M_w > 7$ earthquakes are required to produce static stress changes exceeding the threshold within the ZLM, with $M_w > 8$ earthquakes required to produced 0.1 MPa stress changes at more typical trench-arc distances of 200-300 km (Figure 5.6). Other studies suggest a lower threshold value of 0.01 MPa (Reasenberg & Simpson 1992, King et al. 1994, Hardebeck et al. 1998), whilst some suggest that a threshold value does not exist and that seismicity rate obeys the rate-state friction law for coulomb stress changes of 1 kPa or less (Ziv & Rubin 2000, Kilb et al. 2002, Scholz et al. 2019). Therefore, any magnitude of stress change could in theory induce a change in some part of the magmatic system. However, stress changes lower than the twice-daily tidal peak values on the order of 10^{-3} MPa may be considered insignificant, meaning subduction interface earthquakes of $< M_w$ 7 are unlikely to affect magmatic systems. This may explain the lack of correlation between smaller earthquakes and volcanic eruptions (e.g. Sawi & Manga 2018).

Larger stress changes will push a greater proportion of the system above any given failure threshold (or alternatively, suppress the system below failure) and therefore larger earthquakes have a greater likelihood of producing a significant effect (e.g. Meier et al. 2014). Without knowing the state of the magmatic system prior to the earthquake, it is impossible to say what magnitude of stress change is necessary to cause a significant effect. However, even large earthquakes may not produce detectable changes. For example, the stress change regime may favour magma storage over magma ascent, and even if the regime favours magma ascent, very few dykes ever reach the surface (Gudmundsson 1984*a*). Hence, although there is some statistical evidence for eruption triggering (Linde & Sacks 1998, Sawi & Manga 2018), there may be many more currently undetectable changes in the deeper magmatic system. The state of the magmatic system at the time of the earthquake is also important, with more critically stressed systems that are closer to eruption more likely to be significantly affected (Watt et al. 2009).

5.6.3 Properties of the magmatic system

Although we do not quantitatively model the response of the magmatic system, we consider an illustrative example of how the evolution of the volcanic arc may influence the response to static stress changes. A magma-filled crack of fixed length (e.g. a dyke connecting two magma reservoirs) will respond to changes in the external stress field by changing its opening thickness

$$w = \frac{2l(1-\nu^2)P_o}{E} \quad , \tag{5.10}$$

where w is the half-thickness at the centre of the crack and l is the half-length of the crack (Sneddon & Lowengrub 1969). Making the assumption that the change in P_o is equal to the change in σ_n acting at the dyke wall (as may occur in a dyke where the internal magma pressure is buffered by a deeper magma reservoir) then the change in thickness of the dyke (Δw) caused by the earthquake is given by (increasing thickness positive)

$$\Delta w = \frac{2l(1-\nu^2)\Delta\sigma_n}{E} \quad . \tag{5.11}$$

Using typical dyke aspect ratios of 100:1 to 1000:1 (Gudmundsson 1984*b*, Kusumoto et al. 2013), and normal stress changes of 0.1 to 1 MPa (typical for M_w 8 and M_w 9 earthquakes respectively), Δw will increase on the order of 0.02 to 2%, using ν of 0.25 and E of 80 GPa (e.g. Bonali et al. 2015). Although the volumetric flow rate of magma in dykes is proportional to w^3 (Gudmundsson 2020), these are small changes. However, as a volcanic arc or part of a volcanic arc matures, it may heat up due to continued influx of magma and alter the mechanical properties of the system. Using a Young's modulus of 8 GPa, which may be more appropriate to heated rocks in mature magmatic systems (e.g. Rocchi et al. 2004, Bakker et al. 2016, Heap et al. 2020), the change in w will be an order of magnitude larger, potentially 20%, which will cause a significant effect on magma ascent rates. However, it should also be noted that a hotter, weaker system will act to dampen the transmission of stress changes from the earthquake, which may offset some of this effect.

5.6.4 Earthquakes as a control on magma ascent and storage

Magmatic processes operate across a range of timescales, from individual intrusive events, through periods of magmatic flare up, to entire magmatic epochs (De Saint Blanquat et al. 2011). Therefore, the controls on magmatic systems likely also span multiple timescales; the long-term averaged tectonic stress may be important over the lifespan of the magmatic system, whereas shorter-term changes associated with the earthquake cycle may have more of an influence on individual intrusions or pulses of magmatism.

Observing the effects of earthquakes on deep magmatic systems is challenging, however, we have suggested some possible first-order effects using an homogeneous elastic halfspace model and considering the magmatic system as a series of planar pathways. More advanced modelling should consider density and rigidity layering of the crust (Gudmundsson 2006, Maccaferri et al. 2011, Rivalta et al. 2015, Kavanagh et al. 2017) and the inclusion of magma reservoirs with different geometries and time dependent, non-elastic rheologies (Albino et al. 2010, Segall 2016, Currenti 2018, Liao et al. 2018). The effect of the evolving crustal stress field over one or more earthquake cycles, due to processes such as viscoelastic relaxation of the lower crust, afterslip, and interseismic stress recovery is also an interesting question (e.g. Hardebeck & Okada 2018). The role of earthquakes in influencing magma ascent and storage depends on the relative importance of static stress changes compared with other mechanisms of changing magmatic overpressures, such as magma recharge and crystallisation and volatile exsolution (e.g. Tait et al. 1989, Gregg et al. 2013, Degruyter et al. 2016). The extent to which static stress changes alter the crustal stress field is therefore an important question (e.g. Hardebeck & Okada 2018). While earthquake-induced stress changes may likely be smaller than those caused by internal magmatic processes, the timescales over which static stress changes are applied may be much shorter.

5.7 Conclusions

The stress change regimes defined here may be used to better understand how magmatic systems may respond to static stress changes caused by megathrust earthquakes at subduction zones. Overall, the stress changes caused by subduction zone earthquakes favour magma ascent, since horizontal compressive stresses are relaxed. However, the more complete analysis of the stress changes performed here reveals extra complexity in the gradient with depth of horizontal stress change and in the vertical component of stress change. Notably, large regions of the volcanic arc may experience unclamping of horizontal pathways at depth, therefore favouring magma storage near the base of the crust. The responses of magmatic systems to earthquake-induced stress changes may depend on the stress change regime and magnitude experienced, as well as the state of the magmatic system, with a greater impact expected for weaker, more thermally mature volcanic arcs.

CHAPTER 6

DISCUSSION AND CONCLUSIONS

6.1 Thesis summary

This thesis contributes to furthering our understanding of the relationships and interactions between large tectonic earthquakes and magmatism. This includes an investigation into the transcrustal magmatic system concept using magnetotellurics (Chapter 2), statistical analyses of modern global earthquake and eruption records, both at the global scale over decadal timescales (Chapter 3) and at more localised scales over timescales of months to several years (Chapter 4), and modelling of the effects of static stress changes from subduction zone megathrust earthquakes on magmatic arcs (Chapter 5). To conclude, this final chapter now summarises the scientific contributions of this thesis and highlights opportunities for the continued development of the work presented here.

6.2 Transcrustal magmatic systems

As a foundation for the subsequent chapters, Chapter 2 combines reviews of magnetotelluric surveys at Andean volcanoes and laboratory-derived electrical conductivity relationships to develop simplified models of magmatic systems. In general, the observed electrical conductivity anomalies beneath Andean volcanoes are consistent with a three layer model comprising a deep (>10 km) partial melt reservoir, overlain by intermediate depth (≈5 km) saline magmatic fluids, and capped by shallow (<3 km) clay alteration layers. However, additional geophysical and petrological data suggest that partial melt is also present, at least transiently, at intermediate depths. Therefore, intermediate depth anomalies beneath arc volcanoes are likely characterised by coexisting partial melt and exsolved saline magmatic fluids, which may represent active porphyry (copper) systems.

The deep electrical conductivity anomalies attributed to partial melt are generally vertically extensive, consistent with a transcrustal magmatic system (Sparks et al. 2019). The deep and intermediate depth anomalies are also often connected, further supporting the transcrustal concept. However, where these anomalies are not connected, the magnetotelluric data are more consistent with a deeper reservoir episodically supplying a shallower reservoir (Gudmundsson 2006). Several of the intermediate depth electrical conductivity anomalies imaged beneath Andean volcanoes form dipping structures (e.g. Lastarria, Laguna del Maule, and Tinguiruirica), which may highlight the importance of structures in controlling magma and magmatic fluid pathways in the upper crust.

The important role of saline magmatic fluids in generating the intermediate depth electrical conductivity anomalies is inferred as the electrical conductivity of partial melt is too low to explain some of the intermediate depth anomalies beneath Andean volcanoes. Direct sampling of hypersaline fluids from an intermediate depth anomaly at Kakkonda also supports this interpretation (Uchida et al. 2000). Intermediate depth brine lenses may have important economic potential through the extraction of high enthalpy geothermal energy and important metals (Watanabe et al. 2017, Blundy et al. 2021). However, only a few of the studied Andean volcanoes (e.g. Láscar and Laguna del Maule) display very strong ($\geq$1 S m^{-1}) intermediate depth electrical conductivity anomalies indicative of hypersaline brines with large fluid fractions (>0.1). This observation is consistent with the rarity of large well-mineralised porphyry copper deposits, despite porphyry-type alteration being common in volcanic arcs (Richards 2018).

Chapter 2 shows how the magnetotelluric method can be used to interpret the locations and quantities of partial melt and magmatic fluid present beneath subduction zone volcanoes; extending this work to review magmatic systems in other tectonic settings could provide further insights into the nature of crustal magmatism. However, interpretations of magmatic systems using magnetotelluric data alone are far from unique. Therefore, to further constrain the interpretation of magnteotelluric data, gaps in the available laboratory-derived electrical conductivity relationships must be addressed. In particular, it would be useful to have more generalised electrical conductivity relationships for silicate melts, while the electrical conductivity of hypersaline brines also requires further study. Most importantly, the spatial connectivity of melt and fluids as a function of pressure, fluid and rock composition, and fluid fraction are poorly constrained, especially at low fluid fractions and in crystalline rocks.

6.3 Spatiotemporal tectono-magmatic relationships

Chapter 3 and Chapter 4 use statistical methods to investigate the spatiotemporal relationships between large earthquakes and volcanic eruptions. At the global scale, Chapter 3 reveals a positive correlation between seismic moment release and volcanic eruption rates, with decadal timescale fluctuations between periods of high and low seismic and volcanic activity. Randomised simulations shows that the chance of this correlation occurring by chance is <5%. However, at regional scales, not all regions display the same correlation, and for those regions which do, the correlation is neither as strong nor as significant as it is at the global scale. This suggests that the triggering of volcanic eruptions following nearby large earthquakes (e.g. Linde & Sacks 1998) does not cause the observed global correlation. The cause of the global correlation therefore remains unclear, although potential explanations include the triggering of distant eruptions (>1000 km) by earthquake-induced dynamic stresses, modulation of global earthquake and eruption rates by variations in Earth's rotational velocity, or natural synchronisation of earthquakes and eruptions over repeating cycles.

Over shorter timescales (several months to 5 years) and more localised scales (<1000 km), Chapter 4 finds that post-earthquake eruption rates are around 25% above average within 750 km and timescales of at least 1 year, and possibly 2 to 4 years, following $M_w \geq 7$ earthquakes. This finding is equivalent to the eruption triggering reported by previous studies, with eruption rates 25% above average being intermediate between the approximately 10% increase in eruption rates reported by Sawi & Manga (2018) and the approximately 50% increase found by Nishimura (2017). Above average post-earthquake eruption rates can be explained by stress changes from large earthquakes destabilising magmatic systems, leading to volcanic eruptions (Hill et al. 2002). Furthermore, for individual earthquakes, above average post-earthquake eruption rates tend to be more pronounced if the pre-earthquake eruption rates were also above average. This suggests that many eruptions do not completely release the built up magmatic pressures, either at an individual volcano or across a volcanic region more generally, so that earthquakes which occur during times of high volcanic activity coincide with more volcanoes in near critical states. However, in general, pre-earthquake eruption rates are around 10% below average within 750 km and timescales of 182 days, and possibly 1 year, prior to $M_w \geq 7$ earthquakes. The cause of these below average pre-earthquake eruption rates at local to regional scales is unclear. Clamping of magmatic pathways prior to earthquakes could be one possible explanation, although as described in Chapter 5, this would be most consistent with reverse faulting earthquakes, whereas Chapter 4 shows that the below average pre-earthquake eruption rates are actually associated with deep earthquakes and shallow normal or strike-slip earthquakes.

To investigate the causes of the spatiotemporal relationships between large earthquakes and volcanic eruptions, Chapter 4 also analyses the effects of earthquake magnitude, slip orientation, and depth. This analysis reveals that eruption rate changes associated with deep earthquakes (≥70 km) are of greater magnitude and more significant than eruption rate changes associated with shallow earthquakes (< 70 km). This is especially the case for the below average pre-earthquake eruption rates, but it also applies to the above average post-earthquake eruption rates. The reasons for this are unclear, but given that deep earthquakes mainly occur within subducted slabs, the location of deep earthquakes below the volcanic arc could be important. Alternatively, deep subduction zone earthquakes may be more directly related to magma genesis at subduction zones, which occurs due to the release of fluids from the subducted slab (Tatsumi 1989). By contrast, shallow earthquakes show different eruption rate variations depending on their slip orientation; shallow reverse earthquakes generally display above average eruption rates, while shallow normal earthquakes generally show below average eruption rates, and shallow strike-slip earthquakes generally exhibit below average pre-earthquake eruption rates and above average post-earthquake eruption rates. The reasons for this relationship between the prevailing crustal stress regime and volcanic eruption rates are unclear.

Together, Chapter 3 and Chapter 4 reveal an interesting set of spatiotemporal relationships between large earthquakes and volcanic eruptions across a range of scales. Understanding these relationships has implications for earthquake and volcanic risk, as well as understanding tectono-magmatic processes in general. However, the processes responsible for the correlation between earthquake and eruption rates at the global scale, as well as the below average eruption rates prior to large earthquakes at more localised scales, remain unclear and require further study. The same is also true for the apparent importance of deep earthquakes and the different eruption rate variations associated with earthquakes of different slip orientations. Over the coming decades, further scrutiny of these relationships will be possible using new earthquake and eruption data, with longer time-series allowing for more robust statistical analyses. Furthermore, recent advances in remote sensing of volcanoes (Biggs & Pritchard 2017) will decrease the number of eruptions recorded with uncertain start dates. Additionally, remote sensing of volcanoes has started to identify non-eruptive responses to large earthquakes (e.g. Pritchard et al. 2013, Hill-Butler et al. 2020), and understanding these will shed further light on tectono-magmatic interactions.

6.4 Tectono-magmatic interactions

Chapter 5 develops a new approach to considering static stress changes produced by large earthquakes, which involves calculating the spatial distribution of the normal stress changes resolved in three mutually-perpendicular directions. In general, for magmatic systems, increased compressive normal stresses (‘clamping’) acting on a magmatic pathway are expected to inhibit magma transport along that pathway, whereas decreased compressive normal stresses (‘unclamping’) are expected to promote magma transport along that pathway (Bonali et al. 2013). Chapter 5 applies this method to subduction zone megathrust earthquakes, for which the general static stress change is the relaxation of horizontal compressional stresses in the volcanic arc (Walter & Amelung 2007). Analysing the normal stress change distributions confirms that unclamping of arc-parallel structures is the main change, but there are also complexities in the normal stress changes on arc-perpendicular and horizontal structures, as well as variation in normal stress changes with depth.

To better understand the complex spatial distribution of stress changes associated with earthquakes, Chapter 5 defines stress change regimes depending on the normal stress changes resolved in three mutually-perpendicular directions and how these vary with depth. For subduction zone megathrust earthquakes, seven stress change regimes can be defined. Three of these regimes strongly encourage magma ascent in dykes by unclamping vertical magmatic pathways with increasing magnitude towards the surface, combined with clamping horizontal pathways. However, two of the regimes may encourage stalling and storage of magma in sills near the base of the crust by unclamping horizontal magmatic pathways at depth. These different regimes, combined with heterogeneous magmatic pathway orientations in volcanic arcs, may help explain the different observed responses of volcanoes to large earthquakes (Ebmeier et al. 2016, Farías & Basualto 2020). In particular, following megathrust earthquakes, the volcanic arc adjacent to the rupture zones experiences unclamping of vertical arc-parallel structures across all crustal depths, which could encourage magma ascent from deep crustal reservoirs or magma or magmatic fluid ascent from intermediate depth reservoirs (as described in

Chapter 3). However, except for very large earthquakes or short trench-arc distances, the volcanic arc adjacent to the rupture zone also experiences unclamping of horizontal structures with increasing magnitude with depth, which may instead favour magma storage in deep reservoirs.

The modelling in Chapter 5 makes some testable predictions that could be further investigated using observational data. For example, stress changes in the volcanic arc are greater following larger magnitude earthquakes, suggesting that larger earthquakes should have a greater impact on the magmatic system. However, Chapter 4 shows that statistical evidence for eruption triggering is actually weaker for $M_w \geq 8$ earthquakes than for M_w 7 earthquakes. As noted in Chapter 4, this could simply reflect the low number of $M_w \geq 8$ earthquakes currently recorded in modern earthquake catalogues, with more data being needed to properly test this. Alternatively, given that shallow thrust earthquakes represent approximately half of all recorded $M_w \geq 8$ earthquakes, the lack of evidence for eruption triggering following $M_w \geq 8$ earthquakes may suggest that unclamping of horizontal structures at depth following large shallow thrust earthquakes, which favours magma storage over magma ascent, is an important mechanism.

Similarly, the magnitude of unclamping on vertical arc-parallel structures adjacent to the earthquake rupture zone is greater than the magnitude of unclamping on vertical arc-perpendicular structures beyond the earthquake rupture tips. This suggests that the effects on the magmatic system may be different adjacent to the rupture zone and beyond the rupture tips. However, when considering all subduction thrust earthquakes, Figure 6.1 shows that it is difficult to identify any difference in the locations of eruptions before and after the earthquakes. This may be partly due to the fact that the different earthquakes have different rupture lengths, meaning that the parts of the volcanic arc that are adjacent to and beyond the rupture tips varies between earthquakes. Alternatively, this could represent the role of other potentially important factors such as the regional stress field, which itself is influenced by factors such as the dip of the subducting slab and pre-existing structures. Using the stress change regime approach for individual earthquakes while considering these additional factors may help further understand how large subduction thrust earthquakes affect magamatic systems.

The stress change regimes approach in Chapter 5 could also be extended to other earthquake types. However, it would also be useful to model the effects of these static stress changes explicitly, rather than only considering clamping and unclamping of magmatic pathways. For example, modelling could consider the effects of stress changes on magma (and brine) reservoirs of different shapes and physical properties, as well as considering non-elastic effects such as visco-elastic and poro-elastic responses of the reservoirs to stress changes (e.g. Gudmundsson 2006, Albino et al. 2010, Liao et al. 2021).

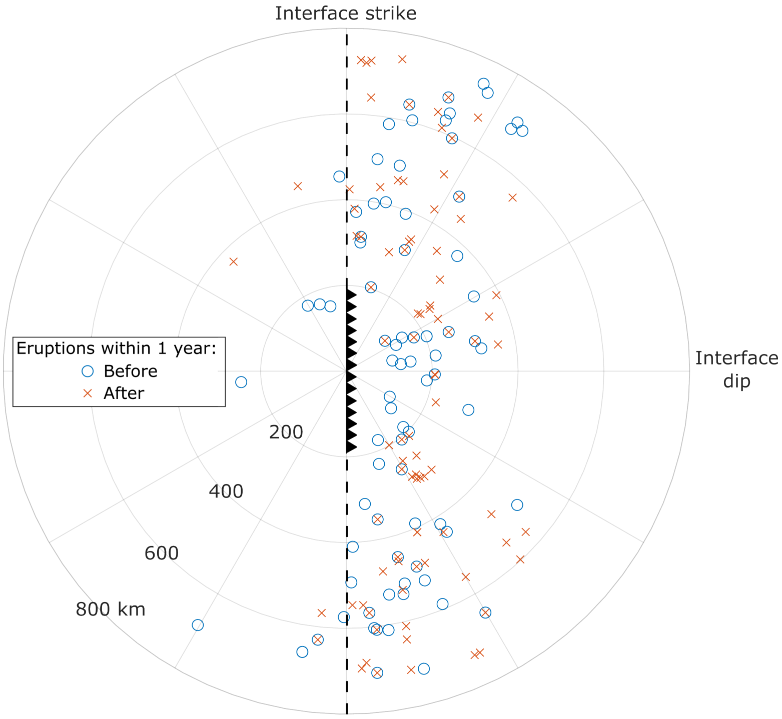

Figure 6.1: The locations of VEI ≥ 2 eruptions within 750 km and 1 year before (blue circles) and after (red crosses) $M_w \geq 7$ subduction megathrust earthquakes. The earthquake fault planes have been rotated such that each earthquake centroid is located at the centre of the plot, with the earthquake fault plane (i.e. the interface between the subducting slab and the overlying continental crust) trending north-south and dipping to the east; note that due to the different earthquake sizes, the earthquake rupture tips will be located at different distances from the centre of the plot. Most eruptions are located in the hanging wall of the earthquake fault planes, consistent with volcanic arcs located in the continental crust above the subduction interface and mantle wedge. The earthquake and eruption records used in this analysis are the same as described in Chapter 4, with subduction interface thrust earthquakes selected based on suitable locations and focal mechanisms consistent with subduction interface thrusting.

6.5 Synthesis and outlook

This thesis demonstrates the importance and complexity of tectono-magmatic relationships (Figure 6.2). Some of these relationships can be explained by the effects of earthquake-driven stress changes on magmatic systems, while others remain unexplained and require further investigation. However, the crustal stress field also varies across a range of distances and timescales due to other processes, such as topographic changes. Understanding how crustal stress field changes across a range of scales interact within the broader stress regime controlled by global plate tectonics, and how this affects the development of magmatic systems and the locations of melt and fluid in the crust, is of key importance. This is starting to be considered from a porphyry copper perspective, where the importance of long-term compression leading to the trapping and evolution of magmas at depth, prior to relatively faster relaxation of these stresses and the rise of fertile magmas and the formation of porphyry copper deposits, has been proposed (Tosdal & Richards 2001, Bertrand et al. 2014). Going forwards, this approach should be continued across magmatic systems more generally, with the effects of even shorter-term stress changes like those associated with earthquakes, also being considered.

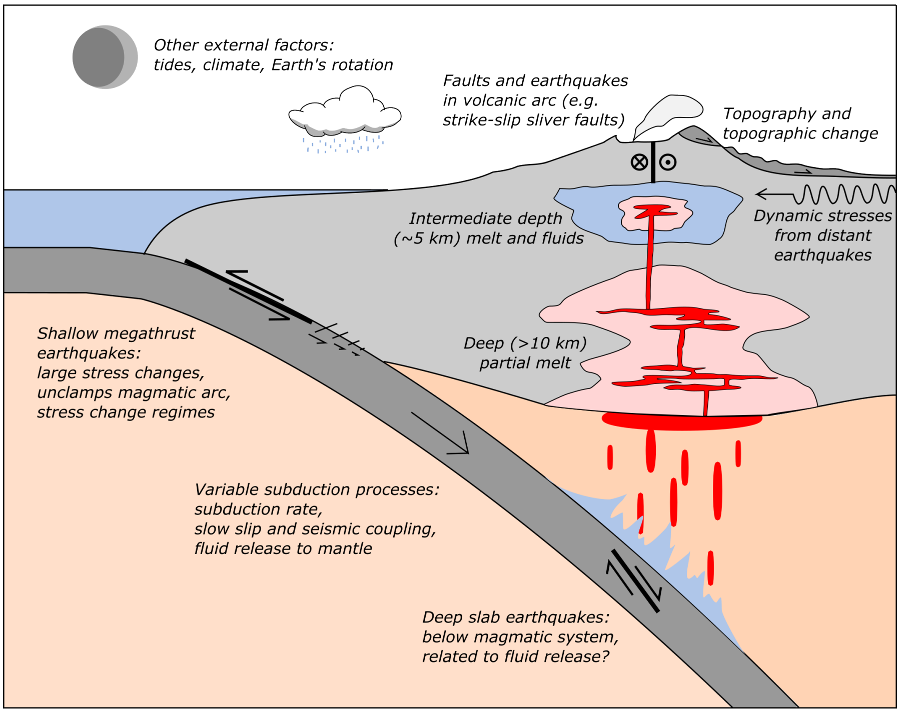

Figure 6.2: Summary representation showing the complexity of tectono-magmatic relationships.

APPENDIX A

ANDEAN VOLCANO MAGNTOTELLURIC IMAGES

This appendix contains images of the electrical conductivity anomalies imaged by the Andean volcano magnetotelluric studies described in Chapter 2, given here from north to south.

Paniri (Mancini et al. 2019):

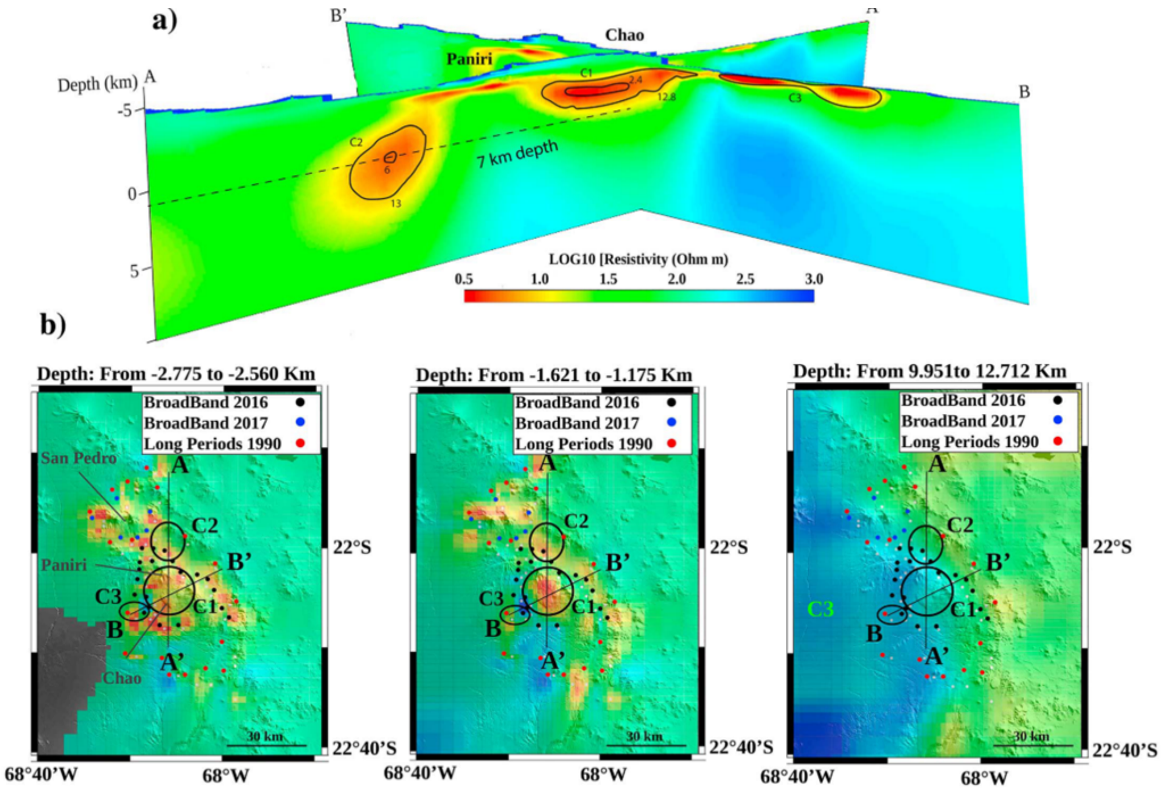

Uturuncu (Comeau et al. 2016):

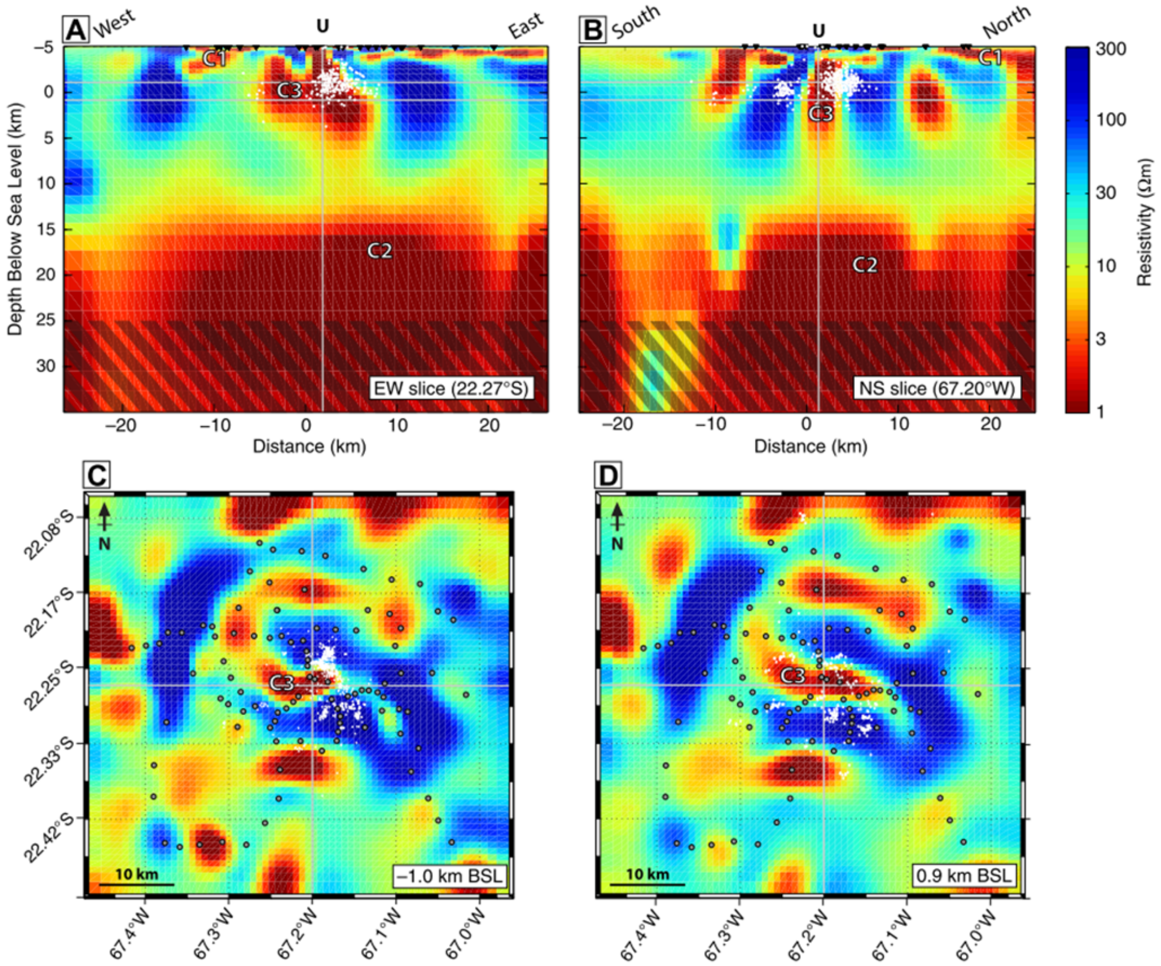

Láscar (Díaz et al. 2012):

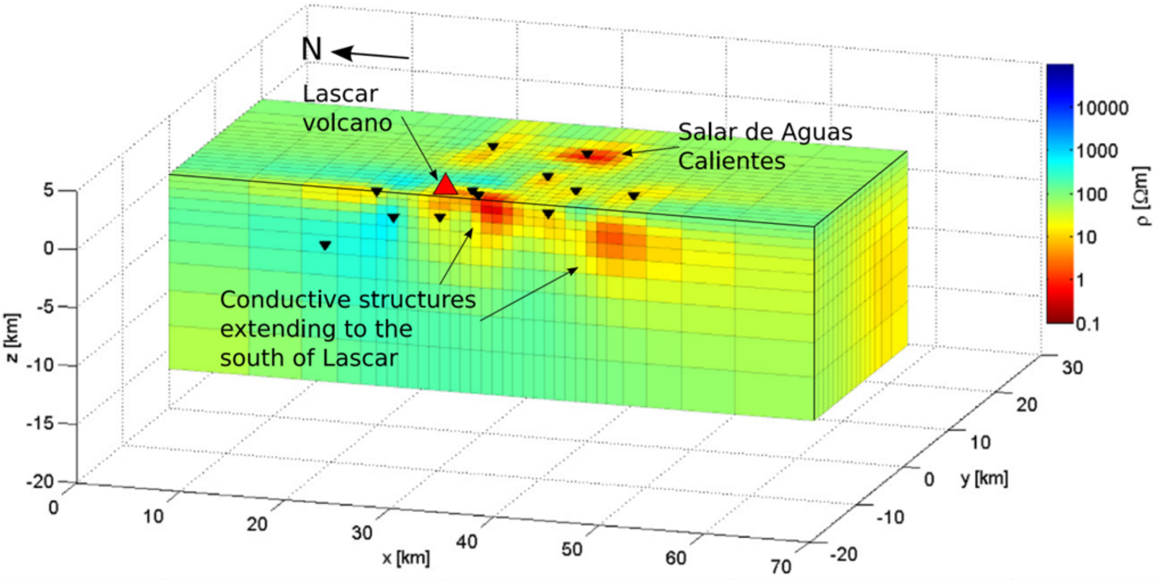

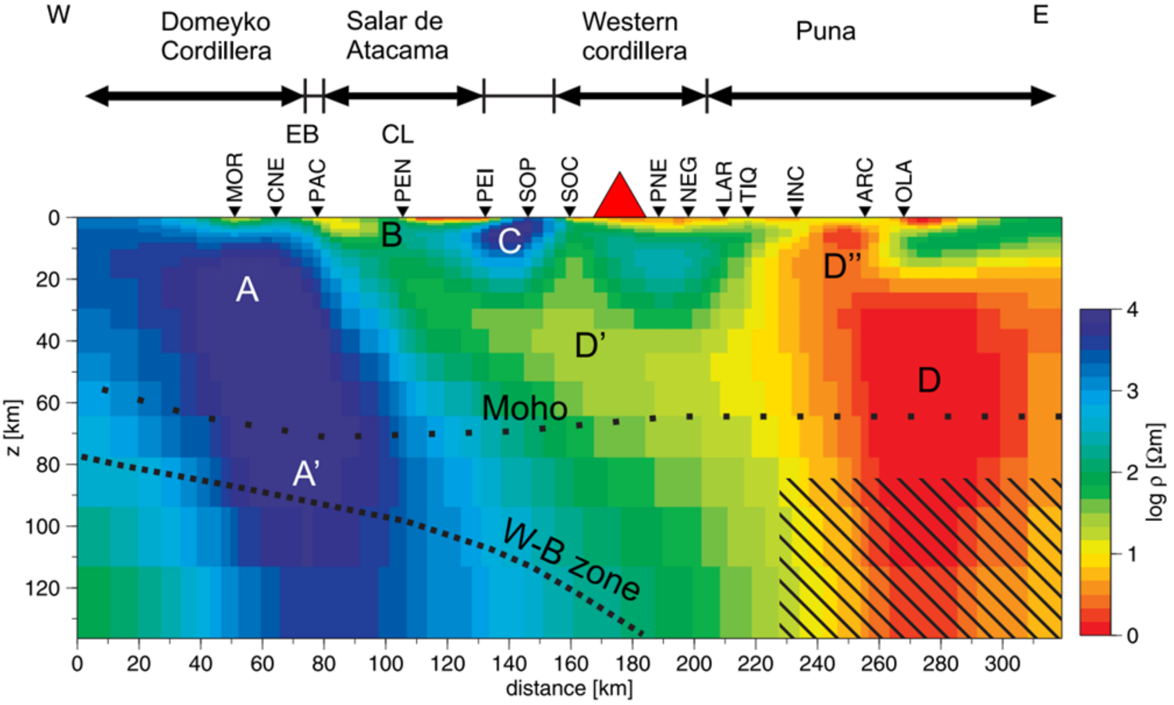

Lastarria (Díaz et al. 2015):

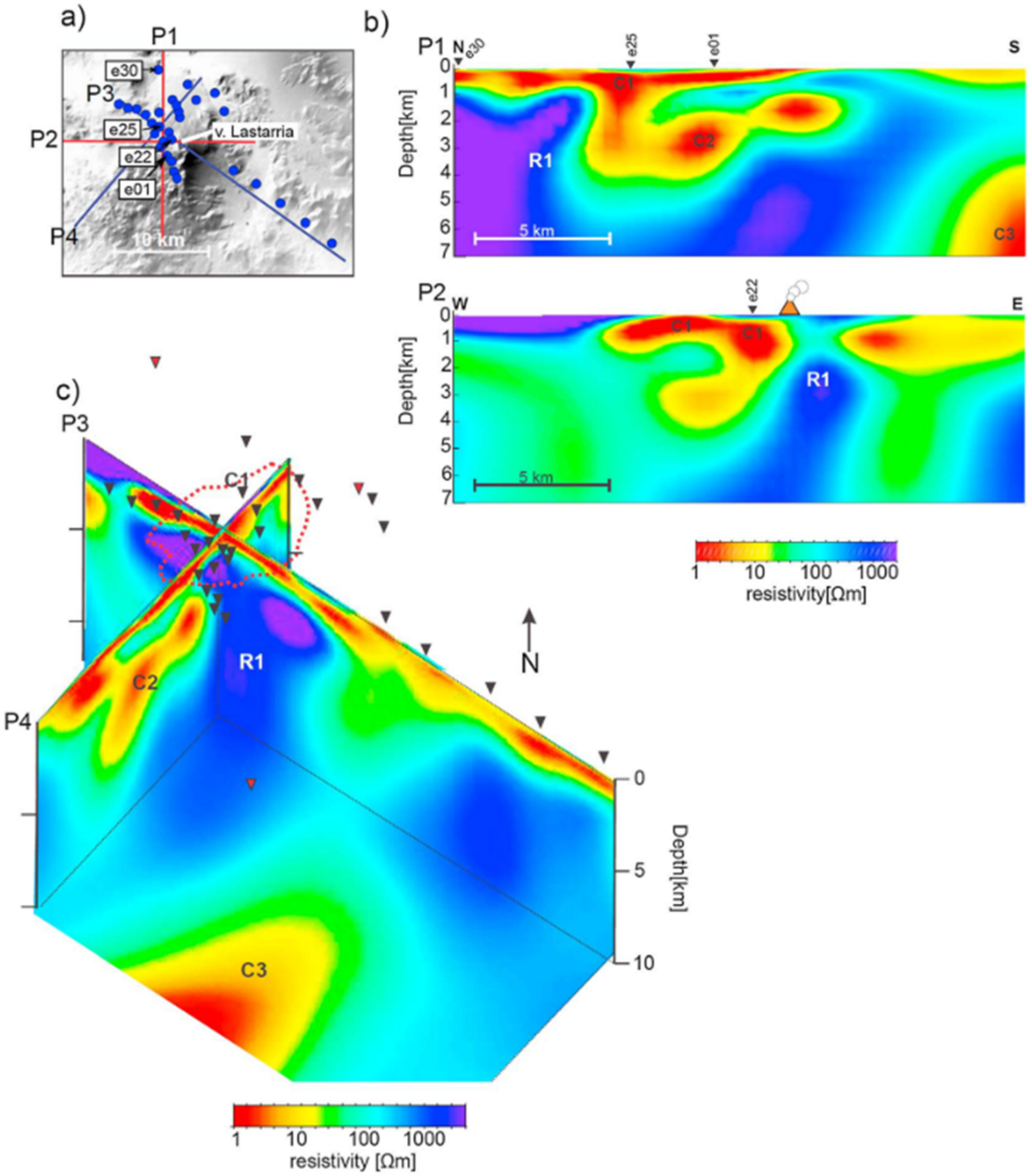

Laguna del Maule (Cordell et al. 2018):

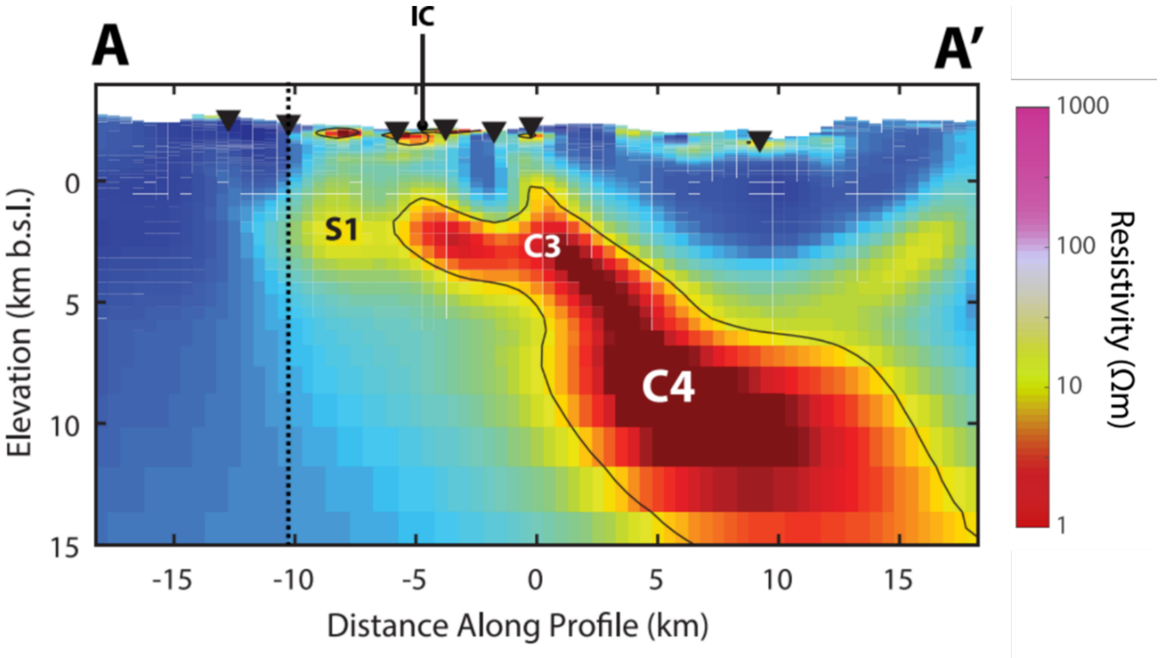

Tinguiruirica (Pearce et al. 2020):

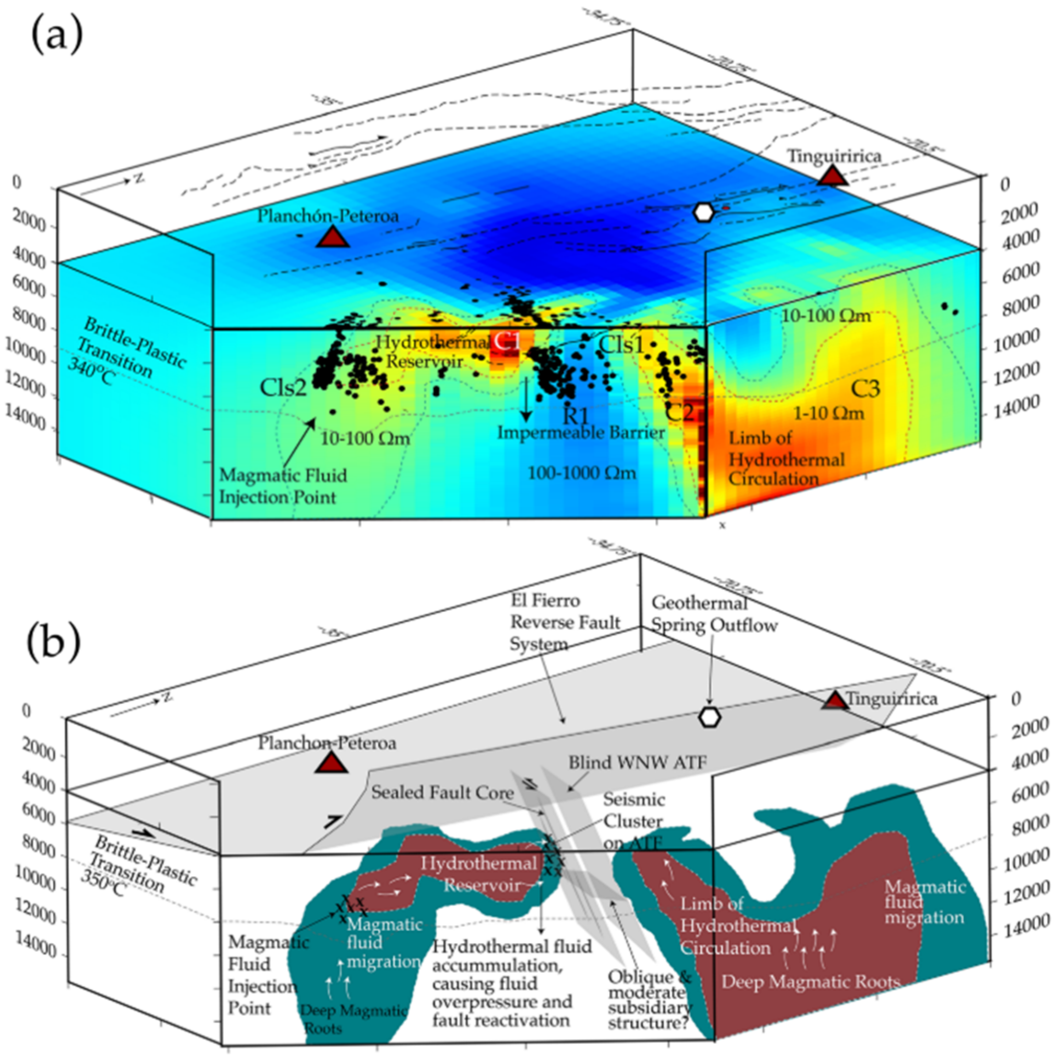

Villarrica (Pavez et al. 2020):

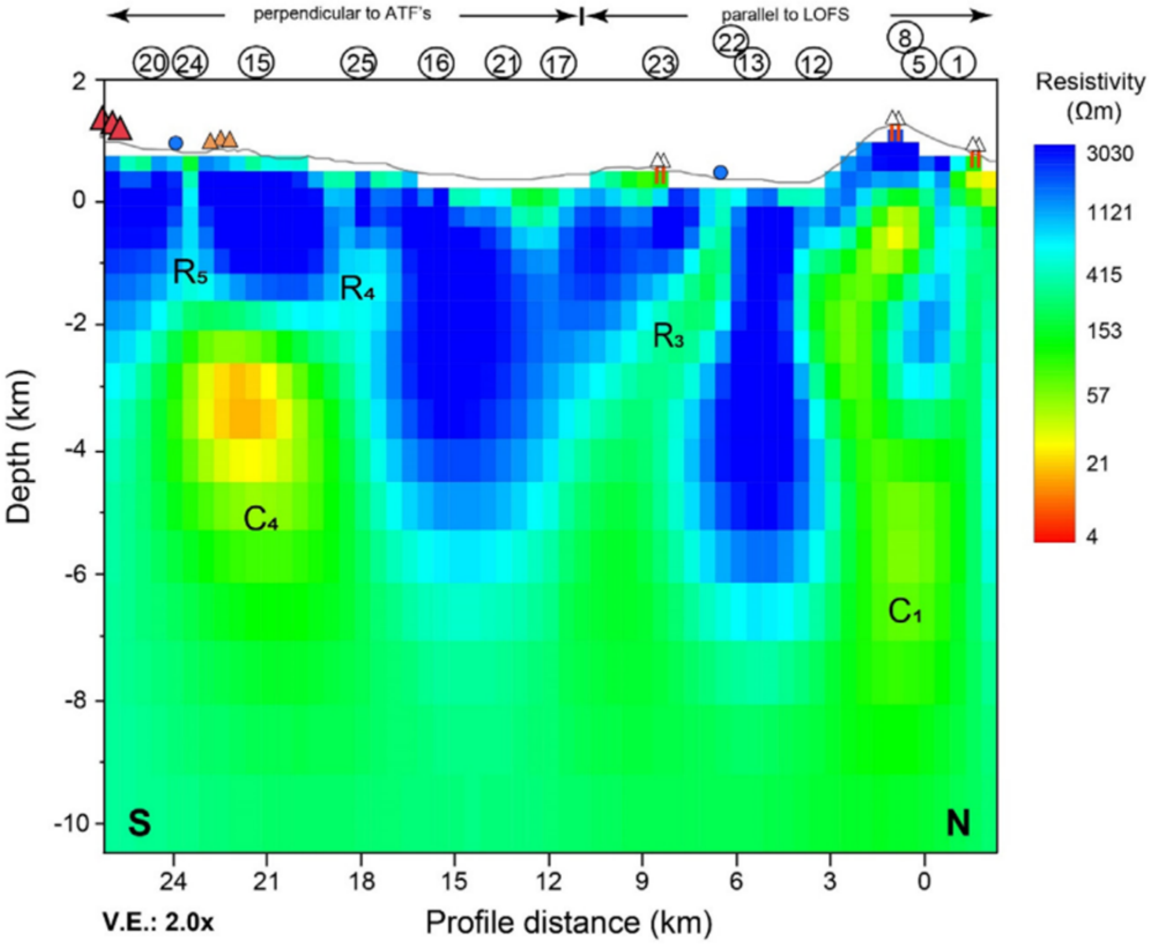

Osorno (Díaz et al. 2020):

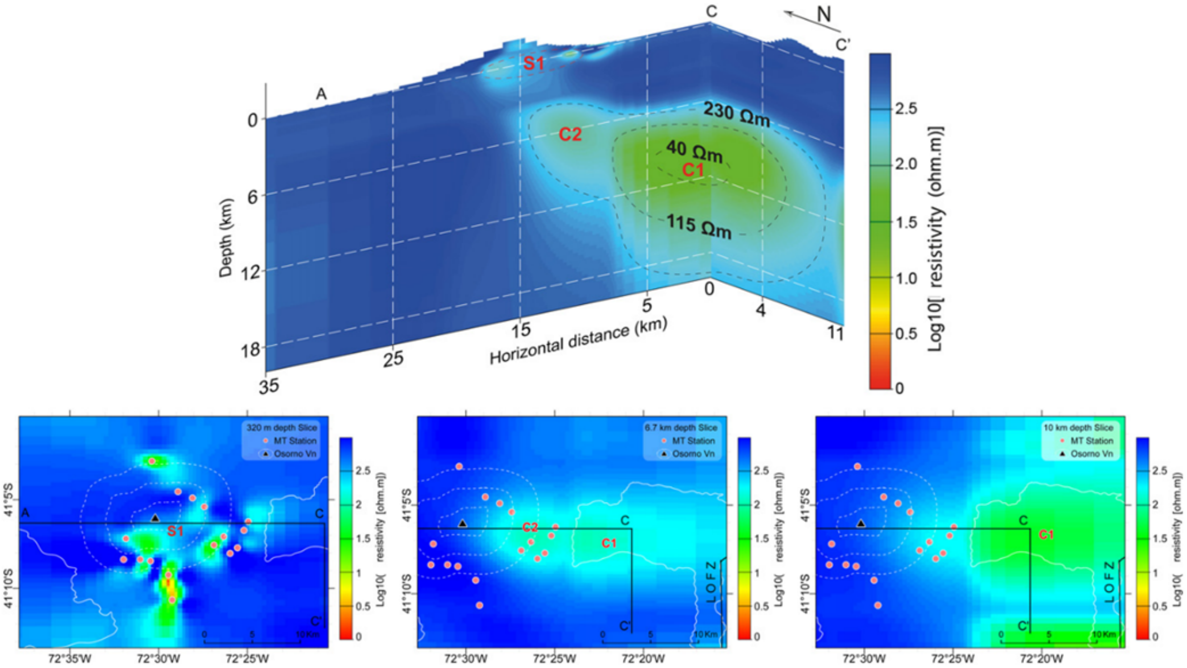

BIBLIOGRAPHY

Acocella, V. (2014), 'Structural control on magmatism along divergent and convergent plate boundaries: Overview, model, problems', *Earth-Science Reviews* **136**, 226–288.

Acocella, V., Bellier, O., Sandri, L., Sébrier, M. & Pramumijoyo, S. (2018), 'Weak tectono-magmatic relationships along an obliquely convergent plate boundary: Sumatra, Indonesia', *Frontiers in Earth Science* **6**, Article 3.

Acocella, V. & Funiciello, F. (2010), 'Kinematic setting and structural control of arc volcanism', *Earth and Planetary Science Letters* **289**(1-2), 43–53.

Afanasyev, A., Blundy, J., Melnik, O. & Sparks, S. (2018), 'Formation of magmatic brine lenses via focussed fluid-flow beneath volcanoes', *Earth and Planetary Science Letters* **486**, 119–128.

Aizawa, K., Koyama, T., Hase, H., Uyeshima, M., Kanda, W., Utsugi, M., Yoshimura, R., Yamaya, Y., Hashimoto, T., Yamazaki, K. et al. (2014), 'Three-dimensional resistivity structure and magma plumbing system of the Kirishima Volcanoes as inferred from broadband magnetotelluric data', *Journal of Geophysical Research: Solid Earth* **119**(1), 198–215.

Aizawa, K., Utsugi, M., Kitamura, K., Koyama, T., Uyeshima, M., Matsushima, N., Takakura, S., Inagaki, H., Saito, H. & Fujimitsu, Y. (2022), 'Magmatic fluid pathways in the upper crust: insights from dense magnetotelluric observations around the Kuju Volcanoes, Japan', *Geophysical Journal International* **228**(2), 755–772.

Alam, M. & Kimura, M. (2004), 'Statistical analysis of time-distance relationship between volcanic eruptions and great earthquakes in Japan', *Earth, planets and space* **56**(2), 179–192.

Albino, F., Pinel, V. & Sigmundsson, F. (2010), 'Influence of surface load variations on eruption likelihood: application to two Icelandic subglacial volcanoes, Grímsvötn and Katla', *Geophysical journal international* **181**(3), 1510–1524.

Allen, T. & Hayes, G. (2017), 'Alternative rupture-scaling relationships for subduction interface and other offshore environments', *Bulletin of the Seismological Society of America* **107**(3), 1240–1253.

Anderson, D. (1974), 'Earthquakes and the rotation of the earth', *Science* **186**(4158), 49–50.

Anderson, E. (1951), *The dynamics of faulting and dyke formation with applications to Britain*, Oliver and Boyd, Edinburgh.

Annen, C. (2009), 'From plutons to magma chambers: Thermal constraints on the accumulation of eruptible silicic magma in the upper crust', *Earth and Planetary Science Letters* **284**(3-4), 409–416.

Annen, C., Blundy, J. & Sparks, R. (2006), 'The genesis of intermediate and silicic magmas in deep crustal hot zones', *Journal of Petrology* **47**(3), 505–539.

Asano, Y., Saito, T., Ito, Y., Shiomi, K., Hirose, H., Matsumoto, T. et al. (2011), 'Spatial distribution and focal mechanisms of aftershocks of the 2011 off the Pacific coast of Tohoku Earthquake', *Earth, Planets and Space* **63**, 669–673.

Audétat, A. & Edmonds, M. (2020), 'Magmatic-hydrothermal fluids', *Elements: An International Magazine of Mineralogy, Geochemistry, and Petrology* **16**(6), 401–406.

Bachmann, O. & Huber, C. (2016), 'Silicic magma reservoirs in the earth's crust', *American Mineralogist* **101**(11), 2377–2404.

Bai, T., Thurber, C., Lanza, F., Singer, B., Bennington, N., Keranen, K. & Cardona, C. (2020), 'Teleseismic tomography of the Laguna del Maule volcanic field in Chile', *Journal of Geophysical Research: Solid Earth* **125**(8), e2020JB019449.

Bakker, R., Frehner, M. & Lupi, M. (2016), 'How temperature-dependent elasticity alters host rock/magmatic reservoir models: A case study on the effects of ice-cap unloading on shallow volcanic systems', *Earth and Planetary Science Letters* **456**, 16–25.

Barbosa, N., Hunziker, J., Lissa, S., Saenger, E. & Lupi, M. (2019), 'Fracture unclogging: A numerical study of seismically induced viscous shear stresses in fluid-saturated fractured rocks', *Journal of Geophysical Research: Solid Earth* **124**(11), 11705–11727.

Barrientos, S. E. (1994), 'Large thrust earthquakes and volcanic eruptions', *Pure and Applied Geophysics* **142**, 225–237.

Bautista, B., Bautista, M., Stein, R., Barcelona, E., Punongbayan, R., Laguerta, E. et al. (1996), Relationship of regional and local structures to Mount Pinatubo activity, *in*

C. Newhall & R. Punongbayan, eds, 'Fire and Mud: Eruptions and lahars of Mount Pinatubo, Philipines', University of Washington Press, Seattle, pp. 351–370.

Beaufort, D., Rigault, C., Billon, S., Billault, V., Inoue, A., Inoué, S., Patrier, P. & Ferrage, E. (2015), 'Chlorite and chloritization processes through mixed-layer mineral series in low-temperature geological systems - a review', *Clay Minerals* **50**(4), 497–523.

Bebbington, M. & Marzocchi, W. (2011), 'Stochastic models for earthquake triggering of volcanic eruptions', *Journal of Geophysical Research: Solid Earth* **116**(B5).

Becerril, L., Galindo, I., Gudmundsson, A. & Morales, J. (2013), 'Depth of origin of magma in eruptions', *Scientific reports* **3**(1), 1–6.

Becker, T., Hashima, A., Freed, A. & Sato, H. (2018), 'Stress change before and after the 2011 M9 Tohoku-oki earthquake', *Earth and Planetary Science Letters* **504**, 174–184.

Ben-Naim, E., Daub, E. & Johnson, P. (2013), 'Recurrence statistics of great earthquakes', *Geophysical Research Letters* **40**(12), 3021–3025.

Bendick, R. & Bilham, R. (2017), 'Do weak global stresses synchronize earthquakes?', *Geophysical Research Letters* **44**(16), 8320–8327.

Bertrand, E., Caldwell, T., Hill, G., Wallin, E., Bennie, S., Cozens, N., Onacha, S., Ryan, G., Walter, C., Zaino, A. et al. (2012), 'Magnetotelluric imaging of upper-crustal convection plumes beneath the Taupo Volcanic Zone, New Zealand', *Geophysical Research Letters* **39**(2).

Bertrand, G., Guillou-Frottier, L. & Loiselet, C. (2014), 'Distribution of porphyry copper deposits along the western Tethyan and Andean subduction zones: Insights from a paleotectonic approach', *Ore Geology Reviews* **60**, 174–190.

Bettinelli, P., Avouac, J.-P., Flouzat, M., Bollinger, L., Ramillien, G., Rajaure, S. & Sapkota, . (2008), 'Seasonal variations of seismicity and geodetic strain in the Himalaya induced by surface hydrology', *Earth and Planetary Science Letters* **266**(3-4), 332–344.

Biggs, J. & Pritchard, M. (2017), 'Global volcano monitoring: What does it mean when volcanoes deform?', *Elements* **13**(1), 17–22.

Blaser, L., Krüger, F., Ohrnberger, M. & Scherbaum, F. (2010), 'Scaling relations of earthquake source parameter estimates with special focus on subduction environment', *Bulletin of the Seismological Society of America* **100**(6), 2914–2926.

Blundy, J., Afanasyev, A., Tattitch, B., Sparks, S., Melnik, O., Utkin, I. & Rust, A. (2021), 'The economic potential of metalliferous sub-volcanic brines', *Royal Society Open Science* **8**(6), 202192.

Bonali, F., Tibaldi, A. & Corazzato, C. (2015), 'Sensitivity analysis of earthquake-induced static stress changes on volcanoes: the 2010 M w 8.8 Chile earthquake', *Geophysical Journal International* **201**(3), 1868–1890.

Bonali, F., Tibaldi, A., Corazzato, C., Tormey, D. R. & Lara, L. E. (2013), 'Quantifying the effect of large earthquakes in promoting eruptions due to stress changes on magma pathway: The Chile case', *Tectonophysics* **583**, 54–67.

Bonini, M. (2019), 'Seismic loading of fault-controlled fluid seepage systems by great subduction earthquakes', *Scientific reports* **9**(1), 1–12.

Boschetty, F., Ferguson, D., Cortés, J., Morgado, E., Ebmeier, S., Morgan, D., Romero, J. & Silva Parejas, C. (2022), 'Insights into magma storage beneath a frequently erupting arc volcano (Villarrica, Chile) from unsupervised machine learning analysis of mineral compositions', *Geochemistry, Geophysics, Geosystems* **23**(4), e2022GC010333.

Bosl, W. & Nur, A. (2002), 'Aftershocks and pore fluid diffusion following the 1992 Landers earthquake', *Journal of Geophysical Research: Solid Earth* **107**(B12), ESE–17.

Brace, W. & Kohlstedt, D. (1980), 'Limits on lithospheric stress imposed by laboratory experiments', *Journal of Geophysical Research: Solid Earth* **85**(B11), 6248–6252.

Brantut, N. & David, E. (2019), 'Influence of fluids on VP/VS ratio: increase or decrease?', *Geophysical Journal International* **216**(3), 2037–2043.

Brodsky, E., Sturtevant, B. & Kanamori, H. (1998), 'Earthquakes, volcanoes, and rectified diffusion', *Journal of Geophysical Research: Solid Earth* **103**(B10), 23827–23838.

Brudy, M., Zoback, M., Fuchs, K., Rummel, F. & Baumgartner, J. (1997), 'Estimation of the complete stress tensor to 8 km depth in the KTB scientific drillholes: Implications for crustal strength', *Journal of Geophysical Research* **102**, 18453–18475.

Bufe, C. & Perkins, D. (2005), 'Evidence for a global seismic-moment release sequence', *Bulletin of the Seismological Society of America* **95**(3), 833–843.

Bürgmann, R. (2018), 'The geophysics, geology and mechanics of slow fault slip', *Earth and Planetary Science Letters* **495**, 112–134.

Byerlee, J. (1978), 'Friction of rocks', *Pure and Applied Geophysics* **116**, 615–626.

Canales, J., Nedimović, M., Kent, G., Carbotte, S. & Detrick, R. (2009), 'Seismic reflection images of a near-axis melt sill within the lower crust at the Juan de Fuca ridge', *Nature* **460**, 89–93.

Cannata, A., Di Grazia, G., Montalto, P., Aliotta, M., Patanè, D. & Boschi, E. (2010), 'Response of Mount Etna to dynamic stresses from distant earthquakes', *Journal of Geophysical Research: Solid Earth* **115**(B12).

Carr, M. (1977), 'Volcanic activity and great earthquakes at convergent plate margins', *Science* **197**(4304), 655–657.

Cashman, K., Sparks, R. & Blundy, J. (2017), 'Vertically extensive and unstable magmatic systems: a unified view of igneous processes', *Science* **355**(6331), eaag3055.

Cembrano, J., Herve, F. & Lavenu, A. (1996), 'The Liquine Ofquie fault zone: a long-lived intra-arc fault system in southern Chile', *Tectonophysics* **259**, 55–66.

Cembrano, J. & Lara, L. (2009), 'The link between volcanism and tectonics in the southern volcanic zone of the Chilean Andes: A review', *Tectonophysics* **471**(1-2), 96–113.

Chamberlain, K., Morgan, D. & Wilson, C. (2014), 'Timescales of mixing and mobilisation in the Bishop Tuff magma body: perspectives from diffusion chronometry', *Contributions to Mineralogy and Petrology* **168**(1), 1–24.

Chaussard, E. & Amelung, F. (2014), 'Regional controls on magma ascent and storage in volcanic arcs', *Geochemistry, Geophysics, Geosystems* **15**(4), 1407–1418.

Chave, A. & Jones, A. (2012), *The magnetotelluric method: Theory and practice*, Cambridge University Press.

Chmielowski, J., Zandt, G. & Haberland, C. (1999), 'The central Andean Altiplano-Puna magma body', *Geophysical Research Letters* **26**(6), 783–786.

Churchill, R., Werner, M., Biggs, J. & Fagereng, Å. (2022), 'Afterslip moment scaling and variability from a global compilation of estimates', *Journal of Geophysical Research: Solid Earth* **127**(4), e2021JB023897.

Cigolini, C., Laiolo, M. & Coppola, D. (2007), 'Earthquake-volcano interactions detected from radon degassing at Stromboli (Italy)', *Earth and Planetary Science Letters* **257**(3-4), 511–525.

Clemens, J. & Mawer, C. (1992), 'Granitic magma transport by fracture propagation', *Tectonophysics* **204**(3-4), 339–360.

Cloos, M. (2001), 'Bubbling magma chambers, cupolas, and porphyry copper deposits', *International geology review* **43**(4), 285–311.

Cochran, E., Vidale, J. & Tanaka, S. (2004), 'Earth tides can trigger shallow thrust fault earthquakes', *Science* **306**(5699), 1164–1167.

Collettini, C., Niemeijer, A., Viti, C. & Marone, C. (2009), 'Fault zone fabric and fault weakness', *Nature* **462**(7275), 907–910.

Comeau, M., Unsworth, M. & Cordell, D. (2016), 'New constraints on the magma distribution and composition beneath Volcán Uturuncu and the southern Bolivian Altiplano from magnetotelluric data', *Geosphere* **12**(5), 1391–1421.

Cooper, K. (2017), 'What does a magma reservoir look like? The "Crystal's-Eye" view', *Elements* **13**(1), 23–28.

Cooper, K. (2019), 'Time scales and temperatures of crystal storage in magma reservoirs: Implications for magma reservoir dynamics', *Philosophical Transactions of the Royal Society A* **377**(2139), 20180009.

Copley, A. (2014), 'Postseismic afterslip 30 years after the 1978 Tabas-e-Golshan (Iran) earthquake: observations and implications for the geological evolution of thrust belts', *Geophysical Journal International* **197**(2), 665–679.

Cordell, D., Unsworth, M. & Díaz, D. (2018), 'Imaging the Laguna del Maule Volcanic Field, central Chile using magnetotellurics: Evidence for crustal melt regions laterally-offset from surface vents and lava flows', *Earth and Planetary Science Letters* **488**, 168–180.

Cordell, D., Unsworth, M., Lee, B., Díaz, D., Bennington, N. & Thurber, C. (2020), 'Integrating magnetotelluric and seismic images of silicic magma systems: A case study from the Laguna del Maule Volcanic Field, central Chile', *Journal of Geophysical Research: Solid Earth* **125**(11), e2020JB020459.

Crews, J. & Cooper, C. (2014), 'Experimental evidence for seismically initiated gas bubble nucleation and growth in groundwater as a mechanism for coseismic borehole water level rise and remotely triggered seismicity', *Journal of Geophysical Research: Solid Earth* **119**(9), 7079–7091.

Crisp, J. (1984), 'Rates of magma emplacement and volcanic output', *Journal of Volcanology and Geothermal Research* **20**(3-4), 177–211.

Currenti, G. (2018), 'Viscoelastic modeling of deformation and gravity changes induced by pressurized magmatic sources', *Journal of Volcanology and Geothermal Research* **356**, 264–277.

Dahm, T. (2000), 'Numerical simulations of the propagation path and the arrest of fluid-filled fractures in the earth', *Geophysical Journal International* **141**(3), 623–638.

Daines, M. & Pec, M. (2015), Migration of melt, *in* H. Sigursson, ed., 'The encyclopedia of volcanoes', Elsevier, pp. 49–64.

Darwin, C. R. (1840), 'On the connexion of certain volcanic phenomena in south america; and on the formation of mountain chains and volcanos, as the effect of the same power by which continents are elevated', *Transactions of the Geological Society, London* **5**, 601–631.

Daub, E., Ben-Naim, E., Guyer, R. & Johnson, P. (2012), 'Are megaquakes clustered?', *Geophysical Research Letters* **39**(6).

Davison, A. (2003), *Statistical Models*, Cambridge University Press.

De la Cruz-Reyna, S. (1991), 'Poisson-distributed patterns of explosive eruptive activity', *Bulletin of Volcanology* **54**(1), 57–67.

De la Cruz-Reyna, S., Tárraga, M., Ortiz, R. & Martínez-Bringas, A. (2010), 'Tectonic earthquakes triggering volcanic seismicity and eruptions. case studies at tungurahua and popocatépetl volcanoes', *Journal of Volcanology and Geothermal Research* **193**(1-2), 37–48.

De Saint Blanquat, M., Horsman, E., Habert, G., Morgan, S., Vanderhaeghe, O., Law, R. & Tikoff, B. (2011), 'Multiscale magmatic cyclicity, duration of pluton construction, and the paradoxical relationship between tectonism and plutonism in continental arcs', *Tectonophysics* **500**(1-4), 20–33.

De Silva, S., Self, S., Francis, P., Drake, R. & Carlos, R. (1994), 'Effusive silicic volcanism in the Central Andes: The Chao dacite and other young lavas of the Altiplano-Puna Volcanic Complex', *Journal of Geophysical Research: Solid Earth* **99**(B9), 17805–17825.

Degruyter, W., Huber, C., Bachmann, O., Cooper, K. & Kent, A. (2016), 'Magma reservoir response to transient recharge events: The case of Santorini volcano (Greece)', *Geology* **44**(1), 23–26.

Deligne, N., Coles, S. & Sparks, R. (2010), 'Recurrence rates of large explosive volcanic eruptions', *Journal of Geophysical Research: Solid Earth* **115**(B6).

Delle Donne, D., Harris, A., Ripepe, M. & Wright, R. (2010), 'Earthquake-induced thermal anomalies at active volcanoes', *Geology* **38**(9), 771–774.

Di Giacomo, D., Engdahl, E. & Storchak, D. (2018), 'The ISC-GEM Earthquake Catalogue (1904-2014): status after the Extension Project.', *Earth System Science Data* **10**(4).

Díaz, D., Brasse, H. & Ticona, F. (2012), 'Conductivity distribution beneath Lascar volcano (Northern Chile) and the Puna, inferred from magnetotelluric data', *Journal of Volcanology and Geothermal Research* **217**, 21–29.

Díaz, D., Heise, W. & Zamudio, F. (2015), 'Three-dimensional resistivity image of the magmatic system beneath Lastarria volcano and evidence for magmatic intrusion in the back arc (northern Chile)', *Geophysical Research Letters* **42**(13), 5212–5218.

Díaz, D., Zúñiga, F. & Castruccio, A. (2020), 'The interaction between active crustal faults and volcanism: A case study of the Liquiñe-Ofqui Fault Zone and Osorno volcano, southern Andes, using magnetotellurics', *Journal of Volcanology and Geothermal Research* **393**, 106806.

Dickinson, W. (1973), 'Widths of modern Arc-Trench gaps proportional to past duration of igneous activity in associated magmatic arcs', *Journal of Geophysical Research* **78**(17), 3376–3389.

Doglioni, C., Carminati, E., Cuffaro, M. & Scrocca, D. (2007), 'Subduction kinematics and dynamic constraints', *Earth-Science Reviews* **83**(3-4), 125–175.

Dominguez, S., Lallemand, S., Malavieille, J. & von Huene, R. (1998), 'Upper plate deformation associated with seamount subduction', *Tectonophysics* **293**(3-4), 207–224.

Doser, D. & Robinson, R. (2002), 'Modeling stress changes induced by earthquakes in the southern Marlborough region, South Island, New Zealand', *Bulletin of the Seismological Society of America* **92**(8), 3229–3238.

Driesner, T. & Heinrich, C. (2007), 'The system H2O-NaCl. Part I: Correlation formulae for phase relations in temperature-pressure-composition space from 0 to 1000 C, 0 to 5000 bar, and 0 to 1 XNaCl', *Geochimica et Cosmochimica Acta* **71**(20), 4880–4901.

Drymoni, K., Browning, J. & Gudmundsson, A. (2020), 'Dyke-arrest scenarios in extensional regimes: Insights from field observations and numerical models, Santorini, Greece', *Journal of Volcanology and Geothermal Research* p. 106854.

Dziewonski, A., Chou, T.-A. & Woodhouse, J. (1981), 'Determination of earthquake source parameters from waveform data for studies of global and regional seismicity', *Journal of Geophysical Research: Solid Earth* **86**(B4), 2825–2852.

Ebmeier, S., Elliott, J., Nocquet, J.-M., Biggs, J., Mothes, P., Jarrín, P., Yépez, M., Aguaiza, S. et al. (2016), 'Shallow earthquake inhibits unrest near Chiles-Cerro Negro volcanoes, Ecuador-Colombian border', *Earth and Planetary Science Letters* **450**, 283–291.

Edmonds, M., Cashman, K., Holness, M. & Jackson, M. (2019), 'Architecture and dynamics of magma reservoirs', *Philosophical Transactions of the Royal Society A* **377**(2139), 20180298.

Edmonds, M. & Woods, A. (2018), 'Exsolved volatiles in magma reservoirs', *Journal of Volcanology and Geothermal Research* **368**, 13–30.

Eggert, S. & Walter, T. (2009), 'Volcanic activity before and after large tectonic earthquakes: observations and statistical significance', *Tectonophysics* **471**(1-2), 14–26.

Ekström, G., Nettles, M. & Dziewoński, A. (2012), 'The global CMT project 2004-2010: Centroid-moment tensors for 13,017 earthquakes', *Physics of the Earth and Planetary Interiors* **200**, 1–9.

Elders, W., Friðleifsson, G. & Albertsson, A. (2014), 'Drilling into magma and the implications of the Iceland Deep Drilling Project (IDDP) for high-temperature geothermal systems worldwide', *Geothermics* **49**, 111–118.

Ellsworth, W. (2013), 'Injection-induced earthquakes', *Science* **341**(6142), 1225942.

Farías, C. & Basualto, D. (2020), 'Reactivating and calming volcanoes: the 2015 MW 8.3 Illapel megathrust strike', *Geophysical Research Letters* **47**(16), e2020GL087738.

Feigl, K., Le Mével, H., A.S., T., Córdova, L., Andersen, N., DeMets, C. & Singer, B. (2014), 'Rapid uplift in Laguna del Maule volcanic field of the Andean Southern Volcanic zone (Chile) 2007-2012', *Geophysical Journal International* **196**(2), 885–901.

Feuillet, N., Beauducel, F. & Tapponnier, P. (2011), 'Tectonic context of moderate to large historical earthquakes in the Lesser Antilles and mechanical coupling with volcanoes', *Journal of Geophysical Research: Solid Earth* **116**(B10).

Feuillet, N., Cocco, M., Musumeci, C. & Nostro, C. (2006), 'Stress interaction between seismic and volcanic activity at Mt Etna', *Geophysical Journal International* **164**(3), 697–718.

Fournier, R. (1999), 'Hydrothermal processes related to movement of fluid from plastic into brittle rock in the magmatic-epithermal environment', *Economic Geology* **94**(8), 1193–1211.

Freed, A. (2005), 'Earthquake triggering by static, dynamic, and postseismic stress transfer', *Annual Reviews of Earth and Planetary Sciences* **33**, 335–367.

Freed, A. & Lin, J. (2001), 'Delayed triggering of the 1999 Hector Mine earthquake by viscoelastic stress transfer', *Nature* **411**(6834), 180–183.

Fujimoto, K., Takahashi, M., Doi, N. & Kato, O. (2000), High permeability of Quaternary granites in the Kakkonda geothermal area, northeast Japan, *in* 'World Geothermal Congress, Kyushu-Tohoku, Japan', pp. 1139–1144.

Furlan, C. (2010), 'Extreme value methods for modelling historical series of large volcanic magnitudes', *Statistical Modelling* **10**(2), 113–132.

Gaillard, F. (2004), 'Laboratory measurements of electrical conductivity of hydrous and dry silicic melts under pressure', *Earth and Planetary Science Letters* **218**(1-2), 215–228.

Ghiorso, M. & Gualda, G. (2015), 'An H2O-CO2 mixed fluid saturation model compatible with rhyolite-MELTS', *Contributions to Mineralogy and Petrology* **169**(6), 1–30.

Girona, T., Huber, C. & Caudron, C. (2018), 'Sensitivity to lunar cycles prior to the 2007 eruption of Ruapehu volcano', *Scientific reports* **8**(1), 1476.

Glazner, A., Bartley, J., Coleman, D., Gray, W. & Taylor, R. (2004), 'Are plutons assembled over millions of years by amalgamation from small magma chambers?', *GSA today* **14**(4/5), 4–12.

Global Volcanism Program (2013), 'Volcanoes of the World, v. 4.9.1', Smithsonian Institution. Downloaded 2 November 2020.

Glover, P., Hole, M. & Pous, J. (2000), 'A modified Archie's law for two conducting phases', *Earth and Planetary Science Letters* **180**(3-4), 369–383.

Godoy, B., Lazcano, J., Rodríguez, I., Martínez, P., Parada, M., Le Roux, P., Wilke, H.-G. & Polanco, E. (2018), 'Geological evolution of Paniri volcano, central Andes, northern Chile', *Journal of South American Earth Sciences* **84**, 184–200.

Goltz, A., Krawczynski, M., Gavrilenko, M., Gorbach, N. & Ruprecht, P. (2020), 'Evidence for superhydrous primitive arc magmas from mafic enclaves at Shiveluch volcano, Kamchatka', *Contributions to Mineralogy and Petrology* **175**(12), 1–26.

Gomez, C., Dvorkin, J. & Vanorio, T. (2010), 'Laboratory measurements of porosity, permeability, resistivity, and velocity on Fontainebleau sandstones', *Geophysics* **75**(6), E191–E204.

Gonnermann, H. & Taisne, B. (2015), Magma transport in dykes, *in* H. Sigurdsson, ed., 'The Encyclopedia of Volcanoes, 2nd Edition', Elsevier, pp. 216–224.

Grant, F. & West, G. (1965), *Interpretation theory in applied geophysics*, McGraw-Hill.

Grasso, J.-R. & Sornette, D. (1998), 'Testing self-organized criticality by induced seismicity', *Journal of Geophysical Research: Solid Earth* **103**(B12), 29965–29987.

Gregg, P., De Silva, S. & Grosfils, E. (2013), 'Thermomechanics of shallow magma chamber pressurization: Implications for the assessment of ground deformation data at active volcanoes', *Earth and Planetary Science Letters* **384**, 100–108.

Grosfils, E. (2007), 'Magma reservoir failure on the terrestrial planets: Assessing the importance of gravitational loading in simple elastic models', *Journal of Volcanology and Geothermal Research* **166**(2), 47–75.

Gudmundsson, A. (1984*a*), 'Formation of dykes, feeder-dykes, and the intrusion of dykes from magma chambers', *Bulletin Volcanologique* **47**(3), 537–550.

Gudmundsson, A. (1984*b*), 'Tectonic aspetcs of dykes in northwestern iceland', *Jokull* **34**, 81–96.

Gudmundsson, A. (1986), 'Formation of crystal magma chambers in Iceland', *Geology* **14**(2), 164–166.

Gudmundsson, A. (2002), 'Emplacement and arrest of sheets and dykes in central volcanoes', *Journal of Volcanology and Geothermal Research* **116**(3-4), 279–298.

Gudmundsson, A. (2005), 'The effects of layering and local stresses in composite volcanoes on dyke emplacement and volcanic hazards', *Comptes Rendus Geoscience* **337**(13), 1216–1222.

Gudmundsson, A. (2006), 'How local stresses control magma-chamber ruptures, dyke injections, and eruptions in composite volcanoes', *Earth-Science Reviews* **79**(1-2), 1–31.

Gudmundsson, A. (2011), 'Deflection of dykes into sills at discontinuities and magma-chamber formation', *Tectonophysics* **500**(1-4), 50–64.

Gudmundsson, A. (2012), 'Magma chambers: Formation, local stresses, excess pressures, and compartments', *Journal of Volcanology and Geothermal Research* **237**, 19–41.

Gudmundsson, A. (2020), *Volcanotectonics*, 1st edn, Cambridge University Press.

Gudmundsson, A., Marinoni, L. & Marti, J. (1999), 'Injection and arrest of dykes: implications for volcanic hazards', *Journal of Volcanology and Geothermal Research* **88**(1-2), 1–13.

Guéguen, Y. & Palciauskas, V. (1994), *Introduction to the Physics of Rocks*, Princeton University Press.

Guo, X., Li, B., Ni, H. & Mao, Z. (2017), 'Electrical conductivity of hydrous andesitic melts pertinent to subduction zones', *Journal of Geophysical Research: Solid Earth* **122**(3), 1777–1788.

Guo, X., Zhang, L., Behrens, H. & Ni, H. (2016), 'Probing the status of felsic magma reservoirs: Constraints from the P-T-H2O dependences of electrical conductivity of rhyolitic melt', *Earth and Planetary Science Letters* **433**, 54–62.

Gusev, A. (2008), 'Temporal structure of the global sequence of volcanic eruptions: Order clustering and intermittent discharge rate', *Physics of the Earth and planetary interiors* **166**(3-4), 203–218.

Gusev, A. (2014), 'The fractal structure of the sequence of volcanic eruptions worldwide: Order clustering of events and episodic discharge of material', *Journal of Volcanology and Seismology* **8**(1), 34–53.

Han, T., Best, A., Sothcott, J., North, L. & MacGregor, L. (2015), 'Relationships among low frequency (2 Hz) electrical resistivity, porosity, clay content and permeability in reservoir sandstones', *Journal of Applied Geophysics* **112**, 279–289.

Hardebeck, J., Nazareth, J. & Hauksson, E. (1998), 'The static stress change triggering model: Constraints from two southern California aftershock sequences', *Journal of Geophysical Research: Solid Earth* **103**(B10), 24427–24437.

Hardebeck, J. & Okada, T. (2018), 'Temporal stress changes caused by earthquakes: A review', *Journal of Geophysical Research: Solid Earth* **123**(2), 1350–1365.

Harris, A. & Ripepe, M. (2007), 'Regional earthquake as a trigger for enhanced volcanic activity: evidence from MODIS thermal data', *Geophysical Research Letters* **34**(2).

Hashin, Z. & Shtrikman, S. (1962), 'A variational approach to the theory of the effective magnetic permeability of multiphase materials', *Journal of applied Physics* **33**(10), 3125–3131.

Hayes, G., Moore, G., Portner, D., Hearne, M., Flamme, H., Furtney, M. & Smoczyk, G. (2018), 'Slab2, a comprehensive subduction zone geometry model', *Science* **362**(6410), 58–61.

Heap, M., Villeneuve, M., Albino, F., Farquharson, J. I., Brothelande, E., Amelung, F. et al. (2020), 'Towards more realistic values of elastic moduli for volcano modelling', *Journal of Volcanology and Geothermal Research* **390**, 106684.

Heidbach, O., Rajabi, M., Cui, X., Fuchs, K., Müller, B., Reinecker, J. et al. (2018), 'The World Stress Map database release 2016: Crustal stress pattern across scales', *Tectonophysics* **744**, 484–498.

Heinrich, C. (2005), 'The physical and chemical evolution of low-salinity magmatic fluids at the porphyry to epithermal transition: a thermodynamic study', *Mineralium Deposita* **39**(8), 864–889.

Heuret, A., Lallemand, S., Funiciello, F., Piromallo, C. & Faccenna, C. (2011), 'Physical characteristics of subduction interface type seismogenic zones revisited', *Geochemistry, Geophysics, Geosystems* **12**(1), QO1004.

Hildreth, W. & Moorbath, S. (1988), ‘Crustal contribtuions to arc magmatism in the Andes of central Chile’, *Contributions to Mineralogy and Petrology* **98**(4), 455–489.

Hill-Butler, C., Blackett, M., Wright, R. & Trodd, N. (2020), ‘The co-incidence of earthquakes and volcanoes: assessing global volcanic radiant flux responses to earthquakes in the 21st century’, *Journal of Volcanology and Geothermal Research* **393**, 106770.

Hill, D. P., Pollitz, F. & Newhall, C. (2002), ‘Earthquake-volcano interactions’, *Physics Today* **55**(11), 41–47.

Hill, D. P. et al. (1993), ‘Seismicity remotely triggered by the magnitude 7.3 Landers, California, earthquake’, *Science* **260**, 1617–1623.

Hill, G., Caldwell, T., Heise, W., Chertkoff, D., Bibby, H., Burgess, M., Cull, J. & Cas, R. (2009), ‘Distribution of melt beneath Mount St Helens and Mount Adams inferred from magnetotelluric data’, *Nature Geoscience* **2**(11), 785–789.

Holdsworth, R. (2004), ‘Weak faults-rotten cores’, *Science* **303**(5655), 181–182.

Huybers, P. & Langmuir, C. (2009), ‘Feedback between deglaciation, volcanism, and atmospheric CO2’, *Earth and Planetary Science Letters* **286**(3-4), 479–491.

Hyndman, R., Yamano, M. & Oleskevich, D. (1997), ‘The seismogenic zone of subduction thrust faults’, *Island Arc* **6**(3), 244–260.

Iacovino, K., Matthews, S., Wieser, P., Moore, G. & Bégué, F. (2021), ‘VESIcal Part I: An open-source thermodynamic model engine for mixed volatile (H2O-CO2) solubility in silicate melts’, *Earth and Space Science* **8**(11), e2020EA001584.

International Seismological Centre (2020), ‘ISC-GEM Earthquake Catalogue’.

Ito, K. (1993), ‘Cutoff depth of seismicity and large earthquakes near active volcanoes in Japan’, *Tectonophysics* **217**(1-2), 11–21.

Jarrard, R. (1986), ‘Relations among subduction parameters’, *Reviews of Geophysics* **24**(2), 217–284.

Jaxybulatov, K., Shapiro, N., Koulakov, I., Mordret, A., Landès, M. & Sens-Schöenfelder, C. (2014), ‘A large magmatic sill complex beneath the Toba caldera’, *science* **346**(6209), 617–619.

Jay, J., Pritchard, M., West, M., Christensen, D., Haney, M., Minaya, E., Sunagua, M., McNutt, S. & Zabala, M. (2012), 'Shallow seismicity, triggered seismicity, and ambient noise tomography at the long-dormant Uturuncu Volcano, Bolivia', *Bulletin of Volcanology* **74**(4), 817–837.

Jenkins, A., Biggs, J., Rust, A. & Jara, R. (2021), 'A systematic approach to mapping regimes of earthquake-induced static stress changes acting on magmatic pathways', *Journal of Geophysical Research: Solid Earth* **126**(1), e2020JB020242.

Jenkins, A., Biggs, J., Rust, A. & Rougier, J. (2021), 'Decadal timescale correlations between global earthquake activity and volcanic eruption rates', *Geophysical Research Letters* **48**(16), e2021GL093550.

Johnson, C., Bürgmann, R. & Pollitz, F. (2015), 'Rare dynamic triggering of remote M≥ 5.5 earthquakes from global catalog analysis', *Journal of Geophysical Research: Solid Earth* **120**(3), 1748–1761.

Johnson, G. & Anderson, L. (1981), *A laboratory study of some physical properties of sulfide ores in igneous and metamorphic rocks from the Burnt Nubble area, Somerset County, Maine*, US Department of the Interior, Geological Survey.

Jolly, A. (2019), 'On the shallow volcanic response to remote seismicity', *Geology* **47**(1), 95–96.

Jull, M. & McKenzie, D. (1996), 'The effect of deglaciation on mantle melting beneath Iceland', *Journal of Geophysical Research: Solid Earth* **101**(B10), 21815–21828.

Kanamori, H. & Anderson, D. (1975), 'Theoretical basis of some empirical relations in seismology', *Bulletin of the Seismological Society of America* **65**(5), 1073–1095.

Kanamori, H. & Kikuchi, M. (1993), 'The 1992 Nicaragua earthquake: a slow tsunami earthquake associated with subducted sediments', *Nature* **361**(6414), 714–716.

Kasahara, J. (2002), 'Tides, earthquakes, and volcanoes', *Science* **297**(5580), 348–349.

Kasai, K., Sakagawa, Y., Komatsu, R., Sasaki, M., Akaku, K. & Uchida, T. (1998), 'The origin of hypersaline liquid in the Quaternary Kakkonda granite, sampled from well WD-1a, Kakkonda geothermal system, Japan', *Geothermics* **27**(5-6), 631–645.

Kavanagh, J. (2018), Mechanisms of magma transport in the upper crust — dyking, *in* 'Volcanic and igneous plumbing systems', Elsevier, pp. 55–88.

Kavanagh, J., Menand, T. & Sparks, R. (2006), 'An experimental investigation of sill formation and propagation in layered elastic media', *Earth and Planetary Science Letters* **245**(3-4), 799–813.

Kavanagh, J., Rogers, B., Boutelier, D. & Cruden, A. (2017), 'Controls on sill and dyke-sill hybrid geometry and propagation in the crust: The role of fracture toughness', *Tectonophysics* **698**, 109–120.

Kearey, P., Klepeis, K. & Vine, F. (2009), *Global Tectonics*, 3rd edn, Wiley Blackwell, Oxford.

Kesler, S., Bodnar, R. & Mernagh, T. (2013), 'Role of fluid and melt inclusion studies in geologic research', *Geofluids* **13**(4), 398–404.

Kilb, D., Gomberg, J. & Bodin, P. (2002), 'Aftershock triggering by complete Coulomb stress changes', *Journal of Geophysical Research: Solid Earth* **107**(B4), ESE–2.

Kilgour, G., Saunders, K., Blundy, J., Cashman, K., Scott, B. & Miller, C. (2014), 'Timescales of magmatic processes at Ruapehu volcano from diffusion chronometry and their comparison to monitoring data', *Journal of Volcanology and Geothermal Research* **288**, 62–75.

Kimura, M. (1994), 'Relationship between volcanic eruption and large earthquakes in the vicinity of Japan', *Annuals, Disas. Prev. Inst. Kyoto Univ.* **37**(1), 293–317.

King, G. C. P., Stein, R. S. & Lin, J. (1994), 'Static stress changes and the triggering of Earthquakes', *Bulletin of the Seismological Society of America* **84**(3), 935–953.

Klug, J., Singer, B., Kita, N. & Spicuzza, M. (2020), 'Storage and evolution of Laguna del Maule rhyolites: Insight from volatile and trace element contents in melt inclusions', *Journal of Geophysical Research: Solid Earth* **125**(8), e2020JB019475.

Krawczynski, M., Grove, T. & Behrens, H. (2012), 'Amphibole stability in primitive arc magmas: effects of temperature, H2O content, and oxygen fugacity', *Contributions to Mineralogy and Petrology* **164**(2), 317–339.

Kruszewski, M. & Wittig, V. (2018), 'Review of failure modes in supercritical geothermal drilling projects', *Geothermal Energy* **6**(1), 1–29.

Kusumoto, S., Geshi, N. & Gudmundsson, A. (2013), 'Aspect ratios and magma overpressures of non-feeder dikes observed in the Miyake-jima volcano (Japan), and fracture toughness of its upper part', *Geophysical research letters* **40**(6), 1065–1068.

Kutterolf, S., Jegen, M., Mitrovica, J., Kwasnitschka, T., Freundt, . & Huybers, P. (2013), ' detection of Milankovitch frequencies in global volcanic activity', *Geology* **41**(2), 227–230.

Lara, L. E., Naranjo, J. A. & Moreno, H. (1994), 'Rhyodacitic fissure eruption in Southern Andes (Cordón Caulle, 40.5° S) after the 1960 (Mw:9.5) Chilean earthquake: a structural interpretation', *Pure and Applied Geophysics* **138**(1-2), 225–237.

Lara, L., Lavenu, A., Cembrano, J. & Rodríguez, C. (2006), 'Structural controls of volcanism in transversal chains: resheared faults and neotectonics in the Cordón Caulle-Puyehue area (40.5 S), Southern Andes', *Journal of Volcanology and Geothermal Research* **158**(1-2), 70–86.

Larsen, G. (2000), 'Holocene eruptions within the Katla volcanic system, south Iceland: characteristics and environmental impact', *Jökull* **49**, 1–28.

Laumonier, M., Gaillard, F., Muir, D., Blundy, J. & Unsworth, M. (2017), 'Giant magmatic water reservoirs at mid-crustal depth inferred from electrical conductivity and the growth of the continental crust', *Earth and Planetary Science Letters* **457**, 173–180.

Laumonier, M., Gaillard, F. & Sifre, D. (2015), 'The effect of pressure and water concentration on the electrical conductivity of dacitic melts: Implication for magnetotelluric imaging in subduction areas', *Chemical Geology* **418**, 66–76.

Laštovičková, M. (1991), 'A review of laboratory measurements of the electrical conductivity of rocks and minerals', *Physics of the Earth and Planetary Interiors* **66**(1-2), 1–11.

Lay, T. (2015), 'The surge of great earthquakes from 2004 to 2014', *Earth and Planetary Science Letters* **409**, 133–146.

Lee, B., Unsworth, M., Árnason, K. & Cordell, D. (2020), 'Imaging the magmatic system beneath the Krafla geothermal field, Iceland: A new 3-D electrical resistivity model from inversion of magnetotelluric data', *Geophysical Journal International* **220**(1), 541–567.

Lees, J. (2007), 'Seismic tomography of magmatic systems', *Journal of Volcanology and Geothermal Research* **167**(1-4), 37–56.

Lemarchand, N. & Grasso, J.-R. (2007), ‘Interactions between earthquakes and volcano activity’, *Geophysical Research Letters* **34**(24).

Lesher, C. & Spera, F. (2015), Thermodynamic and transport properties of silicate melts and magma, *in* ‘The encyclopedia of volcanoes’, Elsevier, pp. 113–141.

Levandowski, W., Herrmann, R., Briggs, R., Boyd, O. & Gold, R. (2018), ‘An updated stress map of the continental United States reveals heterogeneous intraplate stress’, *Nature Geoscience* **11**, 433–437.

Levin, B., Sasorova, E., Gurianov, V. & Yarmolyuk, V. (2019), The relationship between global volcanic activity and variations in the velocity of Earth’s rotation, *in* ‘Doklady Earth Sciences’, Vol. 484, Springer, pp. 146–150.

Lévy, L., Gibert, B., Sigmundsson, F., Flóvenz, Ó., Hersir, G., Briole, P. & Pezard, P. (2018), ‘The role of smectites in the electrical conductivity of active hydrothermal systems: electrical properties of core samples from Krafla volcano, Iceland’, *Geophysical Journal International* **215**(3), 1558–1582.

Liao, Y., Soule, S. & Jones, M. (2018), ‘On the mechanical effects of poroelastic crystal mush in classical magma chamber models’, *Journal of Geophysical Research: Solid Earth* **123**(11), 9376–9406.

Liao, Y., Soule, S., Jones, M. & Le Mével, H. (2021), ‘The mechanical response of a magma chamber with poroviscoelastic crystal mush’, *Journal of Geophysical Research: Solid Earth* **126**(4), e2020JB019395.

Lin, C.-H. (2017), ‘Dynamic triggering of volcano drumbeat-like seismicity at the Tatun volcano group in Taiwan’, *Geophysical Journal International* **210**(1), 354–359.

Lin, J. & Stein, R. S. (2004), ‘Stress triggering in thrust and subduction earthquakes, and stress interaction between the southern San Andreas and nearby thrust and strike-slip faults’, *Journal of Geophysical Research: Solid Earth* **109**(B2), 1–19.

Linde, A., Sacks, I., Johnston, M., Hillt, D. & Bilham, R. (1994), ‘Increased pressure from rising bubbles as a mechanism for remotely triggered seismicity’, *Nature* **371**(6496), 408–410.

Linde, A. T. & Sacks, I. (1998), ‘Triggering of volcanic eruptions’, *Nature* **395**, 888–890.

Lister, J. (1995), ‘Fluid-mechanical models of the interaction between solidification and flow in dykes’, *Physics and chemistry of dykes* pp. 115–124.

Luginbuhl, M., Rundle, J. & Turcotte, D. (2018), ‘Natural time and nowcasting earthquakes: are large global earthquakes clustered?’, *Pure and Applied Geophysics* **175**, 661–670.

Lund, B. & Zoback, M. (1999), ‘Orientation and magnitude of in situ stress to 6.5 km dpeth in the Baltic Shield’, *International Journal of Rock Mechanics and Mining Sciences* **36**, 169–190.

Lupi, M. & Miller, S. (2014), ‘Short-lived tectonic switch mechanism for long-term pulses of volcanic activity after mega-thrust earthquakes’, *Solid Earth* **5**, 13–24.

Lupi, M., Trippanera, D., Gonzalez, D., D’amico, S., Acocella, V., Cabello, C., Stef, M. & Tassara, A. (2020), ‘Transient tectonic regimes imposed by megathrust earthquakes and the growth of NW-trending volcanic systems in the Southern Andes’, *Tectonophysics* **774**, 228204.

Maccaferri, F., Bonafede, M. & Rivalta, E. (2010), ‘A numerical model of dyke propagation in layered elastic media’, *Geophysical Journal International* **180**(3), 1107–1123.

Maccaferri, F., Bonafede, M. & Rivalta, E. (2011), ‘A quantitative study of the mechanisms governing dike propagation, dike arrest and sill formation’, *Journal of Volcanology and Geothermal Research* **208**(1-2), 39–50.

Maccaferri, F., Rivalta, E., Keir, D. & Acocella, V. (2014), ‘Off-rift volcanism in rift zones determined by crustal unloading’, *Nature Geoscience* **7**, 297–300.

Maccaferri, F., Rivalta, E., Passarelli, L. & Aoki, Y. (2016), ‘On the mechanisms governing dike arrest: Insight from the 2000 Miyakejima dike injection’, *Earth and Planetary Science Letters* **434**, 64–74.

Magee, C., Jackson, C.-L. & Schofield, N. (2013), ‘The influence of normal fault geometry on igneous sill emplacement and morphology’, *Geology* **41**(4), 407–410.

Magee, C., Stevenson, C., Ebmeier, S., Keir, D., Hammond, J., Gottsmann, J., Whaler, K., Schofield, N., Jackson, C., Petronis, M. et al. (2018), ‘Magma plumbing systems: a geophysical perspective’, *Journal of Petrology* **59**(6), 1217–1251.

Mancini, R., Díaz, D., Brasse, H., Godoy, B. & Hernández, M. (2019), 'Conductivity distribution beneath the San Pedro-Linzor volcanic chain, North Chile, using 3-D magnetotelluric modeling', *Journal of Geophysical Research: Solid Earth* **124**(5), 4386–4398.

Manga, M., Beresnev, I., Brodsky, E., Elkhoury, J., Elsworth, D., Ingebritsen, S., Mays, D. & Wang, C.-Y. (2012), 'Changes in permeability caused by transient stresses: Field observations, experiments, and mechanisms', *Reviews of Geophysics* **50**(2).

Manga, M. & Brodsky, E. E. (2006), 'Seismic triggering of eruptions in the far field: Volcanoes and geysers', *Annual Review of Earth and Planetary Sciences* **34**, 263–291.

Marzocchi, W. (2002), 'Remote seismic influence on large explosive eruptions', *Journal of Geophysical Research: Solid Earth* **107**(B1), EPM–6.

Mason, B., Pyle, D., Dade, W. & Jupp, T. (2004), 'Seasonality of volcanic eruptions', *Journal of Geophysical Research: Solid Earth* **109**(B4).

Matsushima, N., Utsugi, M., Takakura, S., Yamasaki, T., Hata, M., Hashimoto, T. & Uyeshima, M. (2020), 'Magmatic–hydrothermal system of Aso Volcano, Japan, inferred from electrical resistivity structures', *Earth, Planets and Space* **72**(1), 1–20.

McGarr, A. (2014), 'Maximum magnitude earthquakes induced by fluid injection', *Journal of Geophysical Research: Solid Earth* **119**(2), 1008–1019.

McNutt, S. & Roman, D. (2015), Volcanic seismicity, *in* 'The encyclopedia of volcanoes', Elsevier, pp. 1011–1034.

Mead, S. & Magill, C. (2014), 'Determining change points in data completeness for the Holocene eruption record', *Bulletin of Volcanology* **76**(11), 874.

Meier, M.-A., Werner, M., Woessner, J. & Wiemer, S. (2014), 'A search for evidence of secondary static stress triggering during the 1992 Mw7. 3 Landers, California, earthquake sequence', *Journal of Geophysical Research: Solid Earth* **119**(4), 3354–3370.

Menand, T. (2008), 'The mechanics and dynamics of sills in layered elastic rocks and their implications for the growth of laccoliths and other igneous complexes', *Earth and Planetary Science Letters* **267**(1-2), 93–99.

Menand, T., Daniels, K. & Benghiat, P. (2010), 'Dyke propagation and sill formation in a compressive tectonic environment: Solid earth', *Journal of Geophysical Research* **115**(B8), B08201.

Mendoza, C. & Hartzell, S. (1988), 'Aftershock patterns and main shock faulting', *Bulletin of the Seismological Society of America* **78**(4), 1438–1449.

Metcalfe, A., Moune, S., Komorowski, J.-C., Kilgour, G., Jessop, D. E., Moretti, R. & Legendre, Y. (2021), 'Magmatic processes at La Soufrière de Guadeloupe: Insights from crystal studies and diffusion timescales for eruption onset', *Frontiers in Earth Science* **9**, 617294.

Métivier, L., de Viron, O., Conrad, C., Renault, S., Diament, M. & Patau, G. (2009), 'Evidence of earthquake triggering by the solid earth tides', *Earth and Planetary Science Letters* **278**(3-4), 370–375.

Michael, A. (2011), 'Random variability explains apparent global clustering of large earthquakes', *Geophysical Research Letters* **38**(21).

Michell, J. (1759), 'Conjectures concerning the cause, and observations upon the phænomena of earthquakes; particularly of that great earthquake of the first November, 1755, which proved so fatal to the city of Lisbon, and whose effects were felt as far as Africa and more or less throughout almost all Europe; by the Reverend John Michell, MA Fellow of Queen's College, Cambridge.', *Philosophical Transactions of the Royal Society of London* (51), 566–634.

Miller, C., Williams-Jones, G., Fournier, D. & Witter, J. (2017), '3D gravity inversion and thermodynamic modelling reveal properties of shallow silicic magma reservoir beneath Laguna del Maule, Chile', *Earth and Planetary Science Letters* **459**, 14–27.

Moore, J. & Saffer, D. (2001), 'Updip limit of the seismogenic zone beneath the accretionary prism of southwest Japan: An effect of diagenetic to low-grade metamorphic processes and increasing effective stress', *Geology* **29**(2), 183–186.

Mora-Stock, C. (2015), Seismic Structure and Seismicity of the Villarrica Volcano (Southern Central Chile), PhD thesis, Christian-Albrechts-Universität.

Mora-Stock, C., Thorwart, M., Wunderlich, T., Bredemeyer, S., Hansteen, T. & Rabbel, W. (2012), 'Comparison of seismic activity for llaima and villarrica volcanoes prior to and after the maule 2010 earthquake', *International Journal of Earth Sciences* **103**(7), 2015–2028.

Morgado, E., Parada, M., Contreras, C., Castruccio, A., Gutiérrez, F. & McGee, L. (2015), 'Contrasting records from mantle to surface of Holocene lavas of two nearby arc volcanic complexes: Caburgua-Huelemolle Small Eruptive Centers and Villarrica Volcano, Southern Chile', *Journal of Volcanology and Geothermal Research* **306**, 1–16.

Mpodozis, C. & Cornejo, P. (2012), 'Cenozoic tectonics and porphyry copper systems of the chilean andes', *Society of Economic Geologists Special Publication* **16**, 329–360.

Muir, D., Blundy, J., Rust, A. & Hickey, J. (2014), 'Experimental constraints on dacite pre-eruptive magma storage conditions beneath Uturuncu volcano', *Journal of Petrology* **55**(4), 749–767.

Mulargia, F. & Bizzarri, A. (2014), 'Anthropogenic triggering of large earthquakes', *Scientific reports* **4**, 6100.

Murotani, S., Satake, K. & Fujii, Y. (2013), 'Scaling relations of seismic moment, rupture area, average slip, and asperity size for M9 subduction-zone earthquakes', *Geophysical Research Letters* **40**(19), 5070–5074.

Nakamura, K. (1977), 'Volcanoes as possible indicators of tectonic stress orientation - principle and proposal', *Journal of Volcanology and Geothermal Research* **2**(1), 1–16.

Namiki, A., Rivalta, E., Woith, H. & Walter, T. (2016), 'Sloshing of a bubbly magma reservoir as a mechanism of triggered eruptions', *Journal of Volcanology and Geothermal Research* **320**, 156–171.

Namiki, A., Rivalta, E., Woith, H., Willey, T., Parolai, S. & Walter, T. (2019), 'Volcanic activities triggered or inhibited by resonance of volcanic edifices to large earthquakes', *Geology* **47**(1), 67–70.

Nelson, P. & Van Voorhis, G. (1983), 'Estimation of sulfide content from induced polarization data', *Geophysics* **48**(1), 62–75.

Nettles, M., Ekström, G. & Koss, H. (2011), 'Centroid-moment-tensor analysis of the 2011 off the Pacific coast of Tohoku Earthquake and its larger foreshocks and aftershocks', *Earth, planets and space* **63**(7), 519–523.

Newhall, C. & Self, S. (1982), 'The volcanic explosivity index (VEI) an estimate of explosive magnitude for historical volcanism', *Journal of Geophysical Research: Oceans* **87**(C2), 1231–1238.

Ni, H., Chen, Q. & Keppler, H. (2014), 'Electrical conductivity measurements of aqueous fluids under pressure with a hydrothermal diamond anvil cell', *Review of Scientific Instruments* **85**(11), 115107.

Ni, H., Keppler, H. & Behrens, H. (2011), 'Electrical conductivity of hydrous basaltic melts: implications for partial melting in the upper mantle', *Contributions to Mineralogy and Petrology* **162**(3), 637–650.

Nishimura, T. (2017), 'Triggering of volcanic eruptions by large earthquakes', *Geophysical Research Letters* **44**(15), 7750–7756.

Nostro, C., Stein, R. S., Cocco, M., Belardinelli, M. E. & Marzocchi, W. (1998), 'Two-way coupling between Vesuvius eruptions and southern Apennine earthquakes, Italy, by elastic stress transfer', *Journal of Geophysical Research* **103**(B10), 24487–24504.

Ogawa, Y., Ichiki, M., Kanda, W., Mishina, M. & Asamori, K. (2014), 'Three-dimensional magnetotelluric imaging of crustal fluids and seismicity around Naruko volcano, NE Japan', *Earth, Planets and Space* **66**(1), 1–13.

Okada, Y. (1992), 'Internal deformation due to shear and tensile faults in a half-space', *Bulletin of the Seismological Society of America* **82**(2), 1018–1040.

Olivieri, M. & Spada, G. (2015), 'Ice melting and earthquake suppression in Greenland', *Polar science* **9**(1), 94–106.

Pacheco, J., Sykes, L. & Scholz, C. (1993), 'Nature of seismic coupling along simple plate boundaries of the subduction type: Solid earth', *Journal of Geophysical Research* **98**(B8), 14133–14159.

Pagli, C. & Sigmundsson, F. (2008), 'Will present day glacier retreat increase volcanic activity? Stress induced by recent glacier retreat and its effect on magmatism at the Vatnajökull ice cap, Iceland', *Geophysical Research Letters* **35**(9).

Pall, J., Zahirovic, S., Doss, S., Hassan, R., Matthews, K., Cannon, J. et al. (2018), 'The influence of carbonate platform interactions with subduction zone volcanism on palaeo-atmospheric CO2 since the Devonian', *Climate of the Past* **14**, 857–870.

Palladino, D. & Sottili, G. (2014), 'Earth's spin and volcanic eruptions: evidence for mutual cause-and-effect interactions?', *Terra Nova* **26**(1), 78–84.

Papale, P. (2018), 'Global time-size distribution of volcanic eruptions on Earth', *Scientific reports* **8**(1), 1–11.

Parsons, T. & Geist, E. (2012), 'Were global m≥ 8.3 earthquake time intervals random between 1900 and 2011?', *Bulletin of the Seismological Society of America* **102**(4), 1583–1592.

Parsons, T., Segou, M. & Marzocchi, W. (2014), 'The global aftershock zone', *Tectonophysics* **618**, 1–34.

Parsons, T. & Velasco, A. (2011), 'Absence of remotely triggered large earthquakes beyond the mainshock region', *Nature Geoscience* **4**(5), 312–316.

Pavez, C., Tapia, F., Comte, D., Gutierrez, F., Lira, E., Charrier, R. & Benavente, O. (2016), 'Characterization of the hydrothermal system of the Tinguiririca Volcanic Complex, Central Chile, using structural geology and passive seismic tomography', *Journal of Volcanology and Geothermal Research* **310**, 107–117.

Pavez, M., Schill, E., Held, S., Díaz, D. & Kohl, T. (2020), 'Visualizing preferential magmatic and geothermal fluid pathways via electric conductivity at Villarrica Volcano, S-Chile', *Journal of Volcanology and Geothermal Research* **400**, 106913.

Peacock, J., Mangan, M., McPhee, D. & Wannamaker, P. (2016), 'Three-dimensional electrical resistivity model of the hydrothermal system in Long Valley Caldera, California, from magnetotellurics', *Geophysical Research Letters* **43**(15), 7953–7962.

Pearce, R., Sánchez de la Muela, A., Moorkamp, M., Hammond, J., Mitchell, T., Cembrano, J., Araya Vargas, J., Meredith, P., Iturrieta, P., Pérez-Estay, N. et al. (2020), 'Reactivation of fault systems by compartmentalized hydrothermal fluids in the Southern Andes revealed by magnetotelluric and seismic data', *Tectonics* **39**(12), e2019TC005997.

Peng, Z., Hill, D., Shelly, D. & Aiken, C. (2010), 'Remotely triggered microearthquakes and tremor in central California following the 2010 Mw 8.8 Chile earthquake', *Geophysical Research Letters* **37**(24).

Petford, N., Cruden, A., McCaffrey, K. & Vigneresse, J.-L. (2000), 'Granite magma formation, transport and emplacement in the Earth's crust', *Nature* **408**, 669–673.

Petford, N., Kerr, R. & Lister, J. (1993), ‘Dike transport of granitoid magmas’, *Geology* **21**(9), 845–848.

Piersanti, A., Spada, G., Sabadini, R. & Bonafede, M. (1995), ‘Global post-seismic deformation’, *Geophysical Journal International* **120**(3), 544–566.

Piña-Varas, P., Ledo, J., Queralt, P., Marcuello, A. & Perez, N. (2018), ‘On the detectability of Teide volcano magma chambers (Tenerife, Canary Islands) with magnetotelluric data’, *Earth, Planets and Space* **70**(1), 1–11.

Pinel, V. & Jaupart, C. (2000), ‘The effect of edifice load on magma ascent beneath a volcano’, *Philosophical Transactions of the Royal Society of London. Series A: Mathematical, Physical and Engineering Sciences* **358**(1770), 1515–1532.

Pinel, V. & Jaupart, C. (2005), ‘Some consequences of volcanic edifice destruction for eruption conditions’, *Journal of Volcanology and Geothermal Research* **145**, 68–80.

Pollitz, F., Bürgmann, R. & Romanowicz, B. (1998), ‘Viscosity of oceanic asthenosphere inferred from remote triggering of earthquakes’, *Science* **280**(5367), 1245–1249.

Pollitz, F. & Sacks, S. (1997), ‘The 1995 Kobe, Japan, earthquake: A long-delayed aftershock of the offshore 1944 Tonankai and 1946 Nankaido earthquakes’, *Bulletin of the Seismological Society of America* **87**(1), 1–10.

Pollitz, F., Stein, R., Sevilgen, V. & Bürgmann, R. (2012), ‘The 11 April 2012 east Indian Ocean earthquake triggered large aftershocks worldwide’, *Nature* **490**(7419), 250–253.

Pommier, A. & Le-Trong, E. (2011), ‘“SIGMELTS”: A web portal for electrical conductivity calculations in geosciences’, *Computers & Geosciences* **37**(9), 1450–1459.

Prejean, S., Hill, D., Brodsky, E., Hough, S., Johnston, M., Malone, S., Oppenheimer, D., Pitt, A. & Richards-Dinger, K. (2004), ‘Remotely triggered seismicity on the United States west coast following the M w 7.9 Denali fault earthquake’, *Bulletin of the Seismological Society of America* **94**(6B), S348–S359.

Pridmore, D. & Shuey, R. (1976), ‘The electrical resistivity of galena, pyrite, and chalcopyrite’, *American Mineralogist* **61**(3-4), 248–259.

Pritchard, M., De Silva, S., Michelfelder, G., Zandt, G., McNutt, S., Gottsmann, J., West, M., Blundy, J., Christensen, D., Finnegan, N. et al. (2018), ‘Synthesis: PLUTONS:

Investigating the relationship between pluton growth and volcanism in the Central Andes', *Geosphere* **14**(3), 954–982.

Pritchard, M. E., Jay, J. A., Aron, F., Henderson, S. T. & Lara, L. E. (2013), 'Subsidence at southern Andes volcanoes induced by the 2010 Maule, Chile earthquake', *Nature Geoscience* **6**, 632–636.

Quist, A. & Marshall, W. (1968), 'Electrical conductances of aqueous sodium chloride solutions from 0 to 800. degree. and at pressures to 4000 bars', *The journal of physical chemistry* **72**(2), 684–703.

Rampino, M., Self, S. & Fairbridge, R. (1979), 'Can rapid climatic change cause volcanic eruptions?', *Science* **206**(4420), 826–829.

Rasmussen, D., Plank, T., Roman, D. & Zimmer, M. (2022), 'Magmatic water content controls the pre-eruptive depth of arc magmas', *Science* **375**(6585), 1169–1172.

Rawson, H., Pyle, D., Mather, T., Smith, V., Fontijn, K., Lachowycz, S. & Naranjo, J. (2016), 'The magmatic and eruptive response of arc volcanoes to deglaciation: Insights from southern Chile', *Geology* **44**(4), 251–254.

Reasenberg, P. A. & Simpson, W. (1992), 'Response of regional seismicity to the static stress change produced by the Loma Prieta earthquake', *Science* **255**(5052), 1687–1690.

Reinsch, T., Dobson, P., Asanuma, H., Huenges, E., Poletto, F. & Sanjuan, B. (2017), 'Utilizing supercritical geothermal systems: a review of past ventures and ongoing research activities', *Geothermal Energy* **5**(1), 1–25.

Richards, J. P. (2018), 'A shake-up in the porphyry world?', *Economic Geology* **113, no. 6**, 1225–1233.

Richards, J. P., Boyce, A. J. & Pringle, M. S. (2001), 'Geologic evolution of the Escondida area, northern Chile: A model for spatial and temporal lo- calization of porphyry Cu mineralization', *Economic Geology* **96**(2), 271–305.

Rikitake, T. & Sato, R. (1989), 'Up-squeezing of magma under tectonic stress', *Journal of Physics of the Earth* **37**(5), 303–311.

Rivalta, E., Taise, B., Bunger, A. & Katz, R. (2015), 'A review of mechanical models of dike propagation: Schools of thought, results and future directions', *Tectonophysics* **638**, 1–42.

Rocchi, V., Sammonds, P. & Kilburn, C. (2004), 'Fracturing of etnean and vesuvian rocks at high temperatures and low pressures', *Journal of Volcanology and Geothermal Research* **132**(2-3), 137–157.

Rogerson, P. (2018), 'Statistical evidence for long-range space-time relationships between large earthquakes', *Journal of Seismology* **22**(6), 1423–1435.

Roman, D. & Heron, P. (2007), 'Effect of regional tectonic setting on local fault response to episodes of volcanic activity', *Geophysical Research Letters* **34**(13), L13310.

Romanowicz, B. (1993), 'Spatiotemporal patterns in the energy release of great earthquakes', *Science* **260**(5116), 1923–1926.

Rosenberg, C. & Handy, M. (2005), 'Experimental deformation of partially melted granite revisited: implications for the continental crust', *Journal of metamorphic Geology* **23**(1), 19–28.

Rougier, J., Sparks, R. & Cashman, K. (2016), 'Global recording rates for large eruptions', *Journal of Applied Volcanology* **5**(1), 11.

Rougier, J., Sparks, R. & Cashman, K. (2018), 'Regional and global under-recording of large explosive eruptions in the last 1000 years', *Journal of Applied Volcanology* **7**(1), 1–10.

Rougier, J., Sparks, R., Cashman, K. & Brown, S. (2018), 'The global magnitude-frequency relationship for large explosive volcanic eruptions', *Earth and Planetary Science Letters* **482**, 621–629.

Rubin, A. (1995), 'Propagation of magma-filled cracks', *Annual Review of Earth and Planetary Sciences* **23**(1), 287–336.

Ruprecht, P. & Plank, T. (2013), 'Feeding andesitic eruptions with a high-speed connection from the mantle', *Nature* **500**(7460), 68–72.

Ryan, G., Peacock, J., Shalev, E. & Rugis, J. (2013), 'Montserrat geothermal system: A 3D conceptual model', *Geophysical Research Letters* **40**(10), 2038–2043.

Rydelek, P. & Sacks, I. (1999), 'Large earthquake occurrence affected by small stress changes', *Bulletin of the Seismological Society of America* **89**(3), 822–828.

Salfity, J. (1985), Lineamientos transversales al rumbo andino en el noroeste Argentino, *in* J. Frutos, R. Oyarzún & M. Pincheira, eds, 'Congreso Geológico Chileno, IV, Antofagasta, Part 2', Universidad del Norte Chile, Antofagasta, pp. 119–137.

Salfity, J. & Gorustovich, S. (1998), The geological evolution of the province of Salta (Argentina) and neighbouring regions, Technical report, Ministry of Production and Employment, Secretariat of Mining, Industry and Energy Resources, Salta, Argentina.

Sasaki, A. (1955), 'On the electrical conduction of pyrite', *Mineralogical Journal* **1**(5), 290–302.

Sawi, T. M. & Manga, M. (2018), 'Revisiting short-term earthquake triggered volcanism', *Bulletin of Volcanology* **80**(7), 57.

Schellart, W. & Rawlinson, N. (2013), 'Global correlations between maximum magnitudes of subduction zone interface thrust earthquakes and physical parameters of subduction zones', *Physics of the Earth and Planetary Interiors* **225**, 41–67.

Scholz, C., Tan, Y. & Albino, F. (2019), 'The mechanism of tidal triggering of earthquakes at mid-ocean ridges', *Nature communications* **10**, 2526.

Scholz, H. (2019), *The mechanics of earthquakes and faulting*, 3rd edn, Cambridge University Press.

Scott, S., Driesner, T. & Weis, P. (2017), 'Boiling and condensation of saline geothermal fluids above magmatic intrusions', *Geophysical Research Letters* **44**(4), 1696–1705.

Segall, P. (2016), 'Repressurization following eruption from a magma chamber with a viscoelastic aureole', *Journal of Geophysical Research: Solid Earth* **121**(12), 8501–8522.

Sepúlveda, F., Lahsen, A., Bonvalot, S., Cembrano, J., Alvarado, A. & Letelier, P. (2005), 'Morpho-structural evolution of the Cordón Caulle geothermal region, Southern Volcanic Zone, Chile: Insights from gravity and ^{40}Ar/^{39}Ar dating', *Journal of volcanology and geothermal research* **148**(1-2), 165–189.

Seropian, G., Kennedy, B., Walter, T., Ichihara, M. & Jolly, A. (2021), 'A review framework of how earthquakes trigger volcanic eruptions', *Nature Communications* **12**(1), 1–13.

Shanker, D., Kapur, N. & Singh, V. (2001), 'On the spatio temporal distribution of global seismicity and rotation of the Earth—a review', *Acta Geodaetica et Geophysica Hungarica* **36**(2), 175–187.

Shearer, P. & Stark, P. (2012), ‘Global risk of big earthquakes has not recently increased’, *Proceedings of the National Academy of Sciences* **109**(3), 717–721.

Shimomura, Y., Nishimura, T. & Sato, H. (2006), ‘Bubble growth processes in magma surrounded by an elastic medium’, *Journal of volcanology and geothermal research* **155**(3-4), 307–322.

Sibson, R. H. (2017), The edge of failure: critical stress overpressure states in different tectonic regimes, *in* J. Turner, D. Healy, R. Hillis & M. Welch, eds, ‘Geomechanics and geology’, Geological Society, London, Special Publications 458.

Siebert, L., Glicken, H. & Ui, T. (1987), ‘Volcanic hazards from Bezymianny-and Bandai-type eruptions’, *Bulletin of Volcanology* **49**(1), 435–459.

Siebert, L., Simkin, T. & Kimberly, P. (2010), *Volcanoes of the World*, 3rd edn, Univ of California Press.

Sillitoe, R. H. (2010), ‘Porphyry Copper Systems’, *Economic Geology* **105**, 3–41.

Simpson, F. & Bahr, K. (2005), *Practical magnetotellurics*, Cambridge University Press.

Singer, D., Berger, V. & Moring, B. (2005), *Porphyry copper deposits of the world: Database, Maps, Grade and Tonnage Models*, US Department of the Interior, US Geological Survey Reston.

Sinmyo, R. & Keppler, H. (2017), ‘Electrical conductivity of NaCl-bearing aqueous fluids to 600 C and 1 GPa’, *Contributions to Mineralogy and Petrology* **172**(1), 1–12.

Skarlatoudis, A., Somerville, P. & Thio, H. (2016), ‘Source-scaling relations of interface subduction earthquakes for strong ground motion and tsunami simulation’, *Bulletin of the Seismological Society of America* **106**(4), 1652–1662.

Sneddon, I. & Lowengrub, M. (1969), *Crack problems in the classical theory of elasticity*, Wiley, New York.

Solano, J., Jackson, M., Sparks, R., Blundy, J. & Annen, C. (2012), ‘Melt segregation in deep crustal hot zones: a mechanism for chemical differentiation, crustal assimilation and the formation of evolved magmas’, *Journal of Petrology* **53**(10), 1999–2026.

Sparks, R. S. J., Annen, C., Blundy, J., Cashman, K. V., Rust, A. & Jackson, M. (2019), ‘Formation and dynamics of magma reservoirs’, *Philosophical Transactions of the Royal Society A* **377**(2139), 20180019.

Sparks, R. S. J. & Cashman, K. V. (2017), 'Dynamic magma systems: Implications for forecasting volcanic activity', *Elements* **13**(1), 35–40.

Spica, Z., Legrand, D., Iglesias, A., Walter, T., Heimann, S., Dahm, T., Froger, J.-L., Rémy, D., Bonvalot, S., West, M. et al. (2015), 'Hydrothermal and magmatic reservoirs at Lazufre volcanic area, revealed by a high-resolution seismic noise tomography', *Earth and Planetary Science Letters* **421**, 27–38.

Stein, R. S. (1999), 'The role of stress transfer in earthquake occurence', *Nature* **402**, 605–609.

Stein, R. S., Barka, A. A. & Dieterich, J. H. (1997), 'Progressive failure on the North Anatolian fault since 1939 by earthquake stress triggering', *Geophysical Journal International* **128**, 594–604.

Stein, R. S., King, G. C. P. & Lin, J. (1992), 'Change in the failure stress on the Southern San Andreas fault system caused by the 1992 magnitude = 7.4 Landers earthquake', *Science* **258**, 1328–1332.

Stimac, J., Goff, F. & Goff, C. (2015), Intrusion-related geothermal systems, *in* 'The encyclopedia of volcanoes', Elsevier, pp. 799–822.

Storchak, D., Di Giacomo, D., Bondár, I., Engdahl, E., Harris, J., Lee, W., Villaseñor, A. & Bormann, P. (2013), 'Public release of the ISC-GEM global instrumental earthquake catalogue (1900-2009)', *Seismological Research Letters* **84**(5), 810–815.

Storchak, D., Di Giacomo, D., Engdahl, E., Harris, J., Bondár, I., Lee, W., Bormann, P. & Villaseñor, A. (2015), 'The ISC-GEM global instrumental earthquake catalogue (1900-2009): introduction', *Physics of the Earth and Planetary Interiors* **239**, 48–63.

Strasser, F., Arango, M. & Bommer, J. (2010), 'Scaling of the source dimensions of interface and intraslab subduction-zone earthquakes with Moment Magnitude', *Seismological Research Letters* **81**(6), 941–950.

Sun, T. & Wang, K. (2015), 'Viscoelastic relaxation following subduction earthquakes and its effects on afterslip determination', *Journal of Geophysical Research: Solid Earth* **120**(2), 1329–1344.

Tagiri, M., Moreno, H., Lṕpez-Escobar, L. & Notsu, K. (1993), 'Two magma types of the high-alumina basalt series of Osorno Volcano, Southern Andes (41 06 S) - plagioclase dilution effect', *Journal of Mineralogy, Petrology and Economic Geology* **88**(7), 359–371.

Taisne, B. & Jaupart, C. (2009), 'Dike propagation through layered rocks', *Journal of Geophysical Research: Solid Earth* **114**(B9).

Tait, S., Jaupart, C. & Vergniolle, S. (1989), 'Pressure, gas content and eruption periodicity of a shallow, crystallising magma chamber', *Earth and Planetary Science Letters* **92**(1), 107–123.

Tajima, R., Matsumoto, Y. & Irikura, K. (2013), 'Comparative study on scaling relations of source parameters for great earthquakes in inland crusts and on subducting plate-boundaries', *Zisin* **66**(3), 31–45.

Takada, Y. & Fukushima, Y. (2013), 'Volcanic subsidence triggered by the 2011 Tohoku earthquake in Japan', *Nature Geoscience* **6**, 636–641.

Takei, Y. (2002), 'Effect of pore geometry on VP/VS: From equilibrium geometry to crack', *Journal of Geophysical Research: Solid Earth* **107**(B2), ECV–6.

Tatsumi, Y. (1989), 'Migration of fluid phases and genesis of basalt magmas in subduction zones', *Journal of Geophysical Research: Solid Earth* **94**(B4), 4697–4707.

Tattitch, B., Chelle-Michou, C., Blundy, J. & Loucks, R. (2021), 'Chemical feedbacks during magma degassing control chlorine partitioning and metal extraction in volcanic arcs', *Nature communications* **12**(1), 1–11.

Ten Grotenhuis, S., Drury, M., Spiers, C. & Peach, C. (2005), 'Melt distribution in olivine rocks based on electrical conductivity measurements', *Journal of Geophysical Research: Solid Earth* **110**(B12).

Thingbaijam, K., Mai, P. & Goda, K. (2017), 'New empirical earthquake source-scaling laws', *Bulletin of the Seismological Society of America* **107**(5), 2225–2246.

Tichelaar, R. & Ruff, L. (1993), 'Depth of seismic coupling along subduction zones', *Journal of Geophysical Research: Solid Earth* **98**(B2), 2017–2037.

Toda, S., Stein, R. S., Reasenberg, P. A. & Dieterich, J. H. (1998), 'Stress transferred by the Mw= 6.5 Kobe, Japan, shock: Effect on aftershocks and future earthquake probabilities', *Journal of Geophysical Research* **103**, 24543–24565.

Toda, S., Stein, R. S., Richards-Dinger, K. & Bozkurt, S. (2005), 'Forecasting the evolution of seismicity in southern California: Animations built on earthquake stress transfer', *Journal of Geophysical Research: Solid Eearth* **110**(B5), 1–17.

Tosdal, R. M. & Richards, J. P. (2001), 'Magmatic and structural controls on the development of porphyry Cu ± Mo ± Au deposits', *Reviews in Economic Geology* **14**, 157–181.

Townend, J., Sherburn, S., Arnold, R., Boese, C. & Woods, L. (2012), 'Three-dimensional variations in present-day tectonic stress along the australia-pacific plate boundary in new zealand', *Earth and Planetary Science Letters* **353**, 47–59.

Townend, J. & Zoback, M. (2000), 'How faulting keeps the crust strong', *Geology* **28**(5), 399–402.

Tuel, A., Naveau, P. & Ammann, C. (2017), 'Skillful prediction of multidecadal variations in volcanic forcing', *Geophysical Research Letters* **44**(6), 2868–2874.

Turner, S. & Costa, F. (2007), 'Measuring timescales of magmatic evolution', *Elements* **3**(4), 267–272.

Uchida, T., Ogawa, Y., Takakura, S. & Mitsuhata, Y. (2000), Geoelectrical investigation of the Kakkonda geothermal field, northern Japan, *in* 'proceedings world geothemal congress, Tohoku-Kyushu, Japan', pp. 1893–1898.

Vella, L. & Emerson, D. (2012), 'Electrical properties of magnetite-and hematite-rich rocks and ores', *ASEG Extended Abstracts* **2012**(1), 1–4.

Vigneresse, J., Barbey, P. & Cuney, M. (1996), 'Rheological transitions during partial melting and crystallization with application to felsic magma segregation and transfer', *Journal of Petrology* **37**(6), 1579–1600.

Voight, B. (2000), 'Structural stability of andesite volcanoes and lava domes', *Philosophical Transactions of the Royal Society of London. Series A: Mathematical, Physical and Engineering Sciences* **358**(1770), 1663–1703.

Voight, B., Janda, R., Glicken, H. & Douglass, P. (1983), 'Nature and mechanics of the Mount St Helens rockslide-avalanche of 18 May 1980', *Geotechnique* **33**(3), 243–273.

Voight, B., Linde, A., Sacks, I., Mattioli, G., Sparks, R., Elsworth, D., Hidayat, D., Malin, P. et al. (2006), 'Unprecedented pressure increase in deep magma reservoir triggered by lava-dome collapse', *Geophysical Research Letters* **33**(3), L03312.

Vrolijk, P. (1990), 'On the mechanical role of smectite in subduction zones', *Geology* **18**(8), 703–707.

Waff, H. (1974), 'Theoretical considerations of electrical conductivity in a partially molten mantle and implications for geothermometry', *Journal of Geophysical Research* **79**(26), 4003–4010.

Walter, T. R. & Amelung, F. (2006), 'Volcano-earthquake interaction at Mauna Loa Volcano, Hawaii', *Journal of Geophysical Research* **111**, B05204.

Walter, T. R. & Amelung, F. (2007), 'Volcanic eruptions following M>9 megathrust earthquakes: Implications for the Sumatra-Andaman volcanoes', *Geology* **35**(6), 539–542.

Wang, K., Hu, Y. & He, J. (2012), 'Deformation cycles of subduction earthquakes in a viscoelastic earth', *Nature* **484**(7394), 327–332.

Ward, K., Zandt, G., Beck, S., Christensen, D. & McFarlin, H. (2014), 'Seismic imaging of the magmatic underpinnings beneath the Altiplano-Puna volcanic complex from the joint inversion of surface wave dispersion and receiver functions', *Earth and Planetary Science Letters* **404**, 43–53.

Watanabe, N., Mogi, T., Yamaya, Y., Kitamura, K., Asanuma, H. & Tsuchiya, N. (2022), 'Electrical conductivity of H2O-NaCl fluids under supercritical geothermal conditions and implications for deep conductors observed by the magnetotelluric method', *Geothermics* **101**, 102361.

Watanabe, N., Numakura, T., Sakaguchi, K., Saishu, H., Okamoto, A., Ingebritsen, S. & Tsuchiya, N. (2017), 'Potentially exploitable supercritical geothermal resources in the ductile crust', *Nature Geoscience* **10**(2), 140–144.

Watanabe, N., Yamaya, Y., Kitamura, K. & Mogi, T. (2021), 'Viscosity-dependent empirical formula for electrical conductivity of H2O-NaCl fluids at elevated temperatures and high salinity', *Fluid Phase Equilibria* **549**, 113187.

Watt, S. F. L., Pyle, D. M. & Mather, T. A. (2009), 'The influence of great earthquakes on volcanic eruption rate along the Chilean subduction zone', *Earth and Planetary Science Letters* **277**(3-4), 399–407.

Wells, D. & Coppersmith, K. (1994), 'New empirical relationships among magnitude, rupture length, rupture width, rupture area, and surface displacement', *Bulletin of the Seismological Society of America* **84**, 974–1002.

Wespestad, C., Thurber, C., Andersen, N., Singer, B., Cardona, C., Zeng, X., Bennington, N., Keranen, K., Peterson, D., Cordell, D. et al. (2019), 'Magma reservoir below Laguna del Maule volcanic field, Chile, imaged with surface-wave tomography', *Journal of Geophysical Research: Solid Earth* **124**(3), 2858–2872.

Wyss, M. & Toya, Y. (2000), 'Is background seismicity produced at a stationary Poissonian rate?', *Bulletin of the Seismological Society of America* **90**(5), 1174–1187.

Yoshino, T., Laumonier, M., McIsaac, E. & Katsura, T. (2010), 'Electrical conductivity of basaltic and carbonatite melt-bearing peridotites at high pressures: Implications for melt distribution and melt fraction in the upper mantle', *Earth and Planetary Science Letters* **295**(3-4), 593–602.

Zaliapin, I. & Kreemer, C. (2017), 'Systematic fluctuations in the global seismic moment release', *Geophysical Research Letters* **44**(10), 4820–4828.

Zandt, G., Leidig, M., Chmielowski, J., Baumont, D. & Yuan, X. (2003), 'Seismic detection and characterization of the Altiplano-Puna magma body, central Andes', *Pure and Applied Geophysics* **160**(3), 789–807.

Zhang, B.-H., Guo, X., Yoshino, T. & Xia, Q.-K. (2021), 'Electrical conductivity of melts: Implications for conductivity anomalies in the Earth's mantle', *National Science Review* **8**, nwab064.

Ziv, A. & Rubin, A. (2000), 'Static stress transfer and earthquake triggering: No lower threshold in sight?', *Journal of Geophysical Research: Solid Earth* **105**(B6), 13631–13642.

Ziv, A., Rubin, A. & Agnon, A. (2000), 'Stability of dike intrusion along preexisting fractures', *Journal of Geophysical Research: Solid Earth* **105**(B3), 5947–5961.

Zoback, M. (1992), 'First and second order patterns of stress in the lithosphere: the World Stress Map Project', *Journal of Geophysical Research: Solid Earth* **97**(B8), 11703–11728.

Zoback, M. & Zoback, M. (1980), 'State of stress in the conterminous United States', *Journal of Geophysical Research* **85**, 6113–6156.

Zoback, M., Zoback, M., Adams, J., Assumpção, M., Bell, S., Bergman, E. et al. (1989), 'Global patterns of tectonic stress', *Nature* **341**, 291–298.